



**Università
degli Studi
di Ferrara**

DOCTORAL COURSE IN
ENGINEERING SCIENCE

CYCLE XXXV

Coordinator: Prof. Stefano TRILLO, PhD

The arterial cardiovascular network: modelling and applications

SCIENTIFIC / DISCIPLINARY SECTOR (SDS) ICAR/01

Candidate:

Francesco PICCIOLI

Supervisors:

Prof. Alessandro VALIANI, PhD


Prof. Valerio CALEFFI, PhD

Years 2019/2022

Declaration of Authorship

I, Francesco PICCIOLI, declare that this thesis titled, "The arterial cardiovascular network: modelling and applications" and the work presented in it are my own. I confirm that:

- This work was done wholly or mainly while in candidature for a research degree at this University.
- Where any part of this thesis has previously been submitted for a degree or any other qualification at this University or any other institution, this has been clearly stated.
- Where I have consulted the published work of others, this is always clearly attributed.
- Where I have quoted from the work of others, the source is always given. With the exception of such quotations, this thesis is entirely my own work.
- I have acknowledged all main sources of help.
- Where the thesis is based on work done by myself jointly with others, I have made clear exactly what was done by others and what I have contributed myself.

Signed: 

Date: 8/3/2023

"All beginnings are hard."

Chaim Potok

Abstract

In silico numerical models, based on the fundamentals of fluid mechanics, are a powerful resource to aid the research in healthcare. These physically-based models represent an asset to comprehensively analyse, understand, and complement information gathered from clinical, *in vivo* data. To provide physiological and trustworthy results, the utmost attention must be posed on the correct representation of the interaction between blood and blood vessels.

This PhD Thesis presents a cardiovascular model composed of a cardiac contraction model representing the left part of the heart properly coupled to the arterial network at the aortic root, therefore accounting for the ventricular-aortic interaction. The model is able to accurately predict the behaviour of the fluid-structure interaction that underlies the dynamics of blood in extended networks. A sophisticated 3-element viscoelastic model is employed for the mechanical characterisation of vessels walls, and applied to obtain the fluid-structure interaction system in which the constitutive equation of the material is directly inserted into the system of partial differential equations. The system is solved recurring to a second-order Finite Volume Method together with an efficient and robust numerical scheme for the integration of hyperbolic balance laws systems.

The first part of the Thesis focuses on the development of a numerical model for extended arterial networks where the viscoelastic contribution given by the constitutive equation is accounted for in all boundary sections of the network itself. In this context, the numerical treatment of junctions is based on the solution of a Riemann problem, and relies on a non-linear system of equations that guarantees the conservation of mass and total pressure in the junction. This numerical approach, which is extended to inlet and outlet sections of the network, is firstly validated in simple test cases and then in networks of increasing complexity.

The second part of the Thesis presents applications of the developed cardiovascular network together with pulse wave analysis to investigate the effect of cardiac properties on arterial pulse waves. A computational proof-of-concept is performed to investigate how cardiac properties affect central and peripheral pulse waves and PPG pulse waves, and to what extent a cardiac dysfunction can be detected by the analysis of these physiological signals. Moreover, the research presents a state-of-the-art application of the cardiovascular model in the field of isolate systolic hypertension, which is a cardiovascular disease that often manifests with an increase in pulse pressure. *In vivo* data of measured blood pressure and velocity and *in silico* data obtained with the proposed numerical model are analysed complementarily to better understand the role of cardiac function and the haemodynamic mechanisms underlying pulse pressure elevation and its amplification in the periphery of the systemic circulation.

Key findings

- The presented Junction Riemann problem is able to treat internal boundary conditions, i.e., branching and merging blood vessels sites, and external boundary conditions, i.e., inlet and outlet sections of the network model, consistently with the mathematical formulation of the governing system and the viscoelastic Standard Linear Solid Model chosen to simulate the fluid-structure interaction, conserving the prescribed order of accuracy.
- Capability of the viscoelastic Standard Linear Solid Model applied to extended arterial networks to properly simulate the physiological behaviour of central and peripheral blood vessels walls when undergoing pressure pulses.
- Strong dependence of the manifestation of the damping effect of blood vessels walls, displayed by the widening of hysteresis loops, on input viscoelastic parameters.
- Left atrium contractility manifests smaller effects on vascular pulse waves than left ventricular contractility, which instead can greatly affect blood pressure shape and amplitude, being a driver of pulse pressure and pulse pressure amplification.
- The timing of the dicrotic notch is eligible to be a left ventricular dysfunction indicator.
- Cardiac valves impairment can be detected from pulse waves analysis.
- Left ventricular ejection and contractility directly influence the aortic flow rate, which, in turns, has a key role in pulse pressure increase and its amplification towards the periphery of the circulation. The mechanics of this phenomenon is backed up by the increase in the forward blood pressure wave.
- PPG signals are suitable as easy-accessible data for cardiac dysfunction monitoring.

Sommario

I modelli numerici per l'emodinamica basati sui fondamenti della meccanica dei fluidi, anche denominati modelli *in silico*, sono una preziosa risorsa per la ricerca in campo sanitario. Questi modelli fisicamente basati rappresentano una risorsa per analizzare, comprendere e integrare in modo esaustivo le informazioni raccolte dai dati clinici, anche detti *in vivo*. Per fornire risultati fisiologici e attendibili, è necessario porre la massima attenzione nella corretta rappresentazione dell'interazione tra il sangue e i vasi sanguigni.

Questa Tesi di Dottorato presenta un modello cardiovascolare composto da un modello di contrazione cardiaca rappresentante la parte sinistra del cuore, propriamente accoppiato alla rete arteriosa in corrispondenza della radice aortica, che permette quindi di tenere conto dell'interazione ventricolo-aortica. Il modello è in grado di prevedere accuratamente il comportamento dell'interazione fluido-struttura che è alla base della dinamica del sangue in reti circolatorie estese. Un sofisticato modello viscoelastico a 3 elementi viene impiegato per la caratterizzazione meccanica delle pareti dei vasi e applicato per ottenere il sistema di interazione fluido-struttura, in cui l'equazione costitutiva del materiale viene inserita direttamente nel sistema di equazioni alle derivate parziali. Il sistema viene risolto ricorrendo a un Metodo ai Volumi Finiti del secondo ordine ed a uno schema numerico efficiente e robusto per l'integrazione di sistemi iperbolici di leggi di bilancio.

La prima parte della Tesi si concentra sullo sviluppo di un modello numerico per reti arteriose estese in cui il contributo viscoelastico dato dall'equazione costitutiva è considerato in tutte le sezioni della rete stessa. A tal scopo, l'implementazione numerica delle giunzioni è basata sulla soluzione di un problema di Riemann, e si basa su un sistema di equazioni non lineari che garantisce la conservazione della massa e della pressione totale in ciascuna giunzione. Questo approccio numerico, che viene esteso alle sezioni in ingresso e di uscita della rete, viene prima convalidato con test semplici e successivamente con reti di complessità crescente.

La seconda parte della Tesi presenta applicazioni del modello cardiovascolare, insieme all'analisi dei segnali d'impulso fisiologici, per studiare l'effetto delle proprietà cardiache sui segnali stessi. Viene eseguita un'analisi di natura computazionale per studiare come le proprietà cardiache influenzano i segnali di impulso arteriosi, centrali e periferici, e i segnali PPG, e in che misura una disfunzione cardiaca possa essere rilevata dall'analisi di questi stessi segnali. Inoltre, la ricerca presenta una applicazione innovativa del modello cardiovascolare nel campo dell'ipertensione sistolica isolata, una malattia cardiovascolare che spesso si manifesta con un aumento della pressione differenziale arteriosa. I dati di pressione e velocità misurati *in vivo* e quelli *in silico* ottenuti con il modello numerico proposto sono stati analizzati in modo complementare, per comprendere meglio il ruolo della funzione cardiaca e i meccanismi emodinamici alla base dell'innalzamento della pressione differenziale arteriosa e della sua amplificazione verso la periferia della circolazione sistemica.

Risultati principali

- Il problema di Riemann presentato alla giunzione è in grado di trattare le condizioni al contorno interne, cioè i siti di biforcazione e confluenza dei vasi sanguigni, e le condizioni al contorno esterne, cioè le sezioni di ingresso e di uscita del modello di rete, coerentemente con la formulazione matematica del sistema di governo e il modello viscoelastico Standard Linear Solid Model scelto per simulare l'interazione fluido-struttura, conservando l'ordine di accuratezza prescritto.
- Capacità del modello viscoelastico Standard Linear Solid applicato a reti arteriose estese di simulare correttamente il comportamento fisiologico delle pareti dei vasi sanguigni centrali e periferici quando vengono sottoposti a impulsi di pressione.
- Forte dipendenza della manifestazione dell'effetto di smorzamento delle pareti dei vasi sanguigni, mostrata dall'allargamento dei cicli di isteresi, dai parametri viscoelastici in ingresso al modello.
- La contrattilità dell'atrio sinistro ha effetti minori sulle onde di impulso vascolari rispetto alla contrattilità del ventricolo sinistro, che invece può influenzare notevolmente la forma e l'ampiezza della pressione arteriosa, essendo determinante per la pressione differenziale e per la sua amplificazione periferica.
- L'analisi dell'incisura dicota è idonea a essere un indicatore di disfunzione ventricolare sinistra.
- Il malfunzionamento delle valvole cardiache può essere rilevata dall'analisi delle onde del polso.
- L'eiezione e la contrattilità del ventricolo sinistro influenzano direttamente la portata aortica che, a sua volta, ha un ruolo chiave nell'aumento della pressione differenziale arteriosa e nella sua amplificazione verso la periferia della circolazione. La meccanica di questo fenomeno è corroborata dall'aumento dell'onda pressoria in avanti.
- I segnali PPG sono dati di facile reperibilità adatti per il monitoraggio della disfunzione cardiaca.

Acknowledgements

First and foremost, I would like to express my sincere appreciation to my supervisors Prof. Alessandro Valiani and Prof. Valerio Caleffi, first of all for giving me the chance to join this PhD programme. Thank you for providing me with support and insightful criticism throughout all these three years. I deeply appreciate the trust and respect you have always had for of my work. A heartfelt thank goes to Valerio, who was always present and believing in this bio–fluid project.

I would like to thank Dr. Giulia Bertaglia, for giving me the burden and honour of keeping her research on blood flow modelling alive and carry it on for the development on the network and following applications in healthcare research. Thank you for your patience and support.

I am especially thankful to Dr. Jordi Alastruey for giving me the chance to undertake my visiting period at the Department of Biomedical Engineering and Imaging Science (BMEIS) at King’s College London and warmly welcoming me in the Haemodynamic Modelling Research Group (HaeMod). I will always remember this collaboration, from which I feel enormously enriched, with extreme positiveness. Thank you for the fruitful and rewarding conversations, and the time you have spent advising me.

I am pleased to acknowledge Dr. Ye Li (School of Cardiovascular Medicine & Sciences, King’s College London) for providing me with in vivo data, which were essential for the analysis on hypertension. I would like to thank Prof. Philip Chowińczyk (School of Cardiovascular Medicine & Sciences, King’s College London) for his support in the completion of the work on hypertension. His clinical oversight was extremely helpful and formative.

I would like to address the interesting collaboration that I have undertaken with Dr. Joaquín Flores Gerónimo (The Hong Kong Polytechnic University), thanking him for for giving me the opportunity to contribute to the development of his project.

I would like to warmly thank my peer colleagues who were, above all, true friends. Thank you for being always someone to rely on and making the workplace a pleasant place to be. Thanks also to the other close people that were present alongside this path, enjoying with me for my accomplishments.

I am hugely thankful to Alice, who has always been my rock to cling to during difficult times and a booster in confidence, supporting me more than anybody else.

Finally, I want to extend my warmest thanks to my family for being always present and backing me up, giving me the wisest advice.

Scientific production

Journal papers produced and in progress during this PhD research project:

Gerònimo, J. F., **F. Piccioli**, and J. Alastruey. Article in preparation.

Piccioli, F., Y. Li, A. Valiani, V. Caleffi, P. Chowienczyk, and J. Alastruey. "Role of cardiac contractility in determining pulse pressure and its peripheral amplification". Submitted to *Circulation* in November 2022.

Piccioli, F., A. Valiani, J. Alastruey, and V. Caleffi. "The effect of cardiac properties on arterial pulse waves: An in-silico study". In: *International Journal for Numerical Methods in Biomedical Engineering*, doi:10.1002/cnm.3658 (2022).

Piccioli, F., G. Bertaglia, V. Caleffi, and A. Valiani. "Modeling blood flow in networks of viscoelastic vessels with the 1-D augmented fluid-structure interaction system". In: *Journal of Computational Physics*, 464: 111364 (2022).

Conference contributes to this PhD research project:

Piccioli, F., Y. Li, A. Valiani, V. Caleffi, P. Chowienczyk, and J. Alastruey. "On the relative role of cardiac and vascular properties in raising pulse pressure". *9th World Congress on Biomechanics*, Taipei City, Taiwan (2022).

Piccioli, F., A. Valiani, J. Alastruey, and V. Caleffi. "On the assessment of cardiac function from pulse waves. A computational study". *7th International Conference on Computational and Mathematical Biomedical Engineering*, Politecnico di Milano, Campus Leonardo, Milan, Italy (2022).

Piccioli, F., G. Bertaglia, A. Valiani, and V. Caleffi. "Consistent treatment of boundary conditions for blood flow modelling in network of viscoelastic vessels". *7th International Conference on Computational and Mathematical Biomedical Engineering*, Politecnico di Milano, Campus Leonardo, Milan, Italy (2022).

Piccioli, F., A. Valiani, J. Alastruey, and V. Caleffi. "Valutazione delle proprietà cardiache tramite l'analisi delle forme d'onda nel sistema cardiovascolare". *XXXVIII Convegno Nazionale di Idraulica e Costruzioni Idrauliche*, Università degli Studi Mediterranea di Reggio Calabria, Reggio Calabria, Italy (2022).

Piccioli, F., Y. Li, A. Valiani, V. Caleffi, P. Chowienczyk, and J. Alastruey. "Ruolo relativo delle proprietà cardiache e vascolari nella determinazione della pressione sanguigna". *XXXVIII Convegno Nazionale di Idraulica e Costruzioni Idrauliche*, Università degli Studi Mediterranea di Reggio Calabria, Reggio Calabria, Italy (2022).

Piccioli, F., G. Bertaglia, A. Valiani, and V. Caleffi. "Consistent treatment of boundary conditions for viscoelastic arterial networks governed by conservative laws with relaxation terms". *Workshop on Efficient high-order time discretization methods for PDEs*, Villa Orlandi, Anacapri, Italy (2022).

Piccioli, F., G. Bertaglia, A. Valiani, and V. Caleffi. "Modellazione del flusso sanguigno in reti di vasi viscoelastici". *XXXVII Convegno Nazionale di Idraulica e Costruzioni Idrauliche*, Online (2021).

Contents

Declaration of Authorship	iii
Abstract	vii
Sommario	ix
Acknowledgements	xi
Scientific production	xiii
Contents	xv
List of Figures	xix
List of Tables	xxiii
List of Abbreviations	xxv
List of Symbols	xxvii
1 Introduction	1
1.1 Background and Motivation	1
1.2 Aims and Objectives	2
1.3 Thesis Outline	3
2 The cardiovascular network	7
2.1 Introduction	7
2.1.1 Composition and type of vessels	7
2.2 The arterial system	8
2.2.1 Stiffness of arteries	8
Pulse wave velocity	9
Arterial compliance	10
2.2.2 Pressure and flow in arteries	11
2.2.3 Pulse wave analysis	14
Wave separation	14
Fiducial points	15
Pulse waveforms indices	17
2.2.4 Measurements of pressure and velocity waveforms	18
2.3 The heart	19
2.3.1 The cardiac cycle	21
2.4 Hypertension	23

3	The haemodynamic mathematical model	25
3.1	Background	25
3.1.1	Mathematical models for viscoelastic materials	25
	The Standard Linear Solid Model	27
3.1.2	Hyperbolic balance laws in fluid mechanics	29
	The Riemann problem	32
	One-dimensional balance laws	34
3.2	The 1-D augmented fluid-structure-interaction (a-FSI) system	37
3.2.1	Friction loss model	39
3.2.2	Tube law	39
	Source term stiffness	41
	Asymptotic limits	41
3.2.3	Eigenstructure and Riemann Invariants	42
3.3	0-D boundary conditions	44
3.3.1	Cardiac contraction model	44
	Cardiac chambers	44
	Cardiac valves	47
	Pulmonary venous flow rate	48
3.3.2	Microvasculature	48
4	Numerical scheme for networks of viscoelastic vessels	51
4.1	Introduction	51
4.2	Numerical method	53
4.2.1	AP-IMEX Runge-Kutta Finite Volume scheme	54
4.2.2	Boundary conditions	56
	Inlet BC	56
	Outlet BC	57
	Junction BC	58
	High order of accuracy at boundaries	61
4.3	Numerical results	62
4.3.1	2-vessel junction	63
	Accuracy analysis and well-balancing property	65
4.3.2	3-vessel junction	67
4.3.3	Human arterial networks	70
	AN37	70
	ADAN56	74
4.4	Concluding remarks	76
5	The effect of cardiac properties on arterial pulse waves	83
5.1	Introduction	83
5.2	Cardiac function assessment using the pulse wave analysis	84
5.2.1	Methods	85
	Cardiovascular model	85
	Significant parameters evaluation	85
	Haemodynamic indices	87
5.2.2	Results	87
	Cardiovascular model verification	87
	Significant cardiac parameters	89
	Haemodynamic indices	91
5.2.3	Discussion	92
5.3	Ventricular ejection and pulse pressure	95

5.3.1	Methods	95
	<i>In vivo</i> data: Invasive cohort	96
	<i>In vivo</i> data: Noninvasive cohorts	96
	<i>In silico</i> data: Computational haemodynamics model	97
	Waveform Post-processing	97
	Statistics	98
5.3.2	Results	98
	Cardiac contractility, arterial compliance and PP	98
	Changes in aortic flow	100
	Relative contributions of contractility and compliance to PP	101
	The role of aortic and peripheral wave reflections	102
5.3.3	Discussion	103
5.4	Concluding remarks	107
6	Conclusions	109
6.1	Overview	109
6.2	Main findings and Original contributions	109
6.2.1	Viscoelasticity in extended networks	110
6.2.2	Key role of ventricular ejection in shaping vascular pulse waves	110
6.3	Future work	111
A	Viscoelastic SLSM parameters of numerical tests	113
B	Simulation of PPG signals	115
C	Cardiac function assessment using the pulse wave analysis	117
C.1	Sensitivity Analysis: reference parameters	117
C.2	Sensitivity Analysis: RMSD	117
D	Ventricular ejection and pulse pressure	119
	Bibliography	125

List of Figures

2.1	Hydraulic–electric analogy	12
2.2	Wave separation analysis for blood pressure wave, p	15
2.3	Schematic representation of the central blood pressure wave with the first (P1) and second (P2) central systolic peaks, and the peripheral blood pressure wave with the first (pSBP) and second (pSBP2) peripheral systolic blood pressures.	16
2.4	Sketch of a cross section of the heart showing the gross anatomy.	20
2.5	Pressure (p_{LV})–volume (v_{LV}) loop for the left ventricle (LV).	21
3.1	Schematic representation of the three behavioural features of a viscoelastic material.	26
3.2	Schemes of the Maxwell, Kelvin-Voigt, and Standard Linear Solid models.	27
3.3	Illustration of the initial condition and solution for a Riemann problem considering one PDE.	32
3.4	Structure of the solution of a Riemann problem for a 2×2 linear hyperbolic system.	33
3.5	Elementary wave solutions of the Riemann problem.	34
3.6	Schematic representation of the 0–D cardiac contraction model.	45
3.7	Pulmonary venous flow rate entering the left atrium in one cardiac cycle.	47
3.8	RCR Windkessel model simulating the microvasculature at terminal vessels.	48
4.1	Schematic representation of the haemodynamic cardiovascular model, and results of central and peripheral blood pressure waveforms.	52
4.2	3–vessel junction scheme.	59
4.3	Results of the 2–vessel junction test performed for a generic artery.	63
4.4	Results of the 2–vessel junction test performed for a generic vein.	64
4.5	Results of the 3–vessel junction test, concerning an aortic bifurcation problem.	68
4.6	Hysteresis loops of the 3–vessel test, concerning an aortic bifurcation, in abdominal aorta and iliac artery.	69
4.7	Results of the AN37 network for the aortic arch and thoracic aorta.	71
4.8	Results of the AN37 network for the right iliac femoral artery and right anterior tibial artery.	72
4.9	Results of the AN37 network for the right ulnar artery and left ulnar artery.	73
4.10	Results of the AN37 network for the left subclavian artery and splenic artery.	74
4.11	Hysteresis loop obtained for the aortic arch II in the AN37 network.	75
4.12	Results of the ADAN56 network for the aortic arch and the thoracic aorta.	76

4.13	Results of the ADAN56 network for the abdominal aorta and the right common carotid artery.	77
4.14	Results of the ADAN56 network for the right internal carotid artery and the right radial artery.	78
4.15	Results of the ADAN56 network for the right renal artery and the right common iliac artery.	79
4.16	Results of the ADAN56 network for the internal iliac artery and the right posterior interosseous artery.	80
4.17	Results of the ADAN56 network for the right femoral artery and the right anterior tibial artery.	81
4.18	Hysteresis loop obtained for various arteries in the ADAN56 network.	82
5.1	Haemodynamic results of the cardiovascular model.	88
5.2	RMSDs computed at the aortic root, brachial and digital arteries for simulations with the increased and decreased cardiac parameters values.	89
5.3	Pulse waveforms at baseline, and with increased and decreased values in the significant cardiac parameters.	90
5.4	Percentage variations in haemodynamic indices with increased and decreased values in the significant cardiac parameters.	91
5.5	The relationship between the systolic index of contractility or arterial compliance and central pulse pressure, peripheral pulse pressure, and pulse pressure amplification in the normotensive cohort.	99
5.6	The relationship between the systolic index of contractility or arterial compliance and central pulse pressure, peripheral pulse pressure, and pulse pressure amplification in the <i>in silico</i> data.	100
5.7	Aortic flow, aortic pressure, and radial pressure waveforms analysis with increasing cardiac contractility and decreasing arterial compliance.	101
5.8	Variations in aortic peak flow, rate of increase in early-systolic aortic flow, and rate of decrease in late-systolic aortic flow with increasing contractility and compliance in the normotensive cohort.	102
5.9	Aortic flow characteristics variations with pharmacological administration in the normotensive cohort.	103
5.10	Variations in central pulse pressure, peripheral PP, and PP amplification with increasing contractility and compliance in the normotensive cohort.	104
5.11	The relationship between peak emission or reflection coefficients and central pulse pressure.	105
D.1	The relationship between the systolic index of contractility or arterial compliance and central pulse pressure, peripheral pulse pressure, and pulse pressure amplification in the hypertensive cohort.	122
D.2	The relationship between the systolic index of contractility and central pulse pressure, peripheral pulse pressure, and pulse pressure amplification in the invasive normotensive cohort.	123
D.3	<i>In vivo</i> central blood pressure waveform variations with administration of dobutamine and noradrenaline.	123
D.4	Variations in central pulse pressure, peripheral pulse pressure, and pulse pressure amplification with normalised contractility and compliance in the normotensive cohort.	124

D.5	Variations in central pulse pressure, peripheral pulse pressure, and pulse pressure amplification with normalised contractility and compliance in the hypertensive cohort.	124
D.6	Variations in central pulse pressure, peripheral pulse pressure, and pulse pressure amplification with normalised contractility and compliance in the hypertensive cohort.	124

List of Tables

2.1	Hypertensive conditions classified by systolic and diastolic blood pressure values.	23
4.1	Parameters of the 2–vessel junction test, valid for a generic artery and a generic vein.	62
4.2	Parameters of the accuracy analysis performed for the 2–vessel junction test, considering a generic artery and a generic vein.	65
4.3	Results of the accuracy analysis performed for the 2–vessel junction test, concerning a generic artery and a generic vein with elastic vessel walls.	66
4.4	Results of the accuracy analysis performed for the 2–vessel junction test, concerning a generic artery and a generic vein with viscoelastic vessel walls.	67
5.1	Vascular and cardiac parameters of the <i>in silico</i> , numerical model.	86
A.1	Viscoelastic SLSM parameters for the aortic bifurcation test: instantaneous Young modulus E_0 , asymptotic Young modulus E_∞ , ratio $z = E_\infty/E_0$, viscosity coefficient η and relaxation time τ_r	113
A.2	Viscoelastic SLSM parameters for the ADAN56 network: instantaneous Young modulus E_0 , asymptotic Young modulus E_∞ , ratio $z = E_\infty/E_0$, viscosity coefficient η and relaxation time τ_r	113
A.3	Viscoelastic SLSM parameters for the AN37 network: instantaneous Young modulus E_0 , asymptotic Young modulus E_∞ , ratio $z = E_\infty/E_0$, viscosity coefficient η and relaxation time τ_r	114
C.1	Reference parameters of the cardiac contraction model for the heart chambers: left atrium (LA) and left ventricle (LV).	117
C.2	Reference parameters of the cardiac contraction model for the heart valves: mitral valve (MV) and aortic valve (AV). The reference A_{min} is equal to zero for both valves.	117
C.3	Root mean square deviations (RMSD) in mmHg resulted from the sensitivity analysis performed in an univariate manner	118
D.1	Characteristics of the <i>in vivo</i> cohorts and <i>in silico</i> model	119
D.2	Variations in haemodynamic quantities with administration of pharmacological drugs in the normotensive cohort	120
D.3	Variations in haemodynamic quantities with administration of GTN in the invasive cohort	121
D.4	Fiducial point variations	121

List of Abbreviations

0-D	0 Dimensional
1-D	1 Dimensional
3-D	3 Dimensional
AbA	Abdominal Aorta
ABP	Augmented Blood Pressure
ADER	Arbitrary high-order DERivatives
a-FSI	augmented Fluid-Structure Interaction
AIx	Augmentation Index
Ao	Aorta
AoRt	Aortic Root
AP	Asymptotic Preserving
AR	Pulse pressure Augmentation Ratio
AV	Aortic Valve
BC	Boundary Condition
BP	Blood Pressure
cPP	central Pulse Pressure
CI	Contractility Index
CO	Cardiac Output
cSBP	central Systolic Blood Pressure
DB	Dobutamine
DBP	Diastolic Blood Pressure
Di	Digital artery
DOT	Dumbser-Osher-Toro
EF	Ejection Fraction
ECG	Electrocardiograph
EDP	End Diastolic Pressure
ESP	End Systolic Pressure
EDV	End Diastolic Volume
ESV	End Systolic Volume
FSI	Fluid-Structure Interaction
FV	Finite Volume
GTN	Glyceryl Trinitrate
HR	Heart Rate
IA	Iliac Artery
IC	Initial Condition
IMEX	IMplicit-EXplicit
IsC	Isovolumetric Contraction
IsR	Isovolumetric Relaxation
IVC	Inferior Vena Cava
IVP	Initial Value Problem
JRP	Junction Riemann Problem
KV	Kelvin-Voigt

LA	Left Atrium
LD	Linearly Degenerate
LTS	Local Time Stepping
LV	Left Ventricle
LVET	Left Ventricular Ejection Time
MAP	Mean Arterial Pressure
MOC	Methods Of Characteristics
MRI	Magnetic Resonance Imaging
MV	Mitral Valve
NA	Noradrenaline
ODE	Ordinary Differential Equation
PA	Pulmonary Artery
PDE	Partial Differential Equation
PP	Pulse Pressure
PPa	Pulse Pressure amplification
PPG	Photoplethysmogram
pPP	peripheral Pulse Pressure
pSBP	peripheral Systolic Blood Pressure
pSBP2	second peripheral Systolic Blood Pressure
PV	Pulmonary Valve / Pulmonary Vein
PVFR	Pulmonary Venous Flow Rate
PWV	Pulse Wave Velocity
RA	Right Atrium
RI	Riemann Invariant
RMSD	Root Mean Square Deviation
RP	Riemann Problem
RK	Runge-Kutta
RTT	Reynolds Transport Theorem
RV	Right Ventricle
SA	Sensitivity Analysis
SBP	Systolic Blood Pressure
SE	Systolic Ejection
SLSM	Standard-Linear-Solid Model
SSP	Strong-Stability-Preserving
SV	Stroke Volume
SVC	Superior Vena Cava
SVR	Systemic Vascular Resistance
TRRS	Two-Rarefactions Riemann Solver
TV	Tricuspid Valve
TVD	Total-Variation-Diminishing
VF	Ventricular Filling

List of Symbols

A	area	m^2
A_0	equilibrium area	m^2
A^*	area of the intermediate constant state the in the JRP	m^2
A_v	annulus area of the valve	m^2
a	wave speed/celerity	m s^{-1}
$B_{AV/MV}$	Bernoulli coefficient of the heart valve	kg/m^5
C	capacitance related to the wall compliance in the RCR model	m^3/Pa
CFL	Courant–Friedrichs–Lewy number	-
c	celerity contribute related to the fluid–structure interaction	m s^{-1}
c_0	reference celerity	m s^{-1}
D	inner diameter	m
d	elastic parameter of the tube law	Pa/m^2
E	Young modulus/elastic modulus of the material	Pa
E_0	instantaneous Young modulus/elastic modulus of the material	Pa
E_∞	asymptotic Young modulus/elastic modulus of the material	Pa
$\mathcal{E}_{LA/LV}$	elastance function of the heart chamber	Pa/m^3
$E_{max,LA/LV}$	maximum elastance of the heart chamber	Pa/m^3
$E_{min,LA/LV}$	minimum elastance of the heart chamber	Pa/m^3
f	friction term	Pa m
\mathcal{H}	Heaviside step function	-
H_1	first Hill function	-
H_2	second Hill function	-
h_0	vessel thickness	m
J	creep of the material	Pa^{-1}
K	stiffness coefficient of the vessel	Pa
$K_{s,LA/LV}$	constant of the heart chamber	s Pa^{-1}
$K_{vc,AV/MV}$	closing coefficient of the valve	$\text{Pa}^{-1}\text{s}^{-1}$
$K_{vo,AV/MV}$	opening coefficient of the valve	$\text{Pa}^{-1}\text{s}^{-1}$
L	length of the vessel	m
\mathcal{L}	inductance related to the fluid inertia in the RCR model	$\text{Pa s}^2/\text{m}^3$
$L_{AV/MV}$	blood inertance of the heart valve	kg/m^3
$l_{AV/MV}$	length of the valve	m
m	vessel wall parameter	-
$m_{1,LA/LV}$	contraction shape parameter of the heart chamber	-
$m_{2,LA/LV}$	relaxation shape parameter of the heart chamber	-
n	vessel wall parameter	-
p	pressure	Pa
p_0	equilibrium pressure	Pa
p_{1D}	inlet pressure at the RCR model	Pa
p^*	pressure of the intermediate constant state in the JRP	Pa
p_C	pressure in the capacitor of the RCR model	Pa
p_{ext}	external pressure	Pa

p_{isov}	isovolumic pressure	Pa
p_{out}	outlet pressure	Pa
q	flow rate	m^3/s
q_{1D}	inlet flow rate at the RCR model	m^3/s
q^*	flow rate of the intermediate constant state the in the JRP	m^3/s
q_{in}	inlet flow rate	m^3/s
q_{out}	outlet flow rate	m^3/s
R	inner radius	m
R_0	equilibrium inner radius	m
R_{in}	inlet inner radius	m
R_{out}	outlet inner radius	m
R_1	first resistance related to the fluid viscosity in the RCR model	Pas/m^3
R_2	second resistance related to the fluid viscosity in the RCR model	Pas/m^3
$R_{s,LA/LV}$	resistive term of the heart chamber	m
r	radial coordinate	-
Re	Reynolds number	-
S	source term of the viscoelastic tube law	$Pa s^{-1}$
T	cardiac cycle duration	s
t	time variable	s
t_{end}	final time	s
t_{onset}	onset time	s
u	blood velocity	$m s^{-1}$
u_0	initial profile solution	$m s^{-1}$
u^*	velocity of the intermediate constant state the in the JRP	$m s^{-1}$
V_f	fluid volume	m^3
V_{net}	total volume entering the LA in one cardiac cycle	m^3
V_c	control volume	m^3
v	velocity profile	$m s^{-1}$
$v_{0,LA/LV}$	initial volume of the heart chamber	m^3
$v_{LA/LV}$	heart chamber volume	m^3
v_{p0}	unstressed volume of the heart chamber	m^3
\vec{v}	fluid velocity	$m s^{-1}$
\vec{v}_s	control surfaces velocity	$m s^{-1}$
W	geometry parameter of the vessel	-
w	characteristic variable	-
Wo	Womersley number	-
x	space variable	m
Z_c	characteristic impedance of the vessel	Pas/m^3
α	dimensionless cross-sectional area	-
α_c	Coriolis coefficient	-
β	eigenvalue of the Jacobian of the source terms matrix	-
Γ	Riemann invariant related to the genuinely non-linear fields	-
Γ^{LD}	Riemann invariant related to the linearly degenerate fields	-
Δp	pressure difference across the valve	Pa
Δq	flow rate gradient	m^3/s
Δx	mesh spacing size	m
Δt	time step	s
ϵ	strain	-
ϵ_0	strain magnitude	-
ϵ_D	strain related to the dashpot	-

ζ	state of the valve	-
η	viscosity coefficient of the material	Pa s
Θ_n	auxiliary function in the Junction Riemann problem	-
λ	eigenvalue of the hyperbolic PDE system	-
μ	blood dynamic viscosity	Pa s
ρ	blood density	kg/m ³
σ	stress	Pa
σ_0	stress magnitude	Pa
σ_D	stress related to the dashpot	Pa
ζ	polynomial order of the friction model	-
$\tau_{1,LA/LV}$	contraction time parameter of the heart chamber	s
$\tau_{2,LA/LV}$	relaxation time parameter of the heart chamber	s
τ_c	retardation/creep time of the material	s
τ_r	relaxation time of the material	s
Ψ	linear path connecting boundary values in the phase-space	-
ψ_{el}	elastic contribution of the transmural pressure	Pa
∂V_c	control surface	m ²

Chapter 1

Introduction

1.1 Background and Motivation

Robust and efficient numerical schemes able to solve fluid mechanics balance laws are at the basis of the analysis of wave propagation phenomena in human cardiovascular networks. One-dimensional (1-D) *in silico* models have been broadly used to study how blood pressure and flow rate affect the biological structure that contains the fluid, namely arterial and venous walls (Reymond et al., 2009; Formaggia, Lamponi, and Quarteroni, 2003; Mynard and Smolich, 2014; Quarteroni, Veneziani, and Vergara, 2016), and they are used to investigate the haemodynamic mechanisms underlying the interaction between pressure and flow, and the dependence of these quantities on cardiac and vascular properties (Segers, Stergiopoulos, and Westerhof, 2000; Gaddum et al., 2017; Vennin et al., 2017; Flores Gerónimo et al., 2021; Li et al., 2021). In fact, it is commonly acknowledged that the use of computational models provides a great assistance to the clinical research, having the possibility to supply data that, otherwise, would require invasive techniques (Formaggia, Quarteroni, and Veneziani, 2009; Ambrosi, Quarteroni, and Rozza, 2012; Willemet, Vennin, and Alastruey, 2016). Furthermore, computational haemodynamics represents a valuable tool to foresee possible occurrences of diseases and the development of pathologies related to the arterial system, as in the case of arterial hypertension (Alastruey et al., 2007; Liang et al., 2011; Alastruey et al., 2012; Alastruey, Parker, and Sherwin, 2012; Liang, Guan, and Alastruey, 2018; Müller et al., 2019), or to the venous system (Toro et al., 2015; Toro, 2016).

Thus, to properly and accurately investigate the propagation of blood in circulatory systems, mathematical models need to consider that blood mechanically interacts with vessel walls and tissues. Vessel walls are indeed deeply affected by internal pressure, undergoing strong deformations, even collapsing in the case of veins under specific circumstances (Murillo, Navas-Montilla, and García-Navarro, 2019; Toro and Siviglia, 2013; Spiller et al., 2017). The fluid-structure interaction (FSI) in blood propagation phenomena requires the introduction of a constitutive law which defines the transfer of energy between blood and vessel wall (Shapiro, 1977; Fung, 1997; Leguy, 2019; Bertaglia, Caleffi, and Valiani, 2020). Mechanically speaking, rheological properties of arteries and veins are well-described by viscoelastic typical features (Armentano et al., 1995b; Armentano et al., 1995a; Zócalo et al., 2008; Valdez-Jasso et al., 2009). The smooth muscle cells lends a viscoelastic behaviour to the wall (Valdez-Jasso et al., 2009; Battista, 2015), which assumes a fundamental role when high frequencies are dominant (Alastruey et al., 2012), whereas when the stress is applied slowly, the viscous behaviour is negligible and the wall behaves as purely elastic (Westerhof et al., 2019). At a macroscopic level, indeed, the vessel wall can be seen as a complex multi-layer viscoelastic structure which deforms under the action of blood pressure (Nichols et al., 2011; Wang, Golob, and Chesler,

2016). Although neglected in some works in favour of simpler elastic models (Toro and Siviglia, 2012; Xiao, Alastruey, and Figueroa, 2014; Boileau et al., 2015; Murillo, Navas-Montilla, and García-Navarro, 2019), viscoelasticity adds a valuable contribution to the representation of the problem, being able to capture damping effects related to a partial loss of energy occurring during the deformation of the vessel (Reymond et al., 2009; Valdez-Jasso et al., 2009; Alastruey et al., 2011; Alastruey et al., 2012; Blanco et al., 2014; Müller, Leugering, and Blanco, 2016; Bertaglia, Caleffi, and Valiani, 2020; Bertaglia et al., 2020; Blanco et al., 2020). This fundamental feature is also observable from hysteresis loops obtained by means of stress and strain measurements in different vessels (Raghu et al., 2011; Bertaglia et al., 2020).

In healthcare research, *in silico* models are frequently used complementarily to *in vivo* data, namely blood signals measurements directly conducted by experienced operators in hospital wards. *In vivo* data represent the real manifestation of the human physiology in several clinical conditions but do not allow an exhaustive fluid mechanics-based analysis of their causes. On the other hand, *in silico* models aid the understanding of such conditions by providing even a great number of numerical simulations conducted in a controlled environment without confounding effects occurring *in vivo*, and mathematical analysis to recognise different contributions to blood pressure waves, achieving essential quantitative results (Parker, 2009; Schultz et al., 2013; Willemet and Alastruey, 2015; Westerhof and Westerhof, 2017; Mynard and Smolich, 2017; Mynard et al., 2020; Mariscal-Harana et al., 2021; Venin et al., 2021). *In vivo* and *in silico* data can be used to infer the haemodynamics of blood-related pathologies, like hypertension, which is a cardiovascular disease whose causes have been largely debated (Segers, Stergiopoulos, and Westerhof, 2000; Avolio et al., 2009). In particular, isolate systolic hypertension is defined by the increase of the pressure difference between the maximum (systolic) and minimum (diastolic) pressure values, i.e., the pulse pressure (Franklin et al., 1997). This typology of hypertension has always been predominately traced to vascular causes, such as decreased arterial compliance, increased stiffness of arteries, and increased reflections at peripheral sites of the vasculature, leading to the anticipation of the arrival of reflected waves that, overlapping with direct waves, results in increased pulse pressure (Safar, Levy, and Struijker-Boudier, 2003; O'Rourke and Nichols, 2005; O'Rourke and Hashimoto, 2007; Hashimoto and Ito, 2010). However, research has recently highlighted that cardiac function, and especially left-ventricular ejection, plays a non-negligible role in raising pulse pressure and amplifying it throughout the vasculature (Schultz et al., 2013; Fok et al., 2014a; Torjesen et al., 2014; Gaddum et al., 2017; Mariscal-Harana et al., 2021; Flores Gerónimo et al., 2021). Analyses conducted by means of *in silico* models may give a better understanding on such haemodynamics mechanisms, integrating experimental evidences.

1.2 Aims and Objectives

This PhD research aims at realising a mathematical model of the human cardiovascular network capable to simulate haemodynamic phenomena that are reflected in clinical evidence. The fundamental aspect to achieve this goal is to develop a model that should be able to properly simulate how blood vessels interact with blood pressure pulses that are generated by the cardiac dynamics. Only by a correct characterisation of this interaction, the propagation of pulse waves can be simulated in a physiologically- and physically-based manner, from the very first site of emission, i.e., the heart, to the most peripheral sites of the circulation. Therefore, utmost

attention has been posed on the mathematical modelling and numerical implementation of the mechanical behaviour of vessels walls in extended vascular networks, as well as in the interpretation of the numerical results. Besides, the other core aspect of the research is the investigation of the effect of cardiac properties on arterial pulse waves, and the explanation of cardiac-related physiological conditions and diseases. This is accomplished by considering the proper numerical coupling between a heart model and the arterial systemic circulation model. Starting from the fundamentals of fluid mechanics, using mathematical, physical and engineering notions, the final application of this research is indeed intended to make a contribution in the health-care research, to highlight aspects that may help finding the solution to problems of great interest in improving human health and quality of life of patients suffering from serious diseases, as in the case of hypertension.

1.3 Thesis Outline

This PhD Thesis is structured in four main chapters that guide the reader from a general introduction of the human cardiovascular network to the mathematical haemodynamic model and the numerical implementation used to obtain *in silico* results, to the final application in hypertension.

Chapter 2 presents an overview on the human cardiovascular system. This Chapter gives the necessary background to understand the methodology of the analysis presented in the following chapters. At first, the composition of vessels is discussed to highlight the reason why vessels wall cannot be regarded as an elastic material, but rather a viscoelastic one. Then, properties and features of the arterial system are presented. Arterial stiffness is discussed, as well as the methodologies usually followed to estimate it. Pivotal concepts of pulse wave velocity and compliance are given. Furthermore, the characteristics of pressure and flow in arteries are discussed and the pulse wave analysis is introduced. With this regard, wave separation and fiducial points analysis are addressed, and some fundamental haemodynamic indices are pointed out. Typical invasive and noninvasive techniques to measure blood pressure and flow rate are also presented. Moreover, an overview on the heart and the cardiac cycle is given. Finally, hypertension is discussed.

Chapter 3 presents the mathematical background for the haemodynamic model employed in this Thesis. Firstly, a general introduction is given on the two core aspects of the haemodynamic model: the mechanics of viscoelastic materials and hyperbolic balance laws in fluid mechanics. On the one hand, the phenomenological aspects underlying the behaviour of viscoelastic materials, which are indeed shown by arteries and, at a smaller extend, veins, are discussed. The mathematical models used to simulate linear viscoelastic materials are presented, in particular the model chosen for this research, namely the Standard Linear Solid Model. On the other hand, hyperbolicity of partial differential equations is defined, as well as the Riemann problem and corresponding solutions. Then, mass and momentum balance laws are introduced together with the closing equation of the governing mathematical system, which is a pressure–area relationship called tube law. Thus, the hyperbolic augmented fluid–structure interaction system (a-FSI), which presents a *stiff* term due to the viscoelastic contribution, is exhaustively presented. Finally, the mathematics governing inlet and outlet boundary conditions is introduced.

Chapter 4 presents the numerical scheme employed for the integration in time and space of the governing system of equations, and the numerical approach proposed

for the treatment of boundary conditions. In particular, a second-order Implicit-Explicit Runge-Kutta Strong-Stability-Preserving method, characterised by three stages for both the implicit and explicit parts is used for the time integration. This method fulfils the requirement to be robust and efficient at all levels of stiffness. For the space integration, a second-order Finite Volume Method is used. Internal boundary conditions, namely junctions among converging vessels, are numerically implemented via the proposed Junction Riemann problem, which is a non-linear system of equations based on a Riemann problem valid at the junction site. This approach allows the consideration of the viscoelastic contribution of vessels walls even at the boundary sections of the domain. The criterion used in the Junction Riemann problem is also extended to inlet and outlet boundary conditions for the same purpose. Trivial 2-vessel tests are performed to validate the numerical implementation of junctions and test the order of accuracy of the model. The numerical approach is then applied to a more complex configuration, namely a 3-vessel test, and eventually to extended arterial networks. Considerations regarding the viscoelastic response of the vessels walls in the different numerical tests, and therefore the relevancy of the viscoelastic parameters of the Standard Linear Solid Model, are carried out.

Chapter 5 presents two applications of the haemodynamic model. The first application consists of a computational proof-of-concept on the effect of cardiac properties on pulse waves in the arterial system. Previous works analysed how variations in arterial, vascular properties, for example due to ageing, affect the afterload and, therefore, cardiac dynamics, by means of numerical models accounting for ventricular-aortic coupling. In this work, the coupling between the heart and the systemic circulation is used for the inverse problem. Arterial pulse waves and meaningful haemodynamic indices are analysed consequently to variations in cardiac parameters to infer the most significant parameters in influencing haemodynamics in the network. In addition, the morphology of photoplethysmograph signals, typically measured in digital arteries and obtainable through smart and fitness devices, or oximeters, has been studied. Photoplethysmograph signals provide easy-to-acquire data for screening cardiovascular function during everyday life and thus pose as a useful tool for a future study of an expanded cohort of subjects. This application offers a first interesting insight on cardiac dysfunctions detection from arterial pulse waves analysis. The second application consists of a complementary study of numerical results and experimental measurements to infer the haemodynamic mechanism underlying the elevation of pulse pressure in hypertension. The *in vivo* dataset is exhaustively presented. This consists of three cohorts of subjects in which central and peripheral pressure and aortic flow velocity were measured invasively or noninvasively. *In vivo* data cover a wide range of physiological conditions, since they comprehend measurements in both normotensive subjects, who also underwent pharmacological intervention to alter their cardiac and vascular conditions, and hypertensive subjects. *In silico*, numerical results are obtained by using the haemodynamic model proposed in this Thesis, and they are firstly validated with *in vivo* data. Then, the numerical model is used to investigate the elevation of pulse pressure in hypertension, and understand the role that cardiac and vascular properties play in this phenomenon. Characteristics of aortic flow rate waveform and the fiducial points in central and peripheral pressure waves are analysed when cardiac and vascular properties of the network are changed independently. Furthermore, wave separation analysis is used to study two key reflection coefficients containing information on direct and reflected pressure waves, and how these coefficients change consequently to cardiac and vascular alterations. All numerical results are backed up by *in vivo* evidences.

Finally, Chapter 6 provides a general discussion on the main issues arising from this Thesis, including considerations regarding the strengths and limitations of the research, an overview of the key findings, and suggested directions for future work.

Chapter 2

The cardiovascular network

2.1 Introduction

The human circulatory system comprises two principal sub-systems, namely the pulmonary circulation and the systemic circulation. The primary function of the pulmonary circulation is to exchange gases across the alveolar membrane inside the lungs, carrying oxygenated blood from the lungs to the left atrium of the heart and discharging deoxygenated blood from the right ventricle into the lungs. This allows the carbon dioxide from the systemic circulation to be breathed out. Blood is ejected from the right ventricle into the pulmonary arteries, and it returns to the left atrium through the pulmonary veins. The systemic circulation transports the oxygenated blood to all tissues and organs of the body through the arterial circulatory system, ejecting it from the left ventricle into the aorta, and it returns the deoxygenated blood to the right atrium through the venous circulatory system. This Thesis is predominantly focused on the arterial circulation, that is thoroughly presented in Section 2.2. The continuously-working pump of the human cardiovascular system is the heart, which is presented in Section 2.3, and it guarantees the blood to flow in both the pulmonary and systemic circulations.

2.1.1 Composition and type of vessels

Vessels walls are anisotropic and heterogeneous tissues, composed of three structural layers with different biomechanical properties (Tortora and DeFrickson, 2013), whose stress-strain relationships are non-linear and frequency dependent (Alastruey, Parker, and Sherwin, 2012). The first layer is the *adventitia*, which is the outermost layer primarily consisting of collagen fibres laminated in a spiral fashion (Hoskins, Lawford, and Doyle, 2017). The second layer is the *media*, which is formed by smooth muscle cells, elastin sheets layered circumferentially, and collagen fibres. The two proteins, i.e., elastin and collagen, are the main determinants of the elastic properties of the wall, of which collagen is much stiffer than elastin. Thus, the viscoelastic properties of arterial walls, and so their mechanical response to blood pressure, are mainly determined by the ratio of elastin to collagen of the media. This ratio changes depending on the type of blood vessel. Arteries, for example, have more collagen and elastin than veins have (Xu and Shi, 2014). Besides collagen and elastin, Alastruey, Parker, and Sherwin (2012) attributes the presence of glycoproteins as another likely contributor to much of the viscous behaviour of the wall. Finally, the *intima* is the innermost layer. It consists of a very thin basement membrane, which is an elastic lamina, and, immediately underneath, a single ply of endothelial cells. This, lining the lumen, is in contact with the flowing blood. (Hoskins, Lawford, and Doyle, 2017; Tortora and DeFrickson, 2013). The internal elastic lamina allows the endothelium to move independently of the media.

Blood vessels are categorised with respect of their diameters. Arteries, characterised by diameters between 1 and 30 mm, carry the blood ejected from the heart to the organs and peripheral sites of the systemic circulation. Arteries are followed by arterioles, with diameters between 10 and 100 μm , and capillaries, with diameters between 4 and 40 μm . Arterioles have very thick muscular and highly innervated walls; the ratio of wall thickness to diameter is ~ 1 (Formaggia, Quarteroni, and Veneziani, 2009). Capillaries are characterised by a very thin wall consisting of only endothelium and basement membrane, and they are generally found in skin and muscles, being responsible for the bulk of exchange between blood and the various tissues. Venules, with diameters ranging from 10 to 200 μm , have all three layers but their wall is much thinner than arterioles with almost absent media layer. Finally, veins, with diameters from 1 to 25 mm, return blood to the heart. The venous system operates at a lower pressure than the arterial system and consequently the veins wall thickness is less than that of arteries.

2.2 The arterial system

This Thesis prevalently focuses on the modelling and analysis of the arterial systemic circulation. Therefore, this Section provides concepts of physiology and biomechanics of the arterial system.

Arteries carry blood from the the heart to the peripheral sites of the network. Systemic arteries undergo relatively high pressures and they are, therefore, composed of thick walls consisting of the three layers described in Section 2.1.1, i.e., adventitia, media, and intima. Arteries are classified in elastic and muscular depending on the wall composition (Hoskins, Lawford, and Doyle, 2017; Davies et al., 2012; Mynard et al., 2020; Kondiboyina et al., 2022). Elastic arteries such as the aorta and its major branches are low resistance vessels and have a high elastin to collagen ratio, resulting in high distensibility. Therefore, central arteries are able to reserve the volume ejected from the heart and enable the storage of energy. Peripheral, distal arteries, namely the arteries that supply blood to organs and those in the limbs, are muscular in nature. Muscular arteries present a thicker media layer characterised by less elastin and more smooth muscle cells than those present in the elastic arteries, and they have a larger wall–thickness to diameter ratio (Alastruey, Parker, and Sherwin, 2012). The smooth muscle cells in the peripheral arteries can change the luminal area (*vasomotion*) to regulate peripheral blood flow and satisfy the local instantaneous metabolic needs.

2.2.1 Stiffness of arteries

From the mechanical point of view, the two most important constituents of arterial walls are elastin, providing elasticity, and collagen, providing strength, whose molecules unfold when the artery expands. When elastin and collagen fibres reach their straightened length, they become extremely stiff.

The stress–strain relationship of an artery is generally represented in pressure–diameter, or pressure–area plots, and it displays a widening pressure–area loop caused by the dissipation of energy during dilation and contraction cycles (Valdez-Jasso et al., 2009; Raghu et al., 2011; Salvi, 2012; Battista, 2015). This phenomenon, typical of viscoelastic materials, is due in particular to the composition of arterial walls in elastin and collagen, and the loop widening depends on the proportion of these two components. In the unstretched configuration and at small distensions, the collagen fibres are quite folded and the mechanical behaviour is dominated by

the elastin, whereas at high extensions the collagen fibres have straightened out, dominating the mechanical behaviour of the artery and conferring stiffness. Smooth muscle cells contract and relax under neural and hormonal control (*vasomotor control*), actively affecting arterial stiffness and playing an important role in the viscoelastic damping of the pulse wave (Armentano et al., 2007; Alastruey, Parker, and Sherwin, 2012). As arteries are composed of a multi-layer structure and each layer has specific mechanical properties, the characterisation of the coefficients related to these properties assumes the utmost relevancy to describe the rheological behaviour of the arterial wall. The composite behaviour of the arterial wall can be portrayed by using viscoelastic models that define a time-varying Young modulus and a viscosity coefficient to account for the mechanical behaviour of the wall when undergoing pressure pulses. For instance, in this Thesis a three-parameter viscoelastic model is used and it is thoroughly addressed in Chapter 3. Such models generally assume that the artery is uniform and homogeneous, i.e., the wall thickness and mechanical composition are the same for different positions around the circumference.

Pulse wave velocity

To estimate arterial stiffness, or arterial distensibility, several methods are presented in the literature and usually employed in clinical practice. One of these methods is given by the measurement of the pulse wave velocity (PWV). PWV-based models to define arterial distensibility are called propagative models (Salvi, 2012). Indeed, a pulse wave is transmitted throughout the vessels of the arterial network, and its speed, also called celerity of the wave, is related to the viscoelastic properties of the vessel wall itself. Specifically, the stiffer the wall, the higher the pulse wave velocity (Salvi, 2012).

PWV cannot be misunderstood with blood flow velocity. The former travels at about two orders of magnitude more than the latter, i.e., m/s for PWV versus cm/s for blood flow velocity. Blood flow velocity also changes in the cardiac cycle (Salvi, 2012). PWV can be assessed measuring simultaneously the pressure waveform at two different sites in the arterial tree, a proximal site and a distal, peripheral one. This enables to calculate the time delay between the pressure waveforms in the two sites, generally considering the "feet" of the pressure waveforms at early-systole. Knowing the distance between the two sites, the PWV is simply calculated as the distance to time delay ratio (Salvi, 2012; Mariscal-Harana et al., 2021). This method is known as the *foot-to-foot method*. The most frequent sites where pressure is measured are at the carotid and femoral arteries due to the possibility to perform noninvasive measurements. The foot-to-foot method can also be used considering blood flow velocity instead of blood pressure, at the aortic arch and in the abdominal aorta (Gaddum et al., 2013). Other methods have been presented in the literature to obtain PWV, such as the *sum of squares method*, which allows to calculate the PWV using simultaneous measurements of blood pressure and velocity at a single site of the arterial network (Davies et al., 2006; Parker, 2009; Abdessalem, Flaud, and Zobaidi, 2018; Mariscal-Harana et al., 2021), the *least squares differencing method* (Gaddum et al., 2013; Mariscal-Harana et al., 2021), and the *cross-correlation method* (Gaddum et al., 2013).

The increase of PWV with ageing is a well established phenomenon (Salvi, 2012; Charlton et al., 2019). During the ageing process, the arterial wall undergoes histological alterations characterised by the degeneration of elastin fibres and a boost in collagen fibres, therefore increasing stiffness. The increase in PWV with ageing is not linear, being faster as age advances.

Arterial compliance

Generally speaking, the mechanical properties of a blood vessel are not linear, as they depend on the pressure they are subjected to and at which they are measured. Several haemodynamic parameters can be used for assessing the mechanical properties of arteries and investigating their viscoelastic properties. One of these is the arterial compliance, which is defined as the change in diameter (or section) of the artery in absolute value, at a given pressure level, for a given arterial length (Salvi, 2012). Therefore, compliance can be seen as the ratio between change in volume and change in pressure of a specific arterial segment. Extending this concept to the whole arterial network, the total systemic arterial compliance is defined as the ability of the arterial system to distend with increasing blood pressure (Alastruey, Parker, and Sherwin, 2012). The total systemic arterial compliance is prevalently located in the most elastic systemic arteries, namely along the aorta. When the vessel wall is characterised by high elasticity, small changes in pressure cause significant variations in volume. Otherwise, when the arterial wall is stiff, the distensibility of the vessel diminishes and significant changes in pressure cause small variations in volume. Hence, compliance decreases with increasing stiffness, and therefore ageing is a cause of compliance loss. Compliance-based models to infer arterial distensibility are called nonpropagative models (Salvi, 2012).

Several methods have been presented in the literature to calculate the arterial compliance. The direct application of the afore-given definition of compliance results in calculating this haemodynamic parameter as the ratio between stroke volume (SV), i.e., the total volume ejected from the left ventricle in one cardiac cycle, and aortic pulse pressure (PP), which is the difference between the maximum and minimum pressure values (Mariscal-Harana et al., 2021). Although the *SV/PP method* represents a first, simple approach to obtain arterial compliance, its validity and accuracy has been proved (Chemla et al., 1998). Another method to compute compliance is the *diastolic decay fitting method* (Frank, 1990), in which blood pressure wave is analysed between the time when the aortic valve closes, usually coinciding with the so-called dicrotic notch in the blood pressure (BP) waveform, and the end of diastole. Indeed, the occurrence of the dicrotic notch distinguishes the heart period in two parts, namely the systole, which starts from the time of the onset of the pulse wave until the dicrotic notch time, and the diastole, from the dicrotic notch time until the end of the heart period. The best fit between the diastolic tract of the pressure wave and an exponential decay curve of the form $p_{exp} = p_{out} + (p_{exp}(t_0) - p_{out})e^{(t-t_0)/\tau}$, with t_0 the time of the dicrotic notch and p_{out} the outflow vascular BP, is found by using a minimization algorithm (Mariscal-Harana et al., 2021). τ is the parameter measuring compliance. Other methods to compute compliance are the *area or two-area methods*, which are based on solving integrals of pressure or pressure and flow rate, respectively, in-between specific times in the cardiac cycle (Randall et al., 1976; Chemla et al., 1998; Westerhof, Lankhaar, and Westerhof, 2009; Mariscal-Harana et al., 2021), and the *iterative methods* based on the minimization of the relative error between the reference and estimated values of either diastolic blood pressure (DBP) or PP (Stergiopoulos, Meister, and Westerhof, 1994; Westerhof, Lankhaar, and Westerhof, 2009; Mariscal-Harana et al., 2021).

Arterial compliance and pulse wave velocity of each vessel are related via a mathematical equation, i.e.,

$$C = \frac{Al}{\rho(PWV)^2}, \quad (2.2.1)$$

where A is the luminal area of the vessel, l is the vessel length, and ρ is the blood flow density (Xiao, Alastruey, and Figueroa, 2014).

2.2.2 Pressure and flow in arteries

Pressure in the systemic arterial network is driven by the cardiac action and the characteristics of the arterial walls. When the heart ejects the stroke volume from the left ventricle into the aorta, this latter expands and the pressure rises.

Arterial pressure is characterised by a pulsatile behaviour, fluctuating periodically between two extreme pressure values with each cardiac cycle. These extreme values are the systolic (SBP) and diastolic (DBP) blood pressure, where SBP is the maximum value, and DBP is the minimum value of the BP waveform. The difference between these two values is the well-known pulse pressure (PP),

$$PP = SBP - DBP. \quad (2.2.2)$$

Hence, PP represents the variation in pressure above the minimum arterial pressure and defines the pulsatile component of BP (Darne et al., 1989; Salvi, 2012; Hoskins, Lawford, and Doyle, 2017). Cardiologists are taught that SBP reflects the cardiac output and the distensibility of the arteries, whereas DBP depends upon the state of the peripheral vessels, and PP is proportional to the stroke volume and inversely proportional to arterial compliance (Formaggia, Quarteroni, and Veneziani, 2009). PP increases with increasing distance from the ejection site due to the stiffening of the arteries, namely towards the peripheral arteries. The pulsatile component of pressure depends on the wave generated by the interaction between the left ventricle and the aortic root, the mechanical properties of the arteries, and the reflected waves (Darne et al., 1989; Salvi, 2012). Therefore, PP is a haemodynamic measure that can be used to estimate arterial distensibility, as presented in Section 2.2.1, and infer pressure-related pathologies and cardiovascular risk (Vennin et al., 2017; Flores Gerónimo et al., 2021).

Given BP variability between SBP and DBP and its periodic behaviour over the cardiac cycle, T , it is useful to define the mean arterial pressure (MAP), which is typically thought of as the steady component of pressure (Darne et al., 1989; Salvi, 2012; Hoskins, Lawford, and Doyle, 2017). From the mathematical point of view, MAP is defined as the integral of blood pressure, $p(t)$, over the cardiac cycle, namely

$$MAP = \frac{1}{T} \int_0^T p(t) dt. \quad (2.2.3)$$

In the clinical practice Eq. (2.2.3) is not of easy-to-use. In clinical practice MAP is often calculated from PP (and vice-versa) by using the formula

$$MAP = DBP + \frac{PP}{3}. \quad (2.2.4)$$

which is a crude approximation of the time-average arterial pressure assuming that the pressure waveform is triangular (Formaggia, Quarteroni, and Veneziani, 2009). Indeed, Eq. (2.2.4) is the simplification of the mathematical definition of MAP expressed by Eq. (2.2.3).

As expressed by Eq. (2.2.4), MAP and PP are two distinct but interdependent arterial pressure quantities, so MAP, like PP, can be used as an indicator of cardiovascular risk due to its dependence on cardiac and vascular parameters. In fact, MAP can also be calculated knowing two haemodynamic parameters, namely the cardiac

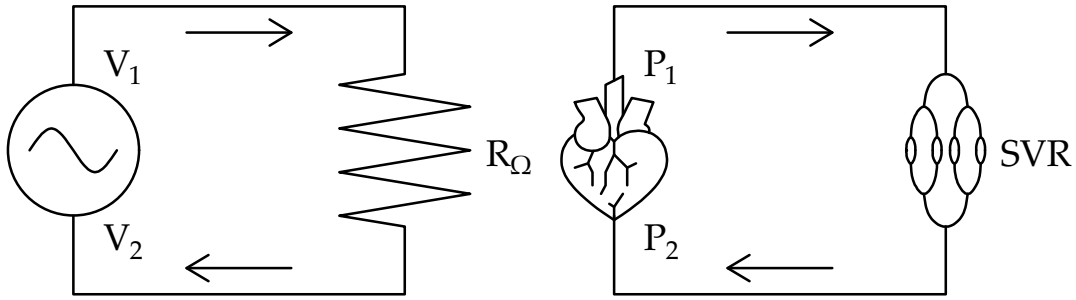


FIGURE 2.1: *Hydraulic–electric analogy. A simple electric circuit (left), the schematic systemic circulation system model (right).*

output (CO) and the systemic vascular resistance (SVR), through the equation

$$MAP = CO \cdot SVR. \quad (2.2.5)$$

The cardiac output is given by the product of two other cardiac quantities, namely the stroke volume (SV) and heart rate (HR), $CO = SV \cdot HR$. Thus, Eq. (2.2.5) becomes

$$MAP = SV \cdot HR \cdot SVR. \quad (2.2.6)$$

Heart-related quantities, i.e., SV, HR, and CO, will be exhaustively presented in Section 2.3.1. When calculated with Eq. (2.2.6), MAP is considered to be an approximately constant value throughout the arterial system (Salvi, 2012).

It is worth highlighting the relationship that holds true between blood pressure and flow. Indeed, in Eq. (2.2.5) MAP depends on CO, which is the total volume ejected from the heart per unit of time, therefore it has the units of a flow rate. This relationship is validated and explained recurring to the hydraulic–electric analogy (Formaggia, Quarteroni, and Veneziani, 2009; Salvi, 2012), according to which the human hydraulic circuit – composed of a pump (the heart) with a rhythmic activity, and tubes (vessels) with flowing liquid (blood) – can be associated to an electric circuit (Figure 2.1). According to Ohm’s law, the potential difference between the extreme points of an electric circuit ($\Delta V = V_1 - V_2$) is obtained by multiplying the current (I) by the resistance of the circuit (R_Ω),

$$\Delta V = I \cdot R_\Omega. \quad (2.2.7)$$

Eq. (2.2.5) is derived directly from Eq. (2.2.7) where the potential difference can be thought of as the difference in blood pressure between the extreme points of the circulation, $\Delta P = P_1 - P_2$. However, assuming that P_2 is much smaller than P_1 , since it represents the venous pressure, and considering the time-averaged blood pressure over the cardiac cycle, ΔP is de facto MAP. Finally, CO represents the current, I , and SVR represents the resistance of the circuit, R_Ω (Salvi, 2012). Hence, the underlying analogy lies in considering the pressure as the voltage and the flow rate as the current, as shown in Figure 2.1, and expressed by Eq. (2.2.5) and Eq. (2.2.7).

The hydraulic–electric analogy is at the base of the so-called lumped-parameter, or zero-dimensional (0-D) models, which allows the computation of blood pressure and flow by splitting the cardiovascular system into a set of compartments regulated by the typical laws of electric circuits. The circuit represented in Figure 2.1, which shows only a resistance-type compartment, is an extreme simplification of a 0-D model, because the number and kind of compartments considered varies depending

on the type of analysis at hand (Formaggia, Quarteroni, and Veneziani, 2009). 0-D models simulating the systemic circulation usually considers, besides the resistance-type compartment, also capacitance- and inductance-type compartments (Kokalari, Karaja, and Guerrisi, 2013; Segers et al., 2003; Vennin et al., 2017; Civilla et al., 2021). In the electric network analogy, all these three compartments are assimilated to the characteristics of blood flow or compliant vessels. The resistance, R , represents the resistance induced to the flow by blood viscosity, the inductance, \mathcal{L} , is assimilated to blood inertia, and the capacitance, C , represents the mass storage and so it is assimilated to the wall compliance (Formaggia, Quarteroni, and Veneziani, 2009). In their general formulation, these parameters relate pressure p with flow rate q and read as

$$p = Rq, \quad \mathcal{L} \frac{dq}{dt} = p, \quad C \frac{dp}{dt} = q. \quad (2.2.8)$$

In this Thesis, 0-D models are used to simulate specific sections of the cardiovascular network model, namely the cardiac contraction model and micro-circulation.

Most arteries experience biphasic flow waveforms with a small amount of backward flow occurring in late systole and early diastole. Blood flow can be described by two non-dimensional parameters, namely the Reynolds and the Womersley numbers. The Reynolds number, Re , in an internal flow of mean sectional velocity u within a pipe or vessel of characteristic diameter D is given by

$$Re = \frac{\rho Du}{\mu}, \quad (2.2.9)$$

where μ is the dynamic viscosity of the Newtonian fluid. From the physical point of view, the Reynolds number can be thought of as the ratio of inertial forces to viscous forces. Thus, when the Reynolds number is large, the inertial forces are dominant over viscous forces, and vice-versa. The Reynolds number is the key parameter that identifies the transition of the flow to turbulence (Formaggia, Quarteroni, and Veneziani, 2009). The Womersley number is used when considering unsteady flow and is defined as (Womersley, 1955)

$$Wo = \frac{D}{2} \sqrt{\frac{2\pi}{\nu T}}, \quad (2.2.10)$$

where $\nu = \mu/\rho$ is the blood cinematic viscosity, and T is taken as the fundamental period of the oscillatory flow, which corresponds, in the case of blood flow, to the cardiac cycle duration. The Womersley number is considered as the frequency parameter of the flow. From the physics point of view, the Womersley number can be regarded as the ratio of pipe diameter to the laminar boundary layer growth over the pulse period T (Formaggia, Quarteroni, and Veneziani, 2009). The Reynolds number and the Womersley number profoundly change throughout the arterial circulation, becoming much lower than unity in the micro-circulation. In the ascending aorta, the Reynolds number is typically 4000 and the Womersley number is 10.5, in the small arteries they become 100 and 1.4, respectively, and 0.5 and 0.014 in arterioles. In particular, low Reynolds numbers in the micro-circulation imply that viscous forces completely dominate any inertial forces in the flow (Formaggia, Quarteroni, and Veneziani, 2009). This means that almost all of the pressure head losses in the circulation occur in the micro-circulation. As in normal physiological condition the Reynolds numbers based on mean velocities are generally well below 2000 through most of the system (Zamir, 2000), blood flow is assumed to be laminar (Alastruey,

Parker, and Sherwin, 2012; Charlton et al., 2018; Mitsotakis et al., 2019). Turbulence may occur, as said, in the ascending aorta where the flow can be highly disturbed during peak ejection, with peak Reynolds numbers through the aortic valve close to 10000 (Seed and Wood, 1971; Stein and Sabbah, 1976), and at other locations under some disease states such as luminal narrowing (stenosis) and abnormal aortic valves (Stein and Sabbah, 1976).

2.2.3 Pulse wave analysis

Pulse wave analysis is the branch of computational haemodynamics that aids the understanding of BP pulse waves to extract clinically-relevant information. Pulse wave analysis is greatly useful for the study of *in vivo* BP measurement. In fact, while *in silico*, numerical results rely on an accurate and *a-priori* knowledge of all the physical properties of the haemodynamic system, *in vivo* studies have far less data available. Moreover, the characterisation of blood pressure by means of only two extreme values, namely the systolic and diastolic blood pressures, neglects the myriad of information that is embodied in the shape of the pressure waveform.

Under normal conditions, a wave generated by the contraction of the heart propagates throughout the arterial system, generating reflections whenever they encounter a discontinuity in the geometrical or mechanical properties of the arteries (Formaggia, Quarteroni, and Veneziani, 2009; Mynard et al., 2020). Bifurcations, high resistance regions, and sites of change in arterial viscoelasticity can give rise to reflections that propagate back towards the heart. These waves, travelling back and encountering other bifurcations, give rise to a very complex pattern of reflected and re-reflected waves that determine the local pressure and velocity waveforms in the arteries.

With pulse wave analysis, characteristic features of the pressure waveforms are obtained and inferences about wave dynamics are made on the bases of theoretical, model-based links with functional properties of the cardiovascular system. Pulse wave analysis is of utmost importance to study the onset and progression of cardiovascular diseases like hypertension, evaluate ageing predictors, and infer the relationship between BP pulse waves measured in different sites of the arterial network (Mynard et al., 2020; Nichols et al., 2011). Several methods have been developed for the analysis of *in vivo* data in both the time and frequency domain. In this Section, pulse wave analysis tools that allow to separate the pulse waveform into physically relevant components, and estimate clinically relevant parameters will be discussed.

Wave separation

Wave separation technique is frequently employed in pulse wave analysis, as it provides quantitative information about forward and backward waves by decomposing the pressure waveform p into two separate signals using principles of fluid dynamics in compliant tubes (Parker, 2009), allowing an exhaustive study of waves phenomena. The forward component of pressure, p_f , quantifies the direct (incident) contribution to BP wave, whereas the backward component of pressure, p_b , quantifies the reflected contribution to BP wave (Figure 2.2). Wave separation only quantifies these two components, being agnostic to the haemodynamic mechanism that give rise to forward or backward waves. Therefore, to investigate this mechanism, model-based analyses or experimental inferences must be conducted.

By using measured pressure and flow waveforms, p and q respectively, pressure wave separation, originally described by Westerhof et al. (1972), is obtained with the

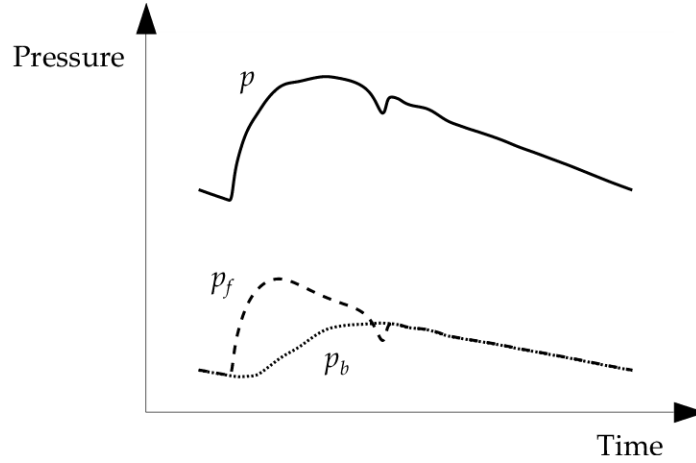


FIGURE 2.2: Wave separation analysis for blood pressure wave, p . Forward component, p_f , and backward component, p_b , are calculated using Eq. (2.2.11).

formula (Swillens et al., 2008; Mynard et al., 2012; Vennin et al., 2021)

$$p_f = \frac{1}{2}(p + Z_c q), \quad p_b = \frac{1}{2}(p - Z_c q), \quad (2.2.11)$$

where Z_c is the characteristic impedance of the vessel,

$$Z_c = \frac{\rho PWV}{A}. \quad (2.2.12)$$

In Eq. (2.2.12), PWV is the pulse wave velocity, A is the vessel cross-sectional area, and ρ is blood density. The characteristic impedance has an important physical meaning, namely that incremental changes in pressure, dp_f , and flow, dq_f , arising from forward waves are intrinsically linked. This physical relation is explicated by the water hammer equation, which is one of the fundamental equations of fluid dynamics and reads (Parker, 2009; Mynard et al., 2020)

$$dp_f = Z_c dq_f. \quad (2.2.13)$$

Eq. (2.2.13) implies that a pressure wave, namely a propagating pressure change, is always accompanied by a corresponding flow wave, i.e., a propagating flow change, and vice-versa (Mynard et al., 2020). Eq. (2.2.13) shows that in a situation where only forward waves exist, pressure and flow waveforms would have an identical shape and their ration would be equal to Z_c . Moreover, according to equations (2.2.12) and (2.2.11), an increase in arterial stiffness, which increases PWV , or a smaller diameter cause a larger blood pressure change for a given flow change. This has important implications for the study of blood pressure with advancing age, which is generally accompanied by an increase in arterial stiffness and cross-sectional area, or cardiovascular diseases.

Fiducial points

As mentioned in the above, the rich superimposition of forward and backward waves shapes blood waveforms that are measured *in vivo* and simulated *in silico*. Hence, some meaningful pressure descriptors can be obtained to guide clinical care and analysis of cardiovascular diseases. These descriptors, called *fiducial points*, are

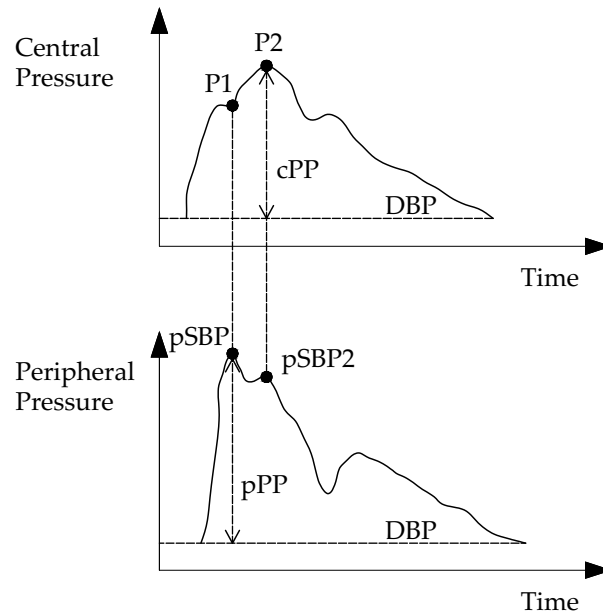


FIGURE 2.3: Schematic representation of the central blood pressure wave with the first (P1) and second (P2) central systolic peaks (upper row), and the peripheral blood pressure wave with the first (pSBP) and second (pSBP2) peripheral systolic blood pressures (lower row). P1 is the determinant of pSBP, P2 is determinant of pSBP2. Central pulse pressure (cPP) is the difference between the central systolic blood pressure and diastolic blood pressure (DBP); peripheral pulse pressure (pPP) is the difference between pSBP and DBP.

usually identified with local and absolute pressure peaks and inflection points observed on BP waves. Fiducial points of the central BP wave are strongly related to those of the peripheral BP wave (Figure 2.3). Two main fiducial points can be identified in the central (aortic or carotid) BP wave. These are called the first and second central systolic peak, and are usually labelled as P1 and P2, respectively. It is always true that the time of occurrence of P1 is smaller than that of P2, namely $t_{P1} < t_{P2}$. P1 and P2 can be either the central BP peak or an inflection point, and their characterisation typically depends on the age of the subject in which they are estimated. In the elderly, P1 is a “shoulder-shaped” inflection point identifying the time when the forward and backward waves meet (Li et al., 2021; Salvi, 2012), and P2 corresponds to the central systolic blood pressure (cSBP), therefore being the absolute pressure peak (Chirinos et al., 2009; Li et al., 2021). In this case, namely when $P1 < P2 = \text{cSBP}$, the waveform is categorised as *Type A* according to the waveforms classification introduced by Murgo et al. (1980). Contrarily, in younger subjects P1 corresponds to the cSBP and P2 is an inflection point occurring later in time, namely $P1 = \text{cSBP} > P2$. In this case the waveform is categorised as *Type C* (Murgo et al., 1980). Peripheral fiducial points depend on P1 and P2 of the central BP wave. The first peripheral systolic blood pressure (pSBP), which is used as an index to assess clinical risk related to hypertension and to guide clinical care, is proven to be determined by P1 in the central BP wave, whereas the second peripheral systolic blood pressure (pSBP2) is determined by P2 in the central BP wave (Li et al., 2021), consistently with the concept that a central wave component arises earlier within the cardiac cycle than the peripheral wave component it generates. Finally, the afore-mentioned dicrotic notch is a fiducial point able to provide information on the left ventricular ejection

timing, in fact it corresponds to the closure of the aortic valve. This is a local minimum of the BP wave occurring after the SBP. The dicrotic notch is more evident in central arteries, that are closer to the ejection site, than in peripheral arteries.

Secondary fiducial points for central and peripheral BP waves have been presented and defined by Charlton et al. (2019), who have also detailed fiducial points identifiable on the photoplethysmogram (PPG) pulse waves. Photoplethysmography is a widely-used, noninvasive measurement technique that aids remote cardiovascular monitoring, containing information on ventricular function and ventricular-vascular interaction, and provides a wealth of information on the onset of diseases and mechanical cardiac activity (Nichols et al., 2011). The recording site is remote from the heart. Commonly, PPG signals are measured at the periphery of a limb, like the wrist or finger, and they are widely measured by pulse oximeters and consumer devices, as smart watches. Photoplethysmographic traces are very similar to pressure waves recorded in the carotid artery and bear a like relationship to the ascending aortic pressure wave. It must be recognised, however, that PPG pulse waves do not record pressure, but the volume change in multiple small arterial vessels (Nichols et al., 2011; Charlton et al., 2019). Pulse wave analysis applied to PPG signals provides a myriad of clinically-relevant information. To name a few, PPG pulse waves contain information on the heart rate, pulse wave variability, respiratory rate, arterial blood oxygen saturation, vascular age, and left ventricular ejection time. Moreover, it can detect atrial fibrillation, identify obstructive sleep apnea, monitor the spread of infection diseases and sleep, assess mental stress and response to exercise, and predict information on cardiovascular risk (Sabry et al., 2022; Charlton et al., 2018; Charlton et al., 2022)

Pulse waveforms indices

A multitude of indices providing information on direct and reflected BP waves can be obtained through the pulse wave analysis. The most important one is the augmentation index (AIx), which offers an indication of the incidence of reflected waves on the total pulse pressure. The contribution of the backward wave on the total BP wave is related to both its early superimposition onto the forward wave and the magnitude and distribution of the reflected wave. AIx is calculated as the ratio between the augmented blood pressure (ABP) due to the reflected waves, with $ABP = P_2 - P_1$ of the central BP wave, and PP (Li et al., 2021),

$$AIx = \frac{P_2 - P_1}{PP} \times 100. \quad (2.2.14)$$

Consequently, AIx is positive when cSBP corresponds to P2 and is greater than P1, hence typically in the elderly subject, otherwise, AIx is negative when cSBP corresponds to P1 and is greater than P2, which occurs generally in the younger subject (Salvi, 2012). AIx is conditioned by several biomechanical interactions. Factors affecting AIx are both vascular and cardiac, such as arterial stiffness, the magnitude and variability in reflected waves in relation to systemic vascular resistances, cardiac contractility and relaxation properties, ventricular outflow patterns, heart rate, and forward waves. AIx is also driven by subject height (distance of reflections sites) and sex (McEniery et al., 2005; Mynard et al., 2020). Given the several factors affecting AIx, one could question if wave reflection is indeed the primary driver for systolic augmentation. However, a key principal of fluid dynamics in elastic tubes is that in the absence of wave reflection pressure and flow waveforms will be identical, albeit scaled by characteristic impedance Z_c , as introduced in Section 2.2.3. Therefore, any

difference between these waveforms must be ascribed to wave reflection (Parker, 2009; Westerhof and Westerhof, 2017). O'Rourke and Mancia (1999) reasonably defined AIx as the "manifestation" of early wave reflection, but not its measure. Thus, although AIx is a very useful marker of cardiovascular risk (Nürnberg et al., 2002; Weber et al., 2004; Weber et al., 2010), its limitation related to the quantification of the biomechanical phenomenon of wave reflection should not be overlooked (Mynard et al., 2020).

As previously mentioned, PP increases as the distance of the pulse wave from the ejection site increases. This phenomenon is called pulse pressure amplification, and it is mainly traced back to the presence of blood pressure reflected waves in the periphery of the circulation, namely near reflection sites (radial, brachial, femoral arteries, etc.). Under undamaged viscoelastic properties of the arterial wall, backward, reflected waves superimpose onto forward, direct waves prevalently in early-systole. On the contrary, in central sites like the ascending aorta, backward waves arrive later in time, and they superimpose onto the forward waves prevalently during late-systole. Therefore, the determination of PP in central site is only marginally caused by the presence of reflected waves (Salvi, 2012). Different approaches have been proposed to quantify PP amplification. The simplest approach consists in the measurement of the difference, in absolute values, between the peripheral SBP and the central SBP. Alternatively, a measure of the PP amplification can be obtained by calculating the ratio of central (cPP) to peripheral (pPP) pulse pressure. Likewise, the pulse pressure augmentation ratio (AR) is defined by the percentage increase in pulse pressure between the peripheral site and the central site (McEniery et al., 2005; Salvi, 2012; Li et al., 2021),

$$AR = \frac{cPP - pPP}{cPP} \times 100. \quad (2.2.15)$$

Another meaningful characteristic of the central BP wave that can be studied with pulse wave analysis is the rate of rise in early-systole, namely the portion of the waveform from the foot to the first inflection point, P1. This index is thought of to relate mainly to the incident or forward-travelling pressure wave, namely the pressure arising from the natural overflow of the ventricle. Therefore, this index is an indirect measure of the contractility of the heart (De Hert et al., 2006; Morimont et al., 2012; Li et al., 2021).

2.2.4 Measurements of pressure and velocity waveforms

Numerical models based on computational haemodynamics are a useful tool to study blood flow dynamics and investigate the related diseases. However, to validate these models and to test the reliability of *in silico* results, *in vivo* data are of utmost importance. Different techniques can be employed to measure haemodynamics quantities, namely blood pressure, blood flow rate and velocity, and luminal areas of the vessels. Measurement techniques can be either invasive or noninvasive. The latter, being more accessible and easily-obtainable, are usually performed in superficial arteries such as the carotid, brachial, radial, and femoral arteries (Nichols et al., 2011).

Blood pressure can be recorded noninvasively in superficial arteries using applanation tonometry (Armentano et al., 1995a; Zambanini et al., 2005; Raymond et al., 2009; Vermeersch et al., 2009; Valdez-Jasso et al., 2011; Raymond et al., 2011) or the volume-clamp method (Peñáz, 1973). Applanation tonometry involves "applanating" a superficial artery with a pen-like pressure transducer (Drzewieck, Melbin,

and Noordegraaf, 1983; Kelly, 1989; Hoskins, Lawford, and Doyle, 2017), which requires a good dexterity and experience. The obstacle of operator dependency could be potentially avoided by using wearable devices (Garcia-Ortiz et al., 2012), although attaining and maintaining correct sensor position is a key challenge. Calibration of the pulse waveform is generally performed with brachial cuff pressures, which may involve errors related to the cuff pressure inaccuracies and pulse amplification from brachial to the site of measurement (Verbeke et al., 2005; Picone et al., 2017). The volume-clamp method, then refined and commercialised as the Finapres (Wesseling, 1995; Munir et al., 2008; Guilcher et al., 2011), involves a finger cuff whose air pressure is controlled by a servo that clamps the volume of the finger arteries using an infrared photoplethysmography signal. This method provides high fidelity waveform, and has the benefit of self-calibration (Mynard et al., 2020). Compared to the volume-clamp method, tonometry is more trivial, involves less discomfort, and can be applied to a wide range of arterial sites.

Invasive pressure measurements can be obtained in the aorta and other extra-cranial arteries using pressure- and flow-sensing catheters (Davies et al., 2006). Among these, micromanometer-tipped catheter provide for a high fidelity waveform due to an excellent frequency response, but they are expensive. Fluid-filled catheter, on the other hand, are cheaper but the frequency response can be poor (Nichols et al., 2011; Mynard et al., 2020).

Blood flow rate and velocity are two distinct physical quantities that both involve challenges in accurate measurement. The former refers to the volumetric transport of fluid and is defined over a given arterial cross-section, whereas blood velocity refers to the speed of a moving particle of blood, therefore varying over an arterial cross-section and producing a 'velocity profile'. The profile is typically assumed to be parabolic, which is valid for cylindrical tubes with constant flow. Clearly, this is a simplification of the more complex profile that flow velocity exhibits in curved arteries and with pulsatile flow (Womersley, 1955; Sigovan et al., 2011; Mynard and Steinman, 2012). Blood flow velocity decreases towards the peripheral arteries and the micro-circulation. Indeed, the arterial network is a bifurcating system, so the total flow rate at each level in the systemic circulation remains constant. When the total cross-sectional area of vessels increases, the mean velocity decreases. Perivascular flow probes using transit-time ultrasound methods are considered the gold-standard for invasive flow measurement (Mynard et al., 2020), albeit their use tends to be limited to the clinical assessment of bypass grafts. Blood velocity and flow (including the cardiac output) can also be measured noninvasively with time using Doppler ultrasound (Oates, 2001; Vermeersch et al., 2009; Bertaglia et al., 2020) and magnetic resonance imaging (MRI) (Ibrahim et al., 2010; Reymond et al., 2009; Reymond et al., 2011). Whereas MRI is relatively expensive and most suited to imaging central vessels, Doppler ultrasound is inexpensive and more suited to imaging peripheral arteries (Mynard et al., 2020).

Finally, the internal luminal area can be measured in superficial arteries using ultrasound-based echo-tracking (Levenson et al., 1981; Armentano et al., 1995b; Valdez-Jasso et al., 2011) and MRI (Ibrahim et al., 2010).

2.3 The heart

The heart is a muscular organ comprised almost entirely of myocardium, which is a tissue composed of specialised muscle cells (cardiomyocytes) that differ from other muscle cells in their contractility (lower) and their resistance to fatigue (much

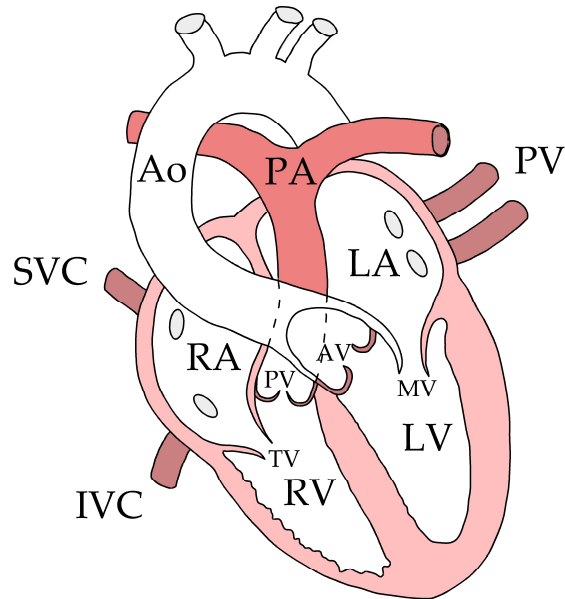


FIGURE 2.4: Sketch of a cross section of the heart showing the gross anatomy. Chambers: LA, left atrium; LV, left ventricle; RA, right atrium; RV, right ventricle. Vessels: Ao, aorta, PA, pulmonary artery; PV, pulmonary veins; SVC, superior vena cava; IVC, inferior vena cava. Valves: AV, aortic valve; MV, mitral valve; PV, pulmonary valve; TV, tricuspid valve. LA is supplied by veins from the lungs, i.e., PV, and transfers blood into the LV through the mitral valve. LV ejects blood into the aorta through the aortic valve. RA collects blood from the venous systemic circulation from superior and inferior venae cavae, and transfers blood into the RV through the tricuspid valve. RV ejects blood into the pulmonary artery thorough the pulmonary valve.

higher) (Formaggia, Quarteroni, and Veneziani, 2009). The heart is surrounded by the pericardium, a serous, inelastic membrane that restricts excessive dilation of the heart and can limit ventricular filling. The heart is composed of four chambers, namely the left and right ventricles, and the left and right atria. The left ventricle is the largest chamber with the thickest walls, and is located posteriorly and leftwards from the right ventricle, which can be thought of as a chamber wrapped around the right side of the left ventricle from the heart base to the apex (Formaggia, Quarteroni, and Veneziani, 2009). The flow across these chambers is regulated by four valves, namely the mitral valve (MV), separating the left atrium (LA) from the left ventricle (LV) and preventing the blood to flow back from the LV to the LA, the aortic valve (AV), controlling the blood flow ejected from the LV into the aorta, the major systemic artery. The MV has two leaflets and is prevented from prolapsing by chordae tendons and papillary muscles running from the cusps of the valve leaflets to the side of the LV. The AV has three simple leaflets that are inserted into the walls of the sinuses of Valsalva, which are roughly hemispherical bulges at the root of the aorta. The AV leaflets are devoid of any attachments and provide mutual support when they are closed (Formaggia, Quarteroni, and Veneziani, 2009). In the right side of the heart, the corresponding valves are the tricuspid (TV) and pulmonary (PV) valves, which govern the flow from the right atrium (RA) into the right ventricle (RV), and that from the RV into the pulmonary arteries, respectively. An illustration of the heart is presented in Figure 2.4. The left and right parts of the heart operate as two

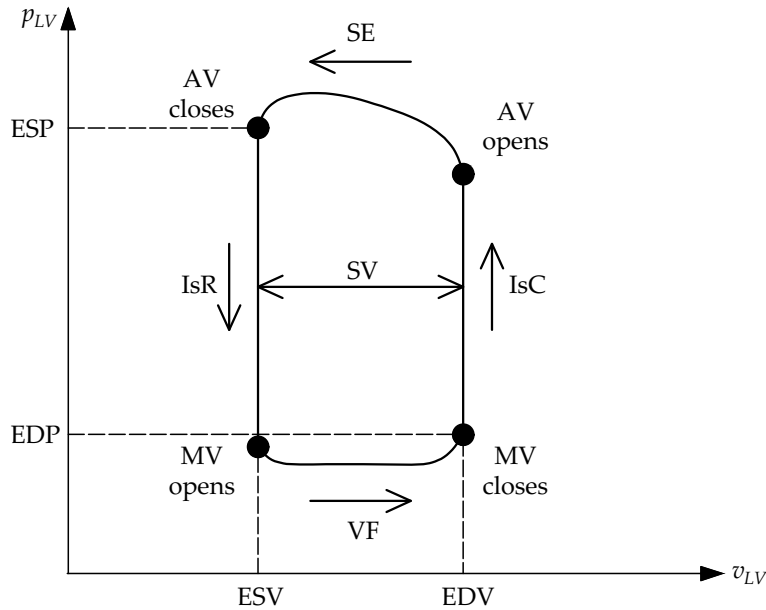


FIGURE 2.5: Schematic representation of the pressure (p_{LV})-volume (v_{LV}) loop for the left ventricle (LV). SE: systolic ejection; IsR: isovolumetric relaxation; VF: ventricular filling; IsC: isovolumetric contraction; EDV, EDP: end diastolic volume and pressure; ESV, ESP: end systolic volume and pressure; SV: stroke volume.

synchronised pumps in parallel: the left side collects oxygenated blood from the pulmonary veins and perfuses the body through the systemic arteries, while the right side collects deoxygenated blood from the systemic veins and perfuses the lungs through the pulmonary arteries. The dynamics of the heart can be summarised in two main phases. During contraction, the first phase, the heart ejects blood from the ventricles into the respective circulations, hence AV and PV are open and MV and TV are closed. During relaxation, the second phase, atria fill with blood returning via the venous circulations, hence AV and PV are closed while MV and TV are open.

This Thesis will focus on the description and modelling of the left part of the heart, namely starting from the pulmonary venous flow rate to the ejection of blood at the aortic root.

2.3.1 The cardiac cycle

The heart beat is a two-stage pumping action over a period of about 1 s. Systole is defined as the period during which the myocardium contracts and blood is ejected from the ventricle. Two ways to characterise systole are used in clinical practice: cardiologists identify the action of the myocardium through the electrocardiograph (ECG), whereas vascular doctors identify systole as the period between the closure of the mitral valve and the subsequent closure of the aortic valve. These two approaches give very similar results. Analogously, diastole is defined either as the period when the myocardium relaxes or the period between the closing of the aortic valve and the closing of the mitral valve. At rest, diastole lasts approximately two thirds of the cardiac period, while with increasing heart rate the diastole shortens and systole remains the same duration, and at maximal heart rate the systole is also shortened (Formaggia, Quarteroni, and Veneziani, 2009).

The ventricular activity is defined by four distinct phases distinguished by the states of the inlet and outlet valves (Figure 2.5). The *isovolumetric contraction* (IsC)

phase occurs when both mitral and aortic valves are closed and the myocardium is contracting. During IsC, the pressure in the LV increases rapidly, exceeding the LA pressure and causing retrograde flow through the mitral valve, and so the closing of the valve itself. The volume in the LV remains unaltered as the blood is incompressible, but it undergoes a significant change in shape as the myocardium contracts.

The *ventricular* or *systolic ejection* (SE) phase starts when the pressure in the LV exceeds that in the aorta, and the aortic valve opens. The aortic pressure rises and the vessel expands due to the ejection of blood from the heart. The pressure difference between the LV and the aorta remains negative¹ as long as the myocardium contracts quickly enough so that the flow into the aorta continues to accelerate up to the peak flow.

After this rapid contraction, the myocardium decelerates the rate of contraction and eventually it ceases to contract and start relaxing. When the rate of contraction of the ventricle becomes less than the volume flow rate in the root of the aorta, the pressure difference between the LV and the aorta is practically zero. This moment coincides with the peak aortic flow rate (Formaggia, Quarteroni, and Veneziani, 2009). Once the peak is reached, the aortic valve starts closing down. As the LV relaxation continues, the pressure difference between the LV and the aorta reverses, becoming positive. This causes the aortic flow to decelerate and, eventually, to reverse, flowing back to the aortic root. Hence, the aortic valve closes, stopping the reversal of flow. The pressure of the LV is still much greater than that of the LA, therefore the mitral valve remains closed, so the closure of the aortic valve marks the start of the *isovolumetric relaxation* (IsR) phase, during which the myocardium keeps relaxing and the LV pressure falls.

When the LA pressure becomes greater than the LV pressure, the mitral valve opens and the *ventricular filling* (VF) phase starts, with the aortic valve that is still closed. VF is characterised by two sub-phases. At first, the passive filling, marked by the so-called E-wave in mitral flow, is driven by the pressure in the atrium plus a suction effect of the LV due to its over-contraction past the equilibrium configuration (Formaggia, Quarteroni, and Veneziani, 2009). Then, the active filling, marked by the A-wave in mitral flow, is generated by the contraction of the left atrium. In healthy young adults at rest, about one third of the filling of the ventricle is contributed by the A-wave. This fraction increases with exercise and with age.

The cardiac output is the average blood volume that is ejected by the LV per unit of time. In a resting healthy adult, CO is about 5–6 l/min. The stroke volume is obtained as the difference between the left ventricular volume at the end of the filling phase (end diastolic volume, EDV) and at the end of the contraction phase (end systolic volume, ESV). SV is typically 70–80 ml. Cardiac dynamics affects SV and CO. Force and rate of ventricular contraction depends on the so-called *preload* and *afterload*. The force of contraction of the myocardium depends on the degree to which it is stretched and therefore the degree of filling of the ventricle prior to contraction (preload). The rate of contraction of the myocardium depends on the load that is experienced, namely the forces that resist ejection (afterload), such as aortic pressure (Formaggia, Quarteroni, and Veneziani, 2009). The venous return is an important driver of the cardiac function. The ability of the heart to change its force of contraction and therefore stroke volume in response to changes in venous return is called the *Frank-Starling mechanism*. Finally, the heart rate is determined by a group of cells

¹By convention, the positive direction along the circulatory system is considered in the direction of mean blood flow, i.e., away from the heart in the arteries and towards the heart in the veins.

TABLE 2.1: Hypertensive conditions classified by diastolic (DBP) and systolic (SBP) blood pressure values (Williams et al., 2018).

Level	DBP [mmHg]	SBP [mmHg]
Optimal (healthy)	DBP < 80	SBP < 120
Normal	80 < DBP < 84	120 < SBP < 129
High normal	85 < DBP < 89	130 < SBP < 139
Grade 1 of hypertension	90 < DBP < 99	140 < SBP < 159
Grade 2 of hypertension	100 < DBP < 109	160 < SBP < 179
Grade 3 of hypertension	DBP \geq 110	SBP \geq 180
Isolate systolic hypertension	DBP < 90	SBP \geq 140

called pacemakers cells, which trigger the contraction of the myocardium. The average HR in the healthy adult subject is 60–75 beats per minute (bpm) (Formaggia, Quarteroni, and Veneziani, 2009; Battista, 2015; Charlton et al., 2019).

2.4 Hypertension

This Section provides the background for hypertension, to better understand the aim and objective of Section 5.3, in which hypertension is addressed through a study application of the cardiovascular numerical model.

Arterial pressure is an important diagnostic parameter for cardiovascular risks. Hypertension, a disease identified with high blood pressure, is still one of the leading causes of morbidity and mortality worldwide (MacMahon et al., 2008; Lim et al., 2012). The number of people with raised blood pressure in the world is increased by 90% during the four decades between 1975 and 2015, with the majority of the increase occurring in low-income and middle-income countries, largely driven by the growth and ageing of the population (Zhou et al., 2017). Hypertension is conventionally classified in ascending order of severity depending on the increase in systolic and/or diastolic pressure values expressed in mmHg (Williams et al., 2018; Bertaglia, 2019), as shown in Table 2.1. A specific hypertensive condition is the *isolate systolic hypertension*, which is characterised by an increase in pulse pressure (Franklin et al., 1997; Salvi, 2012). According to Hoskins, Lawford, and Doyle (2017), this type of hypertension can be present in young subjects (<30 years) due to increase stroke volume, and it is the most common form of hypertension in the adult population (> 50 years) due to increases arterial stiffness.

The aetiology of hypertension remains debated. Accepted causes include ageing, genetics, improper diet, and malfunction of major organs or nervous systems. Nichols et al. (2011) pointed to increase of peripheral resistance and decrease in arterial distensibility as the main causes of hypertension. Both of these causes are responsible for an increased contribution to BP pulse waves of the reflected waves from the peripheral sites of the vascular network. Reflections, however, are created at every site of the arterial network where a change in characteristic impedance occurs, namely with bifurcations, tapering, and changes in mechanical and geometrical properties of the arterial walls (Gaddum et al., 2017; Mynard et al., 2020). Therefore, quantifying and isolating individual reflections is a cumbersome task.

When it is possible to identify a specific, underlying cause for hypertension, such as an obstruction of renal blood flow, hyper-secretion of aldosterone or of epinephrine and norepinephrine, hypertension is referred to as *secondary hypertension*. Contrarily, when the cause cannot be identified in pre-existent diseases or dysfunctions, and hypertension is suspected to stem from vessel stiffening, it is referred to as *essential/primary hypertension* (Battista, 2015; Bertaglia, 2019). In blood vessels, hypertension causes thickening of the tunica media, with a consequent increase in stiffness, accelerates development of atherosclerosis and coronary artery disease and increases systemic vascular resistance. In the heart, hypertension increases the afterload, which forces the ventricle to work harder to eject blood (Tortora and DeFrickson, 2013). Between 90 and 95% of the hypertensive patients are affected by primary hypertension. The remaining 5-10% of cases are secondary hypertension (Tortora and DeFrickson, 2013).

Common clinical practice to treat hypertension is through the use of diuretics, agents that decrease blood pressure by decreasing blood volume as a consequence of the increased elimination of water and salt in the urine. Angiotensin converting enzyme inhibitors block the formation of angiotensin II and thereby promote vasodilation and decrease the secretion of aldosterone. Beta blockers reduce blood pressure by inhibiting the secretion of renin and by decreasing heart rate and contractility. Vasodilators relax the smooth muscle in arterial walls, causing vasodilation and lowering blood pressure by lowering systemic vascular resistance (Tortora and DeFrickson, 2013). The alarming aspect, however, is that approximately one-third of people receiving anti-hypertensive medication still have uncontrolled high blood pressure, which reflects the limited understanding of the pathophysiology underlying the onset of elevated blood pressure and how this could represent a significant economic problem for public healthcare (Hart, 2016).

In this context, research has lately identified cardiac function and systolic ejection as substantial contributors to hypertension, and in particular for isolate systolic hypertension and pulse pressure amplification towards peripheral sites of the arterial network (Segers, Stergiopoulos, and Westerhof, 2000; Fok et al., 2014c; Fok et al., 2014b; Gaddum et al., 2017; Flores Gerónimo et al., 2021). Vennin et al. (2017) defined hypertension as a symptom of various combinations of a number of static, i.e., arterial geometry and stiffness, and dynamic, i.e., ventricular contraction, pathologies. However, thoroughly explaining the relationship between cardiac function and hypertension is a challenging task because it is difficult to decouple the interaction between the arterial impedance and ventricular stroke profile to characterise a patient's pathology. For a concrete step forward to understand the haemodynamic mechanism underlying the elevation of PP and its amplification in the vascular network, and accelerating clinical diagnosis and therapy monitoring of hypertension, complementary *in vivo*–*in silico* approaches should be used. Numerical models offer the possibility to simulate different haemodynamic configurations in physical-based human systemic circulation, isolating single cardiac and vascular contributions to blood pressure. On the other hand, *in vivo* pressure and flow pulse waves can be measured in a multitude of physiological configurations, such as in healthy patients at baseline condition or after pharmacological administration aimed at altering cardiac or vascular properties, and in hypertensive patients. These measurements are essential to validate the numerical results and increasing the reliability of haemodynamic computational models.

Chapter 3

The haemodynamic mathematical model

3.1 Background

This Chapter presents the mathematical background to the haemodynamic model considered in this Thesis. Firstly, in Section 3.1.1, the background on viscoelastic materials is given and the most common viscoelastic models are presented. In particular, the Standard Linear Solid Model (SLSM), which is used in this Thesis to characterise the rheological behaviour of vessels wall, is thoroughly described. Secondly, in Section 3.1.2, the background on balance laws in the framework of fluid mechanics is given. This section addresses the general formulation of conservation and balance laws, the definition of hyperbolic systems of equations, as well as the Riemann problem (RP) and the typology of waves that characterise its solution, namely shock, contact, and rarefactions waves. Moreover, the mass and momentum balance laws are derived in their general formulation, and the pressure–area law is introduced. This latter depends on the mechanical characteristics of vessels wall and it is usually referred to as tube law. Thirdly, in Section 3.2, the mathematical model of the cardiovascular network is presented. This model relies on the so-called augmented fluid–structure interaction (a-FSI) system, which was presented in the previous contributions of Bertaglia et al. (Bertaglia, 2019; Bertaglia, Caleffi, and Valiani, 2020; Bertaglia et al., 2020; Bertaglia et al., 2021). To account for the fluid–structure interaction and therefore to consider the viscoelastic mechanical behaviour of vessels wall when they undergo a pressure pulse, the tube law is included in the governing system of equations based on the SLSM. The “augmented” property is given by the addition of three trivial equations that allow to treat mechanical and geometrical discontinuities along blood vessels. Being the a-FSI system hyperbolic, its eigenstructure is analysed. Finally, Section 3.3 presents the mathematical models used to simulate inlet and outlet boundary conditions (BCs). These are modelled by using lumped–parameter models, namely 0-D models that rely on the hydraulic–electric analogy, as introduced in Chapter 2. The inlet BC represents the cardiac contraction model, and the outlet BC simulates the micro-circulation. Both BC models consist of a combination of the compartments of the 0-D models, i.e., resistance, capacitor, and inductance, which can be in series or in parallel.

3.1.1 Mathematical models for viscoelastic materials

A viscoelastic material is characterised by a mechanical response to a stress that is in-between that of an elastic solid and a viscous liquid, therefore exhibiting both elastic and viscous characteristics when it deforms (Gurting and Sternberg, 1961;

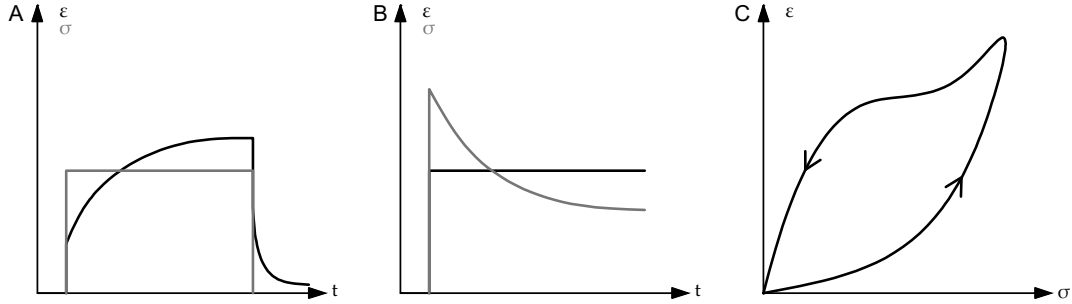


FIGURE 3.1: Schematic representation of the three behavioural features of a viscoelastic material. (A) Creep: when the material is maintained under constant stress, it shows a continuous variation of the deformation over time, composed by an elastic instantaneous strain and a retarded damping effect. (B) Stress relaxation: when the material undergoes a constant deformation, it presents an exponential relaxation of the stress over time after an instantaneous peak. (C) Hysteresis loop determined by loading and unloading phase of the material.

Christensen, 1982; Lakes, 2009; Bertaglia, 2019). In viscoelastic materials, the energy put into the system during the loading phase is not totally recovered during relaxation. Thus, in these materials, the strain depends on the history of the stress, and vice-versa. There are three key features that characterise a viscoelastic material: creep, stress relaxation, and hysteresis (Figure 3.1).

Creep represents the continuous deformation of the material over time when it is kept under constant stress. In particular, a viscoelastic material, when loaded, undergoes an instantaneous deformation (strain), which then increases over time at an ever decreasing strain rate. When the material is unloaded, only part of the deformation accumulated during the loading phase is restored, with an instantaneous recovery of the elastic strain and a delayed recovery of the anelastic deformation over time. Eventually, a permanent strain may remain in the material. In one dimension, the history of the stress σ depends on the time t through the unit Heaviside step function $\mathcal{H}(t)$, defined as 0 for $t < 0$, 1 for $t > 0$, and $1/2$ for $t = 0$, with magnitude (Lakes, 2009):

$$\sigma(t) = \sigma_0 \mathcal{H}(t). \quad (3.1.1)$$

The strain, $\epsilon(t)$ also depending on time, defines the so-called creep compliance (Lakes, 2009):

$$J(t) = \epsilon(t) \sigma_0. \quad (3.1.2)$$

In linear viscoelastic materials, the creep compliance does not depend on the stress level but only on time.

The relaxation time describes the continuous decrease of the stress over time, when it is kept under constant strain, after an instantaneous peak. Assuming that the strain history is a step function with magnitude ϵ_0 beginning at $t = 0$,

$$\epsilon(t) = \epsilon_0 \mathcal{H}(t), \quad (3.1.3)$$

the stress $\sigma(t)$ will decrease with an exponential decay. This decreasing trend is typical of viscoelastic materials due to their relaxation time feature. Also the diastolic decay (relaxation phase) over time of blood pressure in a blood vessel after the systolic (loading) phase is characterised by an exponential trend. Indeed, the exponential relaxation decay of blood pressure is a measure of arterial compliance

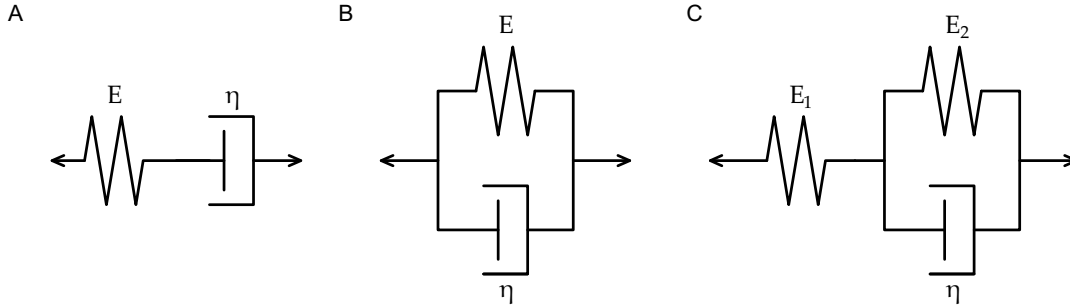


FIGURE 3.2: Schemes of the viscoelastic models: (A) Maxwell model, (B) Kelvin-Voigt model, and (C) Standard Linear Solid model constituted by a first spring in series with a Kelvin-Voigt model. E identify the Young modulus of the spring, and η identifies the viscosity coefficient of the dashpot.

(Mariscal-Harana et al., 2021). The ratio

$$E(t) = \frac{\sigma(t)}{\epsilon_0}, \quad (3.1.4)$$

is called relaxation modulus, or apparent Young modulus, and in linear materials it is independent on the stress level (Lakes, 2009).

Finally, the hysteresis loop describes the dissipation of energy when the material undergoes loading and unloading cycling (Battista, 2015). The energy dissipation associated with hysteresis, as it is when the vessel undergoes dilation and contraction during a cardiac cycle, makes the numerical modelling and simulation of vessels networks a non-trivial matter.

The Standard Linear Solid Model

Although a few of the existent materials behave in a linear way, the theory of linear viscoelasticity provides feasible engineering approximation that is applicable to many field, as in the case of haemodynamic modelling (Bertaglia, 2019). Indeed, it is well known that blood vessels (and living tissues in general) exhibit viscoelastic properties (Fung, 1997; Nichols et al., 2011; Salvi, 2012). In literature, viscoelasticity is accounted for using more or less complex models, which can be linear or not (Holenstein, Niederer, and Anliker, 1980; Bessems et al., 2008; Valdez-Jasso et al., 2009; Wang, Golob, and Chesler, 2016; Ghigo et al., 2017a; Mitsotakis et al., 2019). Considering a viscoelastic model represented by a set of springs and dashpots, where the former represent the elastic elements and the latter correspond to the viscoelastic elements, provides a constitutive relation of linear viscoelasticity (Battista, 2015). Each spring is defined by a Young modulus E , and each dashpot is characterised by a viscosity coefficient η , which takes into account the time dependent relaxation of the material of the wall and its damping effect.

Various configurations of the combination of springs and dashpots can be used to represent a viscoelastic material, as shown in Figure 3.2. The Maxwell (MX) and Kelvin-Voigt (KV) models, schematised in Figure 3.2 A and B respectively, are 2-parameter viscoelastic models. The MX model consists of a spring and a dashpot in series. When undergoing a sudden load maintained constant in time, the mechanical behaviour of MX model is characterised by an instantaneous deformation, which corresponds to the spring immediately stretching, followed by the additional strain of the dashpot that slowly extends, defined by a linear increase (Hoskins, Lawford,

and Doyle, 2017). Once the load is removed, the spring reacts again instantaneously, relaxing, whereas the dashpot does not recover, leading the material to remain with a “creep” strain (Bertaglia, 2019). The KV model consists of a spring and a dashpot in parallel and, when suddenly loaded with a constant stress over time, it does not show an instantaneous deformation but rather a gradual increase of the deformation over time (Hoskins, Lawford, and Doyle, 2017). This is because the spring cannot instantaneously deform since the stress is initially completely absorbed by the dashpot, which holds back the spring, and being transferred to the spring only later in time (Bertaglia, 2019). The same occurs also when the unit is unloaded, and eventually no permanent strain is left.

A specific 3–element viscoelastic model is the Standard Linear Solid Model (SLSM). This model is able to represent the realistic behaviour of vessels wall when undergoing a stress, namely a pressure pulse, exhibiting all three primary features of viscoelasticity: creep, stress relaxation, and hysteresis (Battista, 2015). Regarding hysteresis, the SLSM model allows the representation of the pressure–area loops of the vessel, showing the energy dissipated during the cardiac cycle after the expansion (systolic) and relaxation (diastolic) phases (Nichols et al., 2011; Salvi, 2012; Bertaglia et al., 2020; Piccioli et al., 2022a). The SLSM is composed of a linear elastic spring added in parallel with a MX unit or in series with a KV unit. Both versions of the SLSM reproduce exactly the same mechanical behaviour of the material (Gurting and Sternberg, 1961; Lakes, 2009). In this Thesis, the configuration of the SLSM with the KV unit, represented in Figure 3.2 C, is employed for the formulation of the haemodynamic mathematical model to account for vessels wall viscoelasticity, and it is now presented.

The system of equations describing the SLSM is:

$$\epsilon = \epsilon_1 + \epsilon_2 = \epsilon_1 + \epsilon_D, \quad (3.1.5a)$$

$$\sigma = \sigma_1 = \sigma_2 + \sigma_D, \quad (3.1.5b)$$

$$\sigma_1 = E_1 \epsilon_1, \quad (3.1.5c)$$

$$\sigma_2 = E_2 \epsilon_2, \quad (3.1.5d)$$

$$\sigma_D = \eta \frac{d\epsilon_D}{dt}, \quad (3.1.5e)$$

where ϵ is the total strain, σ is the total stress, and the subscripts D , 1, and 2 identifies the contributes given by the dashpot, and by the first and second springs, respectively. By manipulating the equations in System (3.1.5), the following constitutive law is obtained:

$$\frac{d\sigma}{dt} = E_0 \frac{d\epsilon}{dt} - \frac{1}{\tau_r} (\sigma - E_\infty \epsilon), \quad (3.1.6)$$

where E_0 is the instantaneous Young modulus, E_∞ is the asymptotic Young modulus, and τ_r is the relaxation time (Lakes, 2009; Bertaglia, 2019), which are defined as:

$$E_0 = E_1, \quad E_\infty = \frac{E_1 E_2}{E_1 + E_2}, \quad \tau_r = \frac{\eta}{E_1 + E_2}. \quad (3.1.7)$$

The SLSM is able to exhibit all three primary features of a viscoelastic material. Eq. (3.1.7) clearly defines the mechanical response of the SLSM: when it is loaded, the instantaneous response is attributed only to the first spring, since $E_0 = E_1$. Then, the dashpot starts experimenting the stress as it gradually opens over time. If the load is maintained constant in time, the two springs behave as they were in series, without considering the presence of the dashpot: $1/E_\infty = 1/E_1 + 1/E_2$. At the asymptotic

state, the creep is ascribed only to the spring in parallel with the dashpot. Finally, when the system is unloaded, the first spring relaxes instantaneously, whereas the second has a slower response, being held back by the dashpot (Bertaglia, 2019).

By applying the Laplace transform theory it is possible to derive the creep response of the SLSM, defined by the following function (Lakes, 2009):

$$J(t) = \frac{1}{E_0} e^{-\frac{t}{\tau_c}} + \frac{1}{E_\infty} \left(1 - e^{-\frac{t}{\tau_c}}\right), \quad (3.1.8)$$

where $\tau_c = \eta / E_2$ is the retardation/creep time. Noteworthy, it is also possible to derive the *relaxation function* (Lakes, 2009), which describes the change in stiffness of the material over time, i.e., the apparent Young modulus, starting from the instantaneous Young modulus, E_0 , and ending with the asymptotic Young modulus, E_∞ , through the relaxation time τ_r :

$$E(t) = E_0 e^{-\frac{t}{\tau_r}} + E_\infty \left(1 - e^{-\frac{t}{\tau_r}}\right). \quad (3.1.9)$$

3.1.2 Hyperbolic balance laws in fluid mechanics

Most physical phenomena can be described by a system of partial differential equations (PDEs) consisting of balance laws. In fluid mechanics, balance laws result straightforwardly by applying the fundamental laws for the conservation of extensive (integral) quantities such as, among others, mass and momentum, inside a *closed system*, also called *fluid volume*, V_f . V_f is understood to move at the same velocity of the fluid, therefore no relative velocities occur (Navas-Montilla, 2018). However, the direct application of conservation laws to the fluid volume can be very cumbersome or even impossible in many engineering applications. To overcome this limitation, the integration of the physical laws is performed inside a control volume, V_c , that fits the geometry of the problem, substituting the fluid volume. Consequently, the flux across the boundaries of V_c , hereafter referred as control surfaces, ∂V_c , must be considered in order to ensure conservation (Navas-Montilla, 2018). The Reynolds Transport Theorem (RTT) (Toro, 2009; Quarteroni and Formaggia, 2004a) is employed to relate variations in the fluid volume to variations in the control volume, allowing to express the variation of an extensive quantity inside the fluid volume as the variation of such quantity in the control volume plus the flux of its associated intensive property (e.g., density) across the control surfaces (White, 1998; Navas-Montilla, 2018). Given \mathbf{M} a vector of any extensive property of the fluid and $\mathbf{U} = d\mathbf{M}/dV$ the intensive value of \mathbf{M} per unit volume, RTT is expressed as

$$\frac{d}{dt} \mathbf{M}_{V_f}(t) = \frac{d}{dt} \int_{V_c} \mathbf{U} dV + \int_{\partial V_c} \mathbf{U} (\mathbf{v} - \mathbf{v}_s) \cdot \hat{\mathbf{n}} d\sigma, \quad (3.1.10)$$

where the term $(\mathbf{v} - \mathbf{v}_s)$ expresses the relative velocity between the fluid and control surface, which coincides with the arterial wall, allowing the presence of a permeable lumen (Formaggia, Quarteroni, and Veneziani, 2009), and $\hat{\mathbf{n}}$ is the outer normal of ∂V_c . In Eq. (3.1.10), the term on the left-hand side stands for the total variation of the quantity \mathbf{M} inside the fluid volume V_f , which can be either null when the quantity is conserved, and so the equation is referred to as *conservation law*, or equal to a source. When existing, the source is considered acting on the control volume (Navas-Montilla, 2018), and the equation is properly said a *balance law*.

The differential formulation for a system of balance laws is straightforwardly obtained by assuming an infinitesimal integration volume in the RTT and reads in

its three-dimensional (3-D) divergence form (Navas-Montilla, 2018) as

$$\frac{\partial \mathbf{U}}{\partial t} + \nabla \cdot \mathbf{F}(\mathbf{U}) = \mathbf{S}, \quad (3.1.11)$$

where $\mathbf{U} = \mathbf{U}(x, t)$ is the vector of conserved quantities, $\mathbf{F}(\mathbf{U})$ is the vector of fluxes, and \mathbf{S} is the vector of source terms, which is typically in the form $\mathbf{S} = \mathbf{S}(\mathbf{U}, x)$.

Assuming a null vector of source terms and the problem one-dimensional (1-D), the system of conservation laws in PDE form can be also written in the linear homogeneous form (Toro, 2009; Navas-Montilla, 2018) as

$$\mathbf{U}_t + \mathbf{F}(\mathbf{U})_x = 0, \quad (3.1.12)$$

where the subscripts t and x denote the partial derivatives in time and space, $\partial/\partial t$ and $\partial/\partial x$, respectively, and

$$\mathbf{U} = \begin{pmatrix} u_1 \\ u_2 \\ \vdots \\ u_m \end{pmatrix}, \quad \mathbf{F}(\mathbf{U}) = \begin{pmatrix} f_1 \\ f_2 \\ \vdots \\ f_m \end{pmatrix}. \quad (3.1.13)$$

Each component of the vector of fluxes, f_i , is a function of the u_j components of $\mathbf{U}(x, t)$. Applying the chain rule to the second term in Eq. (3.1.12),

$$\frac{\partial \mathbf{F}(\mathbf{U})}{\partial x} = \frac{\partial \mathbf{F}}{\partial \mathbf{U}} \frac{\partial \mathbf{U}}{\partial x}, \quad (3.1.14)$$

the system of conservation laws can be written in the homogeneous quasi-linear form (Toro, 2009), namely

$$\mathbf{U}_t + \mathbf{A}(\mathbf{U})\mathbf{U}_x = 0, \quad (3.1.15)$$

where $\mathbf{A}(\mathbf{U}) = \partial \mathbf{F} / \partial \mathbf{U}$ is the Jacobian of the flux function $\mathbf{F}(\mathbf{U})$ in Eq. (3.1.12). The entries of the matrix $\mathbf{A}(\mathbf{U})$ are partial derivatives of the components f_i of the vector \mathbf{F} with respect to the components u_j of the vector of conserved variables \mathbf{U} , that is $a_{ij} = \partial f_i / \partial u_j$, namely

$$\mathbf{A}(\mathbf{U}) = \begin{pmatrix} \partial f_1 / \partial u_1 & \cdots & \partial f_1 / \partial u_m \\ \partial f_2 / \partial u_1 & \cdots & \partial f_2 / \partial u_m \\ \vdots & \ddots & \vdots \\ \partial f_m / \partial u_1 & \cdots & \partial f_m / \partial u_m \end{pmatrix}. \quad (3.1.16)$$

If the Jacobian matrix in (3.1.16) does not depend either on \mathbf{U} or x , it would be constant and System (3.1.15) would be said to be *linear*.

System (3.1.15) is said to be *hyperbolic* at a point (x, t) if the Jacobian $\mathbf{A}(\mathbf{U})$ has m real eigenvalues $\lambda_1, \lambda_2, \dots, \lambda_m$ and a corresponding set of m linearly independent right eigenvectors $\mathbf{R}^1, \mathbf{R}^2, \dots, \mathbf{R}^m$. The system is said to be *strictly hyperbolic* if the eigenvalues λ_i are all distinct (Toro, 2009).

When Eq. (3.1.12) entails the presence of source terms $\mathbf{S}(\mathbf{U})$ at the right-hand side of the equation, and it cannot be written in the conservative form, the system of PDE balance laws reads in the general non-conservative non-homogeneous form as

$$\mathbf{U}_t + \mathbf{F}(\mathbf{U})_x + \mathbf{B}(\mathbf{U})\mathbf{U}_x = \mathbf{S}(\mathbf{U}), \quad (3.1.17)$$

where $\mathbf{S}(\mathbf{U}) = (s(u_1), s(u_2), \dots, s(u_m))^T$ is a vector of algebraic expressions that are functions of the conservative variables, and $\mathbf{B}(\mathbf{U})$ is the matrix of the fluxes related to the non non-conservative part of the system.

Under the hypothesis of linearity of the PDEs system, it is now recalled the definition of *characteristic curves*, or simply *characteristics*, which are defined as curves $x = x(t)$ in the t - x plane along which the PDE becomes an ordinary differential equation (ODE) (Wylie and Streeter, 1978; Toro, 2009). Considering $x = x(t)$ and $u = u(x(t), t)$, the rate of change of u along $x = x(t)$ is

$$\frac{du}{dt} = \frac{\partial u}{\partial t} + \frac{dx}{dt} \frac{\partial u}{\partial x} = \frac{\partial u}{\partial t} + a \frac{\partial u}{\partial x}, \quad (3.1.18)$$

where a is called the *characteristic speed* and, according to Eq. (3.1.18), $a = dx/dt$ is the slope of the curve $x = x(t)$ in the t - x plane and is assumed to be constant. Eq. (3.1.18) defines that u is constant along the characteristic curve $x = x(t)$ with characteristic speed a . To define a particular member of the family of characteristic curves satisfying the ODE $a = dx/dt$, an *initial condition* (IC) at time $t = 0$ is needed. The system of equations constituted by a PDE and an IC is said initial value problem (IVP). Given $x(0) = x_0$ as IC, then the single characteristic curve passing through the point $(x_0, 0)$ is

$$x(t) = x_0 + at. \quad (3.1.19)$$

Finally, recalling that u is constant along the characteristic curve, if the initial value of u is known ($u(x, 0) = u_0(x)$ at time $t = 0$), then along the characteristic expressed in Eq. (3.1.19), the solution is

$$u(x, t) = u_0(x_0) = u_0(x - at). \quad (3.1.20)$$

Therefore, given an initial profile $u_0(x)$, the PDE will simply translate this profile with velocity a to the right if $a > 0$ and to the left if $a < 0$, and the shape of the initial profile remains unchanged. This concept is at the base of wave propagation phenomena, where a wave is understood as some recognisable feature of disturbance that travels at a finite speed (Toro, 2009).

To analyse the PDE hyperbolic system in Eq. (3.1.15) and its related IC, it is useful to transform the dependent variables $\mathbf{U}(x, t)$ into a new set of dependent variables $\mathbf{W}(x, t)$, called *characteristic variables* (Toro, 2009). These are defined in virtue of the hyperbolicity of the PDE system as $\mathbf{W} = \mathbf{R}^{-1}\mathbf{U}$, where \mathbf{R}^{-1} is the inverse matrix of $\mathbf{R} = [\mathbf{R}^1, \mathbf{R}^2, \dots, \mathbf{R}^m]$. With mathematical manipulation, System (3.1.15) can be rewritten in the *characteristic form*, namely in terms of the characteristic variables as

$$\mathbf{W}_t + \mathbf{\Lambda}\mathbf{W}_x = 0, \quad (3.1.21)$$

where $\mathbf{\Lambda}$ is a diagonal matrix with diagonal entries that are the eigenvalues λ_i of $\mathbf{A}(\mathbf{U})$. The i -th PDE of System (3.1.21) is

$$\frac{\partial w_i}{\partial t} + \frac{dx}{dt} \frac{\partial w_i}{\partial x} = \frac{\partial w_i}{\partial t} + \lambda_i \frac{\partial w_i}{\partial x} = 0, \quad i = 1, \dots, m, \quad (3.1.22)$$

involving single unknowns $w_i(x, t)$. Note that the characteristic speed is λ_i and there are m characteristic curves satisfying m ODEs of the type $dx/dt = \lambda_i$, for $i = 1, \dots, m$.

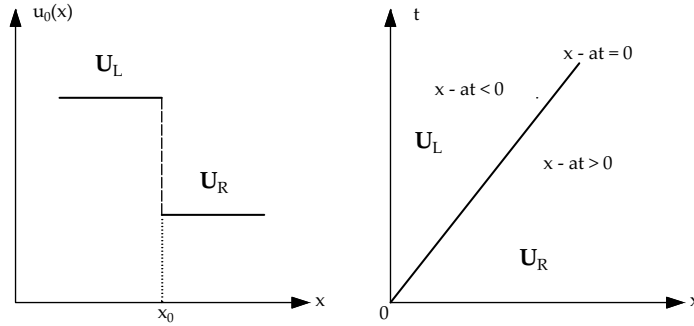


FIGURE 3.3: Illustration of the initial condition (right) and solution (left) for a Riemann problem considering one PDE. At the initial time, the RP consists in two constant states separated by a discontinuity at $x = 0$. The solution is represented in the $x-t$ plane, with the discontinuity propagating with positive characteristic speed a .

The Riemann problem

The Riemann problem (RP) is a IVP where the IC presents a discontinuity. When considering a homogeneous linear PDE, the RP reads as

$$\text{PDE : } \quad u_t + au_x = 0, \quad (3.1.23a)$$

$$\text{IC : } \quad u(x, 0) = u_0(x) = \begin{cases} u_L & \text{if } x < 0, \\ u_R & \text{if } x > 0, \end{cases} \quad (3.1.23b)$$

where u_L and u_R are two constant values. The trivial case would result when $u_L = u_R$. The IC has the discontinuity in $x = 0$, and this propagates in the $x-t$ plane at a speed a , therefore covering a distance $d = at$ in time t . This particular characteristic curve separates those characteristic curves to the left, characterised by the solution u_L , from those curves to the right, characterised by the solution u_R . Therefore, the solution of the RP (3.1.23) is obtained straightforwardly:

$$u(x, t) = u_0(x - at) = \begin{cases} u_L & \text{if } x - at < 0, \\ u_R & \text{if } x - at > 0. \end{cases} \quad (3.1.24)$$

The presented RP and related solutions are shown in Figure 3.3. The only characteristic curve across which the solution of the RP (3.1.24) changes is the one that passes through $x = 0$ and travels at constant celerity.

The RP (3.1.23) can be extended to a hyperbolic system of PDEs and their correspondent ICs in the following generalised IVP (Toro, 2009):

$$\text{PDE : } \quad \mathbf{U}_t + \mathbf{A}\mathbf{U}_x = 0, \quad -\infty < x < \infty, \quad t > 0, \quad (3.1.25a)$$

$$\text{IC : } \quad \mathbf{U}(x, 0) = \mathbf{U}^{(0)}(x) = \begin{cases} \mathbf{U}_L & \text{if } x < 0, \\ \mathbf{U}_R & \text{if } x > 0, \end{cases} \quad (3.1.25b)$$

Assuming to have a RP for a general 2×2 linear system, the waves in the $x-t$ plane with origin in $(0,0)$ will be two, travelling with speeds equal to λ_1 and λ_2 , being $\lambda_1 < \lambda_2$ (Figure 3.4). The solution to the left of the slowest characteristic speed $dx/dt = \lambda_1$ is simply the data state \mathbf{U}_L , whereas that to the right of the fastest characteristic speed $dx/dt = \lambda_2$ is simply the data state \mathbf{U}_R . The wedge between the λ_1 and λ_2 waves is the so-called *star region* and the solution is there denoted as

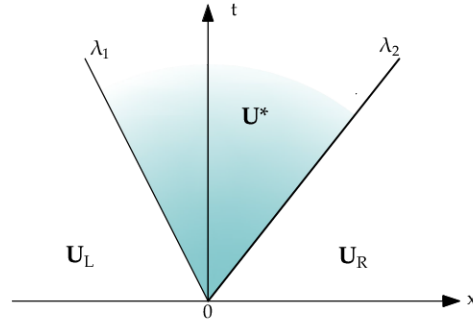


FIGURE 3.4: Structure of the solution of a Riemann problem for a 2×2 linear hyperbolic system. The two waves of the solution travel at speed λ_1 and λ_2 , respectively. The shaded area represents the star region \mathbf{U}^* between the two constant states \mathbf{U}_L and \mathbf{U}_R

\mathbf{U}^* . This is due to the distancing of the two waves emerging from the origin of the initial discontinuity.

In a RP like the one presented in IVP (3.1.25) each i -th characteristic speed, λ_i , associated to the i -th wave in the RP, defines a *characteristic field*, the λ_i -field. This property is typical of hyperbolic systems of balance laws. Therefore, in a general RP for a 2×2 non-linear hyperbolic system there will be two characteristic fields to be defined. Two types of characteristic fields exist, i.e., the *linearly degenerate* (LD) field and the *genuinely non-linear* field (Toro, 2009). A λ_i -characteristic field is said to be linearly degenerate if

$$\nabla \lambda_i(\mathbf{U}) \cdot \mathbf{R}^{(i)}(\mathbf{U}) = 0, \quad \forall \mathbf{U} \in \mathcal{R}^m, \quad (3.1.26)$$

where \mathcal{R}^m is the set of real-valued vectors of m components. A λ_i -characteristic field is said to be genuinely non-linear if

$$\nabla \lambda_i(\mathbf{U}) \cdot \mathbf{R}^{(i)}(\mathbf{U}) \neq 0, \quad \forall \mathbf{U} \in \mathcal{R}^m. \quad (3.1.27)$$

The symbol \cdot denotes the dot product in the phase space, namely the space of vectors $\mathbf{U} = (u_1, \dots, u_m)$, and for a 2×2 system it is called phase space $u_1 - u_2$. $\nabla \lambda_i(\mathbf{U})$ is the gradient of the eigenvalue $\lambda_i(\mathbf{U})$, namely

$$\nabla \lambda_i(\mathbf{U}) = \left(\frac{\partial \lambda_i}{\partial u_1}, \frac{\partial \lambda_i}{\partial u_2}, \dots, \frac{\partial \lambda_i}{\partial u_m} \right)^\top. \quad (3.1.28)$$

The characteristic field defines the wave type. Linearly degenerate fields define the so-called *contact waves*, whereas the genuinely non-linear fields define either *shock waves* or *rarefactions*.

In order to characterise contact waves, shocks, and rarefactions, it is necessary to introduce two more concepts. Firstly, each discontinuous wave solution in a RP travels at a speed S_i associated with the λ_i -characteristic field and, according to the Rankine-Hugoniot condition (Toro, 2009), it holds true that

$$\Delta \mathbf{F} = S_i \Delta \mathbf{U}, \quad (3.1.29)$$

with

$$\Delta \mathbf{U} = \mathbf{U}_R - \mathbf{U}_L, \quad \Delta \mathbf{F} = \mathbf{F}_R - \mathbf{F}_L, \quad \mathbf{F}_L = \mathbf{F}(\mathbf{U}_L), \quad \mathbf{F}_R = \mathbf{F}(\mathbf{U}_R),$$

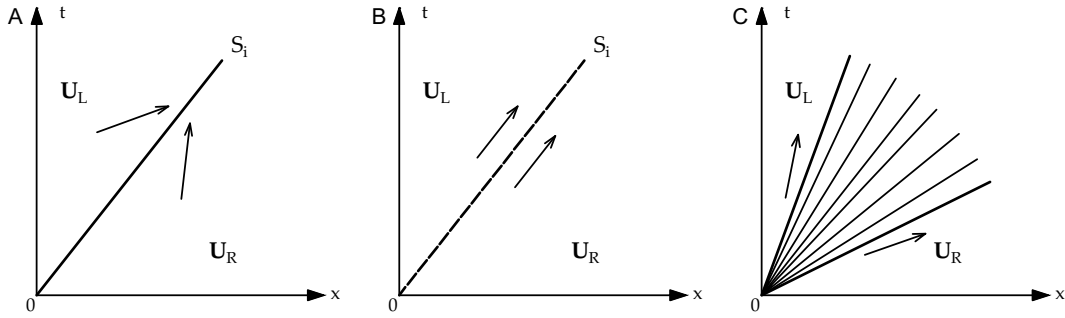


FIGURE 3.5: Elementary wave solutions of the Riemann problem: (A) shock wave of speed S_i , (B) contact wave of speed S_i , and (C) rarefaction wave.

where \mathbf{U}_L and \mathbf{U}_R identifies the states immediately to the left and right of the discontinuity. Secondly, we define the *generalised Riemann Invariants* (RIs) as the relations that hold true, for certain waves, across the wave structure, and lead to the following $(m - 1)$ ODEs

$$\frac{dw_1}{r_1^{(i)}} = \frac{dw_2}{r_2^{(i)}} = \dots = \frac{dw_m}{r_m^{(i)}}. \quad (3.1.30)$$

They relate ratios of changes dw_s of a quantity w_s to the respective component r_s^i of the right eigenvector \mathbf{R}^i corresponding to a λ_i -wave family (Toro, 2009).

Having introduced that, shock, contact discontinuity, and rarefaction waves can be finally defined. Shock waves are jump discontinuities connecting the left and right constant states, and they are related to genuinely non-linear fields. Shock waves satisfy the Rankine-Hugoniot condition and the entropy condition, i.e., $\lambda_i(\mathbf{U}_L) > S_i > \lambda_i(\mathbf{U}_R)$. Contact waves are jump discontinuities connecting the left and right constant states, but they are related to linearly degenerate fields; they satisfy the Rankine-Hugoniot condition and the generalised RIs remain constant across the wave. Also, contact waves satisfy the parallel characteristic condition, i.e., $\lambda_i(\mathbf{U}_L) = \lambda_i(\mathbf{U}_R) = S_i$. Finally, rarefaction waves are smooth transitions connecting the left and right constant states and they are related to genuinely non-linear fields. Across rarefactions, it holds true the constancy of the generalised RIs. They are characterised by the divergence of the characteristics, i.e., $\lambda_i(\mathbf{U}_L) < \lambda_i(\mathbf{U}_R)$. The three wave types are represented in Figure 3.5.

Finally, the 2×2 RP can be generalised in a $N \times N$ RP, maintaining the same general formulation of IVP (3.1.25). In this case, the solution $\mathbf{U}(x, t)$ consists of $N + 1$ constant states separated by N waves. Each characteristic field λ_i corresponds to a wave type. In linear hyperbolic systems with constant coefficients each wave is a discontinuity of speed $S_i = \lambda_i$ and defines a linearly degenerate field. In non-linear hyperbolic systems, the waves may be discontinuities as shock and contact waves, or smooth transition waves like rarefactions. Define the wave type is a crucial condition for the determination of the associated RP.

One-dimensional balance laws

One of the base assumptions in blood flow modelling is to consider blood in large arteries as a constant-density incompressible Newtonian fluid (Formaggia, Quarteroni, and Veneziani, 2009). There are three main ways to derive a 1-D model of an

incompressible fluid flowing in a compliance pipe. The first is to perform an asymptotic analysis starting from the incompressible Navier-Stokes equations by assuming that the radius of the vessel, R , is small compared to its length, l , i.e., $R/l \ll 1$. The second is to assume cylindrical symmetry and integrate the Navier-Stokes equations on a generic section. Otherwise, the governing equations of blood flow can be derived from conservation principles (Toro, 2009; Formaggia, Quarteroni, and Veneziani, 2009).

It is considered a simple compliant tube as a model of an artery with cross-section S , assuming that the axis of the vessel is rectilinear and coincides with the x -axis. The starting point for the derivation of the 1-D governing equations is the RTT, Eq. (3.1.10), for an arbitrary control volume V_c with boundaries ∂V_c and outer normal \hat{n} of the compliant tube considered. Hence, V_c is composed of the arterial wall ∂V_c and the two end sections S_1 and S_2 , which are assumed to be normal to the axis (Formaggia, Quarteroni, and Veneziani, 2009). To obtain the 1-D form of the conservation laws the area-averaged values of the variables \mathbf{U} must be considered, i.e.,

$$\bar{\mathbf{U}} = \frac{1}{A} \int_S \mathbf{U} d\sigma, \quad (3.1.31)$$

where $A = A(x, t) = \int_S d\sigma$ is the area of the cross-section S . So, it is possible to write a volume integral as

$$\int_{V_c} \mathbf{U} dV = \int_{x_1}^{x_2} \left[\int_S \mathbf{U} d\sigma \right] dx = \int_{x_1}^{x_2} A \bar{\mathbf{U}} dx, \quad (3.1.32)$$

where x_1 and x_2 ($x_2 > x_1$) are the x -coordinates of the cross-sections S_1 and S_2 , respectively.

The law of *conservation of mass* in the flexible tube is obtained considering the extensive property, \mathbf{M} in Eq. (3.1.10), to be the total mass inside the control volume, V_c . The correspondent intensive quantity is the blood density, ρ , which is assumed to be constant and so the fluid incompressible. It is assumed that no mass is generated or annihilated within V_c , that the surface ∂V_c is fixed, meaning that the mass flows across the surfaces S_1 and S_2 , and the impermeability of the lumen, which implies $v_s = 0$. Therefore, it holds that

$$\frac{D\mathbf{M}}{Dt} = 0, \quad (3.1.33)$$

implying

$$\frac{d}{dt} \int_{V_c} \rho dV_c + \int_{\partial V_c} \rho \mathbf{v} \cdot \hat{n} d\sigma = 0. \quad (3.1.34)$$

The first term in the left-hand side of Eq. (3.1.34) is the time rate of change of the mass enclosed by the volume V_c , which is fixed and independent of time t . The second term can be rewritten by applying the Gauss' theorem. Hence, Eq. (3.1.34) reads

$$\frac{d}{dt} \int_{V_c} \rho dV_c + \int_{V_c} \nabla \cdot (\rho \mathbf{v}) d\sigma = 0. \quad (3.1.35)$$

The area-averaged quantity is considered to obtain a 1-D formulation of the law, so the reformulations expressed by equations (3.1.31) and (3.1.32) are applied. Reminding that ρ is constant, the area-average density coincides with ρ , and eventually it can be simplified from all terms. Moreover, as x_1 and x_2 are arbitrary it follows that

the integral must vanish. Hence, the conservation of mass reads as

$$\frac{\partial A}{\partial t} + \frac{\partial(A\bar{v}_x)}{\partial x} = 0, \quad (3.1.36)$$

where \bar{v}_x is the area-averaged, x -component of the vector of velocity \mathbf{v} .

The law of *balance of momentum* is obtained considering $\mathbf{M} = \rho\mathbf{v}$ in Eq. (3.1.10), and derives from the direct application of Newton's law on the volume V_c . The total force acting on the volume is divided into surface forces, \mathbf{f}_S , and volume forces, \mathbf{f}_V . The former derives from the stress vector and depends on the pressure, p , and a viscous component (Toro, 2009; Formaggia, Quarteroni, and Veneziani, 2009), whereas \mathbf{f}_V accounts for inertial or gravitational forces. The hypotheses of constant density and impermeable lumen are still valid. In light of Newton's law, the following equation holds:

$$\frac{D\mathbf{M}}{Dt} = \mathbf{f}_S + \mathbf{f}_V. \quad (3.1.37)$$

Rewriting Eq. (3.1.37) using Eq. (3.1.10) results

$$\frac{d}{dt} \int_{V_c} (\rho\mathbf{v}) dV_c + \int_{\partial V_c} \mathbf{v}(\rho\mathbf{v}) \cdot \hat{\mathbf{n}} d\sigma = \mathbf{f}_S + \mathbf{f}_V. \quad (3.1.38)$$

Eq. (3.1.38) states that the time rate of momentum within the fixed control volume is due to the net momentum inflow over the momentum outflow plus surface and volume source terms. Analogously to the derivation of the conservation of mass, the Gauss' theorem is invoked; considering the 1-D formulation and the arbitrariness of spacial coordinates, the balance of momentum law is obtained,

$$\frac{\partial(A\bar{v}_x)}{\partial t} + \frac{\partial(A\bar{v}_x^2)}{\partial x} + \frac{A}{\rho} \frac{\partial p}{\partial x} = -\frac{A}{\rho} d_x + \rho Ag, \quad (3.1.39)$$

where d_x is a term depending on the viscosity of the fluid in its x -component and is a linear function of the area-averaged velocity \bar{v}_x (Formaggia, Quarteroni, and Veneziani, 2009). Hence, the term Ad_x/ρ derives from surface forces, whereas the term ρAg stands for volume forces.

The unknowns in the system of mass and momentum balance laws are the area of the vessel, A , the area-averaged velocity, \bar{v}_x , and the pressure of the vessel, p . The problem is undetermined as the number of unknowns exceeds that of the equations. A common way to close the system is to explicit a relationship between the pressure and the area of the vessel.

Some hypothesis are made to express the *pressure-area law* of the tube. Firstly, it is assumed the static equilibrium in the radial direction of the cylindrical tube. Moreover, the ratio h_0/R , where h_0 is the reference vessel wall thickness, is so small to neglect bending terms, and the wall displaces in the normal direction, so that the longitudinal and circumferential displacements are negligible compared to the radial ones (this hypothesis is widely accepted in the biomedical literature) (Formaggia, Quarteroni, and Veneziani, 2009). The vessel is subjected to a time varying transmural pressure across the surface, $\Delta p = p - p_{ext}$, with p_{ext} being the external pressure that is assumed constant. Homogeneous Dirichlet boundary conditions are assumed (i.e., a clamped vessel). Finally, the reference configuration is the pre-stressed. The general, widely-adopted formulation of the pressure-area law in the

easiest form is

$$p = p_{ext} + \psi_{el}(A; A_0, h_0, E), \quad (3.1.40)$$

where ψ_{el} is the elastic contribution to transmural pressure that depends on the vessel cross-section, $A = A(x)$, the reference (equilibrium) area of the lumen, $A_0 = A_0(x)$, the vessel wall thickness, h_0 , and the mechanical properties of the vessel wall, i.e., the Young modulus $E = E(x)$. The subscript 0 denotes the reference (equilibrium) state, $(p, q) = (p_{ext}, 0)$, with q the blood flow rate (Formaggia, Quarteroni, and Veneziani, 2009; Alastruey, Parker, and Sherwin, 2012). The main properties of ψ_{el} are

$$\frac{\partial \psi_{el}}{\partial A} > 0, \quad \psi_{el}(A_0; A_0, h_0, E) = 0, \quad (3.1.41)$$

for all allowable values of A , A_0 , h_0 , and E (Formaggia, Quarteroni, and Veneziani, 2009). Eq. (3.1.40) assumes that the wall is instantaneously in equilibrium with the pressure forces acting on it, and represents the pressure–area law for vessels in case of an elastic vessel wall. More complex pressure–area laws can be obtained when the viscoelasticity of the vessel wall is considered, resulting in the enrichment of Eq. (3.1.40) with additional terms related to the viscoelastic model chosen. In this Thesis a specific viscoelastic tube law, based on the SLSM presented in Section 3.1.1, is introduced in the governing system of equations in PDE form. The constitutive law has the added value of simulating the proper mechanical response of the vessel wall when undergoing a pressure pulse, which is characterised by all primary features of viscoelastic materials (creep, stress relaxation, and hysteresis, introduced in Section 3.1.1), and is thoroughly presented in the following of this Chapter.

3.2 The 1-D augmented fluid-structure-interaction (a-FSI) system

The well established system of governing equations defining blood flow circulation in compliant vessels is composed of the standard equations of balance of mass and momentum of the fluid mechanics, presented in Section 3.1.2. These were obtained in the 1-D formulation, assuming the fluid to be incompressible and an impermeable vessel wall. Moreover, the hypothesis of large wavelengths with respect to the radius of the vessels is made (Wang, Fullana, and Lagrée, 2015). To obtain the set of balance laws employed in this Thesis, gravity forces in the momentum balance law are neglected, i.e., $\rho Ag = 0$ in Eq. (3.1.39). This hypothesis means simulating blood flow in a subject in the supine position. To make the set of governing equation a determined problem, a constitutive relationship relating the cross-sectional area to the internal pressure is needed, which is the so-called tube law. The tube law in general form is given in Eq. (3.1.40), and it can be expressed both in elastic and viscoelastic formulations. The elastic formulation consists in a first reasonable approximation of the mechanical behaviour of vessels (Müller and Toro, 2014a; Müller and Toro, 2014b; Mynard and Nithiarasu, 2008; Sherwin et al., 2003a; Toro and Siviglia, 2013; Willemet and Alastruey, 2014), whereas the viscoelastic one allows for a more accurate characterization of the FSI occurring between blood flow and vessel walls, considering damping effects (Alastruey, Parker, and Sherwin, 2012; Alastruey et al., 2012; Bertaglia, Caleffi, and Valiani, 2020; Bertaglia et al., 2020; Bertaglia et al., 2021; Mynard and Smolich, 2015; Raghunath et al., 2011). In the proposed model, viscoelasticity is taken into account recurring to the SLSM, previously introduced in Section 3.1.1. SLSM is the simplest viscoelastic model able to exhibit all the three primary features of a viscoelastic material: creep, stress relaxation and hysteresis. Finally,

to ensure a formally correct numerical treatment of possible longitudinal discontinuities of vessels properties, either geometrical or mechanical – i.e., equilibrium cross-sectional area $A_0(x)$, instantaneous Young modulus $E_0(x)$ (or even the asymptotic one, E_∞), and external pressure $p_{ext}(x)$ – three additional closure equations are added to the system, imposing these quantities to be constant in time (Bertaglia, Calceffi, and Valiani, 2020; Castro et al., 2008; Müller and Toro, 2013; Toro and Siviglia, 2013). Thus, the a-FSI system is obtained:

$$\partial_t A + \partial_x(Au) = 0, \quad (3.2.1a)$$

$$\partial_t(Au) + \partial_x(Au^2) + \frac{A}{\rho} \partial_x p = \frac{f}{\rho}, \quad (3.2.1b)$$

$$\partial_t p + d \partial_x(Au) = S, \quad (3.2.1c)$$

$$\partial_t A_0 = 0, \quad (3.2.1d)$$

$$\partial_t E_0 = 0, \quad (3.2.1e)$$

$$\partial_t p_{ext} = 0. \quad (3.2.1f)$$

Here $A(x, t)$ is the cross-sectional area of the vessel, $u(x, t)$ is the cross-sectional averaged blood velocity (previously labelled as \bar{v}_x in Section 3.1.2, $p(x, t)$ is the internal blood pressure, ρ is the blood density. The term f represents the contribution of surface forces related to the viscosity, which were labelled as Ad_x in Eq. (3.1.39). S is the source term related to the viscoelastic modelling of the vessels wall. Variables x and t are space and time, respectively, and subscripts indicate the correspondent partial derivative.

It is possible to write the non-linear non-conservative System (3.2.1) in the general compact form:

$$\partial_t \mathbf{Q} + \partial_x f(\mathbf{Q}) + \mathbf{B}(\mathbf{Q}) \partial_x \mathbf{Q} = \mathbf{S}(\mathbf{Q}), \quad (3.2.2)$$

and, furthermore, in the following quasi-linear form:

$$\partial_t \mathbf{Q} + \mathbf{A}(\mathbf{Q}) \partial_x \mathbf{Q} = \mathbf{S}(\mathbf{Q}), \quad (3.2.3)$$

with $\mathbf{A}(\mathbf{Q}) = \partial f / \partial \mathbf{Q} + \mathbf{B}(\mathbf{Q})$. Here, \mathbf{Q} is the vector of the state variables, $f(\mathbf{Q})$ represents the vector of the analytical fluxes related to the conservative part of the system, while $\mathbf{B}(\mathbf{Q})$ identifies the non-conservative matrix of the problem, and $\mathbf{S}(\mathbf{Q})$ is the vector of the source terms. In matrix formulation, these components are

$$\mathbf{Q} = \begin{pmatrix} A \\ Au \\ p \\ A_0 \\ E_0 \\ p_{ext} \end{pmatrix}, \quad \mathbf{A}(\mathbf{Q}) = \begin{pmatrix} 0 & 1 & 0 & 0 & 0 & 0 \\ -u^2 & 2u & \frac{A}{\rho} & 0 & 0 & 0 \\ 0 & d & 0 & 0 & 0 & 0 \\ 0 & 0 & 0 & 0 & 0 & 0 \\ 0 & 0 & 0 & 0 & 0 & 0 \\ 0 & 0 & 0 & 0 & 0 & 0 \end{pmatrix}, \quad \mathbf{S}(\mathbf{Q}) = \begin{pmatrix} 0 \\ \frac{f}{\rho} \\ S \\ 0 \\ 0 \\ 0 \end{pmatrix},$$

with

$$\frac{\partial f}{\partial \mathbf{Q}} = \begin{pmatrix} 0 & 1 & 0 & 0 & 0 & 0 \\ -u^2 & 2u & 0 & 0 & 0 & 0 \\ 0 & 0 & 0 & 0 & 0 & 0 \\ 0 & 0 & 0 & 0 & 0 & 0 \\ 0 & 0 & 0 & 0 & 0 & 0 \\ 0 & 0 & 0 & 0 & 0 & 0 \end{pmatrix}, \quad \mathbf{B}(\mathbf{Q}) = \begin{pmatrix} 0 & 1 & 0 & 0 & 0 & 0 \\ 0 & 0 & \frac{A}{\rho} & 0 & 0 & 0 \\ 0 & d & 0 & 0 & 0 & 0 \\ 0 & 0 & 0 & 0 & 0 & 0 \\ 0 & 0 & 0 & 0 & 0 & 0 \\ 0 & 0 & 0 & 0 & 0 & 0 \end{pmatrix},$$

being $f(\mathbf{Q}) = (Au, Au^2, 0, 0, 0, 0)^\top$.

The friction model and the tube law are thoroughly explained in the following of this Section, besides other worth-highlighting features of the a-FSI model. Further details on the eigenvalues and eigenvectors characterising the system are also presented.

3.2.1 Friction loss model

In Eq. (3.2.1b) f represents the friction loss term, and, as introduced in Section 3.1.2, it depends on the velocity profile. This is assumed self-similar and axisymmetric, even in sections with large curvatures (e.g., in the aortic arch), and its typical formulation used for blood flow satisfying the no-slip condition is (Alastruey, Parker, and Sherwin, 2012):

$$v(x, r, t) = u \frac{\zeta + 2}{\zeta} \left[1 - \left(\frac{r}{R} \right)^\zeta \right], \quad (3.2.4)$$

where r is the radial coordinate, R is the vessel radius, $R = \sqrt{A}/\sqrt{\pi}$, and $\zeta = (2 - \alpha_c)/(\alpha_c - 1)$ is the polynomial order depending on α_c , the Coriolis coefficient, which accounts for the non-linearity of the sectional integration of the velocity. For blood flow in arteries, it has been demonstrated that the velocity profile is on average close to flat in central arteries and not parabolic (Quarteroni and Formaggia, 2004b), thus $\alpha_c = 1.1$ ($\zeta = 9$) provides the best compromise to fit experimental data (Xiao, Alastruey, and Figueroa, 2014). Contrarily, a parabolic velocity profile is more suitable for non-central arteries. For the velocity profile as in Eq. (3.2.4), the friction loss term is defined as follows (Bertaglia et al., 2020; Quarteroni, Veneziani, and Vergara, 2016; Xiao, Alastruey, and Figueroa, 2014):

$$f = -2(\zeta + 2)\mu\pi u, \quad (3.2.5)$$

where μ is dynamic blood viscosity.

3.2.2 Tube law

The left-hand side of Eq. (3.2.1c) has the same formulation with both the elastic and viscoelastic characterizations of the wall (Bertaglia et al., 2021; Bertaglia, Caleffi, and Valiani, 2020; Bertaglia et al., 2020). This contribution is derived from the simplest case of a pressure-area relationship describing a perfectly elastic behaviour of the vessel wall. Introduced in its general form in Section 3.1.2, the elastic constitutive tube law reads (Formaggia, Lamponi, and Quarteroni, 2003; Matthys et al., 2007; Müller and Toro, 2013; Bertaglia, 2019)

$$p = p_{ext} + \psi_{el} = p_{ext} + K(\alpha^m - \alpha^n). \quad (3.2.6)$$

The elastic contribution of the transmural pressure, ψ_{el} , depends on the dimensionless cross-sectional area, $\alpha = A(x)/A_0(x)$, the stiffness coefficient of the material, $K(x)$, and two specific parameters related to the behaviour of the vessel wall (i.e., artery or vein), m and n . The stiffness coefficient, $K(x)$, and the parameters m and n characterising the mechanical properties of an arterial wall are

$$K = \frac{E_0}{W}, \quad m = 1/2, \quad n = 0, \quad (3.2.7)$$

whereas, in the case of a venous wall (Shapiro, 1977), they are

$$K = \frac{E_0}{12W^3}, \quad m = 10, \quad n = -3/2, \quad (3.2.8)$$

where $E_0(x)$ is the instantaneous Young modulus and

$$W = \frac{h_0}{R_0}, \quad (3.2.9)$$

where R_0 is the radius corresponding to the equilibrium area A_0 , $R_0 = \sqrt{A_0}/\sqrt{\pi}$, and h_0 is the wall thickness. The values of $K(x)$, m , and n of veins are defined differently from those of arteries because when it concerns veins, their possible collapse in the event of negative transmural pressure must be considered (Carpenter and Pedley, 2001; Toro and Siviglia, 2013; Murillo, Navas-Montilla, and García-Navarro, 2019). Collapsed veins typically show a buckled, dumbbell shape configuration with the opposite sites of interior walls touching each other, but yet with some blood flowing in the two extremes (Spiller et al., 2017; Carpenter and Pedley, 2001).

The elastic tube law in the PDE form is then obtained deriving Eq. (3.2.6) with respect to time t , as proposed by Leibinger et al. (2016) and Bertaglia (2019),

$$\frac{\partial p}{\partial t} = \frac{K}{A} (m\alpha^m - n\alpha^n) \frac{\partial A}{\partial t}, \quad (3.2.10)$$

and substituting the continuity equation (3.2.1a) in Eq. (3.2.10),

$$\frac{\partial p}{\partial t} + \frac{K}{A} (m\alpha^m - n\alpha^n) \frac{\partial(Au)}{\partial t} = 0. \quad (3.2.11)$$

Thus, the parameter $d(x, t)$ in Eq. (3.2.1c) is defined as

$$d = \frac{K}{A} (m\alpha^m - n\alpha^n). \quad (3.2.12)$$

Hence, d accounts for the elastic contribution of the vessel wall and is written equally in the elastic and viscoelastic formulation of the tube law.

Since the constitutive tube law in the a-FSI system (3.2.1) accounts for the viscous contribution of the vessel wall behaviour, the source term $S(x, t)$ is found on the right-hand side of Eq. (3.2.1c). This term includes all viscoelastic parameters. In order to define the source term $S(x, t)$, the Barlow's formula (Avallone and Baumeister III, 1916) must be resorted,

$$\sigma = W(p - p_{ext}), \quad (3.2.13)$$

together with the equation $\epsilon = \alpha^m - \alpha^n$ (Bertaglia, 2019). This latter, can be also rewritten using Eq. (3.2.6) as

$$\epsilon = \frac{\psi_{el}}{K}, \quad (3.2.14)$$

where $K(x)$ as defined in equations (3.2.7) and (3.2.8). Deriving with respect to time t equations (3.2.13) and (3.2.14), we obtain

$$\frac{d\sigma}{dt} = W \frac{dp}{dt}, \quad (3.2.15)$$

and

$$\frac{d\epsilon}{dt} = \frac{1}{A} (m\alpha^m - n\alpha^n) \frac{dA}{dt}, \quad (3.2.16)$$

respectively. Finally, substituting equations (3.2.15) and (3.2.16) into the constitutive equation of the SLSM, as presented in Eq. (3.1.6), and using the continuity equation (3.2.1a), the viscoelastic tube law as written in Eq. (3.2.1c) is obtained. Hence, the source term $S(x, t)$ is defined as

$$S = \frac{1}{\tau_r} \left[\frac{E_\infty}{E_0} K(\alpha^m - \alpha^n) - (p - p_{ext}) \right]. \quad (3.2.17)$$

Eq. (3.2.17), and thus Eq. (3.2.1c), directly derive from the constitutive law of the chosen SLSM, which is indeed characterized by three main parameters: the instantaneous Young modulus $E_0(x)$, the asymptotic Young modulus $E_\infty(x)$ and the relaxation time $\tau_r(x)$. The interplay between these three parameters is defined through the following equation (Bertaglia, Caleffi, and Valiani, 2020; Bertaglia et al., 2020):

$$\tau_r = \eta \frac{E_0 - E_\infty}{E_0^2}, \quad (3.2.18)$$

where $\eta(x)$ is the viscosity coefficient of the SLSM.

Source term stiffness

It is worth highlighting that, under physiological conditions, the source term of Eq. (3.2.17) in System (3.2.1) may become *stiff* depending on the spatial discretisation applied, Δx (details on the spacial discretisation are given in Chapter 4, which concerns the adopted numerical scheme). A source term is considered stiff when (Müller, Montecinos, and Toro, 2013):

$$\Delta x \frac{\max\{|\beta_i|\}}{\max\{|\lambda_i|\}} > 1, \quad i = 1, \dots, N, \quad (3.2.19)$$

where β_i is the i -th eigenvalue of the Jacobian of $S(\mathbf{Q})$, λ_i is the i -th eigenvalue of $A(\mathbf{Q})$, and N is the number of unknowns of the system (in this work $N = 6$). It can be evaluated that $\max\{|\beta_i|\} = 1/\tau_r$, which can reach values up to 5 order of magnitude more than the maximum eigenvalue λ_i . Therefore, the relaxation time parameter τ_r , related to viscoelasticity, plays a key role in determining the stiffness of the problem.

Asymptotic limits

The two Young moduli in Eq. (3.2.17), E_0 and E_∞ , are associated to the initial and final phases of the material's deformation, respectively. In a simple relaxation experiment, the law defining how the apparent Young modulus $E(t)$ of the material gradually changes in time, from the instantaneous value to the asymptotic one, is the so-called relaxation function (Lakes, 2009), which is explicated with Eq. (3.1.9). By definition, when dealing with a simple elastic behaviour, the Young modulus is constant in time (Lakes, 2009): $E(t) = E_\infty = E_0$. In fact, analysing the asymptotic limit of Eq. (3.1.9), if $\tau_r \rightarrow 0 \Rightarrow E(t) \rightarrow E_\infty$, thus leading to an elastic mechanism. Noteworthy, through Eq. (3.2.19) it is observable that in this limit System (3.2.1) becomes stiff. On the other hand, also an excessively long relaxation time, $\tau_r \rightarrow \infty$, does

not allow the development of viscoelastic features, resulting $E(t) \rightarrow E_0$. In both cases, the source term of Eq. (3.2.1c), defined in Eq. (3.2.17), tends to zero, $S \rightarrow 0$, which confirms that the formulation of S is coherent with the assumed mechanical behaviour and consistent with the equilibrium limit (Bertaglia et al., 2021; Bertaglia, Caleffi, and Valiani, 2020; Bertaglia et al., 2020). From this analysis, we can deduce that the more $E_\infty \rightarrow E_0$, the more the behaviour of the material becomes purely elastic. Therefore, in the SLSM the ratio $z = E_\infty/E_0$ can be seen as an index of the viscoelasticity of the material. In the a-FSI model here discussed, this ratio is computed by an empirical formula presented in Bertaglia et al. (2020), which is the result of a calibration process carried out considering various hysteresis loops taken from literature (Giannattasio et al., 2008; Salvi, 2012):

$$\frac{E_\infty}{E_0} = e^{-1.3 \cdot 10^{-5} \eta}. \quad (3.2.20)$$

3.2.3 Eigenstructure and Riemann Invariants

It can be demonstrated that System (3.2.1) is hyperbolic (Bertaglia, Caleffi, and Valiani, 2020) and, in contrast with other approaches proposed in literature (e.g., Alastruey et al. (2011) and Montecinos, Müller, and Toro (2014)), this mathematical model preserves its hyperbolicity even when considering the viscoelastic contribution of vessel walls without the need for any mathematical reformulation. Therefore, the a-FSI system is called *natively* hyperbolic. Nevertheless, we highlight here that System (3.2.1) is not *strictly* hyperbolic.

This section presents the nature of the characteristic fields of the a-FSI system, as well as the quantities that are kept constant across these fields, namely the Riemann Invariants (RIs) (Toro, 2009), considering only sub-critical flow cases. Because of hyperbolicity, the matrix $A(Q)$ is diagonalizable with a diagonal matrix containing all real eigenvalues λ_i , with $i = 1, \dots, N$, ($N = 6$, number of unknowns of the problem)

$$\lambda_1 = u - c, \quad \lambda_2 = \lambda_3 = \lambda_4 = \lambda_5 = 0, \quad \lambda_6 = u + c,$$

and a complete set of corresponding linearly independent (right) eigenvectors (Bertaglia, Caleffi, and Valiani, 2020)

$$\begin{aligned} \mathbf{R}_1 &= \gamma_1 \begin{pmatrix} 1 \\ u - c \\ d \\ 0 \\ 0 \\ 0 \end{pmatrix}, & \mathbf{R}_2 &= \gamma_2 \begin{pmatrix} 1 \\ 0 \\ \frac{\rho u^2}{A} \\ 0 \\ 0 \\ 0 \end{pmatrix}, & \mathbf{R}_3 &= \gamma_3 \begin{pmatrix} 0 \\ 0 \\ 0 \\ 1 \\ 0 \\ 0 \end{pmatrix}, \\ \mathbf{R}_4 &= \gamma_4 \begin{pmatrix} 0 \\ 0 \\ 0 \\ 0 \\ 1 \\ 0 \end{pmatrix}, & \mathbf{R}_5 &= \gamma_5 \begin{pmatrix} 0 \\ 0 \\ 0 \\ 0 \\ 0 \\ 1 \end{pmatrix}, & \mathbf{R}_6 &= \gamma_6 \begin{pmatrix} 1 \\ u + c \\ d \\ 0 \\ 0 \\ 0 \end{pmatrix}, \end{aligned}$$

where γ_i are arbitrary scaling factors. In this system, the wave speed $c(x, t)$ results (Bertaglia, Caleffi, and Valiani, 2020; Bertaglia et al., 2020)

$$c = \sqrt{\frac{A}{\rho} \frac{\partial p}{\partial A}} = \sqrt{\frac{A d}{\rho}} = \sqrt{\frac{K}{\rho} (m\alpha^m - n\alpha^n)}, \quad (3.2.21)$$

with the wall stiffness coefficient $K(x)$, and the parameters m , and n defining the mechanical properties of the vessel wall as introduced in Section 3.2.2.

It is recalled to the reader that to determine the λ_i -characteristic field of the hyperbolic system it is sufficient to evaluate the quantity $\nabla \lambda_i \cdot \mathbf{R}_i$, with $i = 1, \dots, N$ and see whether it is equal or different from zero (Toro and Siviglia, 2013). In the former case, the characteristic field is LD and associated to contact discontinuity waves, whereas, in the latter case, the field is genuinely non-linear, hence related to elementary waves, i.e., rarefactions and shock waves (as introduced in Section 3.1.2). The λ_i -characteristic fields with $i = 2, 3, 4, 5$ are LD, whereas the remaining two fields, on waves λ_1 and λ_6 , are genuinely non-linear outside the locus

$$\mathcal{G} \left(m, n, \frac{A}{A_0} \right) = m(m+2)\alpha^m - n(n+2)\alpha^n, \quad (3.2.22)$$

in the m - n - α space. The proof is omitted since it results equivalent to the one presented in Toro and Siviglia (2013). Indeed, the presence of Eq. (3.2.1c) in the a-FSI system here treated does not give rise to additional contributions in the product $\nabla \lambda_i \cdot \mathbf{R}_i$, with $i = 1, 6$, being λ_1 and λ_6 independent from the third component of state variable \mathbf{Q} , $q_3 = p$. Thus, for the standard cases in which $m > 0$ and $n \in [-2, 0]$ (Toro and Siviglia, 2013; Shapiro, 1977; Müller and Toro, 2014b) the λ_1 and λ_6 characteristic fields are confirmed to be genuinely non-linear.

To evaluate the Riemann Invariants associated to each characteristic field, the following $(N - 1)$ ordinary differential equations, with $k = 1, \dots, N$ in this work, need to be computed (Toro, 2009):

$$\frac{dq_1}{r_1^{(i)}} = \dots = \frac{dq_k}{r_k^{(i)}} = \dots = \frac{dq_N}{r_N^{(i)}}. \quad (3.2.23)$$

These equalities relate the rate of change dq_k of the k -th component q_k of state variable \mathbf{Q} to the respective component $r_k^{(i)}$ of the right eigenvector \mathbf{R}_i corresponding to the λ_i -wave family. Considering only the first three equations of the governing hyperbolic system, for the first LD field, namely for λ_2 , it can be written:

$$\frac{dA}{1} = \frac{d(Au)}{0} = \frac{dp}{\frac{\rho u^2}{A}} \quad (3.2.24)$$

resulting in

$$\Gamma_1^{LD} = Au, \quad \Gamma_2^{LD} = p + \frac{1}{2}\rho u^2. \quad (3.2.25)$$

In this way, it is verified that quantities Γ_1^{LD} and Γ_2^{LD} are constant across contact discontinuity waves. The LD fields associated to eigenvalues λ_3 , λ_4 and λ_5 assure jumps of quantities A_0 , E_0 and p_{ext} , consistently with the characterization of the a-FSI system. Concerning the genuinely non-linear fields, for the first eigenvalues, λ_1 ,

the following relationship holds:

$$\frac{dA}{1} = \frac{d(Au)}{u - c} = \frac{dp}{d}, \quad (3.2.26)$$

which, recalling Eq. (3.2.21), returns

$$\Gamma_1^{(1)} = u + \int \frac{c(A)}{A} dA, \quad \Gamma_2^{(1)} = p - \int d(A) dA. \quad (3.2.27)$$

Finally, for the last eigenvalue, λ_6 , the following relationship holds:

$$\frac{dA}{1} = \frac{d(Au)}{u + c} = \frac{dp}{d}, \quad (3.2.28)$$

which gives

$$\Gamma_1^{(6)} = u - \int \frac{c(A)}{A} dA, \quad \Gamma_2^{(6)} = p - \int d(A) dA. \quad (3.2.29)$$

Since the second Riemann Invariant results the same in the two genuinely non-linear fields, it is considered just once and labeled as Γ_3 in the following, whereas the first Riemann Invariants associated to λ_1 and λ_6 are labeled as Γ_1 and Γ_2 , respectively.

It is worth noticing that the integral in Γ_3 can be analytically computed, resulting in

$$\Gamma_3 = p - K(\alpha^m - \alpha^n). \quad (3.2.30)$$

The same holds true for Γ_1 and Γ_2 , but only when dealing with arteries, namely

$$\Gamma_1 = u + 4c, \quad \Gamma_2 = u - 4c. \quad (3.2.31)$$

When available, the analytical expressions of the three RIs associated with the genuinely non-linear fields are employed in the model, within their range of applicability, to reduce the computational cost. Through the use of Γ_1 , Γ_2 and Γ_3 it is possible to implement inlet and outlet BCs. At the inlet, i.e., the aortic root, a flow rate/velocity can be either prescribed or simulated using a cardiac contraction model, whereas at the outlet, namely at all terminal vessels of the network, the pressure is typically prescribed. The numerical coupling at the inlet and outlet sections is presented in Section 4.2.2 of this Thesis. Moreover, the RIs here-presented are used for the numerical implementation of junctions for both elastic and viscoelastic cases, as further discussed in Section 4.2.2.

3.3 0-D boundary conditions

3.3.1 Cardiac contraction model

The cardiac contraction model includes the left atrium (LA), the left ventricle (LV), and the adjacent valves, i.e., mitral valve (MV) and aortic valve (AV). The pulmonary venous flow rate (PVFR) entering the LA is prescribed as a function of time. The cardiac contraction, represented in Figure 3.6, model is employed as inlet BC for the vascular model, as described in Sect. 4.2.2.

Cardiac chambers

The LA and LV are modelled through the time-varying elastance function $\mathcal{E}(t)$. The elastance is the reciprocal of the heart chamber compliance (Sun et al., 1995;

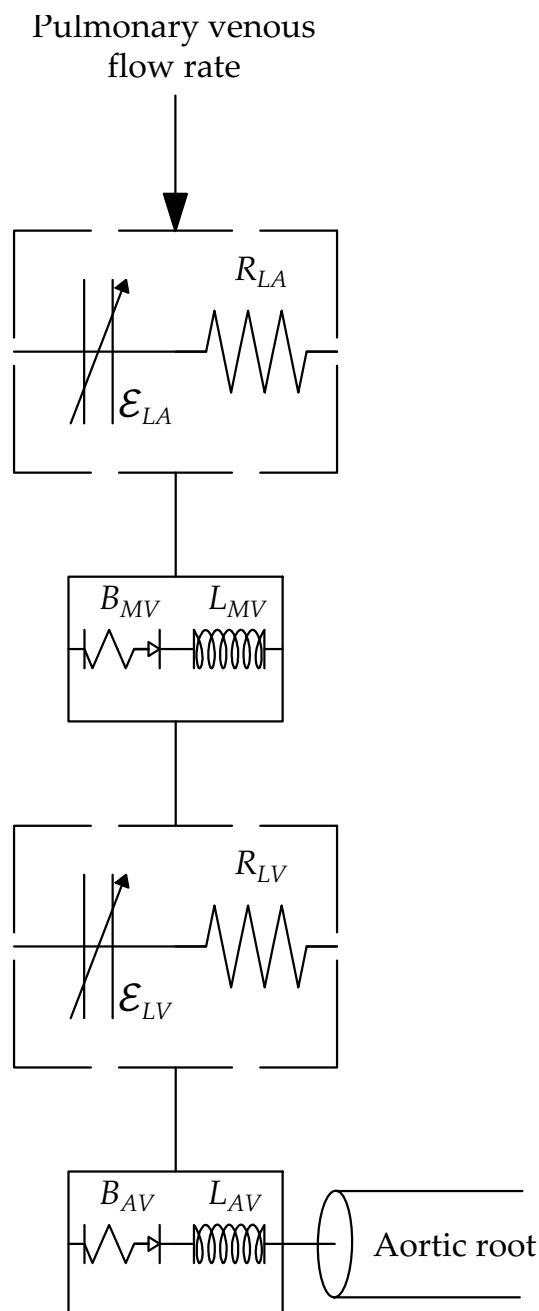


FIGURE 3.6: Schematic representation of the lumped-parameter (0-D) model representing the left heart. The cardiac contraction model operates as inlet boundary condition for the vascular network, with coupling site at the aortic root. \mathcal{E}_c and R_c are the elastance function and resistive term, respectively, for the left atrium, $c = LA$, or left ventricle, $c = LV$. B_v and L_v are the Bernoulli coefficient and blood inertance of the valve, respectively, for the mitral valve, $v = MV$, or the aortic valve, $v = AV$.

Mynard, 2011), and is a measure of the the heart chamber stiffness as it relates the pressure in the cavity $p(t)$ with the cavity volume $v(t)$ by

$$p(t) = \mathcal{E}(t) [v(t) - v_{p0}], \quad (3.3.1)$$

where v_{p0} is the unstressed volume of the heart chamber. Mimicking the myocardium contraction, the elastance changes between its extrema. For a given cardiac state, the time-varying elastance curve is assumed to remain unchanged and independent of alterations on the load (Suga, Sagawa, and Shoukas, 1973). However, according to previous findings (Shroff, Janicki, and Weber, 1983; Shroff, Janicki, and Weber, 1985; Campbell et al., 1982; Little and Freeman, 1987; Latson et al., 1986), the heart chamber pressure is not only related to volume via the elastance function, but also to the heart chamber outflow, q_{out} , through a source resistance term, R_s . Hence, Eq. (3.3.1) is rewritten to account for this flow rate dependence as

$$p(t) = \mathcal{E}(t) [v(t) - v_{p0}] - R_s q_{out}(t). \quad (3.3.2)$$

Performing a basic dimensional analysis, Eq. (3.3.2) is consistent as \mathcal{E} is expressed as a pressure-to-volume ratio, and R_s , being a resistive term, is expressed as a pressure-to-flow rate ratio. The proportionality relation between pressure p and flow rate q_{out} through the resistive term is consistent with the electric-hydraulic analogy frequently used in the lumped-parameters models (Formaggia, Quarteroni, and Veneziani, 2009), and introduced in Section 2.2.2.

The resistive term, R_s , is not constant but it is proportional to the pressure that would be achieved if there was no outflow (Shroff, Janicki, and Weber, 1985), namely

$$R_s = K_s \mathcal{E}(t) [v(t) - v_{p0}] = K_s p_{isov}, \quad (3.3.3)$$

where p_{isov} is the isovolumic pressure, and K_s is a constant. Substituting Eq. (3.3.3) in Eq. (3.3.2), the final equation describing how the cavity pressure varies over time is obtained straightforwardly (Mynard, 2011):

$$p(t) = \mathcal{E}(t) [v(t) - v_{p0}] [1 - K_s q_{out}(t)]. \quad (3.3.4)$$

It can be easily proven that Eq. (3.3.4) is dimensionally consistent.

The elastance $\mathcal{E}(t)$ is defined by the ‘double-Hill’ function (Mynard, 2011; Stergiopoulos, Meister, and Westerhof, 1996; Segers et al., 2000; Maksuti et al., 2016)

$$\mathcal{E}(t) = \left[\frac{E_{max} - E_{min}}{\max(H_1(t)H_2(t))} \right] H_1(t)H_2(t) + E_{min}, \quad (3.3.5)$$

where E_{min} and E_{max} are the minimal and maximal values of the elastance, respectively. E_{min} governs diastolic passive stiffness, hence the filling phase of the chamber (Stergiopoulos, Meister, and Westerhof, 1996), whereas E_{max} is considered to be a measure of systolic contractility (Segers, Stergiopoulos, and Westerhof, 2000; Mynard et al., 2011; Simakov, 2019). Functions $H_1(t)$ and $H_2(t)$,

$$H_1(t) = \frac{(\bar{t}/\tau_1)^{m_1}}{1 + (\bar{t}/\tau_1)^{m_1}} \quad \text{and} \quad H_2(t) = \frac{1}{1 + (\bar{t}/\tau_2)^{m_2}}, \quad (3.3.6)$$

govern the ascending (contraction) and descending (relaxation) tracts of the $\mathcal{E}(t)$ curve, respectively, and they are described by shape m_i and time τ_i parameters, with $i = 1, 2$. In Eq. (3.3.6), \bar{t} is equal to $t - t_{onset}$, with t_{onset} the onset of contraction. The

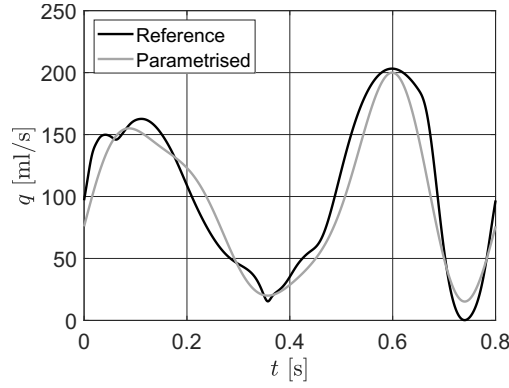


FIGURE 3.7: Pulmonary venous flow rate entering the left atrium in one cardiac cycle: reference (black solid line) and parametrised (gray solid line) via a Fourier function.

cavity volume $v(t)$ is calculated using the continuity equation

$$\frac{dv}{dt} = q_{in}(t) - q_{out}(t), \quad (3.3.7)$$

where $q_{in}(t)$ and $q_{out}(t)$ are the flow rates entering and leaving the heart chamber.

Cardiac valves

Valve dynamics, described by the trans-valvular blood flow rate, $q(t)$, and the opening state of the valve, $\zeta(t)$, ranging from 0 to 1, depend on the pressure difference across the valve, $\Delta p(t)$. Valve dynamics over time is expressed via a system of ODEs (Mynard, 2011),

$$\frac{dq}{dt} = \frac{1}{L(t)} [\Delta p(t) - B(t)q(t) |q(t)|], \quad (3.3.8a)$$

$$\frac{d\zeta}{dt} = \mathcal{F}(\zeta, K_{vo}, K_{vc}, \Delta p) = \begin{cases} [1 - \zeta(t)] K_{vo} \Delta p(t) & \text{if } \Delta p(t) > 0, \\ \zeta(t) K_{vc} \Delta p(t) & \text{if } \Delta p(t) < 0, \end{cases} \quad (3.3.8b)$$

where the coefficients $B(t)$ and $L(t)$ are Bernoulli resistance and blood inertance, respectively. They are expressed as

$$B(t) = \frac{\rho}{2A_v(t)^2} \quad \text{and} \quad L(t) = \frac{\rho l}{A_v(t)}, \quad (3.3.9)$$

where $A_v(t)$ is the orifice area, and l is the valve length (Mynard, 2011). The orifice area ranges from A_{min} to A_{max} potentially accounting for a leaky or stenotic valve,

$$A_v(t) = [A_{max} - A_{min}] \zeta(t) + A_{min}. \quad (3.3.10)$$

The rate of opening or closure of the valve, $d\zeta/dt$, depends on the pressure difference, such that when $\Delta p(t)$ is positive the valve opens and the coefficient K_{vo} is employed; otherwise, the valve closes and K_{vc} is used. High values of these coefficients indicate a rapid opening and closing of the valve, respectively.

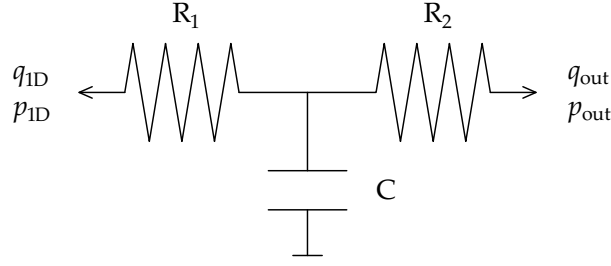


FIGURE 3.8: Schematic representation of the lumped-parameter (0-D), RCR Windkessel model operating as outlet boundary condition at terminal vessels to simulate the microvasculature.

Pulmonary venous flow rate

The input to the cardiac contraction model, represented by the pulmonary venous flow rate, is prescribed as a discretised function of time. The PVFR entering the LA accounts for the flow contributions of all the pulmonary veins. It has a double-peaked shape, with two local maxima, i.e., the systolic (S) and diastolic (D) peaks, and two local minima (Mynard, 2011; Mynard and Smolich, 2015; Sun et al., 1995), as shown in Figure 3.7. In this work, PVFR is parametrised using a Fourier function (Westerhof et al., 1972; Parker, 2009) to simulate a decreased venous return and allow the PVFR to be age-dependent as, conforming to Sun et al. (1995), the S/D ratio increases with age. The PVFR parametrisation is accomplished by assigning six parameters, i.e., the cardiac cycle duration, T , the total volume entering the left atrium in one cardiac cycle, V_{net} , and the four function extrema, and considering the first five Fourier modes:

$$c_n = \cos(n\tau), \quad s_n = \sin(n\tau), \quad \text{with } n = 0, \dots, 4 \quad (3.3.11)$$

where $\tau = \pi(-1 + 2t/T)$ and t is the time variable.

3.3.2 Microvasculature

By linearising the continuity equation (3.2.1a) and the momentum equation (3.2.1b) with respect to reference state $(A, Au, p) = (A_0, 0, 0)$ and integrating them along the vessel domain, i.e., the vessel length L , the system

$$Cd_t(\hat{p} - p_{ext}) = q_{in} - q_{out}, \quad (3.3.12a)$$

$$\mathcal{L}d_t\hat{q} + R\hat{q} = p_{in} - p_{out}, \quad (3.3.12b)$$

is obtained, where $q_{in}(t) = q(0, t)$, $q_{out} = q(L, t)$, $p_{in} = p(0, t)$, $p_{out} = p(L, t)$ are flow rates and pressures at the inlet and outlet sections of the domain, $\hat{p}(t) = L^{-1} \int_0^L p dx$, $\hat{q}(t) = L^{-1} \int_0^L q dx$ are mean pressure and flow rate, respectively, over the entire domain. The coefficients

$$R = -\frac{fL}{A_0^2 u}, \quad \mathcal{L} = \frac{\rho L}{A_0}, \quad C = \frac{A_0 L}{\rho c_0^2}, \quad (3.3.13)$$

are the resistance related to blood viscosity, inductance related to blood inertia, and capacitance related to the wall compliance of the vessel, respectively, with c_0 reference wave speed. System (3.3.12), known as \mathcal{L} -circuit, represents the mathematical

description of an electric circuit. As presented in Section 2.2.2, in this hydraulic–electric analogy pressure corresponds to the electric voltage/potential, whereas flow rate corresponds to current (Milišić and Quarteroni, 2004).

At the outlet of peripheral arteries, the 0-D, lumped–parameter model, named either 3–element Windkessel model or RCR model, is habitually used to simulate the effects of both terminal resistance and terminal compliance on the propagation of pulse waves. The RCR model, depicted in Figure 3.8, is built in analogy with an electric circuit composed of a first resistor, with resistance R_1 , connected in series with a second resistor, R_2 , which is in parallel combination with a capacitor of compliance C (Reymond et al., 2009; Alastruey, Parker, and Sherwin, 2012; Willemet and Alastruey, 2014; Xiao, Alastruey, and Figueroa, 2014; Boileau et al., 2015; Bertaglia et al., 2020). In this Thesis, the peripheral inductance is neglected since it has a minor effect on reflected waves under standard conditions (Alastruey et al., 2008; Alastruey, Parker, and Sherwin, 2012). Moreover, to impose outflow conditions, the RCR model has been defined to have time–constant external pressure, hence $d_t p_{ext} = 0$. The resulting system of equation for the 0-D lumped-parameter model reads (Bertaglia et al., 2020):

$$C \frac{dp_C}{dt} = q_{1D} - q_{out}, \quad (3.3.14a)$$

$$R_1 q_{1D} = p(A_{1D}) - p_C, \quad (3.3.14b)$$

$$R_2 q_{out} = p_C - p_{out}, \quad (3.3.14c)$$

where $p(A_{1D})$ and $q_{1D} = A_{1D}u_{1D}$ are the unknown variables at the final boundary of the 1-D domain, p_C is the pressure at the capacitor and p_{out} and q_{out} are the variables at the outlet of the RCR unit.

The role of the first resistance R_1 in the RCR model is to absorb incoming waves and reduce artificial backward wave reflections in large arteries (Alastruey et al., 2008). Therefore, R_1 is defined to match the characteristic impedance Z_c of the terminal 1-D vessel at the equilibrium state:

$$R_1 = Z_c = \frac{\rho c_0}{A_0}. \quad (3.3.15)$$

It is worth noting that Eq. (3.3.15) is indeed Eq. (2.2.12) where PWV is characterised with respect of the mathematical model at hand, hence with Eq. (??) at the equilibrium state.

Chapter 4

Numerical scheme for networks of viscoelastic vessels

4.1 Introduction

In this Thesis, the viscoelasticity of blood vessels is considered recurring to the Standard Linear Solid Model (SLSM), consisting of a spring in series with a Kelvin-Voigt (KV) unit, the latter composed by a spring and a dash-pot in parallel (Bertaglia, Caleffi, and Valiani, 2020; Bertaglia et al., 2018; Gutierrez-Lemini, 2014; Lakes, 2009), as presented in Section 3.1.1. Most of the models dealing with viscous effects of vessels make use only of the KV unit (Alastruey et al., 2011; Ghigo et al., 2017a; Liang, Guan, and Alastruey, 2018; Montecinos, Müller, and Toro, 2014; Mynard and Smolich, 2015; Wang, Fullana, and Lagrée, 2015). The employment of the more complex SLSM allows a better description of the real mechanical behaviour of biological tissues because, in contrast with the KV model, it permits to include the definition of the exponential relaxation of the stress (pressure) over time (Westerhof and Noordergraaf, 1970; Westerhof et al., 2019). This ability of the model is of great importance since stress relaxation is one of the characteristic features of viscoelastic materials, besides creep and hysteresis (Gurtin and Sternberg, 1961; Lakes, 2009).

As introduced in Chapter 3, the viscoelastic SLSM constitutive tube law is added in PDE form to the system of governing equations, composed of the equations of conservation of mass and momentum, giving rise to the so-called a-FSI system (Bertaglia, Caleffi, and Valiani, 2020; Bertaglia et al., 2020). The a-FSI blood flow model, solved through an Asymptotic-Preserving (AP) IMEX Runge-Kutta scheme in time and a Finite Volume (FV) method in space, has already been validated in previous single-vessel studies, demonstrating its capability to correctly simulate flow rate and pressure trends in patient-specific simulations (Bertaglia, Caleffi, and Valiani, 2020; Bertaglia et al., 2020) and also assessing its sensitivity to uncertainties inherent the viscoelastic parameters involved (Bertaglia et al., 2021).

The numerical model presented in this chapter aims at further developing the recently proposed a-FSI blood flow model, investigating the treatment of networks of viscoelastic vessels and thus the numerical modelling of junctions. Different approaches have been discussed in literature to deal with this topic: in Fullana and Zaleski (2009), the junction is conceived as an elastic tank; in Mynard and Smolich (2015), the junction is modelled via a control volume analysis; in Alastruey, Parker, and Sherwin (2012), Reymond et al. (2009), and Sherwin et al. (2003b), the implementation of the model representing the junction relies on the Method of Characteristics (MOC). However, none of these works take into account the viscoelastic contribution within the numerical implementation of the node, neglecting it in favor of a local elastic approach. To the authors' knowledge, only in Müller, Leugering, and Blanco (2016) a numerical implementation of viscoelastic bifurcations is proposed, via the

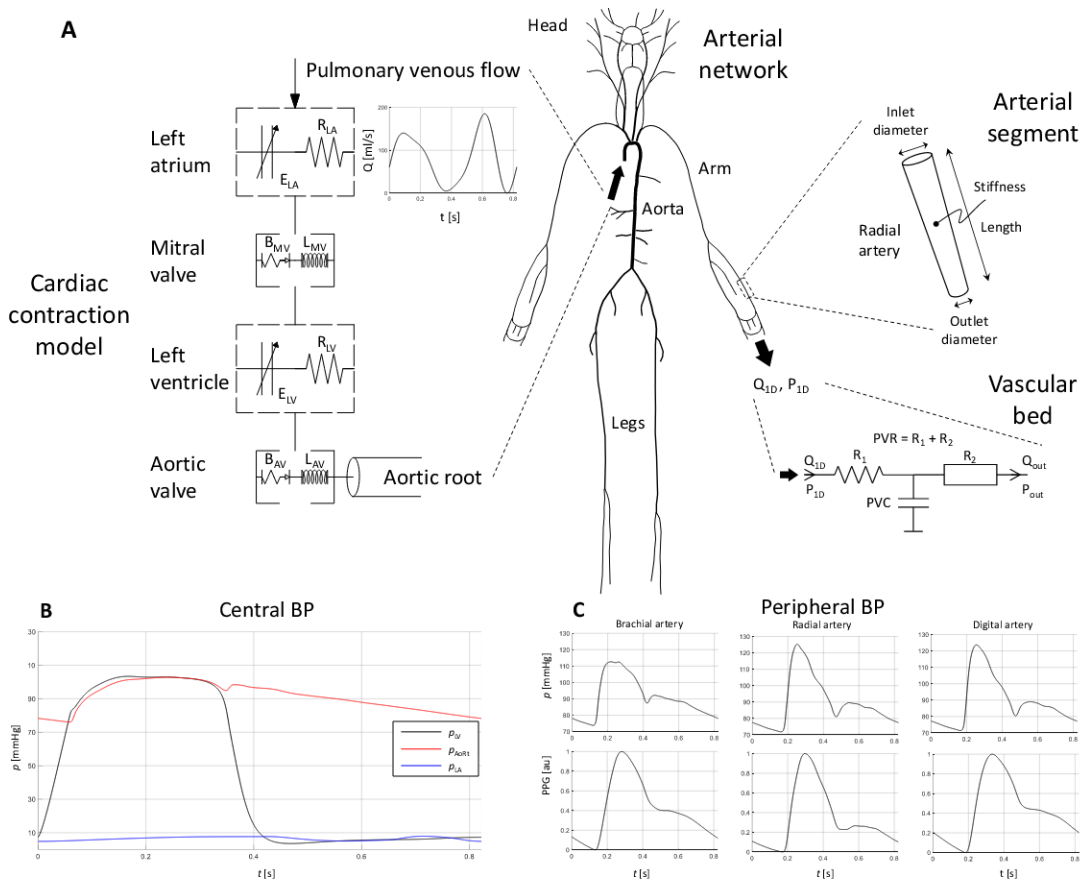


FIGURE 4.1: The schematic representation of the 1-D model vascular network coupled with the 0-D cardiac contraction model (A), central blood pressure waveforms (B), peripheral blood pressure waveforms (C). The cardiovascular network consists of the arterial tree, containing the 116 largest systemic arteries, the left-side heart coupled to the vascular network at the aortic root, and lumped parameter models at 1-D model terminal segments representing the vascular bed. See text for the definition of parameters. It is acknowledged Charlton et al. (2019) for kindly providing the arterial network scheme in part A of this Figure.

solution of a Riemann Problem (RP), but modelling viscoelasticity through the simple KV unit. One of the innovative contribution of this Thesis lays in a detailed treatment of viscoelastic boundary conditions (BCs), accounting for the viscoelastic rheology of vessels through the more appropriate SLSM, presenting an original methodology to be computed at the boundaries of the 1-D physical domain. The proposed methodology, specifically developed for junctions, represents a feasible tool also for inlet and outlet boundaries and naturally derives from the hyperbolic eigenstructure of the a-FSI system.

A schematic representation of the proposed cardiovascular model is shown in Figure 4.1. It includes three key components. First, the 1-D model arterial network consists of 116 arterial segments representing the largest arteries of the thorax, limbs and head (Charlton et al., 2019). Arterial segments are modelled as thin viscoelastic tubes of linearly tapered diameter. Second, the RCR Windkessel model is employed at the terminal vessels as outlet boundary condition (BC), to describe the

resistance and compliance of peripheral vascular beds. Third, a cardiac contraction model representing the left-side heart is coupled to the vascular network as inlet BC. The mathematical background of all these components is exhaustively presented in Chapter 3. This Chapter focuses on the validation of the numerical scheme and the chosen implementation of boundary conditions, in particular of junctions in networks of viscoelastic vessels. Therefore, different test cases have been considered, characterised by increasing complexity and a diverse mechanical behaviour of the vessels. The 0-D cardiac contraction model is not considered for the analyses conducted in this Chapter, but it is considered, and properly validated, for the numerical simulations and analyses presented in Chapter 5.

The rest of this Chapter is structured as follows. In Section 4.2 the numerical model is discussed and the numerical treatment of BCs – at inlet, outlet and junctions – is presented in detail for both the elastic and the viscoelastic cases. The procedure here proposed to implement junctions is valid for both bifurcation and confluence cases. Bifurcations are mostly related to arteries, whereas confluences are mostly related to veins. In Section 4.3 various numerical results are shown and discussed. At first, the trivial 2-vessel junction test is presented for arteries and veins, in both elastic and viscoelastic regimes. In these tests, accuracy analysis of the model is performed as well as well-balancing analysis. Then, a 3-vessel junction problem is analysed concerning a benchmark elastic aortic bifurcation case and performing the same test also with a viscoelastic configuration of the vessels. At last, results concerning the simulation of two benchmark arterial networks are presented, again for both the mechanical characterizations of vessel walls. Both the arterial networks deal with arterial vessels with diameters typical of the human macro-circulation. Blood flow within these vessels is characterized by high Womersley numbers indicating that the respective flow is pulsating (Fung, 1997), strengthening the choice of using the sophisticated a-FSI model to obtain realistic results. The first network replicates an *in vitro* model of arterial tree representing the largest central systemic arteries of the human vascular system, whereas the second one is a reduced version of an anatomically detailed arterial network. Conclusions regarding the numerical model and results presented in this Chapter are drawn in Section 4.4.

4.2 Numerical method

As discussed in Section 3.2.2, the a-FSI system (3.2.1) is a hyperbolic system presenting a *stiff* relaxation term in Eq. (3.2.1c). Indeed, under physiological conditions, the relaxation time can vary from values of order one to very small values if compared to the time scale determined by the characteristic speeds of the system. Therefore, to solve the problem, a robust numerical scheme that works efficiently for all ranges of the relaxation time is needed. This represents a challenging task if one aims at maintaining high order of accuracy and stability of the scheme (Ascher, Ruth, and Spiteri, 1997; Pareschi and Russo, 2001; Pareschi and Russo, 2005). In this Thesis, it was employed an asymptotic-preserving (AP) Implicit-Explicit (IMEX) Runge-Kutta (RK) Finite Volume (FV) approach, which is thoroughly described in the following.

4.2.1 AP-IMEX Runge-Kutta Finite Volume scheme

The stiffly accurate IMEX-SSP2(3,3,2), characterized by 3 stages for both the implicit and explicit parts and second order of accuracy, is adopted for the time discretization of System (3.2.1) (Pareschi and Russo, 2005). This scheme is AP and asymptotic accurate in the zero relaxation limit, meaning that the consistency of the scheme with the equilibrium system is guaranteed and the order of accuracy is preserved in the stiff limit (Bertaglia et al., 2021). As typical for IMEX schemes, an L-stable diagonally implicit Runge–Kutta (DIRK) method is used for the treatment of the stiff part (here represented by the source terms), ensuring elevated robustness; while an explicit strong–stability–preserving (SSP) scheme is provided for all the non–stiff components of the system, to maximize the efficiency (Pareschi and Russo, 2005).

For the space discretization, a second–order FV approach is considered, with a uniform grid of length l_v and $n_{c,v}$ number of cells for each v -th vessel, a mesh spacing $\Delta x_v = l_v/n_{c,v}$, and a global time step size $\Delta t = t^{n+1} - t^n$ satisfying the CFL condition (Toro, 2009):

$$\Delta t \leq \text{CFL} \frac{\min\{\Delta x_v\}}{\max\{\lambda_1, \dots, \lambda_6\}}, \quad v = 1, \dots, n_v, \quad (4.2.1)$$

where $\lambda_1, \dots, \lambda_6$ are the eigenvalues of the system (detailed in Section 3.2.3) and n_v identifies the number of vessels considered. We highlight that a local time stepping (LTS) procedure might also be considered to increment computational efficiency (Müller et al., 2016). For ease of reading, the subscript v is omitted in the following. On the i -th cell, $I_i = [x_{i-\frac{1}{2}}, x_{i+\frac{1}{2}}]$ with $\Delta x = x_{i+\frac{1}{2}} - x_{i-\frac{1}{2}}$, the chosen numerical technique leads to the following final discretization of System (3.2.1):

$$\begin{aligned} \mathbf{Q}_i^{(k)} = \mathbf{Q}_i^n - \frac{\Delta t}{\Delta x} \sum_{j=1}^{k-1} \tilde{a}_{kj} \left[\left(\mathbf{F}_{i+\frac{1}{2}}^{(j)} - \mathbf{F}_{i-\frac{1}{2}}^{(j)} \right) + \left(\mathbf{D}_{i+\frac{1}{2}}^{(j)} + \mathbf{D}_{i-\frac{1}{2}}^{(j)} \right) + \mathbf{B} \left(\mathbf{Q}_i^{(j)} \right) \Delta \mathbf{Q}_i^{(j)} \right] \\ + \Delta t \sum_{j=1}^k a_{kj} \mathbf{S} \left(\mathbf{Q}_i^{(j)} \right), \end{aligned} \quad (4.2.2a)$$

$$\begin{aligned} \mathbf{Q}_i^{n+1} = \mathbf{Q}_i^n - \frac{\Delta t}{\Delta x} \sum_{k=1}^s \tilde{\omega}_k \left[\left(\mathbf{F}_{i+\frac{1}{2}}^{(k)} - \mathbf{F}_{i-\frac{1}{2}}^{(k)} \right) + \left(\mathbf{D}_{i+\frac{1}{2}}^{(k)} + \mathbf{D}_{i-\frac{1}{2}}^{(k)} \right) + \mathbf{B} \left(\mathbf{Q}_i^{(k)} \right) \Delta \mathbf{Q}_i^{(k)} \right] \\ + \Delta t \sum_{k=1}^s \omega_k \mathbf{S} \left(\mathbf{Q}_i^{(k)} \right). \end{aligned} \quad (4.2.2b)$$

Here, \mathbf{Q}_i^n is the vector of the cell–averaged variables at time t^n .

Matrices $\tilde{\mathbf{a}} = (\tilde{a}_{kj})$ and $\mathbf{a} = (a_{kj})$ are $s \times s$ matrices characterizing the explicit and implicit stages, respectively, of the chosen IMEX RK scheme, while the coefficient vectors $\tilde{\boldsymbol{\omega}} = (\tilde{\omega}_1, \dots, \tilde{\omega}_s)$ and $\boldsymbol{\omega} = (\omega_1, \dots, \omega_s)$ represent the explicit and implicit weights, respectively, with s identifying the number of the RK stages (Pareschi and Russo, 2001; Pareschi and Russo, 2005). The resulting scheme is implicit in $\mathbf{S} \left(\mathbf{Q}_i^{(k)} \right)$ and explicit for all the rest. Moreover, being a DIRK scheme, both \tilde{a}_{kj} and a_{kj} are null for $j \geq k$. The set of explicit and implicit matrices and vectors are represented by a double tableau in the usual Butcher notation (Pareschi and Russo, 2005):

$$\begin{array}{c|c} \tilde{c}_k & \tilde{a}_{k,j} \\ \hline & \tilde{\omega}_k^T \end{array} \qquad \begin{array}{c|c} c_k & a_{k,j} \\ \hline & \omega_k^T \end{array}$$

where the coefficients \tilde{c}_k and c_k are given by

$$\tilde{c}_k = \sum_{j=1}^{k-1} \tilde{a}_{kj}, \quad c_k = \sum_{j=1}^k a_{kj}.$$

For the specific IMEX-SSP(3,3,2) Runge–Kutta scheme employed in this Thesis, the general tableaux given in the above are defined as follows,

$$\begin{array}{c|ccc} 0 & 0 & 0 & 0 \\ 1/2 & 1/2 & 0 & 0 \\ 1 & 1/2 & 1/2 & 0 \\ \hline & 1/3 & 1/3 & 1/3 \end{array} \quad \begin{array}{c|ccc} 1/4 & 1/4 & 0 & 0 \\ 1/4 & 0 & 1/4 & 0 \\ 1 & 1/3 & 1/3 & 1/3 \\ \hline & 1/3 & 1/3 & 1/3 \end{array}$$

Indeed, the explicit RK methods are characterised by non-zero entries that lie only strictly below the diagonal of matrix $\tilde{\mathbf{a}}$. Entries at or above the diagonal would cause the right-hand side of Eq. (4.2.2a) to involve $Q_i^{(j)}$, giving a formally implicit method (Bertaglia, 2019).

In equations (4.2.2a) and (4.2.2b), \mathbf{F} is the vector of the numerical fluxes and \mathbf{D} is the vector of the non-conservative jumps, evaluated at each cell boundary through the path-conservative Dumbser–Osher–Toro (DOT) Riemann solver (Dumbser and Toro, 2011a; Dumbser and Toro, 2011b; Leibinger et al., 2016):

$$\mathbf{F}_{i\pm\frac{1}{2}} = \frac{1}{2} \left[f \left(\mathbf{Q}_{i\pm\frac{1}{2}}^+ \right) + f \left(\mathbf{Q}_{i\pm\frac{1}{2}}^- \right) \right] - \frac{1}{2} \int_0^1 \left| \mathbf{A} \left(\Psi \left(\mathbf{Q}_{i\pm\frac{1}{2}}^-, \mathbf{Q}_{i\pm\frac{1}{2}}^+, s \right) \right) \right| \frac{\partial \Psi}{\partial s} ds, \quad (4.2.3)$$

$$\mathbf{D}_{i\pm\frac{1}{2}} = \frac{1}{2} \int_0^1 \mathbf{B} \left(\Psi \left(\mathbf{Q}_{i\pm\frac{1}{2}}^-, \mathbf{Q}_{i\pm\frac{1}{2}}^+, s \right) \right) \frac{\partial \Psi}{\partial s} ds. \quad (4.2.4)$$

To achieve second-order accuracy also in space and to avoid spurious oscillations near discontinuities, boundary extrapolated values $\mathbf{Q}_{i\pm\frac{1}{2}}^\mp$ are computed using a Total-Variation-Diminishing (TVD) method, recurring, at each k -th RK step, to the classical minmod slope limiter (Toro, 2009):

$$\Delta \mathbf{Q}_i^{(k)} = \text{minmod}(\mathbf{Q}_i^{(k)} - \mathbf{Q}_{i-1}^{(k)}, \mathbf{Q}_{i+1}^{(k)} - \mathbf{Q}_i^{(k)}), \quad (4.2.5)$$

hence:

$$\mathbf{Q}_{i\pm\frac{1}{2}}^{(k),\mp} = \mathbf{Q}_i^{(k)} \pm \frac{1}{2} \Delta \mathbf{Q}_i^{(k)}. \quad (4.2.6)$$

Integrals in equations (4.2.3) and (4.2.4) are approximated by a 3-point Gauss–Legendre quadrature formula after that a simple linear path Ψ , connecting left to right boundary values in the phase-space, is chosen (Bertaglia et al., 2018).

It is noted that the numerical method here presented has been demonstrated to be exactly well-balanced (Bertaglia, Caleffi, and Valiani, 2020), hence exactly conserves a rest initial condition (C-property as defined in Bermudez and Vazquez (1994)). Finally, another characteristic worth to be remarked is that, consistently with the form of the source term in Eq. (3.2.1c), the chosen scheme can be reformulated to obtain a totally explicit algorithm. This permits to avoid the adoption of iterative procedures, like Newton–Raphson method, to solve the implicit terms, leading to an additional consistent reduction of the computational cost with respect to standard semi-implicit or fully implicit methods. We underline here that this capability of IMEX schemes, for which the implicit part can be rearranged to compute the involved component of the state variable equation by equation, is valid for many

applications and represents a consistent advantage of these methods. For further details on the totally explicit reformulation, the reader is referred to Bertaglia, Caleffi, and Valiani (2020), Bertaglia et al. (2020), Bertaglia et al. (2021), and Pareschi and Russo (2005).

4.2.2 Boundary conditions

The model presented in this work is characterized by three types of BCs: inlet, outlet, and internal junctions BCs. All types of BCs have been implemented to account for the viscous contribution of the vessel wall. Particularly, in the previous works related to the a-FSI blood flow model (Bertaglia et al., 2021; Bertaglia, Caleffi, and Valiani, 2020; Bertaglia et al., 2020), the pressure at boundary sections was always evaluated neglecting the viscoelastic contribution of the tube law, in favour of a local elastic approach. On the contrary, the here-proposed new approach employs an additional RI, namely Γ_3 , defined in Eq. (3.2.30), to consider the variation of pressure in the 1-D domain induced by the wall viscoelasticity at boundaries. Inlet, outlet, and junction BCs are presented in the following. Finally, the problem of maintaining the high-order of accuracy of the scheme even at boundaries is discussed.

Inlet BC

The a-FSI system allowed to simulate different study tests and arterial network configurations. Depending on the specific simulation at hand, either a prescribed flow rate or a cardiac contraction model is used as inlet BC.

The prescribed flow rate is given as a function of time. In this case, the inflow BC is implemented imposing at each RK step an inlet flow rate q_{in} , recurring to the Γ_2 RI associated with the genuinely non-linear field at the proximal boundary of the physical domain, defined as $\Gamma_1^{(6)}$ in Eq. (3.2.29). To take into account viscoelasticity at the boundary, once the inlet cross-sectional area A_{in} is computed from the inlet prescription, the Γ_3 RI is used in its analytical form, presented in Eq. (3.2.30), for the evaluation of the pressure at the inlet section, p_{in} . The prescribed flow rate as inlet BC is used to perform numerical tests with both arteries and veins. In the case of arterial numerical tests and networks, the RI Γ_2 is employed in its analytical form, defined in Eq. (3.2.31), with a consistent reduction of computational cost (Piccioli et al., 2022a). With arterial network tests, the prescribed flow rate is characterised by the typical waveform of the aortic flow rate and is assigned at the aortic root to simulate the left ventricular ejection into the aorta.

The cardiac contraction model acts as inlet boundary condition to the 1-D model vascular network. The flow rate through the aortic valve, $q_{AV}(t)$, is computed at every time step and prescribed as the inflow to the aortic root. The coupling between the cardiac contraction model and the arterial domain occurs at the aortic root and follows the one presented for the computation of the inlet BC with the prescribed flow rate. Thus, it is accomplished using the RIs Γ_2 and Γ_3 , i.e., Eq. (3.2.31) and (3.2.30), to consider the viscoelastic contribution of the wall of the aorta even at the inlet boundary section, namely the aortic root (Piccioli et al., 2022b). In the cardiac contraction model, the time-dependent variables presented in Sect. 3.3.1 must be computed and updated for every time step. These variables are the valve's flow rate, q_v , and state, ζ_v , and the chambers volume, v_c . Subscript c identifies either the LA or the LV, whereas subscript v identifies either the MV or AV. Equations (3.3.8a) and

(3.3.8b) are integrated in time following the IMEX RK method, treating the equations explicitly since they do not contain *stiff* terms. Thus, the time discretisation of Eq. (3.3.8a) reads

$$q_v^{(k)} = q_v^n + \Delta t \sum_{j=1}^{k-1} \tilde{a}_{kj} \left[\frac{1}{L^{(j)}} \left(\Delta p^{(j)} - B^{(j)} q^{(j)} \left| q^{(j)} \right| \right) \right], \quad (4.2.7a)$$

$$q_v^{n+1} = q_v^n + \Delta t \sum_{k=1}^s \tilde{\omega}_k \left[\frac{1}{L^{(k)}} \left(\Delta p^{(k)} - B^{(k)} q^{(k)} \left| q^{(k)} \right| \right) \right]. \quad (4.2.7b)$$

Here, q_v^n is the flow rate at time t^n , and q_v^{n+1} at $t^{n+1} = t^n + \Delta t$. Matrix $\tilde{\mathbf{a}} = (\tilde{a}_{kj})$ and vector $\tilde{\boldsymbol{\omega}} = (\tilde{\omega}_1, \dots, \tilde{\omega}_s)$ are the coefficients and weights, respectively, characterising the explicit stages of the chosen IMEX RK scheme, as presented in Section 4.2.1. The same time discretisation scheme is applied to the opening state of the valve to obtain the explicit discretisation of Eq. (3.3.8b)

$$\zeta_v^{(k)} = \zeta_v^n + \Delta t \sum_{j=1}^{k-1} \tilde{a}_{kj} \mathcal{F} \left(\zeta_v^{(j)}, K_{vo,v}^{(j)}, K_{vc,v}^{(j)}, \Delta p_v^{(j)} \right), \quad (4.2.8a)$$

$$\zeta_v^{n+1} = \zeta_v^n + \Delta t \sum_{k=1}^s \tilde{\omega}_k \mathcal{F} \left(\zeta_v^{(k)}, K_{vo,v}^{(k)}, K_{vc,v}^{(k)}, \Delta p_v^{(k)} \right). \quad (4.2.8b)$$

For the mitral valve, Δp_{MV} is the pressure difference between the LA and the LV, whereas, for the aortic valve, Δp_{AV} is the pressure difference between the LV and the first section of the aortic root. Heart chamber pressures was calculated using the stress–strain relationship given by Eq. (3.3.4). Finally, applying the IMEX RK method to Eq. (3.3.7), the chamber volume at each RK time step is computed using the inlet and outlet flow rates calculated at the same time step as in Eq. (4.2.7a), and for the final update those calculated by Eq. (4.2.7b), i.e.,

$$v_c^{(k)} = v_c^n + \Delta t \sum_{j=1}^{k-1} \tilde{a}_{kj} \left(q_{v,in}^{(j)} - q_{v,out}^{(j)} \right), \quad (4.2.9a)$$

$$v_c^{n+1} = v_c^n + \Delta t \sum_{k=1}^s \tilde{\omega}_k \left(q_{v,in}^{(k)} - q_{v,out}^{(k)} \right). \quad (4.2.9b)$$

For the LA, $q_{v,in}$ is the pulmonary venous flow rate and $q_{v,out}$ is q_{MV} , whereas for the LV they are q_{MV} and q_{AV} , respectively.

Outlet BC

At outlet sections, namely at the last cell of each terminal vessel of the network, the 3–element Windkessel/RCR model presented in Section 3.3.2 is coupled with the 1-D model through the solution of the problem at the interface. A null outlet pressure $p_{out} = 0$ is assigned in these sections to simulate the blood pressure when the flux reaches the venous system (Boileau et al., 2015; Xiao, Alastruey, and Figueroa, 2014). Following, the variable p_C presented in System (3.3.14) must be computed. This system has two algebraic equations, equations (3.3.14b) and (3.3.14c), and one ODE, Eq. (3.3.14a). Hence, it can be rewritten as a unique ODE problem:

$$\frac{dp_C}{dt} = \frac{1}{C} \left[\frac{1}{R_1} (p(A^*) - p_C) - \frac{1}{R_2} (p_C - p_{out}) \right]. \quad (4.2.10)$$

In this work, this ODE is integrated in time following the IMEX RK method previously discussed in Section 4.2.1, treating the equation explicitly since it does not involve *stiff* terms. Thus, the explicit RK discretization of Eq. (4.2.10) reads

$$p_C^{(k)} = p_C^n + \Delta t \sum_{j=1}^{k-1} \frac{\tilde{a}_{kj}}{C} \left[\frac{1}{R_1} \left(p(A^*)^{(j)} - p_C^{(j)} \right) - \frac{1}{R_2} \left(p_C^{(j)} - p_{out} \right) \right], \quad (4.2.11a)$$

$$p_C^{n+1} = p_C^n + \Delta t \sum_{k=1}^s \frac{\tilde{\omega}_k}{C} \left[\frac{1}{R_1} \left(p(A^*)^{(k)} - p_C^{(k)} \right) - \frac{1}{R_2} \left(p_C^{(k)} - p_{out} \right) \right]. \quad (4.2.11b)$$

Following the same approach used at the inlet interface, in order to couple the 1-D domain with the RCR model, the Γ_1 RI associated with the genuinely non-linear field, defined as $\Gamma_1^{(1)}$ in Eq. (3.2.27), is employed. This yields to a non-linear equation in A^* , solved with Newton's method (see Bertaglia et al. (2020) for more details). Once A^* is obtained, the velocity u^* is computed via Γ_1 and the pressure p^* is computed through the elastic tube law, when the problem is elastic, or using Γ_3 in Eq. (3.2.30) to account also for the viscous contribution of the vessel wall when considering the full viscoelastic problem. Again, when dealing with arteries, the analytical form of the RI Γ_1 in Eq. (3.2.31) is considered.

It is worth to underline that the application of the IMEX RK scheme at the inlet and outlet BCs increases the consistency of the model, maintaining an homogeneous approach among physical domain and boundary sections.

Junction BC

Besides inlet and outlet sections, junctions among two or more blood vessels involve internal boundaries where specific conditions must be imposed to couple the 1-D domains of the branching vessels. The present work proposes a method able to face both the simplest 2-vessel junction, consisting in two linked vessels with either the same or different geometrical and mechanical characteristics, and junctions consisting in more branching vessels (even more than three). In this last case, the model is able to deal with both the bifurcation case, in which a parent vessel separates in two or more daughter vessels (occurring mostly in arterial networks) and the confluence case, in which two or more parent vessels merge in one daughter (generally in venous networks). In Figure 4.2 the scheme of a generic 3-vessel junction is shown.

Generally, 3-D analyses of flow at either bifurcations or confluences show that blood flow becomes very complex at junctions, with the possible development of transient separation and of secondary flows (Quarteroni, Manzoni, and Vergara, 2017; Xiao, Alastruey, and Figueroa, 2014). However, these issues are commonly confined in the proximity of the junction and their effects on pulse wave propagation are neglected due to the *long wavelength approximation* (Alastruey, Parker, and Sherwin, 2012). Moreover, energy losses at junctions are neglected in this work, due to their little contribution (Matthys et al., 2007; Wang, Fullana, and Lagr e, 2015), although some studies account for them (for example considering branching angles (Formaggia, Lamponi, and Quarteroni, 2003; Mynard and Smolich, 2015; Steele et al., 2003; Stettler, Niederer, and Anliker, 1981). The inclusion of coefficients of pressure losses at junctions is beyond the scope of this work and will be considered for future developments.

Junction BC is numerically implemented through the solution of a non-linear system of equations that derives from the RP arising at these internal boundaries, in

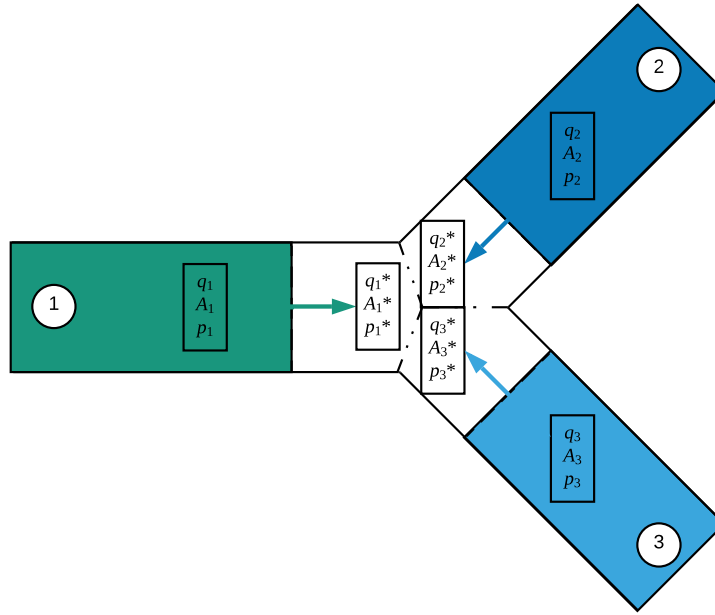


FIGURE 4.2: 3–vessel junction scheme. Reading the figure from left to right, the scheme shows a bifurcation, whereas reading the figure from right to left, it shows a confluence. With respect to the interpretation related to the Junction Riemann Problem, dashed lines represent rarefaction waves, whereas dot–dashed lines represent contact discontinuity waves. The initial conditions of the problem are given by the vector of averaged state variables of the afferent cells of vessel domains, i.e., $q_j = A_j u_j$, A_j and p_j , with $j = 1, 2, 3$, whereas the intermediate constant states are $q_j^* = A_j^* u_j^*$, A_j^* and p_j^* , again with $j = 1, 2, 3$.

the following called Junction Riemann Problem (JRP) (Colombo, Herty, and Sachers, 2008; Colombo and Garavello, 2008).

The solution of elementary one–dimensional RPs involving a set of two balance laws, one for the mass and one for the momentum, is characterized by a single intermediate constant state (the so called *star region*), separated from the initial imposed constant states by non–linear waves, such as shock waves or rarefactions. If the addition of further equations to the set of governing equations results in the enrichment of the eigenstructure of the system with null eigenvalues, as it happens for the augmented System (3.2.1), stationary contact waves become part of the solution. Restricting our analysis to sub–critical flows (i.e., $u < c$) the non–linear waves are directed from the centre towards the periphery and the intermediate states become two, separated from each other by the new contact discontinuity waves (Toro and Siviglia, 2013). The discontinuity between the intermediate states is stationary and remains located at the initial discontinuity of the initial conditions. Now, conceiving the position of the initial discontinuity as a junction section between branches, it becomes clear that the RP partial solution related to each branch consists only of an initial state separated from a single intermediate state by a non–linear wave, while the intermediate states of the two adjacent branches are separated from each other by the contact discontinuities.

The extension of this interpretation to the JRP for a confluence of N branches into a node is straightforward. Again, the initial state of each branch is separated from the *star region* of the same branch by a non–linear wave, while the N intermediate

states of the N branches, which are adjacent to the node, are separated from each other by contact waves. For an application of the same approach to different balance laws, the reader is addressed to Bertaglia and Pareschi (2021), Elshobaki, Valiani, and Caleffi (2018), Elshobaki, Valiani, and Caleffi (2019), Müller and Blanco (2015), and Müller, Leugering, and Blanco (2016).

To properly define a simplified solution of the JRP suitable to act as a junction mathematical model, two assumptions are made *a priori*:

1. The flux is sub-critical, namely the speed index, defined as the ratio between velocity of the fluid and celerity (Shapiro, 1977), is always less than one and therefore the non-linear waves joining 1-D domain states and star region states are directed from the central node towards the periphery (Toro, 2009);
2. Both the resulting non-linear waves are rarefactions, hence the JRP is treated following a Two-Rarefactions Riemann Solver (TRRS) (Toro, 2009).

As an example, referring to Figure 4.2, which clearly illustrates the so-conceived JRP, the initial conditions of the problem are given by the vector of averaged state variables of the afferent cells of vessel domains, i.e., $q_j = A_j u_j$, A_j and p_j , here with $j = 1, 2, 3$, whereas the intermediate constant states are $q_j^* = A_j^* u_j^*$, A_j^* and p_j^* , again with $j = 1, 2, 3$.

Given a general junction connecting N vessels, Q_j^{1D} , $j = 1, \dots, N$, constant states are identified at time t at the junction section, provided by the vectors of averaged state variables at the interface, one for each adjacent cell of the N afferent vessels. If variables are discontinuous across the interface, N new intermediate states originate at the node at time $t + \Delta t$. This set is formed by the starred constant states, Q_j^* , $j = 1, \dots, N$, which identify the $3N$ unknowns of the JRP: q_j^* , A_j^* and p_j^* . Assuming that the non-linear waves are always rarefactions, it is possible to write the non-linear system at junctions recurring to the RIs related to both the genuinely non-linear fields, $\Gamma_{1,2,3}$ defined in equations (3.2.27) and (3.2.29), which identify the variables conserved on rarefaction waves, and the RIs related to the LD fields, $\Gamma_{1,2}^{LD}$ defined in Eq. (3.2.25), which indicate, instead, variables conserved across contact discontinuities. As direct consequence of the inclusion of the RIs of the LD fields in the system, the conservation of mass (Au) and the conservation of total energy ($p + \frac{1}{2}\rho u^2$) at junctions is granted. Thus, the resulting non-linear system arising at each viscoelastic junction, for both arterial and venous systems, reads as follows:

$$\sum_{j=1}^N \Theta_{n_j} A_j^* u_j^* = 0, \quad (4.2.12a)$$

$$\left(p_1^* + \frac{1}{2}\rho u_1^{*2} \right) - \left(p_j^* + \frac{1}{2}\rho u_j^{*2} \right) = 0, \quad j = 2, \dots, N, \quad (4.2.12b)$$

$$u_j^* - u_j^{1D} + \Theta_{n_j} \int_{A_j^{1D}}^{A_j^*} \frac{c(A)}{A} dA = 0, \quad j = 1, \dots, N, \quad (4.2.12c)$$

$$p_j^* - p_j^{1D} - \int_{A_j^{1D}}^{A_j^*} d(A) dA = 0, \quad j = 1, \dots, N, \quad (4.2.12d)$$

where Θ_{n_j} is an auxiliary function such that:

$$\Theta_{n_j} = \begin{cases} +1, & \text{if } \xi_{n_j} = L_j, \\ -1, & \text{if } \xi_{n_j} = 0, \end{cases} \quad (4.2.13)$$

with ξ_{n_j} local coordinate of the j -th vessel, evaluated at node n_j , and L_j vessel length. Noteworthy, that Eq. (4.2.12c) derives from Γ_1 and Γ_2 , whereas Eq. (4.2.12d) derives from Γ_3 . The non-linear system is solvable applying a Newton-Raphson iterative method, using \mathbf{Q}_j^{1D} as initial guess for \mathbf{Q}_j^* (Alastruey et al., 2012).

It is worth stressing that the mechanical behaviour attributed to vessel walls affects the formulation of the junction non-linear system, namely if the vessel is chosen to behave in an elastic or in a viscoelastic way. Indeed, when choosing a simple elastic vessel wall, System (4.2.12) can be simplified as (Alastruey et al., 2012; Müller and Toro, 2014a):

$$\sum_{j=1}^N \Theta_{n_j} A_j^* u_j^* = 0, \quad (4.2.14a)$$

$$\left(p(A_1^*) + \frac{1}{2} \rho u_1^{*2} \right) - \left(p(A_j^*) + \frac{1}{2} \rho u_j^{*2} \right) = 0, \quad j = 2, \dots, N, \quad (4.2.14b)$$

$$u_j^* - u_j^{1D} + \Theta_{n_j} \int_{A_j^{1D}}^{A_j^*} \frac{c(A)}{A} dA = 0, \quad j = 1, \dots, N. \quad (4.2.14c)$$

Hence, in the elastic case the only unknown variables are the area A_j^* and the flow rate $q_j^* = A_j^* u_j^*$, being the pressure $p(A_j^*)$ calculated *a posteriori* via the elastic tube law (Bertaglia, Caleffi, and Valiani, 2020):

$$p = p_{ext} + K \left[\left(\frac{A^*}{A_0} \right)^m - \left(\frac{A^*}{A_0} \right)^n \right]. \quad (4.2.15)$$

High order of accuracy at boundaries

As discussed in Section 4.2.1, the proposed AP-IMEX RK FV scheme is second-order accurate both in time and space. To maintain the second-order of accuracy of the scheme in the whole domain, slope values $\Delta \mathbf{Q}_i$, $i = 1, \dots, n_c$, are computed in every cell of the physical grid, even in those adjacent to either the external or the internal boundary sections of the network, namely inlet/outlet or junction interface, respectively. Following the minmod slope limiter (4.2.5), at each k -th RK step, for each cell i , the slope $\Delta \mathbf{Q}_i^{(k)}$ is computed requiring the vector of averaged variables of both adjacent cells: $\mathbf{Q}_{i-1}^{(k)}$ and $\mathbf{Q}_{i+1}^{(k)}$ (Toro, 2009). However, cells adjacent to the inlet (resp. outlet) present a complication since $\mathbf{Q}_{i-1}^{(k)}$ (resp. $\mathbf{Q}_{i+1}^{(k)}$) is missing. The same applies at junctions, where a daughter (resp. parent) vessel misses $\mathbf{Q}_{i-1}^{(k)}$ (resp. $\mathbf{Q}_{i+1}^{(k)}$). This issue is overcome by computing the vector of variables at boundaries as presented in Section 4.2.2 and assuming that these values are constant within the missing boundary cells, which are conceived as ghost cells. The so-obtained ghost cell vector of averaged variables, $\mathbf{Q}_g^{(k)}$, compensates for the missing one in the slope computation. Hence, for the evaluation of the slope of the first physical cell of the inlet vessel of the network as well as for the first cell of daughter vessels:

$$\Delta \mathbf{Q}_1^{(k)} = \text{minmod}(\mathbf{Q}_1^{(k)} - \mathbf{Q}_g^{(k)}, \mathbf{Q}_2^{(k)} - \mathbf{Q}_1^{(k)});$$

while the formulation of the minmod slope limiter in the last physical cell of each peripheral vessel coupled with the RCR model and in the last cell of parent vessels reads:

$$\Delta \mathbf{Q}_{n_c}^{(k)} = \text{minmod}(\mathbf{Q}_{n_c}^{(k)} - \mathbf{Q}_{n_c-1}^{(k)}, \mathbf{Q}_g^{(k)} - \mathbf{Q}_{n_c}^{(k)}).$$

Once $\Delta Q_i^{(k)}$ is computed, boundary extrapolated values within cell i are obtained through Eq. (4.2.6) and fluxes and non-conservative jumps can be evaluated with equations (4.2.3) and (4.2.4), respectively. We remark that the proposed methodology can be extended to higher-order accuracy in space recurring to different spatial reconstruction, for instance adopting WENO approaches (Cavallini, Caleffi, and Coscia, 2008).

4.3 Numerical results

Following (Müller, Leugering, and Blanco, 2016), the numerical implementation of the junction is first validated via a trivial 2-vessel junction case, which consists in two subsequent compliant vessels linked by a single junction BC, for which the reference solution is given by the simulation of the single continuous vessel not interrupted by the junction. This case is implemented for both vessel types, i.e., artery and vein, prescribing a pulse wave as inlet BC. An accuracy analysis is performed with these two tests to verify the conservation of the second order of accuracy of the scheme in the whole domain, even when junctions are considered. Moreover, *dead-body* simulations, i.e., the steady case with null velocity and uniform pressure, are performed to confirm that no numerical errors, such as spurious velocities, arise during the simulation, therefore respecting the well-balancing of the scheme. Subsequently, a 3-vessel junction test of an ideal human aortic bifurcation is performed. Finally, two examples of human arterial networks are considered, accounting for both elastic and viscoelastic behaviour of the vessels to depict differences deriving from the choice of the mechanical characterization of the vessel wall. When considering the viscoelastic rheological behaviour, BCs at each junction composing the network, as well as at inlet and outlet sections, are implemented as described in Sections 4.2.2, 4.2.2 and 4.2.2.

In all the performed simulations, if not otherwise stated, CFL = 0.9 is imposed. Moreover, for ease of reading, information regarding spatial and temporal discretization is generally given in the caption of figures showing results of the specific tests. Numerical data of viscoelastic simulations of the aortic bifurcation test (Section 4.3.2) and of the two arterial networks (Sections 4.3.3 and 4.3.3) are made publicly available as Supporting Material of Piccioli et al. (2022a) in order to facilitate and encourage further analysis.

TABLE 4.1: Parameters of the 2-vessel junction test, valid for a generic artery (AA) and a generic vein (VV), with l vessel length, R_0 equilibrium internal radius, h_0 wall thickness, p_0 equilibrium internal pressure, E_0 instantaneous Young modulus, E_∞ asymptotic Young modulus, τ_r relaxation time and $\hat{q}, \hat{\sigma}, \hat{t}$ additional parameters of the test used for the inlet condition, defined in Eq. (4.3.1). Note that parameters are equal for both parent and daughter vessels in this trivial test.

Test	l [cm]	R_0 [cm]	h_0 [mm]	p_0 [mmHg]	E_0 [MPa]	E_∞ [MPa]	τ_r [ms]	\hat{q} [cm ³ s ⁻¹]	$\hat{\sigma}$ [s ⁻²]	\hat{t} [s]
AA	20	1.0	0.5	80	2.3	1.6	3.5	100	10000	0.025
VV	20	0.5	0.5	10	3.0	2.6	0.022	10	1000	0.05

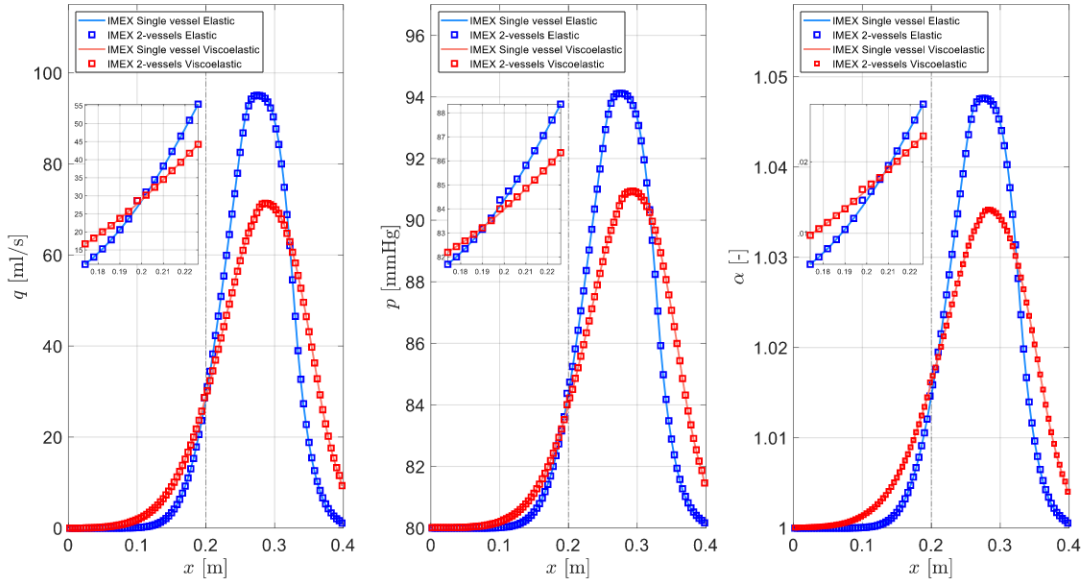


FIGURE 4.3: Results of the 2–vessel junction test performed for a generic artery (AA case). Comparison between the reference solution (single artery) and the numerical solution (2 identical arteries separated by a trivial junction) when considering either an elastic or a viscoelastic wall mechanical behaviour. Results are presented in terms of flow rate (left figure), pressure (central figure) and dimensionless cross-sectional area (right figure) at time $t = 0.068$ s, using $n_c = 50$ cells for each vessel.

4.3.1 2–vessel junction

The 2–vessel junction test has been performed for both blood vessel types, i.e., artery and vein, and for both wall mechanical behaviours, i.e., elastic and viscoelastic. The reference solution is given by the corresponding case of single vessel. To simulate the reference and the numerical solution, each parameter remains the same with the only difference that in the latter a trivial junction is inserted in the middle of the vessel domain. The 2–vessel junction test is purely abstract and specifically aimed at analyzing the numerical approach treating the junction as described in Section 4.2.2. In the following tests, blood density, $\rho = 1050 \text{ kg/m}^3$, and blood viscosity, $\mu = 4 \text{ mPa} \cdot \text{s}$, are assumed as constant for both blood vessel types. Geometrical and mechanical parameters for the arterial case (AA) are taken from Müller, Leugering, and Blanco (2016), whereas parameters for the venous case (VV) are chosen within physiological ranges, as presented in Berne, Koeppen, and Stanton (2010). Regarding the SLSM parameters, the estimation procedure presented in Bertaglia et al. (2020) is followed. The relaxation time τ_r used for the artery is greater than the one used for the vein because the latter is characterized by a more restrained viscoelastic behaviour, which leads to less dissipation of energy, since the venous walls are more deformable, indeed tending to collapse when relatively high external pressures act (Murillo, Navas-Montilla, and García-Navarro, 2019; Spiller et al., 2017). It is worth underlining that few works have been proposed concerning viscoelasticity applied to veins. However, this test is important to highlight the applicability of the junction non-linear system as internal BC for both vessel types, without claiming to be physiologically or clinically relevant.

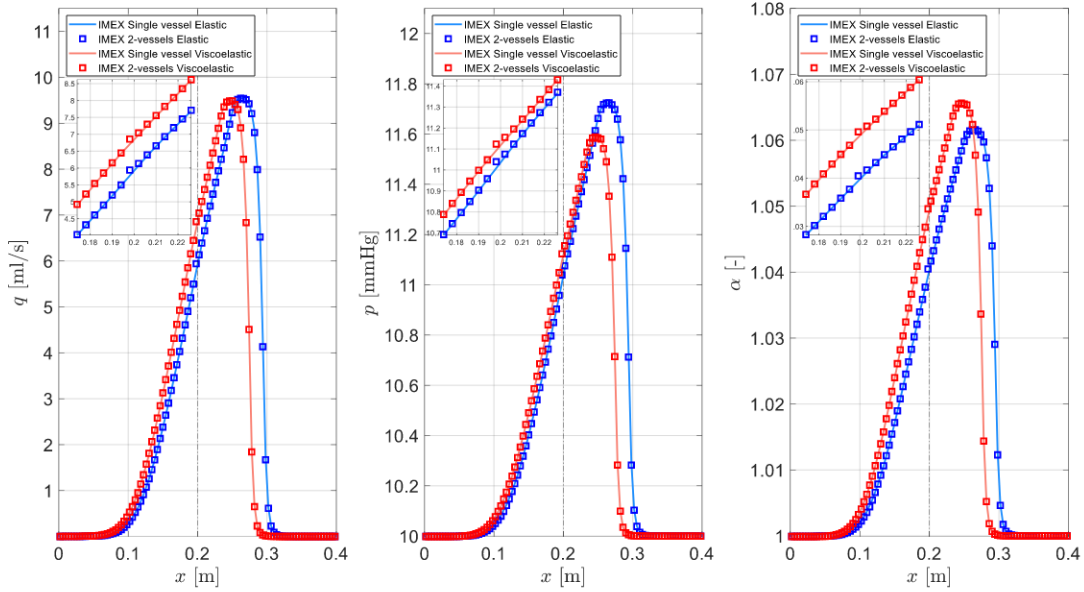


FIGURE 4.4: Results of the 2–vessel junction test performed for a generic vein (VV case). Comparison between the reference solution (single vein) and the numerical solution (2 identical veins separated by a trivial junction) when considering either an elastic or a viscoelastic wall mechanical behaviour. Results are presented in terms of flow rate (left figure), pressure (central figure) and dimensionless cross-sectional area (right figure) at time $t = 0.17$ s, using $n_c = 50$ cells for each vessel.

While at the outlet a simple transparent, reflection-free, BC is imposed, the following flow rate is prescribed at the inlet:

$$q_{in} = \hat{q} \exp \left[-\hat{\sigma} (t - \hat{t})^2 \right], \quad (4.3.1)$$

where the parameters \hat{q} , $\hat{\sigma}$ and \hat{t} are indicated in Table 4.1, together with the other parameters used in these tests. Parameters characterizing the inlet flow rate are taken from Müller, Leugering, and Blanco (2016) for the AA case, whereas, due to the lack of reference data, for the VV case they are chosen consistently with physiological values with the main purpose of testing the model.

Elastic and viscoelastic results presented in Figures 4.3 and 4.4 show a very good agreement between reference and numerical solutions in the junction sections in both AA and VV tests, confirming the correct and robust numerical implementation of the junction even in the innovative viscoelastic case. A better agreement between reference and numerical solutions would only be possible increasing the order of accuracy of the model, as presented in Müller and Blanco (2015). It is worth underlining that these satisfactory results derive from the accurate numerical treatment of the BCs described in Section 4.2.2. Without the discussed combination of numerical techniques for treating internal boundaries, the numerical solution would be characterized by strong perturbations. This is true in these trivial 2–vessel cases, as well as in more complex networks. As already discussed, the treatment of internal boundaries is a delicate task, especially when dealing with very wide networks. Indeed, even a small variation from the presented numerical model set up could provoke cumbersome problems to the network solution. In Figures 4.3 and 4.4, it is also possible to appreciate the viscoelastic contribution given by the SLSM model. It can

TABLE 4.2: Parameters of the accuracy analysis performed for the 2-vessel junction test, considering a generic artery (AA) and a generic vein (VV), referring to Eq. (4.3.2). Values are chosen within standard ranges found in the human body.

Test	l	T_0	\tilde{A}	\tilde{a}	\tilde{P}	\tilde{p}	\tilde{E}_0	\tilde{e}	h_0	E_∞	τ_r
	[cm]	[s]	[mm ²]	[mm ²]	[kPa]	[kPa]	[MPa]	[MPa]	[mm]	[MPa]	[ms]
AA	20	1.0	400	40	10	2.0	2.0	0.2	1.5	1.6	0.36
VV	20	1.0	40	4.0	1.5	0.3	1.76	0.1	0.3	1.5	0.06

be noticed that for the VV case the viscoelastic effect is less evident than in the AA case due to the different viscoelastic parameters assigned to the two vessel walls. Furthermore, different characteristics between cases AA and VV can be observed in terms of dimensionless cross-sectional area α , due to the diverse mechanical behaviour associated to arteries and veins. Indeed, the tube law used for veins defines a more complex behaviour with respect to the one used for arteries, having different coefficients K , m , and n in Eq. (3.2.12), which, for veins, account also for collapsing states.

Accuracy analysis and well-balancing property

The accuracy analysis is performed with the 2-vessel junction test for both the arterial (AA) and the venous (VV) cases. In contrast with the above discussed tests, for these analyses periodic BCs are chosen. Furthermore, a sinusoidal initial condition is imposed as follows:

$$\mathbf{Q}_{IC} = \begin{pmatrix} A_{IC} \\ q_{IC} \\ p_{IC} \\ A_{0,IC} \\ E_{0,IC} \\ p_{ext,IC} \end{pmatrix} = \begin{pmatrix} \tilde{A} + \tilde{a} \sin\left(\frac{2\pi x}{l}\right) \\ -\frac{\tilde{a}l}{T_0} \cos\left(\frac{2\pi x}{l}\right) \\ \tilde{P} + \tilde{p} \cos\left(\frac{2\pi x}{l}\right) \\ \tilde{A} + \tilde{a} \sin\left(\frac{2\pi x}{l}\right) \\ \tilde{E}_0 + \tilde{e} \sin\left(\frac{2\pi x}{l}\right) \\ \tilde{P} + \tilde{p} \cos\left(\frac{2\pi x}{l}\right) \end{pmatrix}. \quad (4.3.2)$$

Parameters for these analyses are listed in Table 4.2. The reference solution is simulated with $n_c = 8019$ number of cells, and for each state variable (area A , flow rate Au , and pressure p) L^1 , L^2 and L^∞ norms are evaluated according to Caleffi, Valiani, and Bernini (2006):

$$L^1 = \sum_{l=1}^{n_c} |\iota(x_l, t^n) - \hat{\iota}_l^n| \Delta x, \quad (4.3.3a)$$

$$L^2 = \sqrt{\sum_{l=1}^{n_c} (\iota(x_l, t^n) - \hat{\iota}_l^n)^2 \Delta x}, \quad (4.3.3b)$$

$$L^\infty = \max |\iota(x_l, t^n) - \hat{\iota}_l^n|, \quad 1 \leq l \leq n_c, \quad (4.3.3c)$$

where $\iota(x_i, t^n)$ and $\hat{\iota}_l^n$ are the analytical and numerical point-values of the state variable. Results accounting for an elastic vessel wall behaviour are presented in Table 4.3, whereas those accounting for a viscoelastic vessel wall behaviour are presented in Table 4.4. The second-order accuracy is achieved for all the evolutionary variables in both the cases, AA and VV.

TABLE 4.3: Results of the accuracy analysis performed for the 2-vessel junction test, concerning a generic artery (AA) and a generic vein (VV). Vessels wall are characterised by an elastic mechanical behaviour. Errors are computed for variables A , Au and p in terms of norms L^1 , L^2 and L^∞ , showing the corresponding order of accuracy. The final time of the simulation is $t_{end} = 0.025$ s for the AA test, and $t_{end} = 0.10$ s for the VV test.

Test	Variable	n_c	L^1	$\mathcal{O}(L^1)$	L^2	$\mathcal{O}(L^2)$	L^∞	$\mathcal{O}(L^\infty)$
AA	A	33	3.69×10^{-8}	-	6.48×10^{-8}	-	1.65×10^{-7}	-
		99	3.96×10^{-9}	2.03	7.07×10^{-9}	2.02	1.86×10^{-8}	1.99
		297	4.34×10^{-10}	2.01	7.79×10^{-10}	2.01	2.07×10^{-9}	2.00
		891	4.75×10^{-11}	2.01	8.54×10^{-11}	2.01	2.28×10^{-10}	2.01
		2673	4.74×10^{-12}	2.10	8.53×10^{-12}	2.10	2.28×10^{-11}	2.10
	Au	33	2.10×10^{-7}	-	3.72×10^{-7}	-	9.37×10^{-7}	-
		99	2.77×10^{-8}	1.84	4.87×10^{-8}	1.85	1.29×10^{-7}	1.95
		297	3.24×10^{-9}	1.95	5.70×10^{-9}	1.95	1.47×10^{-8}	1.98
		891	3.62×10^{-10}	2.00	6.37×10^{-10}	2.00	1.63×10^{-9}	2.00
		2673	3.64×10^{-11}	2.10	6.41×10^{-11}	2.10	1.63×10^{-10}	2.10
	p	33	8.61	-	1.53×10^1	-	3.62×10^1	-
		99	9.43×10^{-1}	2.01	1.69	2.01	4.03	2.00
		297	1.04×10^{-1}	2.01	1.87×10^{-1}	2.01	4.48×10^{-1}	2.00
		891	1.14×10^{-2}	2.01	2.05×10^{-2}	2.01	4.91×10^{-2}	2.01
		2673	1.14×10^{-3}	2.10	2.05×10^{-3}	2.10	4.91×10^{-3}	2.10
VV	A	33	2.98×10^{-8}	-	7.93×10^{-8}	-	5.83×10^{-7}	-
		99	3.30×10^{-9}	2.00	9.17×10^{-9}	1.96	8.07×10^{-8}	1.80
		297	3.58×10^{-10}	2.02	1.03×10^{-9}	1.99	9.89×10^{-9}	1.91
		891	3.91×10^{-11}	2.01	1.15×10^{-10}	2.00	1.12×10^{-9}	1.98
		2673	3.93×10^{-12}	2.10	1.16×10^{-11}	2.09	1.14×10^{-10}	2.08
	Au	33	2.00×10^{-8}	-	6.39×10^{-8}	-	5.07×10^{-7}	-
		99	2.32×10^{-9}	1.96	7.68×10^{-9}	1.93	7.52×10^{-8}	1.74
		297	2.72×10^{-10}	1.95	9.68×10^{-10}	1.89	9.40×10^{-9}	1.89
		891	3.06×10^{-11}	1.99	1.13×10^{-10}	1.96	1.13×10^{-9}	1.92
		2673	3.14×10^{-12}	2.08	1.16×10^{-11}	2.07	1.17×10^{-10}	2.07
	p	33	1.03	-	2.34	-	1.47×10^1	-
		99	1.20×10^{-1}	1.96	3.22×10^{-1}	1.81	2.70	1.54
		297	1.37×10^{-2}	1.97	4.21×10^{-2}	1.85	3.75×10^{-1}	1.80
		891	1.53×10^{-3}	2.00	4.90×10^{-3}	1.96	4.57×10^{-2}	1.92
		2673	1.56×10^{-4}	2.08	5.03×10^{-4}	2.07	4.71×10^{-3}	2.07

The *dead-body* simulation is first performed with periodic BCs, initial null velocity and uniform pressure on the geometry of the 2-vessel junction case. Successively, different configurations, including junctions with multiple branches in which the joined vessels exhibit mechanical and geometrical characteristics different from each other, are considered. Results confirm that neither spurious velocities nor different numerical perturbations arise during the simulation. Therefore, the model is verified to be well-balanced (or, with the same connotation, satisfies the exact conservation property, i.e., C-property (Bermudez and Vazquez, 1994) even when involving junctions.

TABLE 4.4: Results of the accuracy analysis performed for the 2-vessel junction test, concerning a generic artery (AA) and a generic vein (VV). Vessels wall are characterised by a viscoelastic mechanical behaviour. Errors are computed for variables A , Au and p in terms of norms L^1 , L^2 and L^∞ , showing the corresponding order of accuracy. The final time of the simulation is $t_{end} = 0.025$ s for the AA test, and $t_{end} = 0.10$ s for the VV test.

Test	Variable	n_c	L^1	$\mathcal{O}(L^1)$	L^2	$\mathcal{O}(L^2)$	L^∞	$\mathcal{O}(L^\infty)$
AA	A	33	3.47×10^{-8}	-	6.03×10^{-8}	-	1.36×10^{-7}	-
		99	3.75×10^{-9}	2.02	6.58×10^{-9}	2.02	1.48×10^{-8}	2.02
		297	4.13×10^{-10}	2.01	7.25×10^{-10}	2.01	1.64×10^{-9}	2.00
		891	4.52×10^{-11}	2.01	7.95×10^{-11}	2.01	1.80×10^{-10}	2.01
		2673	4.52×10^{-12}	2.10	7.94×10^{-12}	2.10	1.80×10^{-11}	2.10
	Au	33	1.70×10^{-7}	-	2.98×10^{-7}	-	7.51×10^{-7}	-
		99	2.38×10^{-8}	1.79	4.29×10^{-8}	1.77	1.16×10^{-7}	1.70
		297	2.82×10^{-9}	1.95	5.10×10^{-9}	1.94	1.40×10^{-8}	1.92
		891	3.16×10^{-10}	2.00	5.74×10^{-10}	2.00	1.58×10^{-9}	2.00
		2673	3.18×10^{-11}	2.10	5.78×10^{-11}	2.10	1.60×10^{-10}	2.10
	p	33	8.21	-	1.43×10^1	-	3.42×10^1	-
		99	9.14×10^{-1}	2.00	1.60	2.00	3.75	2.01
		297	1.00×10^{-1}	2.01	1.76×10^{-1}	2.01	4.12×10^{-1}	2.01
		891	1.10×10^{-2}	2.01	1.93×10^{-2}	2.01	4.52×10^{-2}	2.01
		2673	1.10×10^{-3}	2.10	1.93×10^{-3}	2.10	4.51×10^{-3}	2.10
VV	A	33	2.91×10^{-8}	-	9.49×10^{-8}	-	7.55×10^{-7}	-
		99	3.26×10^{-9}	2.00	1.11×10^{-8}	1.96	1.15×10^{-7}	1.71
		297	3.57×10^{-10}	2.01	1.21×10^{-9}	2.01	1.38×10^{-8}	1.93
		891	3.88×10^{-11}	2.02	1.34×10^{-10}	2.01	1.54×10^{-9}	2.00
		2673	3.87×10^{-12}	2.10	1.34×10^{-11}	2.10	1.55×10^{-10}	2.09
	Au	33	1.61×10^{-8}	-	7.34×10^{-8}	-	6.33×10^{-7}	-
		99	2.15×10^{-9}	1.83	9.46×10^{-9}	1.86	1.02×10^{-7}	1.59
		297	2.59×10^{-10}	1.93	1.15×10^{-9}	1.91	1.35×10^{-8}	1.91
		891	2.94×10^{-11}	1.99	1.32×10^{-10}	1.97	1.58×10^{-9}	1.95
		2673	2.97×10^{-12}	2.10	1.34×10^{-11}	2.10	1.61×10^{-10}	2.08
	p	33	6.55×10^{-1}	-	2.12	-	1.69×10^1	-
		99	8.89×10^{-2}	1.82	3.25×10^{-1}	1.71	3.54	1.42
		297	1.19×10^{-2}	1.83	4.77×10^{-2}	1.75	5.20×10^{-1}	1.75
		891	1.33×10^{-3}	2.00	5.44×10^{-3}	1.98	6.15×10^{-2}	1.94
		2673	1.37×10^{-4}	2.07	5.69×10^{-4}	2.05	6.48×10^{-3}	2.05

4.3.2 3-vessel junction

A 3-vessel junction test is performed accounting for a bifurcation case (3 arteries) in both the elastic and viscoelastic configuration. The model has been tested also for a venous confluence, but due to the lack of reference solutions to compare with, results are not reported in this Thesis. The 3-vessel junction test represents the bifurcation of the terminal part of the abdominal aorta (AbA) into the two iliac arteries (IAs) that perfuse the legs. Benchmark solutions, as well as geometrical and elastic mechanical parameters, are taken from Boileau et al. (2015) and Xiao, Alastruey, and Figueroa (2014), to which the reader is referred. In fact, the bifurcation test proposed in Boileau et al. (2015) and Xiao, Alastruey, and Figueroa (2014) only considers an elastic vessels wall behaviour. At the inlet, a flow rate resembling the human flow rate waveform at this section of the AbA is prescribed as supplied by Murgo et al.

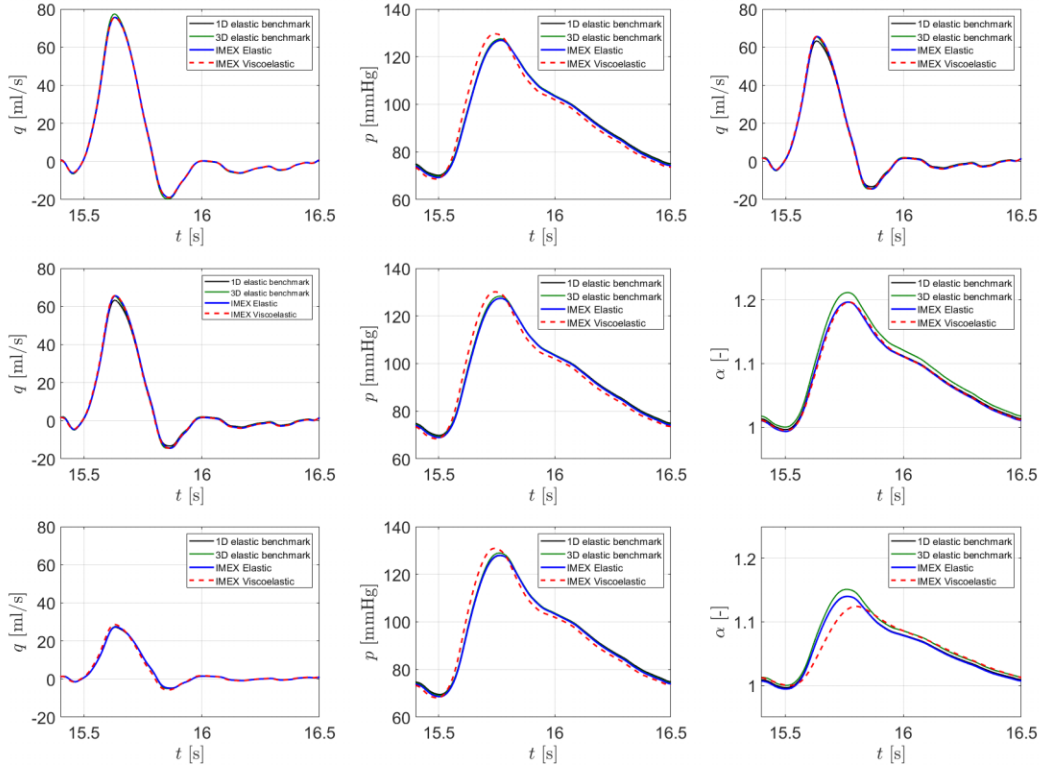


FIGURE 4.5: Elastic and viscoelastic results obtained with the here proposed IMEX RK FV scheme are compared with six different 1-D and one 3-D elastic benchmark solutions taken from Boileau et al. (2015). Results at mid-section of the abdominal aorta (upper row), at junction section (central row) and at mid-section of the left iliac artery (lower row) are shown in terms of flow rate (left column), pressure (central column) and dimensionless cross-sectional area (right column), using $n_c = 5$ cells for each vessel.

(1980), allowing to simulate a physiologically-based test. Flow rate and pressure are simulated at the outlet sections via the RCR model. Resistances and compliance of the two outlets are given by Boileau et al. (2015), as well as the pressure at the outlet of the RCR unit. It is worth to underline that the problem is symmetric, since left and right IAs have the same characteristics. Finally, the velocity profile is characterized by coefficients $\alpha_c = 1.1$ and $\zeta = 9$.

In this test, a comparison between the elastic and viscoelastic numerical approaches is carried out, to investigate how much the viscous terms affect results with respect to a purely elastic bifurcation case. Due to the lack of reference viscoelastic parameters for this specific test, the procedure proposed in Bertaglia et al. (2020) is considered to simulate viscoelasticity, i.e., to fix parameters of the SLSM. In particular:

- the asymptotic Young moduli E_∞ characterizing the three vessels considered in this numerical experiment are taken coincident with the elastic Young moduli used in the corresponding test in Boileau et al. (2015);
- since normally τ_r behaves almost like a biological constant (Bertaglia et al., 2020; Ghigo et al., 2017b), it is fixed equal to the one obtained in the following discussed ADAN56 test (see Section 4.3.3) for all the three vessels.

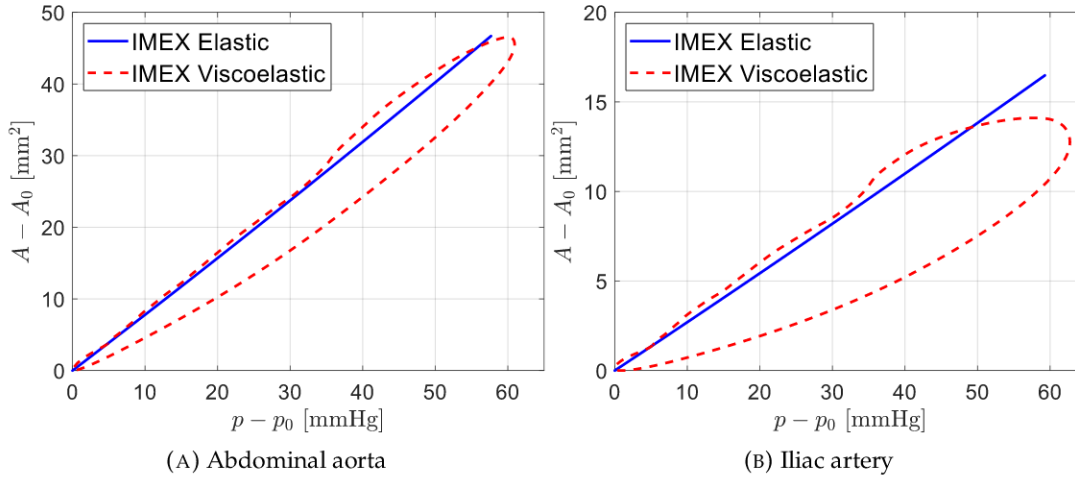


FIGURE 4.6: The elastic line confirms the absence of dissipative effects, in contrast with the wide viscoelastic curve that shows energy dissipation. The loops evolve in counterclockwise. A_0 and p_0 are the equilibrium cross-sectional area and pressure, respectively, whose value coincides with that of the diastolic phase.

Fixed these two parameters, E_0 and η can be evaluated recurring to the following equations:

- Eq. (3.2.18), which gives a mathematical relationship among E_0 , E_∞ and τ_r ;
- Eq. (3.2.20) to compute the ratio E_∞/E_0 .

This estimation procedure allows to have in this bifurcation test a viscoelastic behaviour of vessels similar to that considered in the ADAN56 arterial network, further presented in Section 4.3.3. The reader is referred to Appendix A for the complete set of SLSM parameters of this test.

Figure 4.5 shows numerical results of both elastic and viscoelastic simulations of the aortic bifurcation compared with benchmark solutions, which consist of one 3-D numerical solution and six 1-D numerical solutions performed with six different numerical methods (for further details regarding benchmark solutions see Boileau et al. (2015)). Concerning the elastic simulation, Figure 4.5 demonstrates an excellent agreement between IMEX results and benchmark solutions. Hence, the capability of the proposed methodology, in the elastic formulation, to simulate in detail the multiple wave reflections generated at the bifurcation, which shape pressure, flow rate and area waveforms in the AbA and the two IAs is here confirmed. Regarding viscoelastic results, Figure 4.5 reveals a modest viscous contribution of vessel walls, observing a rather small difference between elastic and viscoelastic solutions. Despite this modest difference, viscoelastic features are clearly observable in Figure 4.6, where hysteresis loops at the AbA mid-section and at the left IA mid-section are shown. The viscous dissipative effect can be observed comparing the wide loop of the viscoelastic simulation to the straight line obtained with the elastic configuration. Indeed, this result agrees with the one presented in Raghu et al. (2011) where elastic/viscoelastic comparisons and consequent hysteresis loops are reported for the same aortic bifurcation test (the reader is referred to the *Rest* case). Also in Raghu et al. (2011) there is no evident discrepancy between waveforms obtained with the two different mechanical behaviours of the vessel wall. Therefore, we can conclude that the IMEX FV method here proposed is well-conceived and robust enough to deal even with viscoelastic junction cases.

4.3.3 Human arterial networks

In this section, results obtained simulating two different networks of the largest central systemic arteries of the human vascular system are presented and discussed. The first network simulates an *in vitro* model composed of 37 main arteries, labeled as AN37 hereinafter, for which experimental measurements of flow rate and pressure are available (Alastruey et al., 2011; Matthys et al., 2007). The second network is a reduced version of the anatomically detailed arterial system, composed of the 56 largest arteries of the human arterial circulation, hence labeled as ADAN56 (Blanco et al., 2014; Blanco et al., 2015). For both networks, the simulated waveforms of the system variables are compared, for selected arteries, to reference solutions (experimental and numerical elastic benchmark) taken from Boileau et al. (2015). Moreover, a viscoelastic simulation is carried out for the same two networks to assess how the SLSM application affects the results. All SLSM viscoelastic parameters, estimated following Bertaglia et al. (2020), are reported in Appendix A for both networks.

AN37

The AN37 arterial tree recalls the one presented in Matthys et al. (2007) and Alastruey et al. (2011), for which *in vitro* pressure and flow rate measurements were acquired at multiple locations. The network is composed by 37 silicon vessels representing the largest central systemic arteries of the human vascular system. At the inlet of the ascending aorta, the condition $q_{in}(t)$ is imposed, which corresponds to the measured *in vitro* flow rate, based on a human cardiac output. Downstream BC is simulated coupling to each 1-D peripheral vessels a single-resistance (R) lumped-parameter model. All these R boundary parameters and the inlet flow rate are supplied by Boileau et al. (2015). The network is simulated through the a-FSI blood flow model solved with the AP-IMEX RK FV scheme, with initial conditions such that $A_{IC} = A_0$, $p_{IC} = p_{ext} = 0$ and $u_{IC} = 0$. The reader is referred to Alastruey et al. (2011), Boileau et al. (2015), and Matthys et al. (2007) for the topological, geometrical and mechanical parameters of the AN37 network. To simulate the viscoelastic case, for consistency with the corresponding elastic case, E_∞ is set equal to the elastic Young modulus given in the references, η is gathered for every silicon tube from Alastruey et al. (2011) (from which experimental results are also taken for comparison), and finally E_0 is computed with Eq. (3.2.20). The velocity profile is characterized by a coefficient $\alpha_c = 1.1$, hence $\zeta = 9$. The spatial discretization is performed setting the cell width $\Delta x = 5$ mm, imposing that at least two cells are used to discretize the shortest vessels.

Comparisons between numerical results, elastic benchmark and experimental data, in terms of pressure and flow rate, are presented in Figures 4.7–4.10 for selected vessels, as well as numerical results in terms of dimensionless cross-sectional area, for which a reference solution is not available in literature. The simulation is run for 15 heartbeats in order to converge to a periodic state, but only the last cardiac cycle is shown. It can be observed that IMEX numerical results are in very good agreement with elastic benchmarks, which consist in six 1-D numerical results obtained with different methods (Boileau et al., 2015). Moreover, IMEX results correctly captures the main features of flow rate and pressure experimental data at the 8 investigated arterial sites, suggesting that the proposed methodology permits to replicate the behaviour of an *in vitro* arterial tree, considering the uncertainties in the experimental measurements and the simplifications of the 1-D formulation, which cause the observable discrepancies.

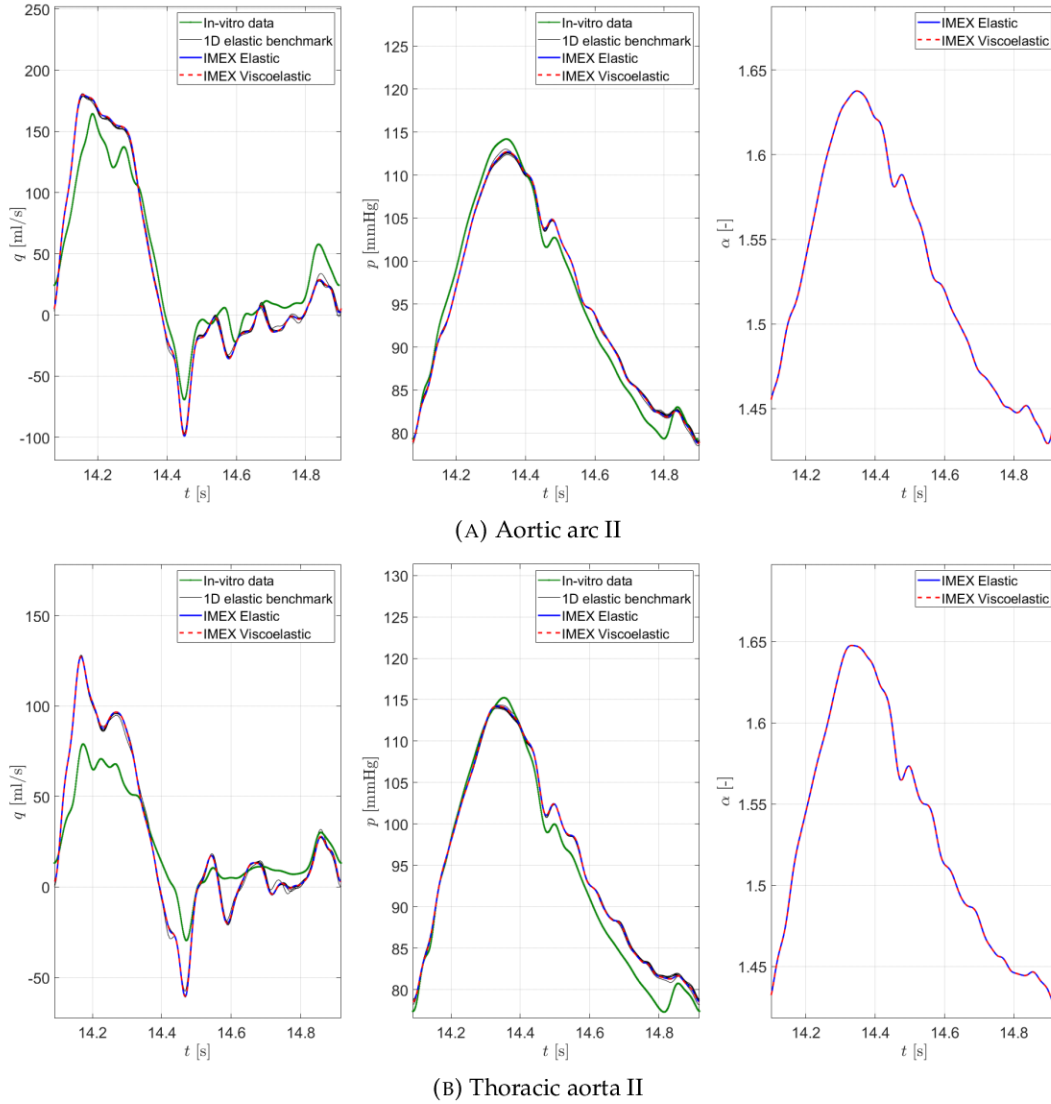


FIGURE 4.7: Results of the AN37 network for 2 selected arteries. Results are obtained with the IMEX RK FV scheme considering both the elastic and the viscoelastic tube law to characterize the mechanical behaviour of vessel walls. Comparison with *in vitro* experimental data and six different numerical elastic benchmark are presented in terms of flow rate (left column) and pressure (central column), while for the dimensionless cross-sectional area (right column) reference results are not available.

As visible from Figures 4.7–4.10, there is no significant distinction between elastic and viscoelastic results. The viscoelastic contribution appears weak in this simulation because, with the fixed SLSM parameters, the relaxation time results very small: $\tau_r \approx \mathcal{O}(10^{-4})$ s, thus approaching the elastic equilibrium limit ($\tau_r \rightarrow 0$), as discussed in Section 3.2.2. This is consistent with Figure 4.11, where the hysteresis loop of the second tract of the aortic arch (aortic arch II) is reported as an example. It can be noticed that the loop is extremely narrow, basically coincident with the elastic line. The instantaneous Young modulus E_0 is the slope of the systolic tract of the loop, namely the loop lower path. For $\tau_r \rightarrow 0$, $E(t) \rightarrow E_\infty$, hence coinciding, even from the very first instants, with the slope of the diastolic tract, E_∞ , which is the loop upper path. Therefore, consistently with the asymptotic limit of the model, with this setting of

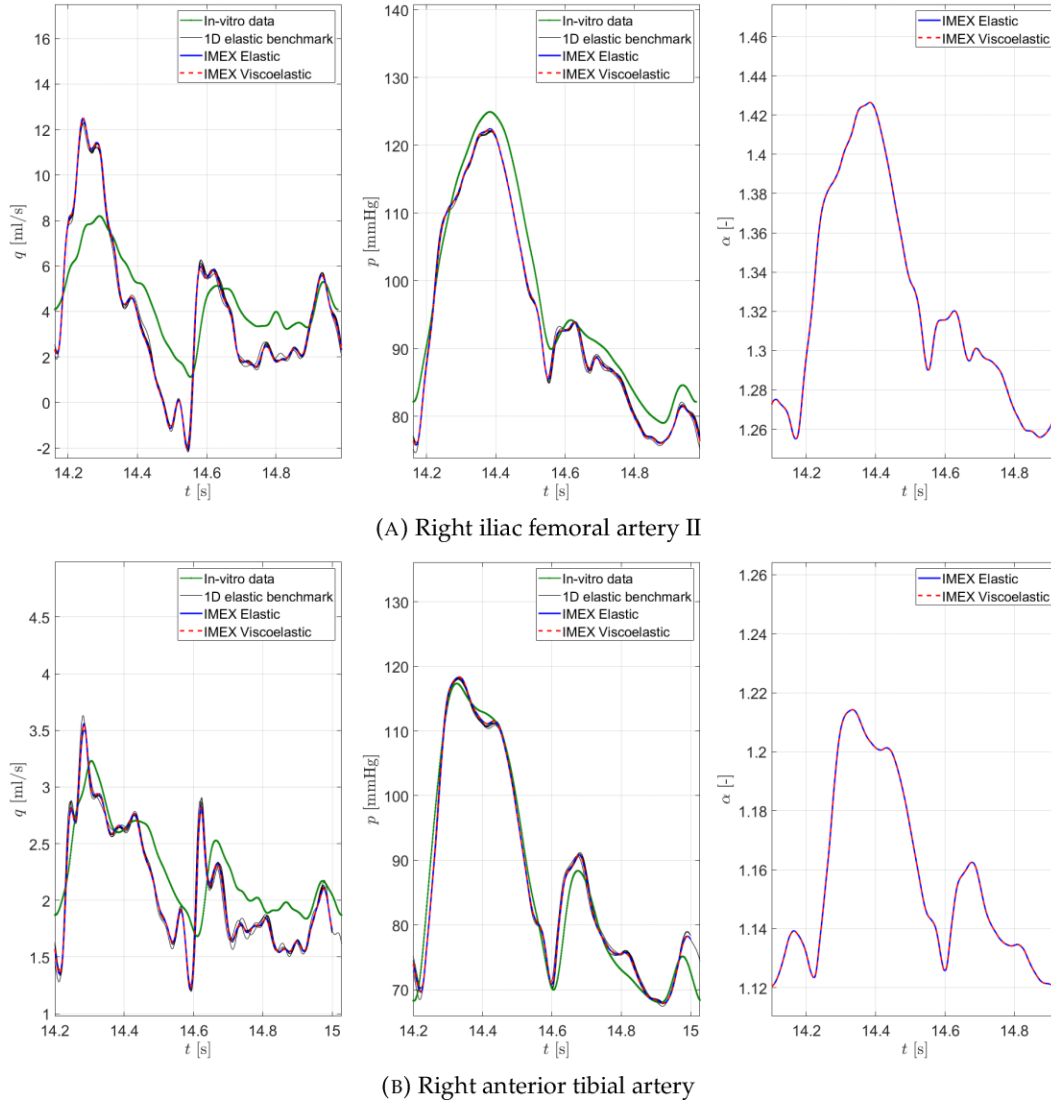


FIGURE 4.8: Results of the AN37 network for 2 selected arteries. Results are obtained with the IMEX RK FV scheme considering both the elastic and the viscoelastic tube law to characterize the mechanical behaviour of vessel walls. Comparison with *in vitro* experimental data and six different numerical elastic benchmark are presented in terms of flow rate (left column) and pressure (central column), while for the dimensionless cross-sectional area (right column) reference results are not available.

viscoelastic parameters the loop remains totally thin.

It can be questioned if the model actually reproduces the viscoelastic contribution. The answer is positive and it can be verified computing the specific damping parameters as presented in Wang and Chesler (2012), which results to be greater than zero, although with a small order of magnitude, $\mathcal{O}(10^{-4})$. We highlight once more that the reason behind these results lays in the specific viscoelastic parameters fixed for the silicon vessels that constitute the AN37 network. To make differences between viscoelastic and elastic results evident in this test, we should have increased the vessel wall viscosity η (and therefore the relaxation time τ_r) with respect to the value given in the reference (Alastruey et al., 2011). However, for consistency with the rest of this work, the parameters given in literature are not changed.

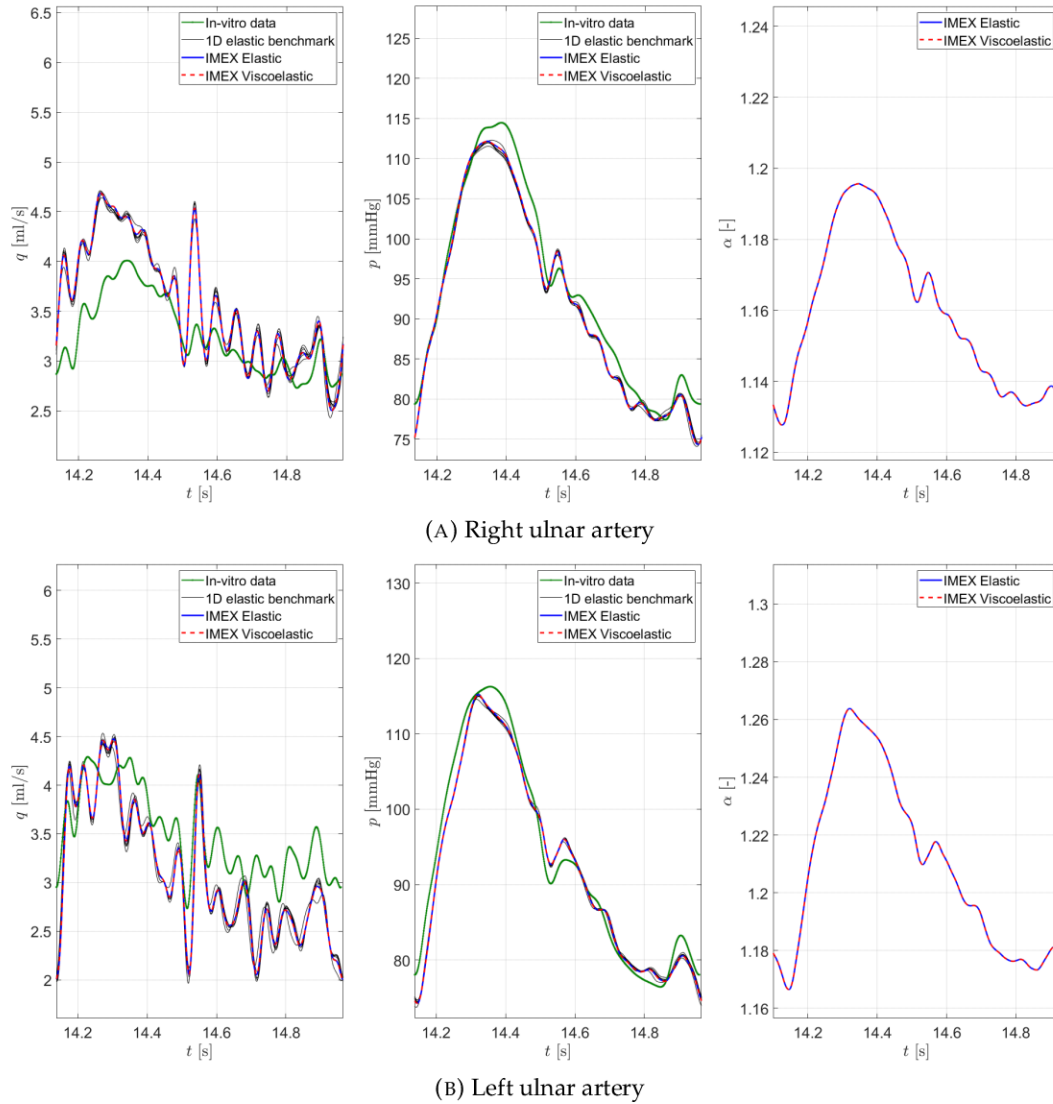


FIGURE 4.9: Results of the AN37 network for 2 selected arteries. Results are obtained with the IMEX RK FV scheme considering both the elastic and the viscoelastic tube law to characterize the mechanical behaviour of vessel walls. Comparison with *in vitro* experimental data and six different numerical elastic benchmark are presented in terms of flow rate (left column) and pressure (central column), while for the dimensionless cross-sectional area (right column) reference results are not available.

It is here stressed that the SLSM, besides being more accurate than other simpler viscoelastic models, is defined by three viscoelastic parameters, hence presenting an additional degree of freedom with respect, for instance, to the widely used KV model. This leads the SLSM to define a richer variety of dynamics and of configurations that permit the convergence towards the asymptotic elastic limit. In this context, it is neither trivial nor predictable to have a viscoelastic waveform that appears clear and distinct from the elastic corresponding case. These three parameters cannot be considered separately but it is their interaction that truly affects the vessel wall behaviour.

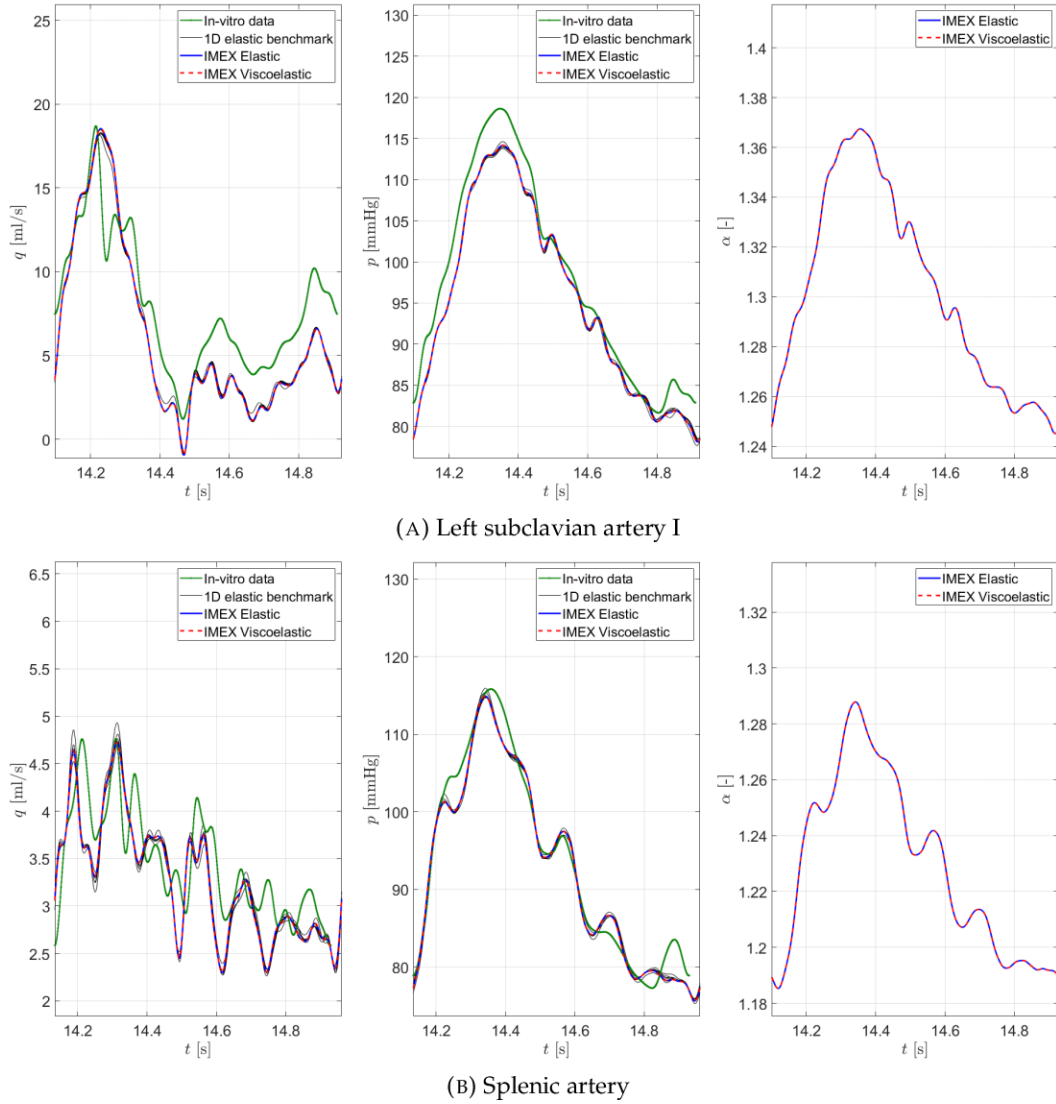


FIGURE 4.10: Results of the AN37 network for 2 selected arteries. Results are obtained with the IMEX RK FV scheme considering both the elastic and the viscoelastic tube law to characterize the mechanical behaviour of vessel walls. Comparison with *in vitro* experimental data and six different numerical elastic benchmark are presented in terms of flow rate (left column) and pressure (central column), while for the dimensionless cross-sectional area (right column) reference results are not available.

ADAN56

ADAN56 represents a reduced version of 56 vessels of the anatomically detailed arterial network presented in Blanco et al. (2014), and Blanco et al. (2015). The network consists in 77 segments linked by junction BCs. At the root of the aortic arch (inlet section), a physiological flow rate, simulating the human cardiac output, is prescribed. Furthermore, there are 31 terminal vessels, in which the outflow and the pressure are simulated via the RCR model. Parameters of the RCR units and the inlet waveform are given by Boileau et al. (2015), as well as all the topological, geometrical and mechanical characteristics of this test in the elastic configuration. With the same approach used in the previous test, following Bertaglia et al. (2020), for the

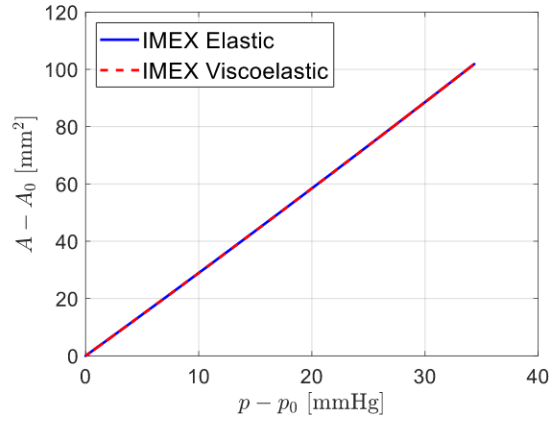


FIGURE 4.11: Hysteresis loop obtained for the aortic arch II in the AN37 network. The viscoelastic loop essentially coincides with the elastic line because of the parameters of the SLSM fixed for this specific test. Since $\tau_r \approx \mathcal{O}(10^{-4}) \rightarrow 0$, the material does not have enough time to develop its viscoelastic response. A_0 and p_0 are the equilibrium cross-sectional area and pressure, respectively, whose value coincides with those of the diastolic phase.

viscoelastic configuration E_∞ is taken from Boileau et al. (2015), η is gathered from Blanco et al. (2014), and, finally, E_0 is computed through Eq. (3.2.20). Initial conditions are $A_{IC} = A_0$, $q_{IC} = 0$, $p_{IC} = p_{ext} = 10$ kPa. Differently from the previous tests, the velocity profile is assumed to be parabolic in every vessel of the network, hence following the Poiseuille law ($\alpha_c = 4/3$, $\zeta = 2$), as specified by Boileau et al. (2015). The spatial discretization is performed setting the cell width $\Delta x = 2.5$ mm, imposing again that at least two cells are used to discretize even the shortest vessels. Results computed with the proposed methodology are compared with six reference benchmarks, consisting in numerical results obtained solving the 1-D blood flow model that accounts for a simple elastic tube law for the mechanic characterization of vessel walls with six different numerical methods (Boileau et al., 2015).

Flow rate and pressure waveforms obtained with the here proposed AP-IMEX RK FV scheme in 12 selected arteries of the network are shown in Figures 4.12–4.17, compared with benchmark solutions. In the same figures, dimensionless cross-sectional area waveforms are presented without a reference solution since it is not available in literature. To assure the convergence to a periodic state, 10 heartbeats are run, but only the last cardiac cycle is here reported. It can be observed that the elastic IMEX simulation is once more in excellent agreement with the elastic benchmark, confirming that the proposed methodology is consistent with the reference elastic configuration.

Regarding the viscoelastic simulation, as expected, a pressure peak damping can be observed with respect to elastic results. This network is characterized by a relaxation time $\tau_r \approx \mathcal{O}(10^{-2})$ s, which is two orders of magnitude greater than the AN37 relaxation time. This is the reason why, if compared to AN37 viscoelastic results, ADAN56 results show greater differences between the two mechanical behaviours of vessel walls. The higher relaxation time of this network allows wider hysteresis loops, as shown in Figure 4.18 for various arteries. Consistently with the viscoelastic model, in Figure 4.18 it can be noticed that, for a fixed area, pressure in the systolic tract is higher than the one in the diastolic tract, as the instantaneous Young modulus, which characterizes the systolic phase, is always greater than the asymptotic one (which, instead, characterizes the diastolic phase). Finally, from the same figure,

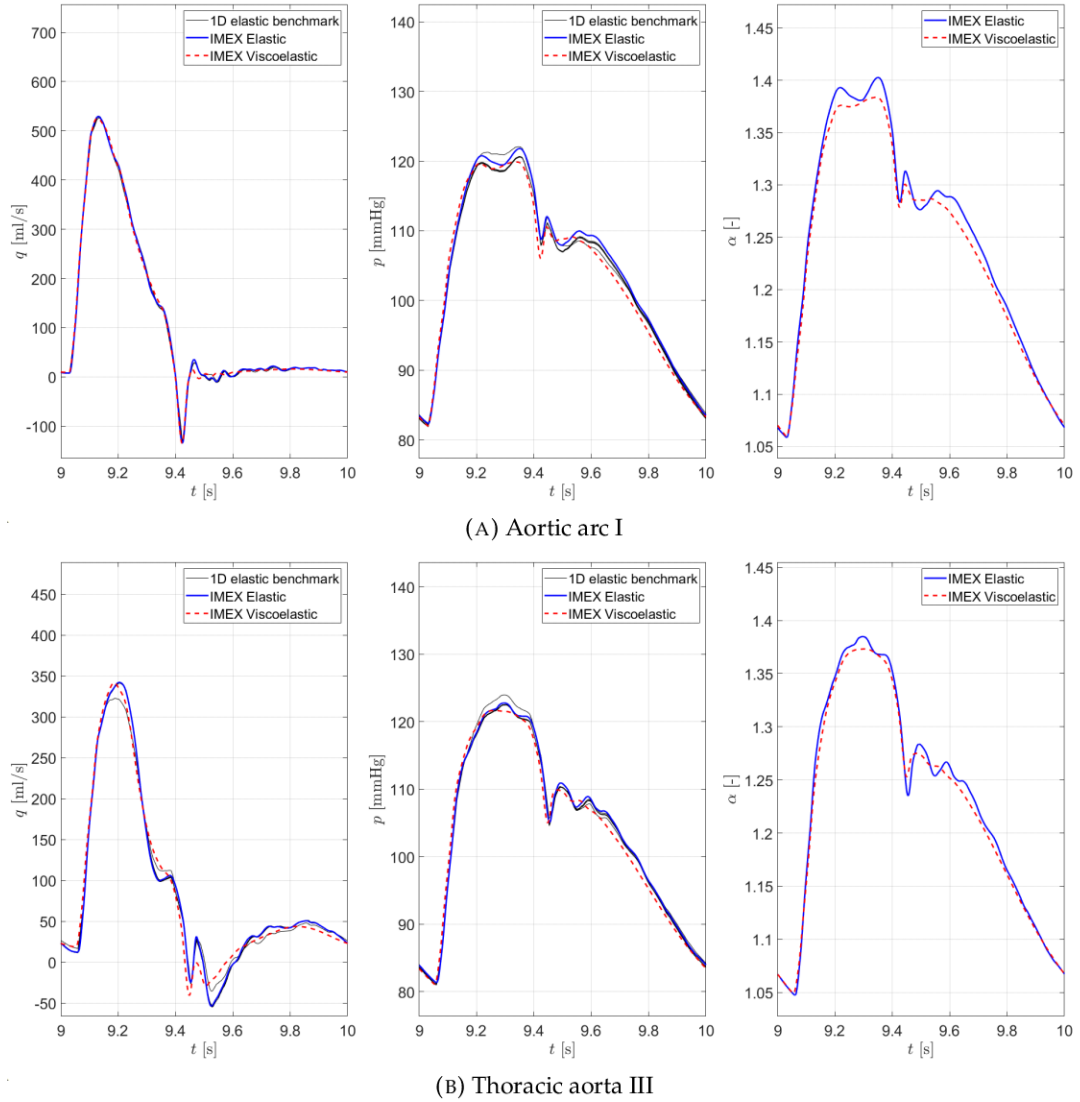


FIGURE 4.12: Results of the ADAN56 network for 2 selected arteries. Results are obtained with the IMEX RK FV scheme considering both the elastic and the viscoelastic tube law to characterize the mechanical behaviour of vessel walls. Comparison with six different 1-D elastic benchmark solutions (Boileau et al., 2015) are presented in terms of flow rate (left column) and pressure (central column), while for the dimensionless cross-sectional area (right column) reference results are not available.

the ability of the model to capture the variety of viscoelastic mechanical behaviours of each vessel in the network can be appreciated.

4.4 Concluding remarks

This Chapter presents an innovative numerical implementation of the a-FSI mathematical model presented in Chapter 3 to simulate cardiovascular networks with vessel walls characterized by a SLSM viscoelastic behaviour and a consistent treatment of boundary conditions, is presented. The a-FSI blood flow model solved with a second-order accurate AP-IMEX RK FV method, which was previously validated

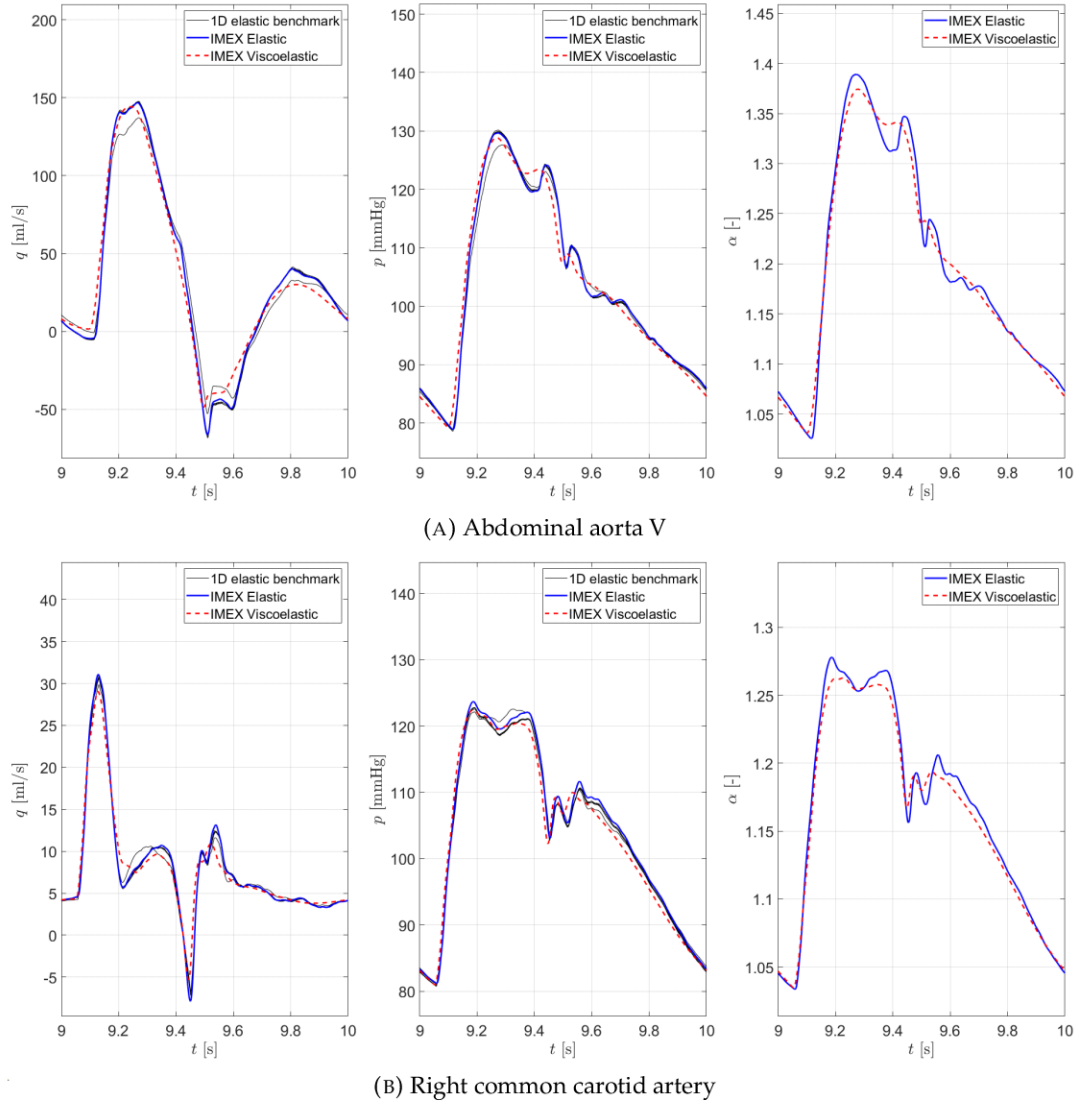


FIGURE 4.13: Results of the ADAN56 network for 2 selected arteries. Results are obtained with the IMEX RK FV scheme considering both the elastic and the viscoelastic tube law to characterize the mechanical behaviour of vessel walls. Comparison with six different 1-D elastic benchmark solutions (Boileau et al., 2015) are presented in terms of flow rate (left column) and pressure (central column), while for the dimensionless cross-sectional area (right column) reference results are not available.

in single-vessel simulations (Bertaglia et al., 2021; Bertaglia, Caleffi, and Valiani, 2020; Bertaglia et al., 2020), is here adopted to study complete viscoelastic networks, demonstrating that the model is able to accurately simulate even complex circulatory systems. Particular attention is posed on the characterization of junctions, which are geometrical singularities identified by at least two branching vessels. The proposed methodology allows considering the viscoelastic contribution of the model given by the constitutive equation, namely the tube law, even in all boundary sections (external and internal), preserving the prescribed order of accuracy. To this aim, to define the Riemann Problem at boundaries an additional Riemann Invariant is employed, which arises from the study of the eigenstructure of the hyperbolic system of equations that form the a-FSI blood flow model. This additional RI directly

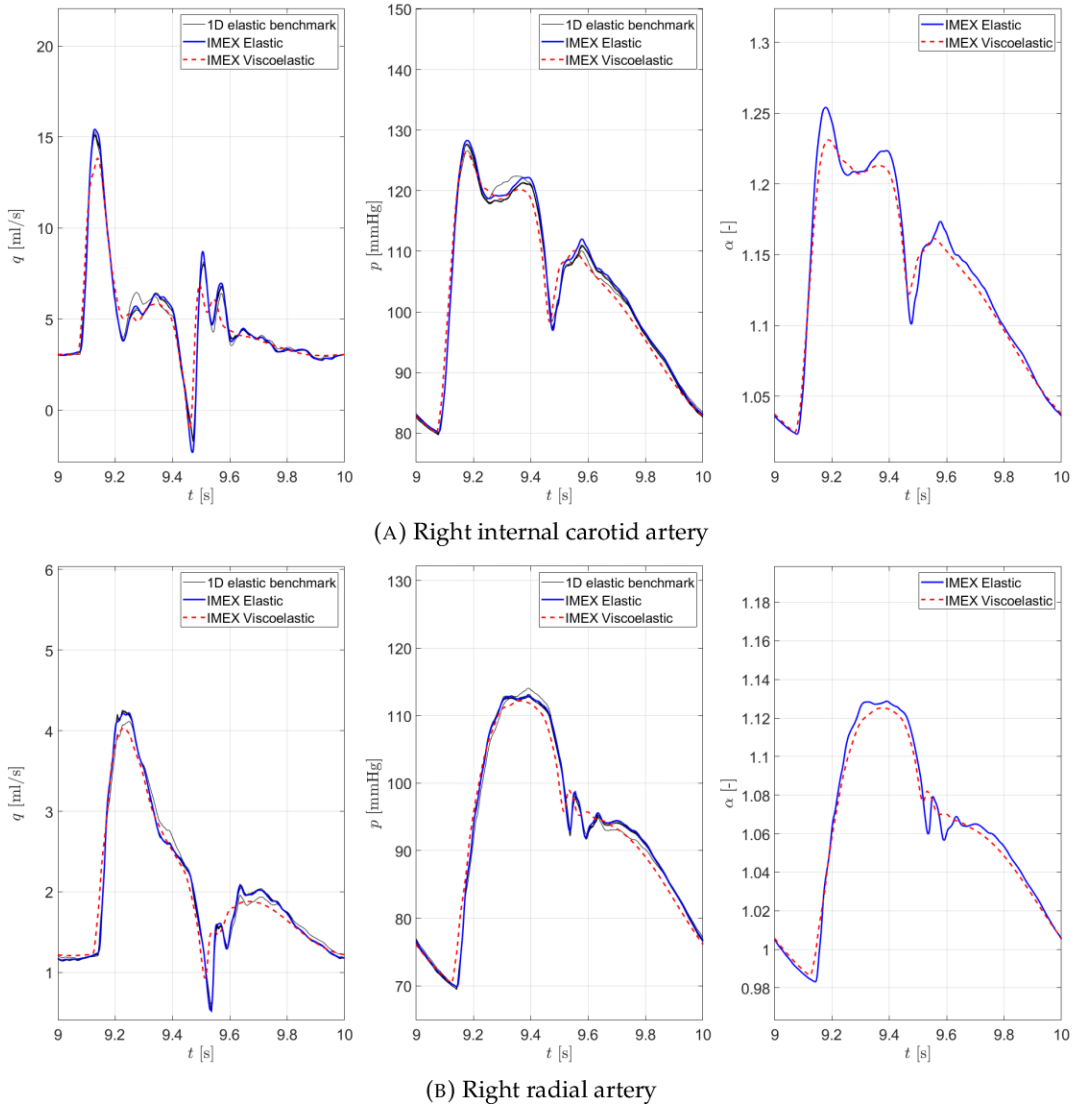


FIGURE 4.14: Results of the ADAN56 network for 2 selected arteries. Results are obtained with the IMEX RK FV scheme considering both the elastic and the viscoelastic tube law to characterize the mechanical behaviour of vessel walls. Comparison with six different 1-D elastic benchmark solutions (Boileau et al., 2015) are presented in terms of flow rate (left column) and pressure (central column), while for the dimensionless cross-sectional area (right column) reference results are not available.

derives from the introduction of the viscoelastic constitutive law in PDE form inside the system of governing equations. Therefore, the proposed treatment of BCs results intrinsically consistent with the mathematical model.

The method has been tested initially on a trivial junction case, named 2-vessel test, to validate it having an exact reference solution and to demonstrate that the second-order of accuracy and the well-balancing of the scheme are preserved even when introducing internal junctions, in both a generic artery and a generic vein. Furthermore, a simple 3-vessel aortic bifurcation case is analysed considering the elastic and the viscoelastic tube law. Results (compared with numerical benchmarks

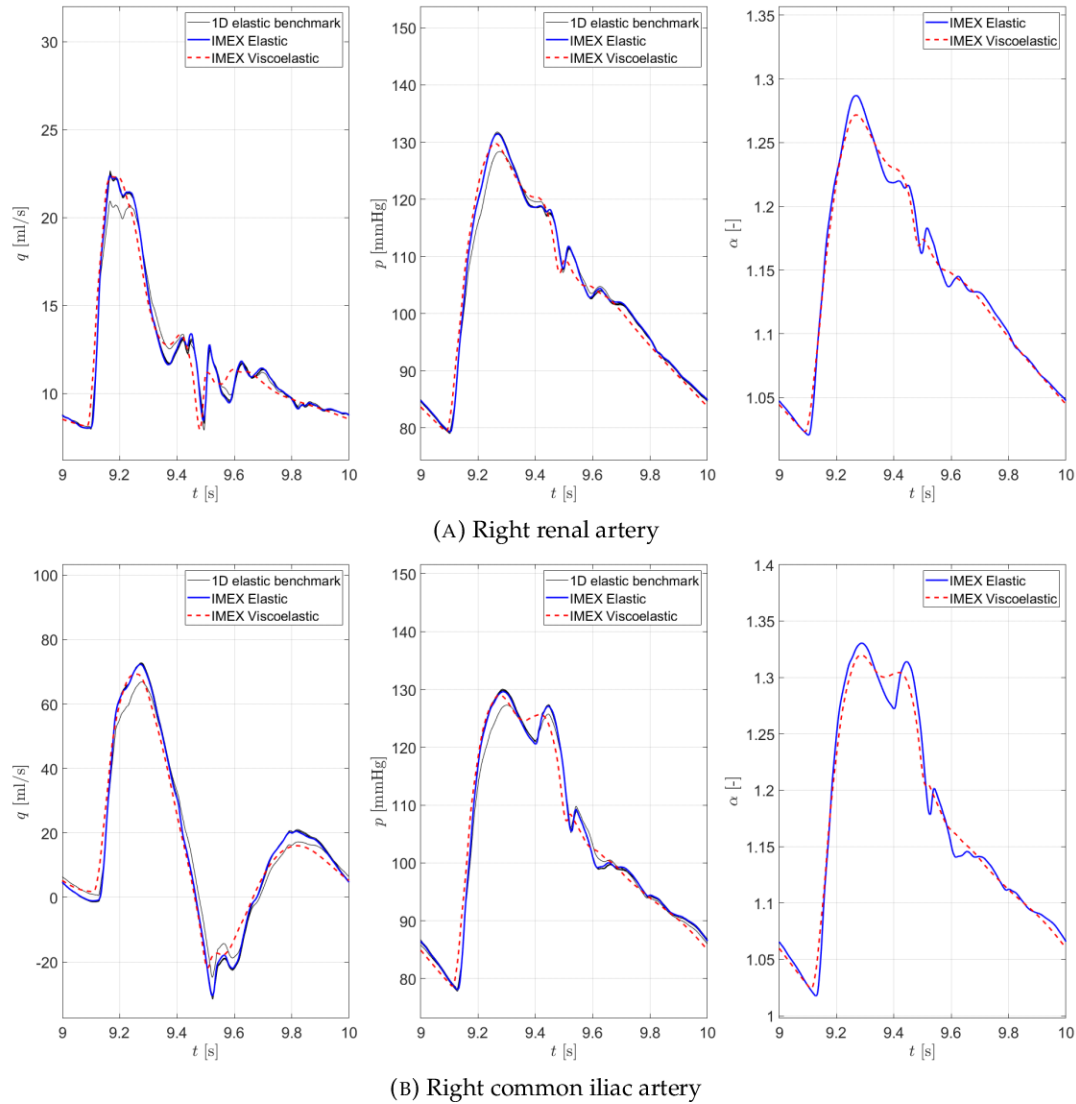


FIGURE 4.15: Results of the ADAN56 network for 2 selected arteries. Results are obtained with the IMEX RK FV scheme considering both the elastic and the viscoelastic tube law to characterize the mechanical behaviour of vessel walls. Comparison with six different 1-D elastic benchmark solutions (Boileau et al., 2015) are presented in terms of flow rate (left column) and pressure (central column), while for the dimensionless cross-sectional area (right column) reference results are not available.

in the elastic configuration) in the viscoelastic configuration confirm that the numerical implementation of the junction non-linear system is consistent with the viscous contribution produced by the mechanical representation of vessel walls via the SLSM. Consequently, two arterial networks are studied. The first one simulates an *in vitro* network composed of 37 silicon tubes that represent the main human arteries, whereas the second represents a reduced version of an anatomical detailed arterial system, consisting of the 56 largest arteries of the human cardiovascular circulation. Numerical results obtained in the two networks, with the elastic and then the viscoelastic characterization of vessels wall, have been positively tested comparing IMEX results with benchmark solutions (experimental data and numerical elastic benchmark for the AN37 and elastic numerical reference solutions for the ADAN56).

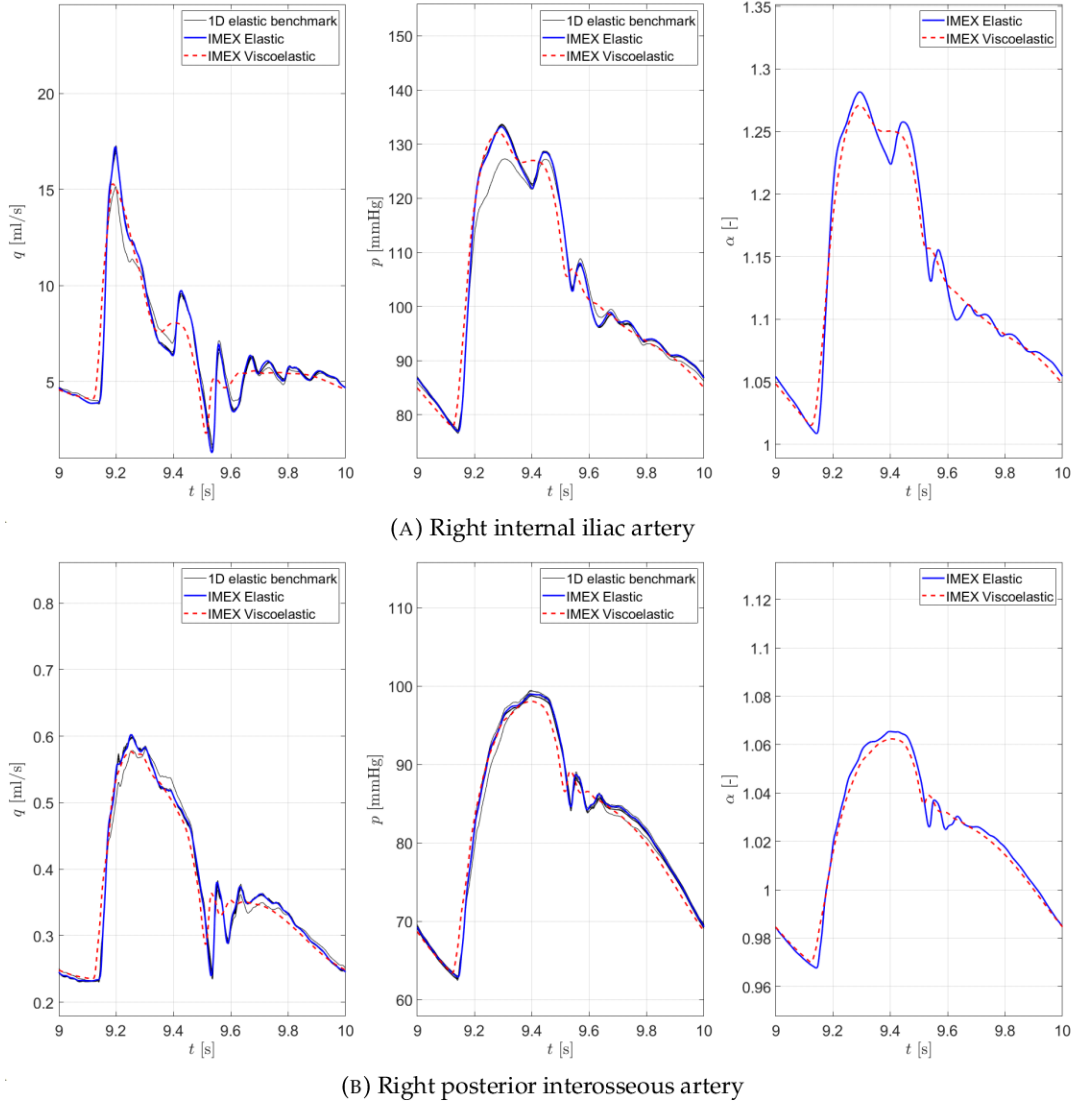


FIGURE 4.16: Results of the ADAN56 network for 2 selected arteries. Results are obtained with the IMEX RK FV scheme considering both the elastic and the viscoelastic tube law to characterize the mechanical behaviour of vessel walls. Comparison with six different 1-D elastic benchmark solutions (Boileau et al., 2015) are presented in terms of flow rate (left column) and pressure (central column), while for the dimensionless cross-sectional area (right column) reference results are not available.

The viscoelastic formulation introduces variations in the system response that are consistent with the mechanical features of the SLSM. Indeed, the damping effect caused by the viscous contribution is visible from the results, and confirmed by the opening of hysteresis loops. However, it is worth underlining the strict dependence of the viscoelastic behaviour, hence the damping effect, on the viscoelastic parameters defining the SLSM. Concerning especially the definition of the relaxation time of the material, which governs the *stiffness* of the a-FSI blood flow model, it has been shown that the asymptotic, elastic regime can be approached either when $\tau_r \rightarrow 0$ or $\tau_r \rightarrow \infty$. In these cases, viscoelastic features of the material cannot manifest and hysteresis loops coincide with the corresponding elastic straight line in the $(p-A)$ plane.

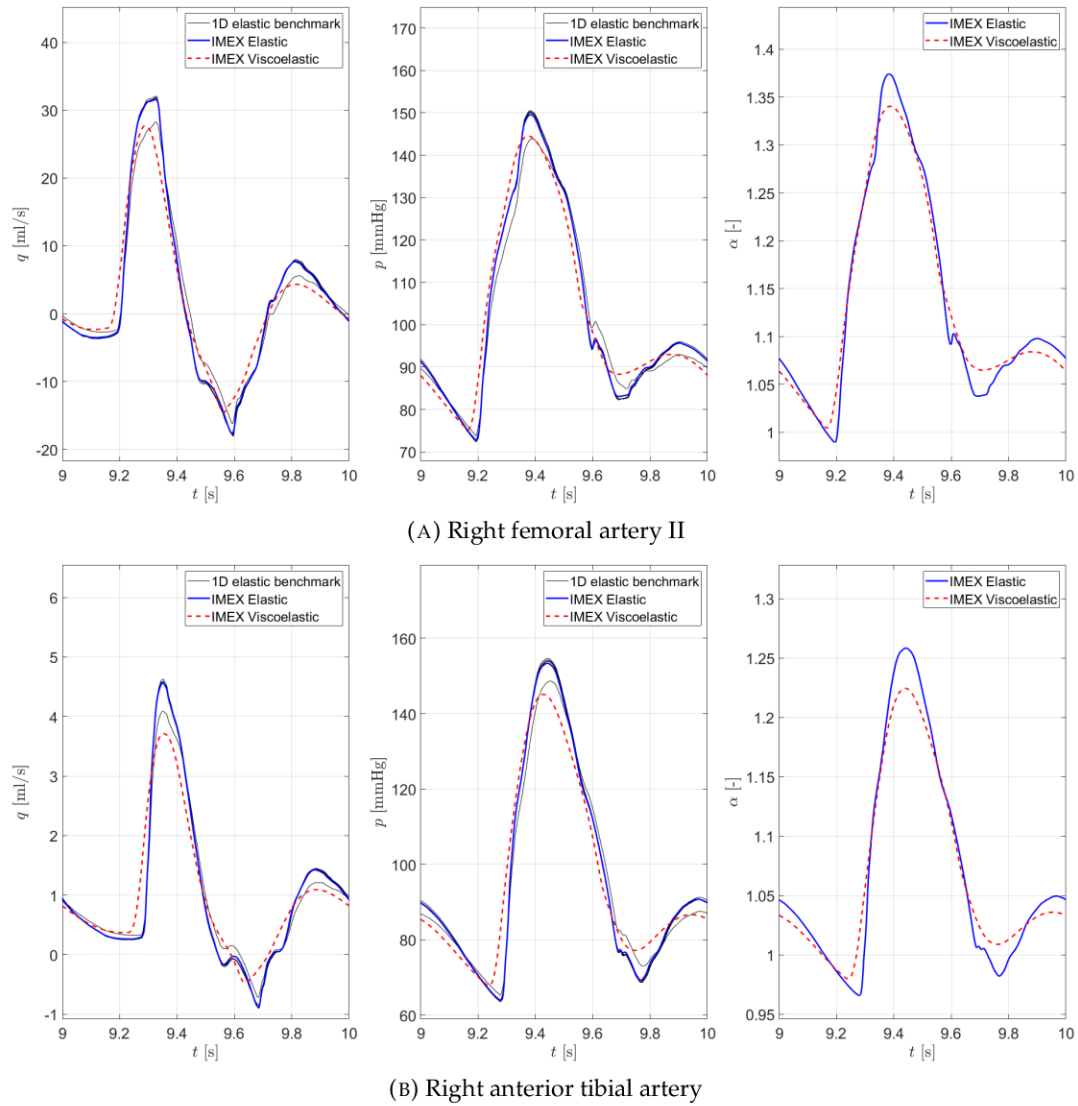


FIGURE 4.17: Results of the ADAN56 network for 2 selected arteries. Results are obtained with the IMEX RK FV scheme considering both the elastic and the viscoelastic tube law to characterize the mechanical behaviour of vessel walls. Comparison with six different 1-D elastic benchmark solutions (Boileau et al., 2015) are presented in terms of flow rate (left column) and pressure (central column), while for the dimensionless cross-sectional area (right column) reference results are not available.

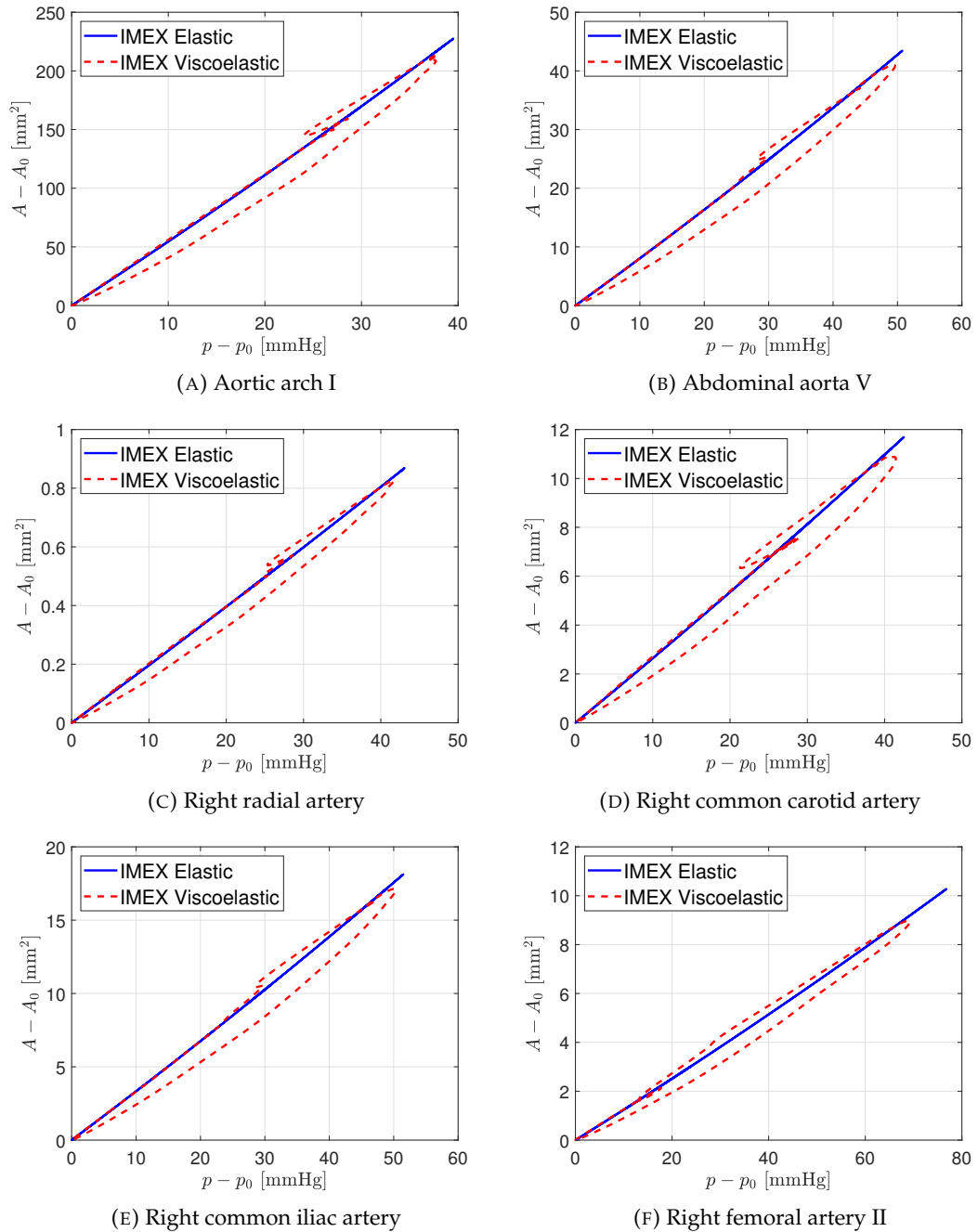


FIGURE 4.18: Hysteresis loop obtained for various arteries in the ADAN56 network. The elastic lines confirms the absence of dissipative effects, in contrast with the wide viscoelastic curves that shows energy dissipation. In the latter, the curve evolves counterclockwise, showing the characteristic feature connected to the dirotic notch. A_0 and p_0 are the equilibrium cross-sectional area and pressure, respectively, whose value coincides with that of the diastolic phase.

Chapter 5

The effect of cardiac properties on arterial pulse waves

5.1 Introduction

This study investigates the effects of cardiac properties variability on arterial pulse wave morphology using blood flow modelling and pulse wave analysis, the background of which is given in Chapter 2. The complete cardiovascular model presented in Chapter 4, inclusive of the lumped-parameter model of the left part of the heart coupled to the one-dimensional model of the arterial network (Figure 4.1), is used to carry out the analysis presented in this Chapter.

Section 5.2 presents a computation proof-of-concept to identify the effect of cardiac properties on arterial pulse waves. At first, the cardiovascular model is validated using reference pulse waveforms in turn verified by comparison with *in vivo* measurements. This validation is specifically designed to verify the performance of the model in returning physiological pulse waves for assigned cardiac properties. Then, a sensitivity analysis is performed to assess the effects of variations in cardiac parameters on central and peripheral pulse waveforms. Results showed that left ventricular contractility, stroke volume, cardiac cycle duration, and heart valves impairment are determinants of central waveforms morphology, pulse pressure and its amplification. Contractility of the left atrium has negligible effects on arterial pulse waves. Results also suggested that it may be possible to infer left ventricular dysfunction by analysing the timing of the dicrotic notch and cardiac function by analysing PPG signals. This study aims at identifying cardiac properties that may be extracted from *in vivo* central and peripheral pulse waves to assess cardiac function.

Section 5.3 is conceived as the natural prosecution of the analysis in Section 5.2, with direct application to hypertension. In particular, this Chapter addresses the study of isolate systolic hypertension and its haemodynamic fundamentals. Peripheral wave reflections and arterial stiffening have been considered the major determinants of raised pulse pressure and isolate systolic hypertension, but recently the importance of ventricular ejection dynamics is also recognised. The analysis is conducted by examining the contributions of aortic compliance and ventricular contractility to variations in aortic flow and increased central and peripheral pulse pressure, and pulse pressure amplification (PPa) in normotensive subjects during pharmacological modulation of physiology, in hypertensive subjects, and *in silico* using the cardiovascular model accounting for ventricular-aortic coupling. Moreover, reflections at the aortic root and from downstream vessels are quantified using emission and reflection coefficients, respectively. Results showed that cPP is strongly associated with contractility and compliance, whereas pPP and PPa are strongly associated with contractility only. Increased contractility by inotropic stimulation raises peak

aortic flow (323.9 ± 52.8 vs 389.1 ± 65.1 ml/s), and the rates of increase (3193.6 ± 793.0 vs 4848.3 ± 450.4 ml/s²) and decrease (1433.6 ± 235.8 vs 2020.0 ± 404.8 ml/s²) in aortic flow, leading to larger cPP (36.1 ± 8.8 vs 59.0 ± 10.8 mmHg), pPP (56.9 ± 13.1 vs 93.0 ± 17.0 mmHg) and PPa (20.8 ± 4.8 vs 34.0 ± 7.3 mmHg). Increased compliance by vasodilation decreases cPP (62.2 ± 20.2 vs 45.2 ± 17.8 mmHg) without altering pPP or PPa. The emission coefficient changes with increasing cPP, but the reflection coefficient do not. These results agrees with *in silico* data obtained by independently changing contractility/compliance over the *in vivo* pathophysiological ranges. This study highlights the key role that ventricular ejection dynamics plays in raising and amplifying PP, by altering aortic flow wave morphology. The diagnosis and treatment of hypertension may therefore improve by targeting systolic ejection patterns.

5.2 Cardiac function assessment using the pulse wave analysis

Pathologies affecting cardiac function are responsible for morbidity and mortality worldwide (Gaddum et al., 2017). Cardiac haemodynamics properties are of paramount importance for the assessment of cardiac function and, hence, cardiovascular risk. Some cardiac properties are assessed invasively. For example, left ventricular filling pressure – which is used to assess left ventricular function – can be measured directly by placing a catheter in the proximal aorta or the left ventricle, or indirectly from the pulmonary artery (Sharma et al., 2002; Reddy and Nishimura, 2021). This is an expensive and time-consuming procedure that carries risk to patients (e.g., blood clot formation and embolization) due to its invasive nature, even when performed in specialized centres (McEniery et al., 2014).

An indirect estimation of cardiac properties by pulse wave analysis may overcome these obstacles. Currently, pulse wave analysis is usually employed to obtain information on vascular properties, such as arterial stiffness (Mynard et al., 2020), but it has the potential to provide information on cardiac function, since changes in cardiac properties affect the morphology of pulse wave signals measured in the vasculature (Huttunen et al., 2020). Nowadays, pulse waves can be acquired non-invasively by wearable devices which are more convenient and less expensive for large-scale screening than invasive exams. In particular, the PPG pulse wave is easily acquired using pulse oximeters, which are frequently used in healthcare settings to measure arterial blood oxygen saturation and pulse rate. PPG signals can also be acquired by devices available to the wider population, such as smartwatches and fitness bands (Wang et al., 2021; Elgendi, 2020).

Databases of *in silico* pulse waves signals representative of cohorts of real subjects can be produced using robust and efficient computational blood flow models for the development and pre-clinical testing of pulse wave analysis algorithms (Ambrosi, Quarteroni, and Rozza, 2012; Willemet, Vennin, and Alastruey, 2016). Virtual subjects are characterised by haemodynamic variables spanning the physiological range, even in disease-related conditions (Jin and Alastruey, 2021; Reymond et al., 2009). Different numerical models can be employed to accomplish this task: 0-D lumped-parameters models for simulating blood flow in distal vessels (Arts et al., 2005; Le Gall et al., 2020; Charlton et al., 2019) and specific organs such as the heart (Mynard, 2011), 1-D models for simulating blood flow in the large arteries of the human circulation (Müller et al., 2016; Piccioli et al., 2022a), and three-dimensional (3-D) models (Jin and Alastruey, 2021), whose use is limited to the simulation of

blood flow in localised regions of the vasculature due to their high computational cost. 1-D models can simulate pulse wave signals with a reasonable accuracy compared with both 3-D models (Xiao, Alastruey, and Figueroa, 2014; Jin and Alastruey, 2021) and experimental data (Matthys et al., 2007), and at much lower computational cost compared to 3-D models. They have, therefore, been used to generate databases of pulse waves for thousands of virtual subjects.

The aim of this study is to investigate the effect of cardiac properties on pulse wave morphology using the 1-D model of the arterial vasculature (Piccioli et al., 2022a) coupled to the 0-D model of cardiac contraction, as outlined in Chapter 4. Previous studies have simulated the ventricular–arterial coupling in 1-D modelling, such as the pioneering work of Formaggia et al. (2006), and, more recently, Liang et al. (2009), however they aimed to infer the effect of arterial changes caused by ageing on cardiac dynamics. The ability of the cardiovascular model to describe physiological pulse waves for assigned cardiac properties is verified using reference pulse waveforms (Mynard and Smolich, 2015; Charlton et al., 2019). A sensitivity analysis (SA) is then performed to study the effect of all cardiac model parameters on central and peripheral pulse waveforms, including the PPG signal in the digital artery, so that the perspective of the problem analysed in Formaggia et al. (2006) and Liang et al. (2009) is reversed.

5.2.1 Methods

Cardiovascular model

The 1-D model vascular network is modelled using the a-FSI system (Bertaglia, Caleffi, and Valiani, 2020; Bertaglia et al., 2020; Bertaglia et al., 2021). Details on the mathematical model of the cardiovascular network and the numerical scheme for space and time integration are exhaustively introduced in chapters 3 and 4. For the analysis conducted in this Chapter, key assumptions for the haemodynamic model are: laminar flow, incompressible and Newtonian fluid (blood density, $\rho = 1060 \text{ kg/m}^3$; blood viscosity, $\mu = 2.5 \text{ mPa s}$), and no energy losses at bifurcations. For the geometrical and mechanical characteristics of the network the reader is referred to Charlton et al. (2019).

Significant parameters evaluation

Given the wealth of parameters involved in the cardiovascular model, a sensitivity analysis is performed to identify those parameters that most affect blood pressure waveforms, labelled hereafter as *significant*. This Section presents the cardiovascular parameters varied in the sensitivity analysis and describes how the significant parameters are identified, whereas the following section introduces the haemodynamic indices studied in the sensitivity analysis.

The parameters defining the cardiovascular model are separated into vascular and cardiac, as indicated in Table 5.1. The former refer to geometrical and mechanical parameters of the arterial tree, including the RCR parameters of terminal branches. Vascular parameters are taken from Charlton et al. (2019). The cardiac parameters are those of the cardiac contraction model. V_{net} and T are also taken from Charlton et al. (2019). The parameters defining chamber elastance and valve dynamics are set in accordance with Mynard and Smolich (2015). Their reference values are listed in Appendix C.1.

TABLE 5.1: Vascular (VV) and cardiac (CC) parameters of the numerical model. VV parameters: vessel length (L), proximal and distal vessel radius (r_{in} and r_{out} , resp.), vessel stiffness (Eh , where E is the Young's modulus and h is vessel thickness) computed via Eq. (2) in (Charlton et al., 2019), reference pressure (p_{ref}), RCR outlet pressure (p_{out}), and RCR resistances and compliance (R_1 , R_2 , C , resp.). CC parameters: total volume entering the LA in one cardiac cycle (V_{net}), cardiac cycle duration (T), minimal and maximal elastance (E_{min} and E_{max} , resp.), shape and time parameters ($m_{1,2}$ and $\tau_{1,2}$, resp.), source resistance (K_s), unstressed and initial volumes (v_{p0} and v_0 , resp.) and onset time of the elastance function (t_{onset}); minimum and maximum valve orifice areas (A_{min} and A_{max} , resp.), valve opening and closure constants (K_{v0} and K_{vc} , resp.), and valve length (l). Subscripts c and v refer to chamber and valve, respectively.

VV	L [m]	r_{in}, r_{out} [m]	Eh [Pa m]	p_{ref} [Pa]	p_{ext} [Pa]
	p_{out} [Pa]	R_1 [Pa s/m ³]	R_2 [Pa s/m ³]	C [m ³ /Pa]	
CC	V_{net} [m ³]	$E_{min,c}$ [Pa/m ³]	$m_{1,c}$ [-], $\tau_{1,c}$ [s]	$v_{p0,c}$ [m ³]	$K_{s,c}$ [s/m ³]
	T [s]	$E_{max,c}$ [Pa/m ³]	$m_{2,c}$ [-], $\tau_{2,c}$ [s]	$v_{0,c}$ [m ³]	$t_{onset,c}$ [s]
	$A_{min,v}$ [m ²]	$K_{v0,v}$ [1/Pa s]	l_v [m]		
	$A_{max,v}$ [m ²]	$K_{vc,v}$ [1/Pa s]			

The sensitivity analysis focuses on the cardiac parameters, since a sensitivity analysis for the vascular parameters has been performed by Charlton et al. (2019).

Sensitivity analysis is performed by varying the cardiac parameters listed in Table 5.1 from their reference values in a univariate manner, i.e., when a parameter is varied, all others remain unchanged. Reference values of heart chamber and valve parameters are listed in Tables C.1 and C.2, respectively. Variations are performed by increasing and decreasing each reference value by a percentage change that depends on the cardiac parameter considered:

- Cardiac parameters, excluding V_{net} , T , and minimum and maximum valves areas, are varied by $\pm 50\%$ from the reference value. Given the lack of baseline physiological variations of these modelling parameters in the literature, a $\pm 50\%$ is chosen to investigate the effect of these parameters on pulse wave morphology. The resulting variations in left ventricular contractility are generally within the physiological range for different clinical scenarios (Mynard and Nithiarasu, 2008), as shown in Section 5.2.2.
- The minimum orifice area of the aortic and mitral valves have a zero reference value, standing for a complete valve closure. Simulations for increased $A_{min,AV}$ and $A_{min,MV}$ are obtained by setting their values to 30 mm², corresponding to a severe aortic regurgitant orifice area (Steeds and Myerson, 2020), and to a severe mitral regurgitation (Carabello, 2001). Decreased values have no physical meaning and were not considered. The maximum orifice areas of the aortic and mitral valves, $A_{max,AV}$ and $A_{max,MV}$ respectively, are decreased to simulate severe stenosis scenarios by setting their values to 1 cm² (Baumgartner et al., 2009). Increased values are obtained increasing their reference value by 50%.
- The total volume entering the network in one cardiac cycle, V_{net} , and cardiac cycle duration, T , are varied as described by Charlton et al. (2019). Maximum and minimum values for both parameters are identified in Charlton's

database. The positive and negative percentage variations from their reference value have been calculated, and the greatest variation in absolute value has been used in the SA. As a result, V_{net} varies by $\pm 40\%$, and T by $\pm 20\%$. The same percentage changes are used for positive and negative variations to avoid SA asymmetry.

Sensitivity analysis simulations are compared in pairs to assess the effect on arterial pressure waveforms of changes in cardiac parameters: (i) *baseline* simulation and (ii) *increased* or *decreased* parameter, respectively. This comparison is made for each parameter at the aortic root, brachial artery, and digital artery. The root mean square deviation (RMSD) is calculated for each pair. RMSDs are found to increase towards the periphery, therefore, the cardiac parameters giving an RMSD in the digital artery above the assigned threshold of 6.5 mmHg are labelled as significant.

Haemodynamic indices

Eleven haemodynamic indices are used in a second sensitivity analysis involving those cardiac parameters identified as significant in Section 5.2.1.

The following four indices of central haemodynamics are considered. Left ventricular contractility, quantified by the contractility index (CI), is the maximum rate of increase in left ventricular pressure during isovolumetric contraction, $dp_{LV}/dt|_{\max}$ (Mynard and Nithiarasu, 2008; Chengode, 2016). The rate of increase in flow rate and pressure at the aortic root in early systole, $\Delta q/\Delta t$ and $\Delta p/\Delta t$, respectively. Δq is calculated as the difference between the peak flow rate, q_{\max} , and the flow rate at the foot of the waveform, q_{\min} , i.e., when the aortic valve opens. Δp is the pulse pressure (Li et al., 2021). Δt is the time interval in-between the occurrences of either q_{\min} and q_{\max} or DBP and SBP. Finally, the maximum rate of decrease of late-systolic flow at the aortic root, $dq/dt|_{\min, AoRt}$, as described in Flores Gerónimo et al. (Flores Gerónimo et al., 2021).

The following four indices of cardiac function are considered: left ventricular ejection time (LVET), stroke volume, left ventricular ejection fraction (EF), and cardiac output. LVET is the time interval between opening and closing of the aortic valve. SV is the difference between simulated left ventricular end-diastolic volume and end-systolic volume. EF is the ratio of SV to EDV. Lastly, CO is equal to $SV \times 60/T$.

The following three vascular indices are considered: PP at a central (aortic root) and peripheral (digital) site, PP_{AoRt} and PP_{Di} respectively, and the PP augmentation ratio ($AR_{AoRt-Di}$) calculated as the percentage increase in PP between the two sites.

5.2.2 Results

Cardiovascular model verification

The vascular network model has been thoroughly tested in previous studies (Bertaglia, Caleffi, and Valiani, 2020; Bertaglia et al., 2020; Piccioli et al., 2022a) and in Chapter 4 of this Thesis. This Section focuses on verifying the ability of the cardiac contractility model coupled to the vascular network model to produce physiological haemodynamics signals. Figure 5.1 compares simulated haemodynamics signals with reference *in silico* data, taken from Mynard and Smolich (2015) and Charlton et al. (2019) in the heart and vasculature, respectively. These reference data are validated against *in vivo* measurements. Since the reference cardiac and vascular models have different cardiac outputs, the cardiac output of the reference vascular model is

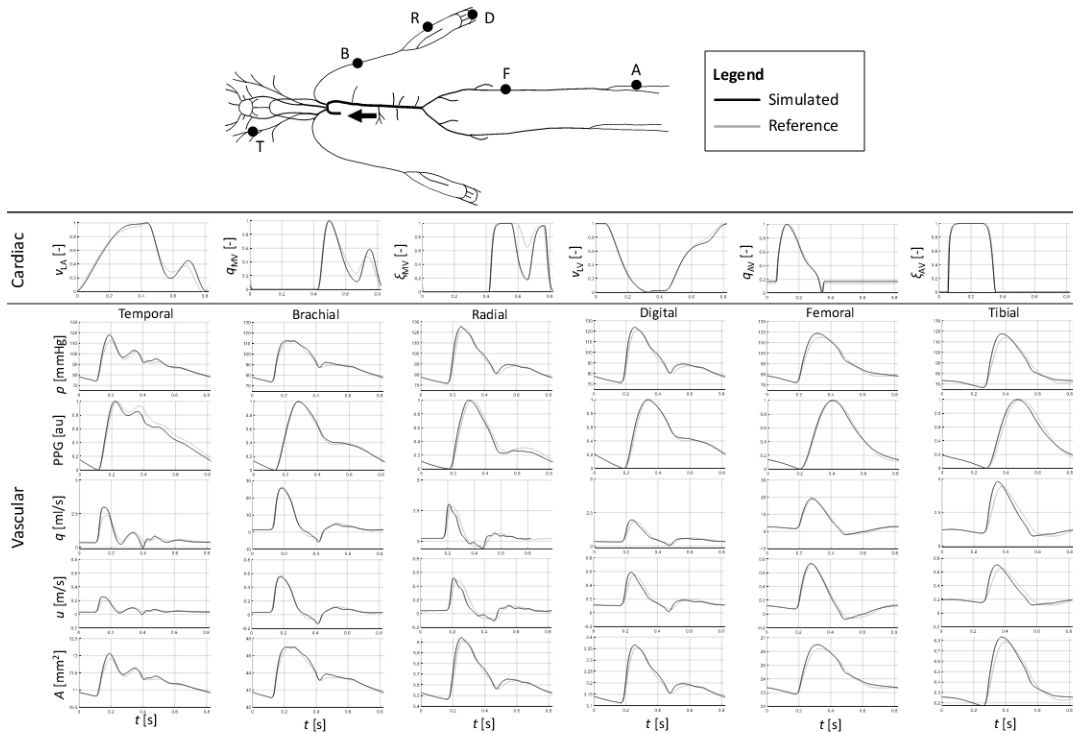


FIGURE 5.1: Haemodynamic results of the cardiovascular model. Simulated waveforms are in black solid lines, reference waveforms are in grey solid lines. Cardiac and vascular reference signals were taken from Mynard and Smolich (2015) and Charlton et al. (2019), respectively. Cardiac signals are volume in the left atrium (v_{LA}), flow rate through the mitral valve (q_{MV}), state of the mitral valve (ζ_{MV}), volume in the left ventricle (v_{LV}), flow rate through the aortic valve (q_{AV}), state of the aortic valve (ζ_{AV}), normalised to compare reference and simulated signals. Vascular signals are internal pressure ($p(t)$), PPG signal, flow rate ($q(t)$), flow velocity ($u(t)$), and luminal cross-sectional area ($A(t)$), in the temporal, brachial, radial, digital, femoral, and tibial arteries, as indicated by the labels in the sketch on the top.

used to assess the accuracy of our model. Therefore, to qualitatively compare simulated cardiac waveforms with the corresponding reference waveforms, both reference and simulated cardiac signals are normalised. The new model replicates well the morphology of all cardiac signals. The mitral trans-valvular flow rate presents its characteristic double-peaked morphology (Luisada et al., 1975; Seo and Mittal, 2013), with the E/A ratio equal to 1.7, consistently with literature values (Sun et al., 1995; Mynard and Smolich, 2015). Furthermore, the state of the aortic valve variable shows a clear distinction between the LV ejection phase when the valve is open and the LV filling phase when it is closed. These results corroborate the ability of the cardiac contraction model to accurately simulate cardiac haemodynamics.

Figure 5.1 shows pulse wave signals (flow rate, flow velocity, luminal cross-sectional area, pressure, and PPG, calculated as shown in Appendix B at six arterial sites: the temporal artery in the head, three peripheral sites in the arm, namely the brachial, radial, and digital arteries, and two in the leg, the femoral and the anterior tibial arteries. Reference and simulated waveforms are in excellent agreement, with percentage relative RMSDs smaller than 1% for all signals and sites, relative to reference signals.

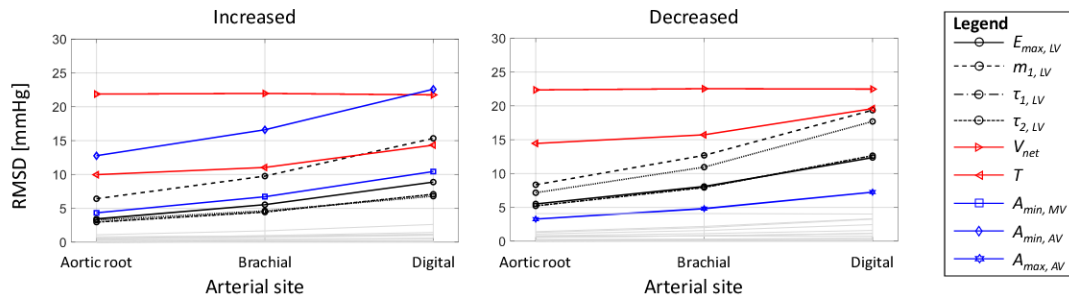


FIGURE 5.2: RMSDs computed at the aortic root, brachial and digital arteries for simulations with the increased (left) and decreased (right) cardiac parameters values. Significant parameters are divided in parameters of left ventricular contractility (black lines), V_{net} and T (red lines), and heart valve-related parameters (blue lines). Grey lines represent all non-significant parameters.

Significant cardiac parameters

RMSDs increase towards the periphery of the vascular network (Figure 5.2), where the threshold of significant cardiac parameter is imposed, i.e., at the digital site. The resulting significant cardiac parameters are found to be the same for both scenarios in which cardiac parameters are either increased or decreased from their baseline values. These are parameters mainly attributed to left ventricular contractility: the maximal elastance, $E_{max,LV}$, the contraction shape parameter $m_{1,LV}$, and the contraction and relaxation time parameters, $\tau_{1,LV}$ and $\tau_{2,LV}$, respectively. The other significant parameters are the minimum orifice area of the valves, $A_{min,AV}$ and $A_{min,MV}$, the maximum orifice area of the aortic valve, $A_{max,AV}$, in the stenotic scenario, the total volume entering the LA in one cardiac cycle, V_{net} , and the cardiac cycle duration, T . No cardiac parameters of LA contractility are found to be significant.

Figure 5.3 shows pulse waveforms both in central and peripheral sites at baseline and with individual variations in the significant cardiac parameters. Changes in wave morphology occur mainly in systole. LV-related parameters produce minor changes in wave morphology in diastole. The timing of the dicrotic notch only changes when $\tau_{2,LV}$ is varied, since this cardiac parameter regulates the timing of the relaxation phase of left ventricular contractility. With increasing $\tau_{2,LV}$ the relaxation phase of the LV is delayed and, hence, the aortic valve closes later, delaying the time of the dicrotic notch.

Regurgitant valve scenarios show significant variations in pulse wave morphology. With increasing $A_{min,AV}$ the flow rate at the aortic root becomes negative in diastole due to the reflux caused by the suction effect of the LV during relaxation. Consequently, arterial diastolic pressure decreases. These results suggest that impairment of the AV has direct effects on arterial pulse waves, both at central and peripheral sites. With increasing $A_{min,MV}$ the late-systolic decrease in flow rate occurs more rapidly than in the case of a healthy valve. During left ventricular contraction, blood volume is not only ejected in the vascular network through the aortic valve, but part of it is also re-ejected in the left atrium through the leaking mitral valve. Pressures in the network with regurgitant MV changes less significantly than the AV regurgitation case due to the mitigating function of the left ventricle and the proper action of the aortic valve. Significant variations in wave morphologies are also observed with severe aortic stenosis. With decreased $A_{max,AV}$ the flow rate at the aortic root

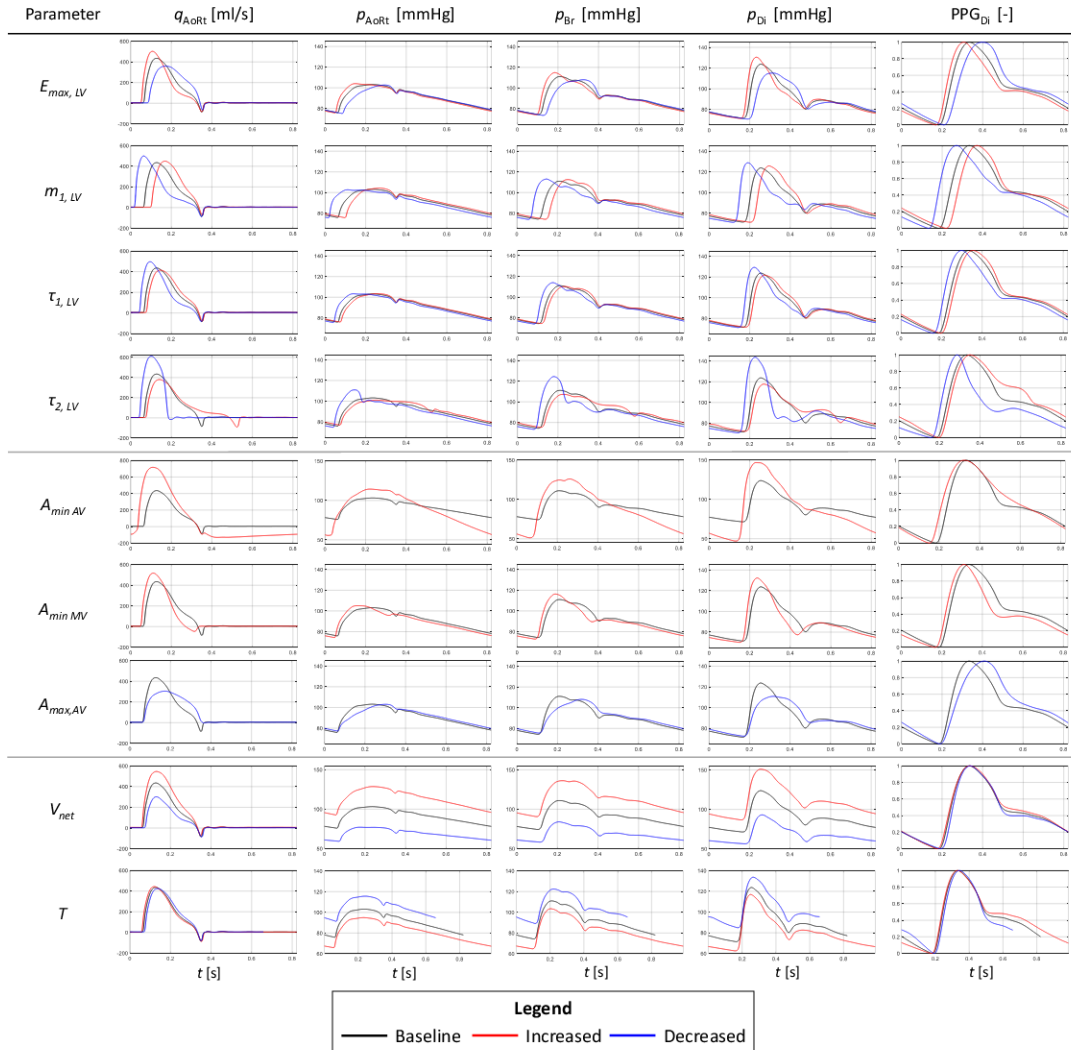


FIGURE 5.3: Pulse waveforms at baseline (black), and with increased (red) and decreased (blue) values in the significant cardiac parameters. The following waveforms are shown: flow rate at the aortic root (q_{AoRt}), pressure at the aortic root (p_{AoRt}), pressure in the brachial artery (p_{Br}), and pressure (p_{Di}) and PPG signal (PPG_{Di}) in the digital artery. Each row represents simulations for a significant cardiac parameter: left ventricular (LV) maximal elastance ($E_{max,LV}$), LV contraction shape parameter ($m_{1,LV}$), LV contraction time parameter ($\tau_{1,LV}$), LV relaxation time parameter ($\tau_{2,LV}$), aortic valve minimum orifice area ($A_{min,AV}$), mitral valve minimum orifice area ($A_{min,MV}$), aortic valve maximum orifice area ($A_{max,AV}$), total volume entering the left atrium in one cardiac cycle (V_{net}), and cardiac cycle duration (T).

becomes more smoothed and with lower peak. In all vascular sites, the rate of increase in early-systolic BP is less steep, with a consequent decrease in PP becoming more evident at the digital site.

Cardiac function, in particular left ventricular contractility, influence PPG morphology, altering shape features of PPG signals that are frequently used to extract physiological information. Variations in PPG signals follow those in digital pressure. The timing of contraction greatly affects the diastolic decay of the PPG signal, as it is with a varied $\tau_{2,LV}$. With a regurgitant aortic valve, the PPG signal shows a

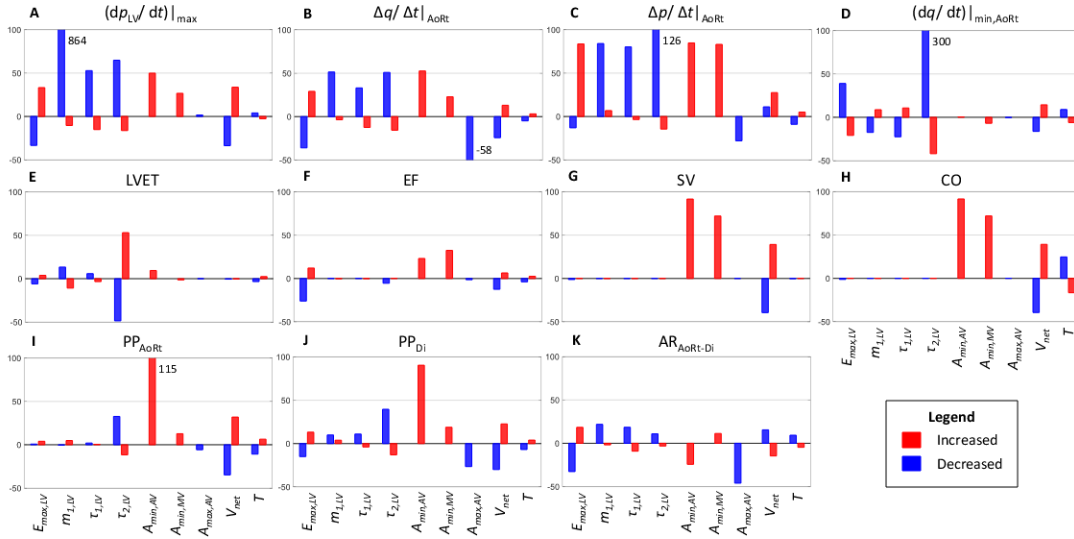


FIGURE 5.4: Percentage variations in haemodynamic indices with increased (red) and decreased (blue) values in the significant cardiac parameters. Y-axis show percentage variations in the indices from their corresponding baseline values. Baseline values: contractility index ($dp_{LV}/dt|_{max}$), 13.96×10^2 mmHg/s; rate of increase in flow rate in early-systole at the aortic root ($\Delta q/\Delta t|_{AoRt}$), 6.45×10^3 ml/s²; rate of increase in pressure in early-systole at the aortic root ($\Delta p/\Delta t|_{AoRt}$), 1.47×10^2 mmHg/s; maximum rate of decrease of late-systolic flow rate at the aortic root ($dq/dt|_{min,AoRt}$), 2.42×10^3 ml/s²; left ventricular ejection time (LVET), 324 ms; ejection fraction (EF), 58 %; stroke volume (SV), 66.4 ml; cardiac output (CO), 4.8 l/min; pulse pressure at the aortic root (PP_{AoRt}), 27.3 mmHg; pulse pressure in the digital artery (PP_{Di}), 52.3 mmHg; and pulse pressure augmentation ratio between the aortic root and the digital artery ($AR_{AoRt-Di}$), 91.8 %.

smoother shape and the dicrotic notch is less evident, consequently to the greater volume ejected in the arterial network during systole. Nonetheless, the diastolic decay replicates well the one of the reference signal. With a stenotic aortic valve the systolic peak of the signal is retarded. Interestingly, in the case of V_{net} variations, PPG pulse waves remain unaltered due to the nearly linear relationship between volume in the network and internal pressure: when only V_{net} varies, the pressure amplitude changes but not the pressure wave morphology.

Haemodynamic indices

Figure 5.4 summarises the percentage variations in haemodynamic indices with changes in significant cardiac parameters. The reference CI ($dp_{LV}/dt|_{max}$) is 13.96×10^2 mmHg/s in agreement with literature data (Mynard and Nithiarasu, 2008; Chenguode, 2016). The observed variations in CI are consistent with physiologic percentage variations in which CI increased by 133% during exercise and decreased by 47% with cardiomyopathy (Mynard and Nithiarasu, 2008). Most of the variations reported in Figure 5.4 A are within this range. CI increases with increasing $E_{max,LV}$ and decreasing $m_{1,LV}$, $\tau_{1,LV}$, and $\tau_{2,LV}$. The most significant variation in CI occur with the decreasing shape parameter $m_{1,LV}$, which defines the slope of the increasing part of the chamber elastance curve. A smaller $m_{1,LV}$ makes the slope steeper raising the rate of increase in p_{LV} . Regurgitant valves and V_{net} cause an increase in CI, whereas T and $A_{max,LV}$ lead to negligible effects on CI. $\Delta q/\Delta t$ and $\Delta p/\Delta t$ at the

aortic root vary similarly to variations in CI, although at different rates (Figure 5.4 B and C). The variations in $\Delta q/\Delta t$ and $\Delta p/\Delta t$ observed with stenotic aortic valve confirm the variations in flow rate and BP waveforms observed in Figure 5.3. The relation between increased left ventricular contractility and aortic root pulse wave morphology produced by our model is consistent with Li et al. (2021). The variations in $\Delta q/\Delta t$ and $\Delta p/\Delta t$ follow the same trend as those in PP_{Di} (Figure 5.4 J), in agreement with the morphology of the central pressure wave being a major determinant of peripheral SBP and correlating with the rate of increase in early-systolic aortic flow (Li et al., 2021; Flores Gerónimo et al., 2021). Moreover, the maximum rate of decrease in late-systolic flow at the aortic root, $dq/dt|_{\min, AoRt}$ in Figure 5.4 D, increases with increasing V_{net} , and decreasing T and LVET, in agreement with Flores Gerónimo et al. (2021).

As for LV properties, both EF and LVET are affected by changes in left ventricular contractility, as shown in Figure 5.4 E and F. EF also increases with regurgitant valves and increasing V_{net} and T . The variation in LVET becomes significant when $\tau_{2,LV}$ is varied: it decreases by -48% with decreasing $\tau_{2,LV}$ and increases by $+52\%$ with increasing $\tau_{2,LV}$. This result is consistent with the physical meaning of the contraction and relaxation time parameters. These influence the time of occurrence of the respective sections of the elastance curve: a decrease in $\tau_{1,LV}$ anticipates contraction and an increase in $\tau_{2,LV}$ delays relaxation, and vice-versa. In the case of AV regurgitation, LVET is the time interval when the area of the AV is greater than its minimum value. SV is not affected by the four cardiac parameters related to left ventricular contractility (Figure 5.4 G), since V_{net} does not change. A significant increase in SV can be observed with simulated valve regurgitant scenarios, of $+92\%$ and $+72\%$ for the AV and MV, respectively. When the AV does not close completely, part of the volume ejected during the contraction returns into the ventricle during relaxation, as pointed out in Section 5.2.2. This causes both the LV end-diastolic and end-systolic volumes to increase, with a greater increase in the former than the latter, thus resulting in an overall increase in SV. Similarly, the LV ejects blood volume through both valves when the MV is impaired. Thus, the LV end-systolic volume decreases and the end-diastolic volume increases. The stenotic aortic valve scenario does not affect significantly LV end-diastolic and end-systolic volumes, hence, SV does not vary. The aortic stenosis causes a slower ejection of the blood volume. Variations in V_{net} cause SV to change symmetrically from the baseline value, demonstrating that, barring leaking valve scenarios, V_{net} is a surrogate of stroke volume. As expected, CO in Figure 5.4 H changes consistently with SV and T , most significantly influenced by the former.

The pulse pressure shows less variation in central sites compared to the periphery (Figure 5.4 I and J). PP increases with increasing left ventricular contractility, i.e., higher peak and rate of increase in elastance. Both central and peripheral PP increase with shortened LVET, observable from variations in $\tau_{2,LV}$. Regurgitant valves and increased V_{net} and T also raise PP, which instead decreases with severe aortic stenosis. Greater contractility augments $AR_{AoRt-Di}$ (Figure 5.4 K), hence enhancing the physiological effect of PP amplification towards peripheral sites (Charlton et al., 2019; Li et al., 2021). $AR_{AoRt-Di}$ decreases with regurgitant AV, caused by the greater increase in PP_{AoRt} compared to PP_{Di} from their baseline values.

5.2.3 Discussion

The analysis presented in Section 5.2 has studied the relationship between cardiac properties and vascular haemodynamics using a state-of-the-art 0-D model

properly coupled to a vascular 1-D model by treating the 0-D model with the IMEX-RK SSP scheme for the time discretisation, consistently with the 1-D model. It has been demonstrated that the presented cardiovascular model correctly reproduces human haemodynamics, consistent with *in vivo* measurements. The sensitivity analysis has shown that variations in cardiac properties are associated with identifiable variations in waveform morphology, suggesting the possibility of applying techniques for inverse problem solving, going from a specific pressure waveform to the changes in cardiac characteristics that generated it. Moreover, LA contractility has negligible effects on vascular pulse waves, suggesting that LA properties can not be derived from a pulse wave analysis. At baseline values, $E_{max,LA}$ is equal to 0.13 mmHg/ml, whereas $E_{max,LV}$ is equal to 2.8 mmHg/ml, producing peak LA and LV pressures of 8 mmHg and 103 mmHg, respectively. Thus, even the variations in LA contractility parameters fail to produce significant changes in LA pressure sufficient to affect vascular haemodynamics. In contrast, left ventricular contractility, stroke volume, cardiac cycle duration, and impaired valves function have a considerable influence on arterial pulse waves, being determinants of central waveforms morphology, pulse pressure and its amplification. The greatest variations in PP were found at peripheral sites rather than central sites, which may be more valuable sites for extracting information about cardiac function by pulse wave analysis. Furthermore, our results have corroborated the findings of previous studies showing strong correlations between left ventricular contractility, aortic blood flow and PP (Flores Gerónimo et al., 2021; Li et al., 2021; Pagoulatou et al., 2021), and the crucial role of cardiac function in both central and peripheral pressure amplitudes (Gaddum et al., 2017; Vennin et al., 2017).

Our results have shown that left ventricular contractility, measured by CI, is related to peak elastance, $E_{max,LV}$, rate of LV contraction, and LVET. An increase in $E_{max,LV}$ allows the LV pressure to reach higher values, as $E_{max,LV}$ and LV pressure are directly related through the strain–stress relationship of the cardiac chamber. CI increases with a faster contraction simulated by decreased $m_{1,LV}$, and time parameters. As $\tau_{1,LV}$ decreases, LV pressure increases more rapidly, and so does pressure and flow rate at the aortic root. Moreover, the decrease in $\tau_{2,LV}$ results in a shortening of LVET, leading to the same SV being ejected in a shorter time interval, making the ejection more impulsive. The increase in contractility correlates with the increase in the PP augmentation ratio, i.e., PP increases more in the periphery than centrally (Figure 5.4 A and K). Furthermore, increased CI is associated with greater SBP peaks in the waveforms (see Figure 5.3). This phenomenon is generally more pronounced towards the periphery, and is evident in the case of decreased $\tau_{2,LV}$. The total blood volume entering the network in one cardiac cycle, V_{net} , and cardiac cycle duration, T , both affect blood pressure in the vascular network. With increasing V_{net} and T , PP increases at both the central and peripheral sites, but the PP augmentation ratio decreases from the baseline simulation. Results have shown that valve impairment affects pulse waves, particularly in the case of a regurgitant and stenotic AV due to its direct coupling with the vascular network. With aortic regurgitation, central PP increases more than peripheral PP due to the increased SV. Central arteries have greater compliance than peripheral ones, hence they undergo a greater cross-sectional area dilation and, so, greater increase in PP. With aortic stenosis there is no variation in SV, and PP changes more significantly in the peripheral site. Further research is needed to investigate the correlation between valve disease and peripheral pressure in a large cohort of *in vivo* subjects with valve dysfunction via noninvasive measurements of peripheral BP.

Some aspects of our cardiovascular model should be underlined. Firstly, some cardiac parameters that characterise the left ventricular contractility and describe the elastance function cannot be measured directly. Therefore, it is cumbersome to define a physiological range of values for these parameters. Secondly, cardiac parameters affect vascular haemodynamics independently of each other, enabling the study of the effect on pulse wave morphology of independent changes in cardiac properties. This is not the case *in vivo*, where it would be challenging to change left ventricular contractility, for example through pharmacological intervention, without affecting the properties of the vasculature, and vice-versa. Finally, an open-loop model has been used and, thus, some parameters must be imposed, e.g. V_{net} , de facto imposing the venous return. This is numerically implemented through the parametrisation of the pulmonary venous flow rate entering the LA. Physiologically, an impaired LV function can affect the venous return, but this cause-effect phenomenon cannot be regarded in an open-loop cardiovascular model. To overcome this limitation, a decreased venous return is included in the sensitivity analysis through a variation in V_{net} . Therefore, the open-loop model does not weaken the results presented. The implementation of a closed-loop will be object of future work.

This work suggests that it may be possible to infer LV dysfunction, such as an impaired relaxation phase, by analysing the timing of the dicrotic notch. Results show that the time of diastole of the pulse waveform only varies with the relaxation time parameter of the LV elastance function, but is not affected by other cardiac parameters. This study also offers valuable insight into in the field of hypertension. Lately, the importance of left ventricular contractility in hypertension has been studied, showing that LV function is a major determinant of blood pressure elevation (Gaddum et al., 2017; Vennin et al., 2017; Li et al., 2017; Flores Gerónimo et al., 2021; Li et al., 2021). Our results support this thesis, as PP increased with increasing left ventricular contractility without changes in vascular properties. Moreover, hypertension has been found to be related to left ventricular hypertrophy, a response to chronic pressure overload (Segers et al., 2000), and heart valves disease (Pai and Varadarajan, 2010; Bonow, 2013; Mrsic et al., 2018). Assessing cardiac properties by arterial pulse wave analysis may allow cardiac function characterisation without the need for invasive catheterization. Results have shown that alterations in blood pressure waves amplify towards the periphery of the systemic circulation (see the RMSDs trends and variations in PP_{Di} and $AR_{AoRt-Di}$ when significant cardiac parameters were varied). Therefore, easily accessible measurements in peripheral arteries could be employed, such as in the radial artery, or one of its surrogates, the digital artery (Millasseau et al., 2000a).

Finally, results have highlighted the importance of studying PPG signals, as already presented in previous works in which machine learning models were employed to determine haemodynamic properties using pulse waves and PPG data (Elgendi, 2020; Wang et al., 2021). Such models could also be applied to infer cardiac properties from peripheral pressure measurements and PPG signals. Coherently with Charlton et al. (2022), this work suggests that LVET can be detected from PPG signals analysis. The morphology and shape-ratios of these signals are affected by diseased aortic valves. Given the popularity of wearable devices, such as FitBits, smartwatches and oxymetries that are able to measure PPG signals, understanding their correlation with cardiac function could provide consumers with personal tools for monitoring cardiac function.

5.3 Ventricular ejection and pulse pressure

Hypertension, a leading cause of morbidity and mortality in the adult population (Lim et al., 2012), arises in large part from an increase in pulse pressure (Franklin et al., 1997) and is a major risk factor for incident cardiovascular events particularly in older individuals (Franklin et al., 1997). However, the haemodynamic basis of this increase is still debated. Historically, peripheral wave reflections and arterial stiffening have been considered the major determinants of the increase in PP and its amplification from the aorta to the periphery (where it is normally measured) (Safar, Levy, and Struijker-Boudier, 2003; O'Rourke and Nichols, 2005; O'Rourke and Hashimoto, 2007; Hashimoto and Ito, 2010). However, studies from Framingham data have shown that peripheral wave reflections provide a relatively small contribution to age-related changes in central PP and augmentation pressure (Mitchell et al., 2010; Torjesen et al., 2014). By contrast, recent studies have emphasized the potential importance of ventricular ejection dynamics, in combination with arterial stiffening, in determining the central and peripheral blood pressure wave in the first half of systole and in elevating BP with hypertension (Chirinos et al., 2009; Sharman et al., 2009; Schultz et al., 2013; Fok et al., 2014a; Torjesen et al., 2014). In particular, left ventricular contractility, measured as the rate of increase in central BP during early systole (Quinones, Gaasch, and Alexander, 1976), has been identified as a major determinant of aortic flow wave morphology, which in turn is a main determinant of PP (Vennin et al., 2017; Vennin et al., 2021) and PPa (Fok et al., 2014a; Gaddum et al., 2017; Flores Gerónimo et al., 2021). Recently, Pagoulatou et al. (2021) have highlighted a strong relationship between an increase in cardiac contractility alone and changes in central and peripheral pulse phenotypes, manifesting with an increase in the forward pressure wave. Quantification of the relative role of left ventricular contractility and arterial stiffening in increasing central PP and amplifying it to the periphery, as well as understanding the underlying haemodynamic mechanisms, could accelerate developments in clinical diagnosis and treatment of hypertension.

The purpose of the present study is to examine the contributions of left ventricular contractility and arterial stiffness to variations in aortic flow wave morphology and increased PP and PPa, and describe the underlying haemodynamic mechanisms. Both *in vivo* and *in silico* data are used. *In vivo* data are obtained in normotensive and hypertensive subjects; in the former, normal physiology was perturbed using vasoactive drugs with divergent effects on the heart and arteries. *In silico* data are simulated using a state-of-the-art model of cardiac dynamics coupled to a distributed model of arterial blood flow that enabled simulation of independent increases in either ventricular contractility or arterial stiffness that cannot be achieved *in vivo*. The effects on cPP, pPP, and PPa, and aortic flow of varying left ventricular contractility or arterial stiffness are examined, and the role played by aortic and peripheral wave reflections in raising cPP is studied. Results shows that ventricular ejection dynamics plays a key role in raising and amplifying PP with hypertension.

5.3.1 Methods

Previously acquired *in vivo* data, both invasive and noninvasive, are used to examine relationships between pressure and aortic flow (Munir et al., 2008; Fok et al., 2014a; Li et al., 2017). All studies described below involving *in vivo* data were approved by the Local Research Ethics Committee, and all patients gave written informed consent.

***In vivo* data: Invasive cohort**

Invasive *in vivo* data includes measurements of central aortic pressure and peripheral (digital artery) pressure previously acquired during diagnostic angiography in 23 patients (age 62 ± 10 years, BP $129 \pm 24/67 \pm 9$ mmHg, means \pm SD; see Table D.1 in Appendix D at the end of this Thesis) (Munir et al., 2008). Patients with acute coronary syndromes, those with significant valvular disease and rhythm other than sinus rhythm, were excluded from the study. Central aortic pressure was measured using a Millar high-fidelity pressure tipped catheter (Millar Instruments, Houston, TX; sampling rate was flat to greater than 100 Hz) positioned in the proximal aortic root. Peripheral pressure waveforms were acquired simultaneously from the digital artery using a servo-controlled finger pressure cuff (Finometer; Finapres Medical Systems, The Netherlands; sampling rate: 128 samples per second). It has been previously shown that digital artery waveforms obtained in this way are virtually identical to radial artery waveforms acquired by tonometry using the SphygmoCor system (Millasseau et al., 2000b). Baseline measurements of central and peripheral pressure were obtained over at least ten cardiac cycles and ensemble averaged. Sublingual glyceryl trinitrate (GTN, 500 μ g), a large vasodilator with some action on ventricular dynamics, was then administered and further measurements were acquired 2 minutes after GTN when haemodynamic responses were stable.

***In vivo* data: Noninvasive cohorts**

The noninvasive *in vivo* data includes measurements of aortic flow and central and peripheral blood pressure in a group of normotensive healthy volunteers ($n=10$, age 47 ± 8 years, BP $103 \pm 15/65 \pm 9$ mmHg, means \pm SD) and hypertensive subjects ($n=93$, age 46 ± 16 years, BP $134 \pm 22/88 \pm 14$ mmHg, means \pm SD) (Fok et al., 2014a). Characteristics of the normotensive and hypertensive cohorts are given in Table D.1 (Appendix D). In both cohorts, central blood pressure waveforms were obtained from the carotid artery in which pressure closely approximates aortic pressure (Chen et al., 1996). Peripheral pressure was measured at the radial artery. In the normotensive cohort, haemodynamic properties were modulated by the administration of pharmacological drugs with different inotropic and vasoactive properties: dobutamine (DB), a positive inotrope with some vasodilator actions (2.5, 5, and 7.5 μ g/kg per minute; Hameln Pharmaceuticals, Gloucester, United Kingdom), and noradrenaline (NA), a vasoconstrictor with some inotropic actions (12.5, 25, and 50 μ g/kg per minute; Aguetant, Bristol, United Kingdom). Each drug was given on a different occasion separated by at least 7 days, and the order was randomized. Radial and carotid pressure waveforms were obtained by applanation tonometry performed by an experienced operator using the SphygmoCor system (AtCor, Australia; sampling rate: 128 samples per second). Waveforms were obtained at rest in all subjects and during each dose of vasoactive drugs in the normotensive subjects. For each measurement, approximately ten cardiac cycles were obtained, and ensemble averaged. Waveforms that did not meet the in-built quality control criteria in the SphygmoCor system were rejected. Brachial BP was measured in triplicate by a validated oscillometric method (Omron 705CP, Omron Health Care, Japan) immediately before measurements of tonometry and used to calibrate radial waveforms, and thus to obtain a mean arterial pressure through integration of the radial waveform. Carotid waveforms were calibrated from MAP and diastolic brachial blood pressures on the assumption of equality between proximal and peripheral DBP (Pauca et al., 1992). Ultrasound imaging was performed by an experienced operator using a Vivid-7 ultrasound platform (General Electric Healthcare, UK). This

provided a measurement of the flow velocity above the aortic valve using pulsed wave Doppler obtained from an apical five-chamber view. Flow velocity was extracted from the envelope of the spectrum, filtered to reduce speckles in late systole and early diastole, and averaged over at least three cardiac cycles.

***In silico* data: Computational haemodynamics model**

To obtain *in silico* data, the cardiovascular model presented in this Thesis, validated and used for the analysis in Section 5.2, is employed to conduct the analyses presented in this Section. Thus, the arterial network is composed of the 116 largest human arteries of the head, thorax, and limbs (including the digital arteries in the hand) (Charlton et al., 2019; Piccioli et al., 2022b). Each artery of the network is characterized by its length, diameter, wall thickness, arterial wall stiffness, and arterial wall viscosity (Piccioli et al., 2022b). The cardiac function is included by coupling the 0-D cardiac contraction model at the aortic root (see Chapter 4). The model parameters are representative of healthy subjects and can be defined for different age groups, from 25 to 75 years old (Charlton et al., 2019). For the purpose of this study, the 45-year-old baseline subject is used to simulate blood flow and pressure at the aortic root and peripheral blood pressure at the radial artery. This model has age-specific mean values for all cardiovascular properties taken from the clinical literature, and approximately matches the mean age of the normotensive and hypertensive cohorts (see Table D.1, Appendix D). Cardiac or vascular parameters are changed independently to obtain haemodynamic properties spanning the range of values measured in the *in vivo* normotensive cohort. To simulate the vasoactive effect of NA and GTN, and to a lesser extent of DB, arterial compliance is modified by changing either geometrical or mechanical vascular parameters of the 45-year-old baseline subject, namely arterial stiffness (i.e., wall thickness and Young's moduli) or luminal diameters, spanning the range of age-specific mean values from the 25- to the 75-year-old baseline subjects (Charlton et al., 2019). To simulate the inotropic action of DB, and to a lesser extent of NA and GTN, left ventricular contractility in the baseline subject is increased by changing the parameters of the heart model. Based on the analysis of the sensitivity of simulated central blood pressure to cardiac parameters presented in Section 5.2 (Piccioli et al., 2022b), the following parameters are varied: (i) the stroke volume within the corresponding values measured *in vivo* (see Table D.2, Appendix D); and (ii) either the time of the left ventricular relaxation phase or the maximum amplitude of the contraction phase of the ventricular elastance function, to produce the range of contractility index values measured *in vivo* (Table D.2).

Waveform Post-processing

For all *in vivo* and *in silico* measurements, cPP, pPP and PPa, obtained as the difference between the peripheral systolic blood pressure and the first systolic shoulder in central pressure (Li et al., 2021) with the assumption of equal diastolic blood pressure, are analysed. Arterial stiffness was measured by arterial compliance (inversely related to stiffness), calculated as the ratio of stroke volume to cPP (Mariscal-Harana et al., 2021). Left-ventricular contractility is measured by the systolic index of contractility (Chengode, 2016), which is calculated as the maximum rate of increase in early-systolic central BP with respect to time (dP/dt) (Quinones, Gaasch, and Alexander, 1976). Traditional wave separations analysis (Parker and Jones, 1990) is used to obtain forward (p_f) and backward (p_b) pressure components of the central pulse pressure wave, so that $p_f + p_b = p - p_d$ with p the total blood pressure

wave and p_d the diastolic blood pressure. Peripheral wave reflections are quantified by the peak reflection coefficient, RC_{peak} , calculated as the ratio of the peak value of p_b to that of p_f . The amount of BP “emitted” at the aortic root towards downstream vessels relative to the amount of BP reaching the aortic root from downstream vessels is calculated using the peak emission coefficient, γ_{peak} , calculated as the ratio of the peak value of p_f to that of p_b (Vennin et al., 2021). All simulations and post-processing calculations are performed using customised Matlab software (The MathWorks, MA).

Statistics

Subject characteristics and results are presented as means \pm SD. The effect of administering pharmacological drugs on haemodynamic quantities is examined using paired t-tests. Baseline haemodynamic quantities are compared with those measured at the maximum drug dose of GTN for the invasive cohort, and DB and NA for the normotensive cohort, taking $p < 0.05$ as significant. Correlation analyses are performed considering Pearson’s (R) and Spearsman’s (r_s) correlation coefficients. Pearson correlation evaluates the linear relationship between two continuous variables, whereas Spearsman correlation evaluates the monotonic relationship and is more suitable for sparse data.

5.3.2 Results

Cardiac contractility, arterial compliance and PP

Both cPP and pPP are moderately to strongly associated with dP/dt for all the experimental data ($R = 0.96$ for the normotensive cohort, Figures 5.5 A, 5.5 C; $R > 0.77$ and 0.76 for the hypertensive and invasive cohorts, respectively). In addition, both pulse pressures are inversely and non-linearly associated with arterial compliance for the normotensive (Figures 5.5 B and 5.5 D) and hypertensive cohorts, although these associations are weaker than the corresponding associations with dP/dt (with Spearsman’s correlation coefficients $r_s < -0.71$ and -0.45 , respectively). For all *in vivo* cohorts, PPa is moderately to strongly associated with dP/dt ($R = 0.87$ for the normotensive cohort, Figure 5.5 E; $R = 0.81$, and 0.70 for hypertensive and invasive cohorts, respectively) and shows a moderate to weak inverse correlation with arterial compliance ($r_s = -0.61$ for the normotensive cohort, Figure 5.5 F; $r_s = -0.30$ for the hypertensive cohort). The correlations are the highest ($R > 0.87$ and $r_s < -0.61$) for the measurements in normotensive subjects, in whom haemodynamics are perturbed and therefore the range of variation in dP/dt and compliance is the greatest. The correlations between PP and dP/dt , and PP and compliance are not confounded by a correlation between dP/dt and compliance ($R = -0.16$ and -0.31 in normotensive and hypertensive cohort, respectively). Figures D.1 and D.2 in Appendix D show the correlation analysis for the hypertensive and invasive cohorts.

Administration of dobutamine significantly increases dP/dt (349.9 ± 101.2 vs 754.0 ± 186.3 mmHg/s, $p < 0.001$) and lead to larger cPP (36.1 ± 8.8 vs 59.0 ± 10.8 mmHg), pPP (56.9 ± 13.1 vs 93.0 ± 17.0 mmHg) and PPa (20.8 ± 4.8 vs 34.0 ± 7.3 mmHg) ($p < 0.001$ each) in the normotensive cohort. In contrast, no significant changes in dP/dt , cPP, pPP and PPa are observed with administration of noradrenaline. Arterial compliance is found to be significantly decreased by dobutamine (1.63 ± 0.49 vs 1.03 ± 0.22 ml/mmHg, $p < 0.001$) and, to a smaller amount, by noradrenaline (1.63 ± 0.49 vs 1.29 ± 0.36 ml/mmHg, $p = 0.04$). In the invasive cohort, administration of glyceryl trinitrate significantly decreases cPP (62.2 ± 20.2 vs 45.2

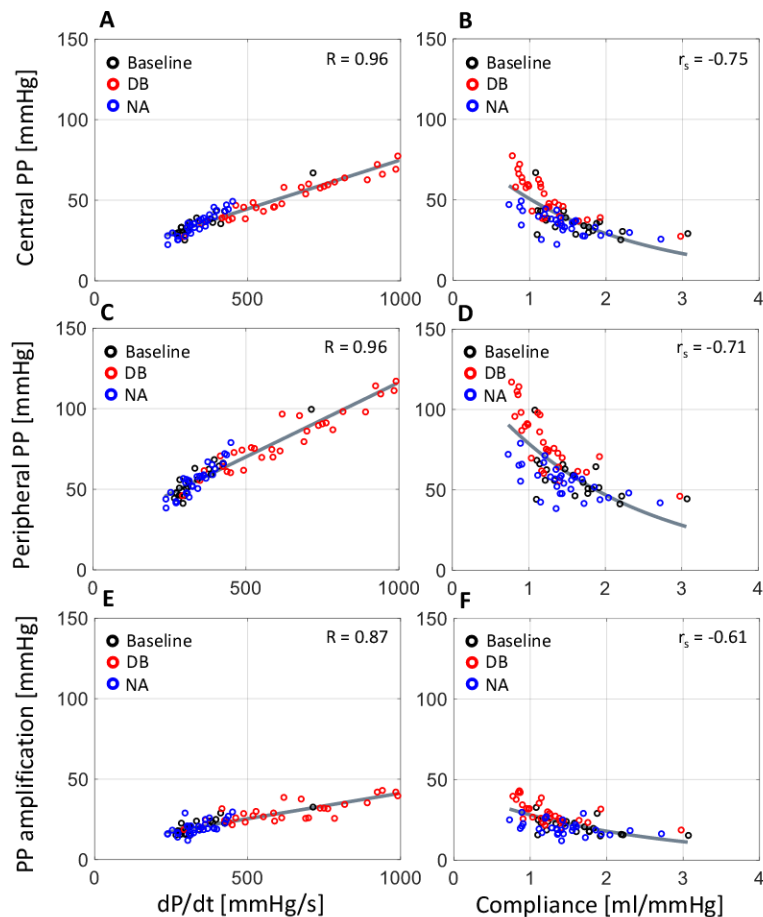


FIGURE 5.5: The relationship between the systolic index of contractility (dP/dt , left panels) or arterial compliance (right panels) and central pulse pressure (top), peripheral pulse pressure (middle), and pulse pressure (PP) amplification (bottom) in the normotensive cohort receiving rising dose infusions of dobutamine (DB) and norepinephrine (NA) (see text for details). Pearson correlation coefficients (R) are provided for dP/dt ((A) $R=0.96$, (C) $R=0.96$, (E) $R=0.87$) and Spearman correlation coefficients (r_s) are given for compliance ((B) $r_s=-0.75$, (D) $r_s=-0.71$, (F) $r_s=-0.61$).

± 17.8 mmHg, $p = 0.004$) and increases the time constant of the exponential decay of BP in diastole (0.47 ± 0.19 vs 0.82 ± 0.68 s, $p = 0.02$), a measure of arterial stiffness (Mariscal-Harana et al., 2021) (see Section 2.2.1), but does not affect dP/dt , pPP and PPa. Tables D.2 and D.3 in Appendix D show these haemodynamic variables for the normotensive and invasive cohorts, at baseline and after administration of pharmacological drugs.

In silico, variations of dP/dt with compliance held constant lead to strong direct associations with cPP, pPP and PPa (Figures 5.6 A, 5.6 C and 5.6 E), whereas changes in arterial compliance with dP/dt held constant produces strong, inverse, and non-linear associations with cPP, pPP and PPa (Figures 5.6 B, 5.6 D and 5.6 F). The range of variability in dP/dt and compliance, as well as the correspondent variations in PPs and PPa, are consistent with those observed *in vivo* in Figure 5.5 and Figures D.1 and D.2 (Appendix D).

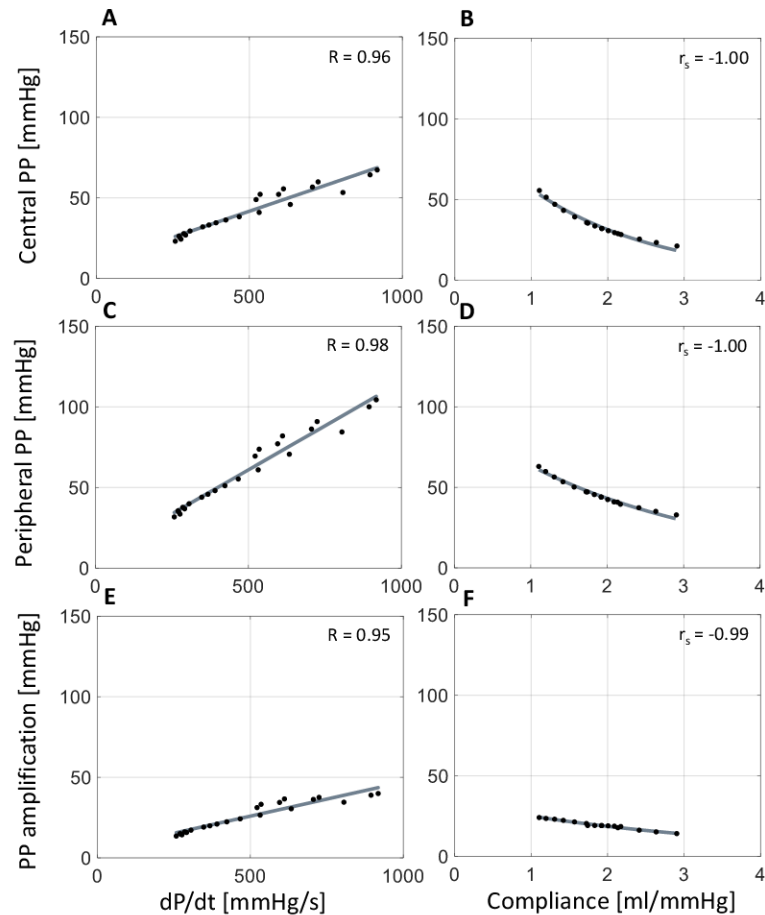


FIGURE 5.6: The relationship between the systolic index of contractility (dP/dt , left panels) or arterial compliance (right panels) and central pulse pressure (top), peripheral pulse pressure (middle), and pulse pressure (PP) amplification (bottom), in the *in silico* data. Pearson correlation coefficients (R) are provided for dP/dt ((A) $R=0.96$, (C) $R=0.98$, (E) $R=0.95$) and Spearman correlation coefficients (r_s) are given for compliance ((B) $r_s=-1.0$, (D) $r_s=-1.0$, (F) $r_s=-0.99$).

Changes in aortic flow

In silico, independent increases in left ventricular contractility (by increasing the amplitude of the contraction phase in the LV elastance function and maintaining a constant stroke volume) raises peak aortic flow, and the rates of increase in early-systolic aortic flow and decrease in late-systolic aortic flow (Figure 5.7 A). In contrast, little variation in aortic flow wave morphology is observed when compliance was independently changed (Figure 5.7 D). These numerical results are in agreement with *in vivo* flow data from the normotensive cohort for increasing contractility and compliance (Figure 5.8). *In vivo* results shows also a more prominent increase in aortic peak flow, rate of increase in early-systolic aortic flow, and rate of decrease of late-systolic aortic flow when DB was administered compared to NA and the baseline condition. The stroke volume and the volume ejected up to the peak aortic flow do not change with drug administration (Figure 5.9). Moreover, administration of dobutamine significantly increases the peak aortic flow (323.9 ± 52.8 vs 389.1 ± 65.1 ml/s, $p = 0.015$), the rate of increase in early-systolic aortic flow (3193.6 ± 793.0 vs 4848.3 ± 450.4 ml/s², $p < 0.001$), and the late of decrease in late-systolic aortic

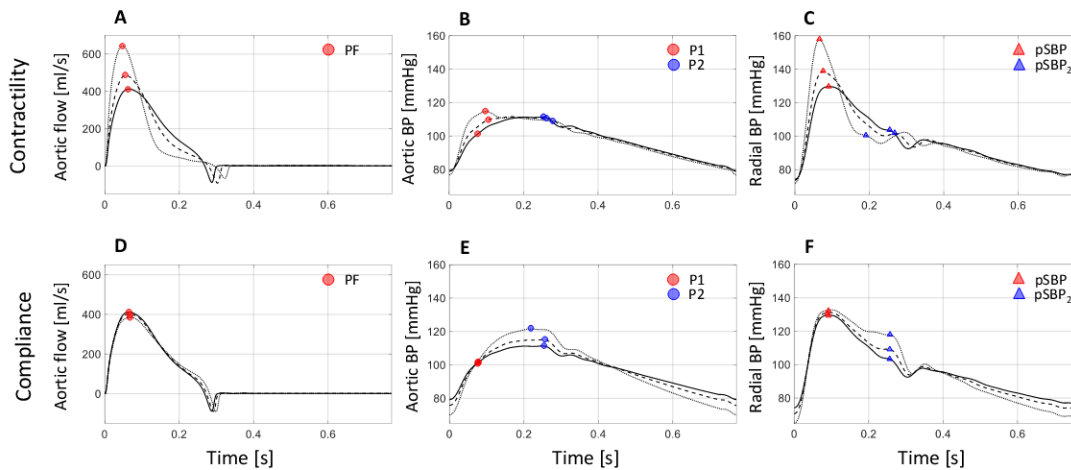


FIGURE 5.7: Aortic flow (left), aortic pressure (centre), and radial pressure (right) waveforms with increasing cardiac contractility (top) and decreasing arterial compliance (bottom) in the 45-year-old virtual subject from baseline (solid lines; dashed and dotted lines indicated variations from baseline). Increasing contractility raised the peak aortic flow (PF) (A), first systolic shoulder in central pressure (P1) (B), and peripheral systolic blood pressure (pSBP) (C). Decreasing compliance increased the peak or second shoulder in central pressure (P2) (E) and the second peak or shoulder in the peripheral systolic blood pressure (pSBP2) (F), without affecting the peak aortic flow (D).

flow (1433.6 ± 235.8 vs 2020.0 ± 404.8 ml/s², $p = 0.001$), without altering stroke volume ($p = 0.78$), whereas administration of noradrenaline did not affect aortic flow haemodynamic quantities (Table D.2, Appendix D).

The type of variations in the flow waveform observed in early systole with changes in contractility (Figure 5.7 A) are also present in the aortic and peripheral BP waves: the first inflection point (P1) and dP/dt raise in the aortic BP wave (Figure 5.7 B); the peripheral systolic BP (pSBP) values and dP/dt increase in the peripheral BP wave (Figure 5.7 C). Notably, P1 becomes the central systolic peak with high contractility, and then defined cPP. Independent decreases in compliance do not affect the BP waveform in early systole (Figures 5.7 E and 5.7 F), but lead to an increase in the (i) second systolic peak (P2) in the aortic BP wave (Figure 5.7 E) and (ii) second systolic peak (pSBP2) in the peripheral BP wave (Figure 5.7 F). Fiducial points pSBP and pSBP2 vary by +10% and -2%, respectively, when P1 was increased by +9%, and by +2% and +13%, respectively, when P2 changed by the same amount (Table D.4, Appendix D). pSBP remains the peripheral pressure peak with variations in either contractility or compliance. *In silico* results of fiducial points variations in central BP waves with changes in contractility and compliance (Figures 5.7 B and 5.7 E) are corroborated by *in vivo*, central BP waves when DB and NA were administered (Figure D.3, Appendix D).

Relative contributions of contractility and compliance to PP

In the normotensive cohort, variations in cardiac contractility and arterial compliance within their respective physiological ranges lead to greater contractility-driven increases in cPP (Figure 5.10 A), pPP (Figure 5.10 B) and PPa (Figure 5.10 C) than compliance-driven decreases in the same quantities. A rise in dP/dt from

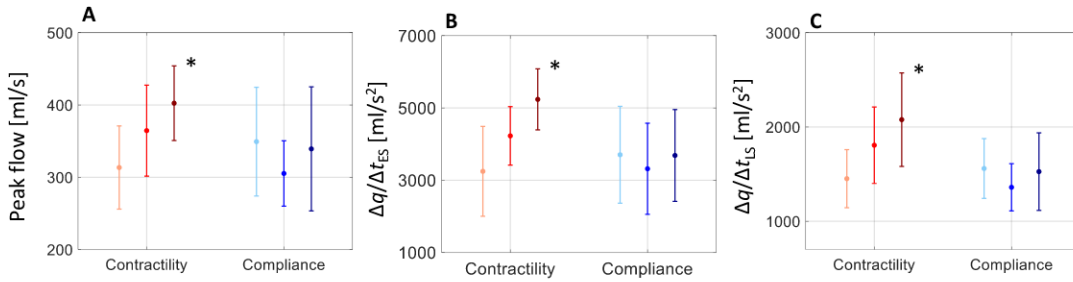


FIGURE 5.8: Variations in (A) aortic peak flow (PF), (B) rate of increase in early-systolic aortic flow ($\Delta q/\Delta t_{ES}$), and (C) rate of decrease in late-systolic aortic flow ($\Delta q/\Delta t_{LS}$) with increasing contractility (light-red line, $dP/dt < 489$ mmHg/s; red line, $489 < dP/dt < 740$ mmHg/s; dark-red line, $dP/dt > 740$ mmHg/s) and compliance (light-blue line, $C < 1.5$ ml/mmHg; blue line, $1.5 < C < 2.3$ ml/mmHg; dark-blue line, $C > 2.3$ ml/mmHg) in the normotensive cohort. All quantities are shown as mean \pm SD. Asterisks indicate a significant difference between the first and third groups (PF: $p < 0.001$, $\Delta q/\Delta t_{ES}$: $p < 0.001$, $\Delta q/\Delta t_{LS}$: $p = 0.005$).

230 to 990 mmHg/s increases cPP, pPP, and PPa by +163%, +155%, and +143%, respectively, whereas an increase in compliance from 0.7 to 3 ml/mmHg drops cPP, pPP, and PPa by 72%, 70%, and 64%, respectively (Figure D.4, Appendix D). These trends are also observed in the hypertensive cohort (Figure D.5) in which a rise in dP/dt from 230 to 830 mmHg/s yields even greater increases in cPP, pPP, and PPa (+194%, +208%, and +482%, respectively) and smaller compliance-driven decreases in the same quantities (61%, 43%, and 49%, respectively, when compliance increased from 0.6 to 2.8 ml/mmHg). Similar results are obtained using the *in silico* model (Figure D.6): cPP, pPP, and PPa varies by +169%, +217%, and +185%, respectively, with a variation in contractility from 250 to 920 mmHg/s, and by -65%, -50%, and -41%, respectively, with a variation in compliance from 1.1 to 2.9 ml/mmHg.

The role of aortic and peripheral wave reflections

cPP is directly and strongly associated with a wide range of values of the peak emission coefficient at the aortic root, γ_{peak} , for the normotensive ($R = 0.76$) and hypertensive ($R = 0.75$) cohorts (Figures 5.11 A and 5.11 B), and shows a strong to moderate inverse correlation with a relatively narrower range of values of the peripheral wave reflection coefficient RC_{peak} , for the same two cohorts (Figures 5.11 D and 5.11 E; $R = -0.74$ and $R = -0.66$, respectively). *In silico*, cPP also increases with increasing γ_{peak} (Figure 5.11 C) and decreasing RC_{peak} (Figure 5.11 F). Increasing contractility lead to larger γ_{peak} values than decreasing compliance, in agreement with the *in vivo* normotensive data: the increase in γ_{peak} is significant with administration of DB, a mainly inotropic drug, and it is not with administration of NA, a mainly vasoactive drug (Figure 5.11 A) ($p < 0.001$ vs $p = 0.5$, Table D.2, online-only Data Supplement). Furthermore, *in silico* RC_{peak} decreases with increasing contractility and, to a much lesser extent, with variations in arterial compliance (Figure 5.11 F), also in agreement with the normotensive data (Figure 5.11 D): RC_{peak} decreases more significantly with the administration of DB than NA ($p < 0.001$ vs $p = 0.03$, Table D.2).

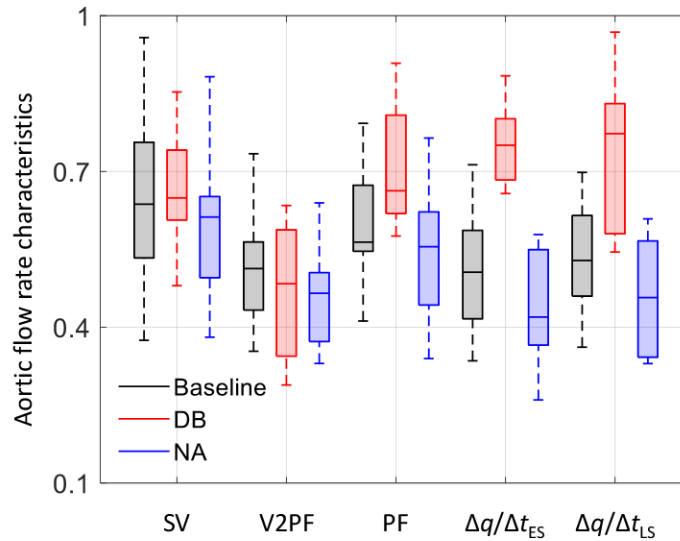


FIGURE 5.9: Variations in stroke volume (SV), volume ejected up the peak aortic flow (V2PF), aortic peak flow (PF), rate of increase in early-systolic aortic flow ($\Delta q/\Delta t_{ES}$), and rate of decrease in late-systolic aortic flow ($\Delta q/\Delta t_{LS}$) at baseline physiological conditions (black box plots), and with dobutamine (red box plots) and nora-drenaline (blue box plots) administration. Aortic flow characteristics are reported on the y-axis in a normalised range for ease of comparison.

5.3.3 Discussion

Increased PP is the major haemodynamic change contributing to incident hypertension in ageing populations. It could result from arterial stiffening, increased peripheral wave reflections generated from the vasculature, or altered ventricular ejection dynamics. This study suggests that left ventricular contractility directly affects the aortic flow waveform which emerges as a main driver of the increase in PP and its amplification to the periphery, whereas arterial compliance does not alter aortic flow and has a relative smaller effect on PP and its amplification. Furthermore, pressure waves emitted at the aortic root, which are directly determined by aortic flow wave morphology (Vennin et al., 2021), have a much greater contribution to the increase in PP with hypertension than pressure waves reflected from downstream to the aorta. Taken together, these results suggest that ventricular ejection dynamics play a key role in PP elevation and amplification with hypertension, in agreement with recent findings using only clinical data or models that did not account for ventricular-aortic coupling and had to resort to speculative assumptions on the underlying haemodynamic mechanisms (Chirinos et al., 2009; Fok et al., 2014a; Schultz et al., 2013; Sharman et al., 2009).

This study used a complementary mix of *in silico* and *in vivo* data. *In silico* simulations allowed us to test theoretical predictions by varying contractility and compliance independently of each other over their *in vivo* pathophysiological ranges, and in the absence of experimental errors. *In vivo* data measured in normotensive subjects, whose haemodynamic quantities was altered by inotropic/vasoactive drugs, and hypertensive subjects, further strengthened the *in silico* results without resorting to modelling hypotheses.

Within the range of contractility and compliance values measured in the normotensive and hypertensive cohorts of the study, cPP, pPP, and PPa show a greater

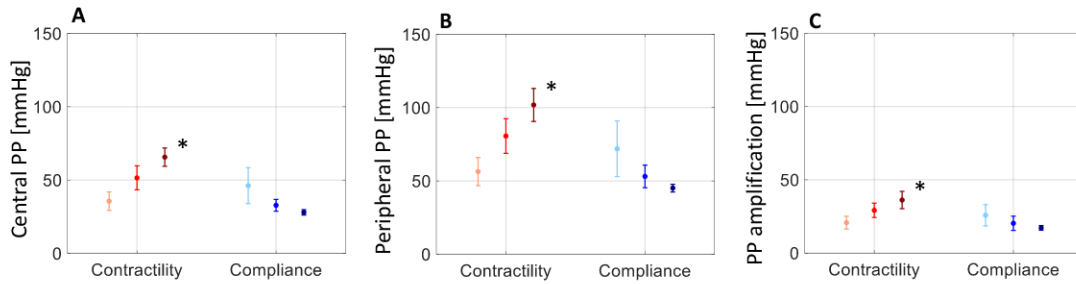


FIGURE 5.10: Variations in (A) central pulse pressure (PP), (B) peripheral PP, and (C) PP amplification with increasing contractility (light-red, $dP/dt < 489$ mmHg/s; red, $489 < dP/dt < 740$ mmHg/s; dark-red, $dP/dt > 740$ mmHg/s) and compliance (light-blue, $C < 1.5$ ml/mmHg; blue, $1.5 < C < 2.3$ ml/mmHg; dark-blue, $C > 2.3$ ml/mmHg) in the normotensive cohort. All quantities are shown as mean \pm SD. Asterisks indicate a significant difference between the first and third groups.

variation with contractility (Figure 5.10). The predominant effect of contractility is more prominent in the hypertensive cohort, despite haemodynamic properties in the normotensive cohort being modulated by administration of pharmacological drugs with different inotropic and vasoactive properties. The predominant effect of contractility is also validated by the Framingham Heart study (Mitchell et al., 2010), in which data from 6417 healthy subjects were analysed. This analysis showed that a smaller percentage change in dP/dt than in compliance corresponded an equal variation in cPP and pPP (67% vs 90% variation in dP/dt and compliance, respectively, for 20 mmHg change in cPP and 18 mmHg change in pPP), meaning that changes in PP are more sensitive to changes in contractility than in compliance. These *in vivo* results are confirmed by the physics-based computational model in which contractility and compliance could be varied in isolation (Figure D.6, Appendix D); hence avoiding any confounding effects of compliance when varying contractility by the positive inotrope dobutamine or of contractility when varying compliance by the vasoconstrictor noradrenaline or the vasodilator glyceryl trinitrate. Having established that the model can reproduce the changes in PPs with contractility or compliance observed *in vivo*, the model enabled us to identify distinct haemodynamic mechanisms underlying the increases in cPP, pPP and PPa with contractility and compliance. The mechanisms of cPP increase are first analysed.

Changes in contractility alter the aortic flow waveform in early systole (Figure 5.7 A), producing noticeable changes in peak aortic flow, rate of increase in early-systolic aortic flow, and rate of decrease in late-systolic aortic flow. All these changes are statistically significant with administration of dobutamine in the normotensive cohort (Figure 5.8), corroborating previous studies on the strong relation among systolic flow ejection and PP (Vennin et al., 2017; Flores Gerónimo et al., 2021). Alterations in the aortic flow wave in early systole have a direct effect on the aortic pressure wave via the water hammer equation ($\Delta p = Z_c \cdot \Delta q$, with Z_c the characteristic impedance depending on vascular properties only, and Δp and Δq the changes in aortic pressure and flow in early systole (Parker, 2009)), before the arrival of downstream reflected waves. When vascular properties are unchanged, Δp in early systole is directly proportional to Δq and a major contributor to systolic hypertension.

Changes in compliance do not produce the alterations in aortic flow wave morphology observed with varying contractility (Figures 5.7 D and 5.8), although they can still affect the rate of increase in pressure in early systole (i.e., dP/dt) via changes

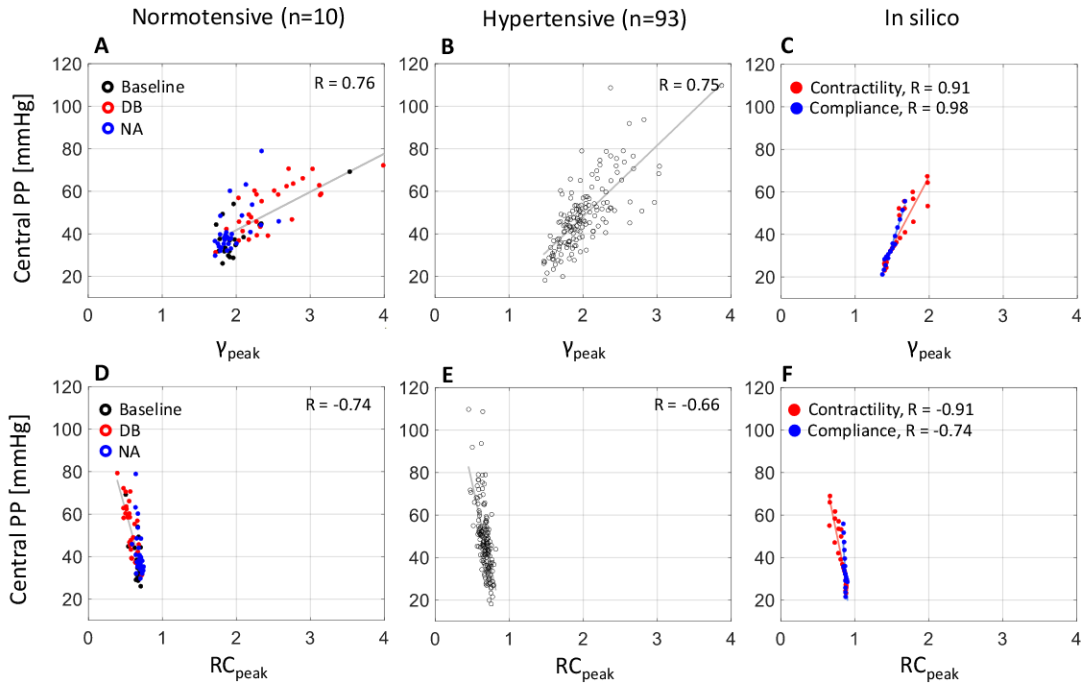


FIGURE 5.11: The relationship between peak emission (γ_{peak} , top) or reflection (RC_{peak} , bottom) coefficients and central pulse pressure (PP). Left: normotensive cohort receiving rising dose infusions of dobutamine (DB) and noradrenaline (NA) (Pearson correlation coefficients (A) $R=0.76$, (D) $R=-0.74$). Centre: hypertensive cohort ((B) $R=0.75$, (E) $R=-0.66$). Right: increasing cardiac contractility (red dots) or decreasing arterial compliance (blue dots) from baseline in the 45-year-old virtual subject ((C) $R=0.91$ for contractility and $R=0.98$ for compliance; (F) $R=-0.91$ for contractility and $R=-0.74$ for compliance).

in Z_c through the water hammer equation. However, dP/dt do not vary significantly *in vivo* with administration of the vasoconstrictor noradrenaline or the vasodilator glyceryl trinitrate (Tables D.2 and D.3, Appendix D). Instead, compliance produces changes in aortic pressure in late systole, when the BP wave can be described by a space-independent Windkessel model (Vennin et al., 2017) and, hence, wave propagation phenomena is less relevant to explain increases in PP with decreases in compliance. Indeed, it has been found a greater variation in the amount of pressure waves emitted from the aortic root to downstream vessels with dobutamine-induced changes in contractility than with noradrenaline-induced changes in compliance (Figure 5.11 A). This result is also confirmed *in silico* with independent changes in contractility and compliance (Figure 5.11 C).

Variations in the amount of pressure waves emitted at the aortic root, quantified by the peak emission coefficient γ_{peak} (Figures 5.11, top panels), have a more predominant role in increasing cPP than variations in pressure waves reflected downstream the aorta, quantified by the reflection coefficient RC_{peak} (Figures 5.11, bottom). This result suggests a smaller contribution to increased cPP of peripheral wave reflections than wave activity occurring at the aortic root, in agreement with studies from Framingham showing a small contribution of peripheral wave reflections to age-related changes in cPP and augmentation pressure (Mitchell et al., 2010; Torjensen et al., 2014). Although *in vivo* γ_{peak} do not significantly vary with noradrenaline administration compared to baseline ($p = 0.48$, Table D.2, Appendix D), γ_{peak} still

shows an increasing trend with decreasing compliance, namely at high pulse (Figures 5.11 A and 5.11 C). This can be explained using the water hammer equation. Decreased compliance leads to increased Z_c , producing an increase in the amplitude of the forward pressure wave since in early systole, when reflected waves have not yet arrived from the periphery, the pressure increase Δp is equal to Δp of the forward wave: if the cardiac output Δq is unaltered, the uprise in pressure will be proportional to the increase in Z_c .

The mechanisms underlying changes in pPP and PPa are now considered. Increased contractility by administration of dobutamine raise both pPP and PPa, whereas increased or decreased compliance by administration of glyceryl trinitrate or noradrenaline do not alter pPP or PPa (Tables D.2 and D.3, Appendix D). This finding suggests that contractility is the main driver for increased pPP and PPa, in agreement with the *in silico* data shown in Figure 5.7, whereas compliance is a driver for increased cPP only. Contractility determines the first inflection point (P1) on the central blood pressure wave (Figure 5.7 B) and the peripheral systolic blood pressure (pSBP) on the peripheral pressure wave (Figure 5.7 C), both occurring in early systole. Therefore, pPP – and hence PPa – is determined by a wave propagation phenomenon initiated by the a change in aortic flow wave morphology: the propagation of the early systolic raise in BP towards the periphery, which is in agreement with experimental (Gaddum et al., 2017) and theoretical (Flores Gerónimo et al., 2021) results. On the other hand, arterial compliance determines central (Figure 5.7 E) and peripheral (Figure 5.7 F) pressure peaks later in systole (P2 and pSBP2, respectively), with pSBP2 having a smaller magnitude than the contractility-dependent pSBP. As a result compliance affects mainly cPP rather than pPP, in agreement with results using a central-to-peripheral transfer function (Li et al., 2021). The association of compliance with cPP has been previously described by the Windkessel effect of central elastic arteries (Vennin et al., 2017), where compliance undergoes a greater variation than in peripheral muscular arteries (higher smooth muscle content) (Kondiboyina et al., 2022; Reymond, Westerhof, and Stergiopoulos, 2012), consistent with physiological changes observed with ageing (Van Bortel and Spek, 1998; Charlton et al., 2019).

This study is subject to several limitations. Carotid pressure is an imperfect surrogate of aortic pressure and subject to calibration errors. *In vivo* measurements of pressure and aortic flow velocity were not simultaneous and inevitably subject to experimental error that can propagate when calculating flow derived quantities, such as rate of increase in early-systolic aortic flow. However, these errors are likely to be random and unlikely to influence the conclusions of our study which have also been confirmed by a physics-based cardiovascular model. Further validation of our results using more accurate methods for measuring flow, such as magnetic resonance, would therefore be valuable. *In vivo*, it is challenging to alter left ventricular contractility through pharmacological interventions without affecting other haemodynamic properties, including arterial compliance, and vice-versa. Dobutamine does not affect uniquely inotropy and may have some vasodilator actions affecting compliance, and noradrenaline and glyceryl trinitrate do not affect uniquely compliance and may have some inotropic actions. The *in silico* model is therefore used to address this limitation of *in vivo* data in determining the extent PPs, PPa, and aortic flow depend on properties of the heart and arterial tree, by varying independently the cardiac and vascular parameters and avoiding *in vivo* confounding factors. Finally, although the *in vivo* normotensive cohort used in this study is limited, values of haemodynamics quantities obtained in the normotensive cohort are corroborated by other studies effected in larger cohorts. The Framingham Heart Study (Mitchell et al., 2010) showed

values of central and peripheral SBPs, total compliance, and dP/dt (64 ± 8 mmHg, 115 ± 11 mmHg, 1.71 ± 0.53 ml/mmHg, 328.7 ± 82.4 mmHg/s, respectively) in agreement with those in Table D.1 in Appendix D. Moreover, the relationship between PPs and dP/dt showed in this work is corroborated by the ACCT study (McEniery et al., 2005) conducted on a cohort of 4001 healthy subjects, which showed that cPP, pPP increase with ageing contemporary to the increase in dP/dt .

5.4 Concluding remarks

This Chapter shows applications of the arterial cardiovascular model to investigate the effect of cardiac properties on blood pulse waves in the vasculature.

Section 5.2 presents a theoretical, computationally-based study to arouse interest in assessing cardiac function from arterial pressure waves and peripheral PPG signals. A cardiovascular model accounting for the numerical ventricular-aortic coupling has been validated by showing its ability to simulate accurately cardiac and vascular haemodynamics when compared with reference models validated using *in vivo* measurements. Results were in excellent agreement. The effect of the parameters of the cardiac contraction model on vascular pulse waves has been studied through a sensitivity analysis, identifying the most significant parameters. In the sensitivity analysis, those parameters that have no clinical characterisation have been varied symmetrically by $\pm 50\%$, obtaining values of left ventricular contractility in agreement with literature. Stenotic and regurgitant valves scenarios have also been considered by varying the correspondent cardiac parameters in accordance with physiological values. Specific haemodynamic indices have been identified to understand how central and peripheral properties varied.

Results from the cardiovascular model suggest that cardiac parameters related to LV contraction and systolic ejection can be potentially identified by pulse wave analysis. Altered contractility affects aortic flow rate and pressure waveforms, which in turn affect pulse pressure in central and peripheral sites. An impaired LV relaxation phase can be identified from the analysis of the dicrotic notch timing. Moreover, stenotic and regurgitant valves affect the flow rate at the aortic root and pressure waveforms throughout the vasculature. Pulse pressure was found to increase with aortic regurgitation, and to decrease with aortic stenosis. We have demonstrated that an altered venous return in the left atrium affects left ventricular contractility and arterial pulse pressures. In addition, the variations in pulse waves caused by changes in cardiac function were found to amplify towards the periphery of the systemic vasculature, suggesting the suitability of peripheral sites (e.g., radial and digital arteries) for assessing cardiac function. Finally, PPG signals in the periphery were found to vary with changes in cardiac parameters and diseased valves, suggesting that further work on the analysis of peripheral PPG signals could improve cardiac dysfunction detection from easily-accessible pulse waves measurements.

Section 5.3 presents a study where *in vivo* and *in silico* data were used complementarily to infer the role of cardiac contraction on isolated systolic hypertension. Results suggest that isolated systolic hypertension is more likely a result of dynamic (i.e., ventricular) than static (i.e., vascular) pathologies. Therefore, interventions that influence left ventricular dynamics with a direct action on systolic ejection and aortic flow rate may be particularly effective in reducing PP and systolic hypertension, independent of vascular properties. Having established that peripheral systolic BP, which is used to assess clinical risk associated with hypertension and guide clinical care (Li et al., 2021) is mainly determined by ventricular dynamics also highlights

the importance of targeting the ventricle when treating hypertension. Furthermore, having ascertained that PP amplification is mainly determined by contractility, and hence an indication of ventricular inotropy, noninvasive measurements of PP amplification from carotid (a surrogate for aortic pressure) to brachial or radial artery could offer cheap, pressure-based, assessment of left ventricular function.

By using a complementary mix of *in vivo* and *in silico* data, results show that ventricular contractility influences systolic ejection, shaping aortic flow morphology and playing a primary role in raising and amplifying pulse pressure with hypertension. Arterial compliance is found to play a secondary role and peripheral wave reflections to play a minor role. The diagnosis and clinical treatment of hypertension may therefore improve by targeting systolic ejection patterns and aortic flow.

Chapter 6

Conclusions

6.1 Overview

The goal of this PhD Thesis was to propose a numerical model able to simulate physiological haemodynamics of the arterial circulatory system to contribute to the study of cardiovascular diseases.

The first part of this Thesis is purely computational and based on concepts of fluid mechanics and numerical analysis. It focuses on the numerical implementation of extended networks of viscoelastic vessels in order to obtain results that correctly reproduce physiological pulse waves. Vessels wall viscoelasticity is considered in all sections of the network where arteries converge and at the inlet and outlet sections. At junctions, a Riemann problem was proposed consisting of a nonlinear system of equations based on the conservation of mass and total pressure and the Riemann Invariants characterising the hyperbolic PDE governing system. A specific Riemann Invariant, relating pressure and area, allowed to consider the viscoelastic contribution. This numerical approach was then extended also to inlet and outlet boundary conditions. The proposed numerical scheme was validated using trivial test cases, corroborating the preservation of the second-order accuracy even when considering viscoelastic boundary conditions. The approach was then tested with increasing-complexity networks, validating the obtained results with reference waveforms.

The second part of this Thesis employs the proposed cardiovascular model to investigate the relationship between cardiac dynamics and vascular properties. A sensitivity analysis was performed on pressure pulse waves when cardiac parameters of the cardiac contraction model were altered. This allowed to identify the parameters regulating cardiac dynamics that most affect pulse waves in the circulation, and therefore to study the underlying relationships between cardiac function and vascular haemodynamics. Then, a complementary *in silico-in vivo* study was carried out to examine the role of cardiac dynamics and vascular properties in elevating pulse pressure in isolate systolic hypertension. Numerical results, obtained by varying cardiac and vascular properties in the cardiovascular model, were validated with experimental data gathered in cohorts of subjects whose physiological conditions were altered with pharmacological intervention. Furthermore, waveforms of central and peripheral blood pressure and aortic flow rate were analysed with increasing contractility and decreasing vascular compliance, and reflection coefficients were studied.

6.2 Main findings and Original contributions

The achievements of the presented research can be differentiated in two main parts: the implementation of the numerical model for networks with viscoelastic

vessels, and the application of this model to investigate the effects of cardiac properties on vascular waveforms.

6.2.1 Viscoelasticity in extended networks

The mathematical model to simulate blood flow in compliant vessels has been presented with particular emphasis on its augmented fluid–structure interaction form. The proposed model allows the simulation of the viscoelastic mechanical behaviour of arterial and venous walls. From a mathematical point of view, this is straightforwardly accomplished by considering the source term in the tube law of the governing PDE system. The source term contains all three viscoelastic parameters of the Standard Linear Solid Model, therefore its consideration allows an easy transition from a purely elastic characterisation of the wall to a viscoelastic one, enabling a correct description of the cross-sectional luminal area deformation when undergoing pressure pulses. Having all viscoelastic information enclosed in the source term avoids the presence of second order derivatives and permits to work with a purely hyperbolic system of equations. The proposed Junction Riemann problem allows the viscoelastic contribution to be considered in all internal and external boundary sections without decreasing the order of accuracy prescribed by the FV IMEX-SSP2 RK scheme, even when dealing with a stiff source term, thus confirming its asymptotic preserving property. The model has been exhaustively validated with success, showing a satisfying agreement with both 1-D and 3-D reference waveforms, in test cases characterised by increasing complexity and different viscoelastic formulations. The consistency between the system response and the mechanical features of the Standard Linear Solid Model was confirmed. Indeed, the damping effect is observable by the opening of the hysteresis loops, but the extent of its manifestation strictly depends on the viscoelastic parameters that define the Standard Linear Solid Model.

6.2.2 Key role of ventricular ejection in shaping vascular pulse waves

The proposed cardiovascular model was validated with reference waveforms of cardiac and vascular haemodynamics. The sensitivity analysis performed on the parameters of the cardiac contraction model provided interesting insights into the amount of information related to cardiac function inferable from vascular pulse waves. Results showed that the contractility of the left atrium has a little effect on pressure waves, which are instead significantly influenced by the contractility of the left ventricle. It was proved that the timing of the dicrotic notch is an indicator of ventricular dysfunction. Moreover, simulations of impaired heart valves have shown significant changes in pulse waves. A regurgitant or stenotic aortic valve alters aortic flow rate and central and peripheral pressure waves. A dysfunction in the mitral valve, albeit with minor effect, was also inferred from pulse wave analysis. Variations in pulse waves caused by alterations in cardiac function were found to be amplified towards the periphery of the vasculature. Finally, PPG signals were found to vary with altered cardiac function and diseased valves.

The effect of cardiac function on vascular pulse waves was also investigated with specific application to isolate systolic hypertension, which often manifests with an increase in pulse pressure. *In vivo* and *in silico* results showed the overwhelming importance of contractility and left ventricular ejection in raising pulse pressure. The rooted knowledge of the influence of vascular properties, such as arterial compliance and stiffness, in elevating pulse pressure was not denied, but an additional

contribution to this haemodynamic phenomenon was highlighted. Results showed that ventricular contractility plays a major role in the shaping the aortic flow rate, which has direct implications on the determination of central and peripheral blood pressure waves. Increased contractility raised pulse pressure and, in particular, its amplification in peripheral sites of the vasculature. A decrease in vascular compliance produced an increase in central pulse pressure, but had little influence on pulse pressure amplification. The underlying haemodynamics mechanism was identified as the increase in the forward-travelling pressure wave, which resulted to be greater than that in the backward-travelling pressure wave, at high pulse pressure and contractility. This was also corroborated by the increase in the first systolic peak in both central and peripheral blood pressure waves, becoming determinants for pulse pressure.

6.3 Future work

One of the main future goals, for a further development of this PhD research, consists in the numerical implementation of a closed-loop circulatory system, therefore comprehensive of the venous and pulmonary circulations, as well as the splanchnic circulation, which actually contains almost 25% of blood volume in adult humans, therefore having important implications for systemic haemodynamics. The implementation of the closed loop would be realised using the 1-D augmented fluid-structure interaction system as this is capable of dealing with different mechanical configurations of vessels walls, as presented for trivial venous tests. Organs would be treated as 0-D lumped-parameters models. The realisation of the entire human circulation would provide an even more effective tool to substantially support studies of cardiac and circulatory diseases and broad-spectrum medical applications.

The application of uncertainty quantification theory represents a valuable approach to quantitative characterise and understand uncertainties related to the viscoelastic parameters for the simulation of pulse waves in the cardiovascular network. Indeed, the effect of viscoelastic formulation on the manifestation of the damping behaviour could be statistically quantified, also depending on the site of analysis in the network, i.e., the response in pulse waves morphology at a specific arterial site caused by a variation in viscoelastic properties in either the same site or another. The work carried out by means of a univariate sensitivity analysis could also be improved using more refined uncertainty quantification techniques. This would produce more solid results regarding the effects of cardiac parameters variations in vascular pulse waves.

The work on cardiac function assessment by pulse wave analysis, although purely computational, is considered to be useful in clinical research. Peripheral sites have been shown to be easily-accessible measurements sites for detecting cardiac function, as the alterations in pulse waves are amplified compared to central sites. However, the study should be refined and further backed up. For this purpose, a large measurement campaign should be performed with both healthy and heart-diseased subjects in order to have access to a multitude of *in vivo* pulse waves for different physiological scenarios. With this regard, PPG signals represent a valuable resource to cardiac dysfunction analysis from pulse waves as they are obtainable from a large portion of the population by means of smart devices. Machine learning algorithms, which are commonly used today as they can process huge amounts of data in an automatised manner, represent a feasible tool to further develop the detection of cardiac dysfunction from pulse wave analysis.

Finally, the study on pulse pressure elevation in isolate systolic hypertension has important clinical implications. It highlights the non-negligible contribution of left ventricular contractility to this cardiovascular disease, which has been usually overlooked in favour of the vascular contribution related to arterial stiffness. Future developments of this work would involve the analysis of additional *in vivo* data of wider cohorts with diverse physiological conditions. Besides, the completion of the cardiovascular model would be useful to the study of hypertension because it could highlight other driving factors for pulse pressure increase, as well as the presence of compensatory haemodynamic mechanisms.

Appendix A

Viscoelastic SLSM parameters of numerical tests

Tables A.1, A.2 and A.3 report the Standard Linear Solid Model (SLSM) parameters for every bifurcation/network test implemented in this work, namely for the 3-vessel test (aortic bifurcation), the AN37 and the ADAN56. It is reminded to the reader that ADAN56 is characterized by a unique set of viscoelastic parameters for the entire network. Tables are reported here to facilitate the assessment of further analysis.

TABLE A.1: Viscoelastic SLSM parameters for the aortic bifurcation test: instantaneous Young modulus E_0 , asymptotic Young modulus E_∞ , ratio $z = E_\infty/E_0$, viscosity coefficient η and relaxation time τ_r .

Vessel name	E_0 [MPa]	E_∞ [MPa]	z [-]	η [kPa·s]	τ_r [ms]
Abdominal aorta	1.4293	0.6667	0.466	58.664	21.89
Iliac artery	3.8986	0.9333	0.239	109.97	21.45

TABLE A.2: Viscoelastic SLSM parameters for the ADAN56 network: instantaneous Young modulus E_0 , asymptotic Young modulus E_∞ , ratio $z = E_\infty/E_0$, viscosity coefficient η and relaxation time τ_r .

Vessel name	E_0 [MPa]	E_∞ [MPa]	z [-]	η [kPa·s]	τ_r [ms]
\forall vessels	0.4431	0.3000	0.677	30.00	21.87

TABLE A.3: Viscoelastic SLSM parameters for the AN37 network: instantaneous Young modulus E_0 , asymptotic Young modulus E_∞ , ratio $z = E_\infty/E_0$, viscosity coefficient η and relaxation time τ_r . In vessel names, R. stands for the right artery and L. stands for the left artery.

Vessel name	E_0 [MPa]	E_∞ [MPa]	z [-]	η [kPa·s]	τ_r [ms]
Ascending aorta	1.6860	1.6	0.949	4.0268	0.12
Innominate	1.6846	1.6	0.950	3.9654	0.12
R. Carotid	1.6869	1.6	0.948	4.0702	0.12
R. Subclavian I	1.6857	1.6	0.949	4.0120	0.12
R. Subclavian II	1.6843	1.6	0.950	3.9493	0.12
R. Radial	1.6851	1.6	0.949	3.9869	0.12
R. Ulnar	1.6872	1.6	0.948	4.0837	0.13
Aortic arch I	1.6853	1.6	0.949	3.9945	0.12
L. Carotid	1.6863	1.6	0.949	4.0403	0.12
Aortic arch II	1.6846	1.6	0.950	3.9631	0.12
L. Subclavian I	1.6865	1.6	0.949	4.0519	0.12
L. Subclavian II	1.6879	1.6	0.948	4.1153	0.13
L. Radial	1.6861	1.6	0.949	4.0299	0.12
L. Ulnar	1.6874	1.6	0.948	4.0904	0.13
Thoracic aorta I	1.6857	1.6	0.949	4.0149	0.12
Intercostals	1.6857	1.6	0.949	4.0120	0.12
Thoracic aorta II	1.6843	1.6	0.950	3.9493	0.12
Celiac I	1.6855	1.6	0.949	4.0057	0.12
Celiac II	1.6854	1.6	0.949	3.9990	0.12
Splenic	1.6833	1.6	0.950	3.9059	0.11
Gastric	1.6877	1.6	0.948	4.1032	0.13
Hepatic	1.6849	1.6	0.950	3.9762	0.12
Abdominal aorta I	1.6847	1.6	0.950	3.9664	0.12
L. Renal	1.6836	1.6	0.950	3.9196	0.12
Abdominal aorta II	1.6861	1.6	0.949	4.0299	0.12
R. Renal	1.6858	1.6	0.949	4.0199	0.12
Abdominal aorta III	1.6851	1.6	0.949	3.9869	0.12
R. Iliac femoral I	1.6872	1.6	0.948	4.0837	0.13
R. Iliac femoral II	1.6884	1.6	0.948	4.1374	0.13
Iliac femoral R. III	1.6831	1.6	0.951	3.8929	0.11
L. Iliac femoral I	1.6868	1.6	0.949	4.0622	0.12
L. Iliac femoral II	1.6874	1.6	0.948	4.0904	0.13
L. Iliac femoral III	1.6871	1.6	0.948	4.0795	0.12
R. Anterior tibial	1.6835	1.6	0.950	3.9117	0.12
R. Posterior tibial	1.6864	1.6	0.949	4.0434	0.12
L. Posterior tibial	1.6832	1.6	0.951	3.8980	0.11
L. Anterior tibial	1.6843	1.6	0.950	3.9493	0.12

Appendix B

Simulation of PPG signals

The PPG is conceived as a measurement of volumetric change of arterial blood in a tissue (Charlton et al., 2019; Huttunen et al., 2020). From an operational standpoint, PPG signals were calculated, following the methodology presented by Charlton et al. (2019), depending on the site of analysis:

- At the most peripheral vessels of the circulation (e.g., the digital artery), the PPG was calculated from the volume of blood stored in the terminal Windkessel model:

$$PPG(t) = \int_0^t q_{1D}(t') - q_{out}(t') dt', \quad (\text{B.0.1})$$

where q_{1D} is the inflow to the terminal Windkessel, and q_{out} is the outflow, as shown in Fig. 4.1.

- At local microvasculature sites of the arterial network (e.g., the wrist), the typical Windkessel scheme was employed once again to model blood volume dynamics and calculate the PPG. The validity of this hypothesis relies on the fact that vascular beds receive blood from arterioles that diverge from the afferent major artery (e.g., the radial artery at the wrist), overcoming the impasse caused by the lack of modelling of these arterioles within the 1-D arterial network due to their small size. Hence, the inflow and inlet pressure of the Windkessel model were set equal to the flow and pressure of the arterial segment, q_{1D} and p_{1D} , respectively. The PPG was calculated using Eq. (B.0.1), in which q_{out} was obtained as

$$q_{out}(t) = \frac{p_{1D}(t) - p_{out}}{R}, \quad (\text{B.0.2})$$

and defining

$$R = \frac{\langle p_{1D}(t) \rangle - p_{out}}{\langle q_{1D}(t) \rangle}. \quad (\text{B.0.3})$$

In (B.0.3), p_{out} is the outflow pressure, and $\langle p_{1D} \rangle$ and $\langle q_{1D} \rangle$ are the blood pressure and flow rate, respectively, obtained at the site of analysis and averaged over the cardiac cycle.

In both cases, the PPG was finally obtained by normalising the pulsatile variation in blood volume within the range $[0, 1]$.

Appendix C

Cardiac function assessment using the pulse wave analysis

C.1 Sensitivity Analysis: reference parameters

Reference values for V_{net} and T were 66.3 ml and 0.822 s, respectively (Charlton et al., 2019). Tables C.1 and C.2 show the reference cardiac parameters (Mynard and Smolich, 2015) that were increased by +50 % and decreased by -50 % in the sensitivity analysis.

TABLE C.1: Reference parameters of the cardiac contraction model for the heart chambers: left atrium (LA) and left ventricle (LV).

Chamber	E_{min} [$\frac{\text{Pa}}{\text{cm}^3}$]	E_{max} [$\frac{\text{Pa}}{\text{cm}^3}$]	K_S [$\frac{\text{s}}{\text{cm}^3}$]	v_{p0} [cm^3]	v_0 [cm^3]	m_1 [-]	τ_1 [s]	m_2 [-]	τ_2 [s]	t_{onset} [s]
LA	12.0	17.3	250	3.00	7.10	1.99	0.042	11.2	0.138	0.00
LV	9.33	373	500	1.00	136	1.32	0.215	21.9	0.362	0.65

TABLE C.2: Reference parameters of the cardiac contraction model for the heart valves: mitral valve (MV) and aortic valve (AV). The reference A_{min} is equal to zero for both valves.

Valve	A_{max} [cm^2]	l [cm]	K_{vo} [$\text{Pa}^{-1}\text{s}^{-1}$]	K_{vo} [$\text{Pa}^{-1}\text{s}^{-1}$]
MV	5.1	2.0	0.2	0.4
AV	4.9	1.0	0.2	0.2

C.2 Sensitivity Analysis: RMSD

Table C.3 shows the RMSD evaluated in the three sites of analysis in the network, i.e., the aortic root (AoRt), the brachial artery (Br), and the digital artery (Di). Results are reported for each cardiac parameter and for both variations, i.e. ± 50 %.

TABLE C.3: Root mean square deviations (RMSD) in mmHg resulted from the sensitivity analysis performed in an univariate manner. The *Increased* and *Decreased* columns stand for the simulations with the increased or decreased cardiac parameter, respectively. The amount of variation for each parameter is addressed in Sect 5.2.1. Cardiac parameters are classified per cardiac site, namely left ventricle (LV), left atrium (LA), aortic valve (AV), and mitral valve (MV). The total volume entering the LA in a cardiac cycle, V_{net} , and the cardiac cycle duration T are not attributed to any cardiac site because they describe overall cardiac function. Significant parameters are reported in bold.

Cardiac site	Param.	Increased			Decreased		
		<i>AoRt</i>	<i>Br</i>	<i>Di</i>	<i>AoRt</i>	<i>Br</i>	<i>Di</i>
-	V_{net}	21.9	22.0	21.8	22.4	22.5	22.5
	T	10.0	11.0	14.3	14.5	15.7	19.6
LV	E_{max}	3.43	5.54	8.88	5.51	8.08	12.4
	E_{min}	0.80	0.92	1.19	0.58	0.82	1.14
	m_1	6.42	9.76	15.3	8.34	12.7	19.4
	τ_1	2.97	4.45	7.08	5.22	7.94	12.6
	m_2	0.63	0.97	1.44	1.41	2.19	3.32
	τ_2	3.26	4.62	6.80	7.17	10.9	17.7
	v_{p_0}	0.07	0.10	0.14	0.06	0.09	0.12
	K_s	1.09	1.67	2.62	1.30	2.01	3.26
	LA	E_{max}	0.35	0.38	0.42	0.78	0.78
E_{min}		0.03	0.09	0.14	0.04	0.04	0.04
m_1		0.02	0.08	0.12	0.04	0.09	0.13
τ_1		0.02	0.07	0.10	0.03	0.03	0.03
m_2		0.03	0.09	0.14	0.01	0.06	0.10
τ_2		0.05	0.09	0.12	0.26	0.27	0.28
v_{p_0}		0.07	0.09	0.14	0.03	0.03	0.03
K_s		0.02	0.07	0.10	0.04	0.09	0.13
AV	A_{max}	0.55	0.78	1.10	3.27	4.82	7.25
	A_{min}	12.8	16.6	22.6	-	-	-
	l	0.47	0.72	1.0	0.56	0.80	1.16
	K_{vo}	0.09	0.09	0.15	0.17	0.32	0.51
	K_{vc}	0.29	0.43	0.61	0.80	1.13	1.59
MV	A_{max}	0.09	0.12	0.15	4.09	4.09	4.02
	A_{min}	4.34	6.73	10.4	-	-	-
	l	0.04	0.09	0.13	0.04	0.09	0.14
	K_{vo}	0.03	0.07	0.11	0.04	0.09	0.12
	K_{vc}	0.02	0.07	0.11	0.02	0.07	0.11

Appendix D

Ventricular ejection and pulse pressure

TABLE D.1: Characteristics of the *in vivo* cohorts and *in silico* model. Values are numbers, percentage, or means \pm SD. BMI, body mass index; HR, heart rate; cSBP, central systolic blood pressure; pSBP, peripheral systolic blood pressure; DBP, diastolic blood pressure; LVOT diameter, left ventricular outflow tract diameter; SV, stroke volume; dP/dt , contractility index, C, arterial compliance.

Characteristics	Normotensive cohort	Hypertensive cohort	Invasive cohort	In silico model
n	10	93	23	1
Age [year]	47 \pm 8	46 \pm 16	62 \pm 10	45
Sex [male %]	77	59	78	100
BMI [kg/m ²]	–	26.5 \pm 9.2	29.1 \pm 3.6	–
HR [bpm]	65 \pm 8	66 \pm 10	61 \pm 10	72
cSBP [mmHg]	103.2 \pm 15.4	134.4 \pm 22.3	129.3 \pm 23.6	103.7
pSBP [mmHg]	119.6 \pm 16.9	144.4 \pm 21.6	139.9 \pm 26	124.6
DBP [mmHg]	65.6 \pm 9.0	88.1 \pm 13.7	67.0 \pm 9.2	75.8
LVOT diameter [cm]	1.87 \pm 0.18	1.96 \pm 0.25	–	2.5
SV [ml]	59.9 \pm 13.0	77.9 \pm 24.8	–	66.4
dP/dt [mmHg/s]	349.9 \pm 101.2	421.9 \pm 112.4	378.8 \pm 130.5	347.4
C [ml/mmHg]	1.6 \pm 0.5	1.3 \pm 0.5	–	1.9

TABLE D.2: Variations in haemodynamic quantities with administration of pharmacological drugs in the normotensive cohort. Haemodynamic quantities of the normotensive cohort measured at baseline (second column), maximum dose of dobutamine (DB = 7.5 $\mu\text{g}/\text{kg}$ per minute, third column), and maximum dose of noradrenaline (NA = 50 $\mu\text{g}/\text{kg}$ per minute, fourth column). Haemodynamic quantities are central pulse pressure (cPP), peripheral pulse pressure (pPP), pulse pressure (PP) amplification, contractility index (dP/dt), arterial compliance, stroke volume, peak flow, rate of increase in early-systolic aortic flow ($\Delta q/\Delta t_{ES}$), rate of decrease in late-systolic aortic flow ($\Delta q/\Delta t_{LS}$), peak emission coefficient (γ_{peak} , see main article for details), and peak reflection coefficient (RC_{peak} , see main article for details). Values are reported as mean \pm SD. Two-sample t-tests were performed to compare the haemodynamic quantities at baseline and with drug administration. Results are reported in the third and fourth columns as t(df) = t-value, where df stands for degrees of freedom from the t-test statistics. Asterisks indicate a significant difference between the haemodynamic variable at baseline and after maximum drug dose administration.

	Baseline	DB (max dose)	NA (max dose)
cPP [mmHg]	36.1 \pm 8.8	59.0 \pm 10.8 t(28) = -6.2, p < 0.001 *	36.8 \pm 8.9 t(28) = -0.2, p = 0.85
pPP [mmHg]	56.9 \pm 13.1	93.0 \pm 17.0 t(28) = -6.4, p < 0.001 *	57.8 \pm 12.4 t(28) = -0.2, p = 0.86
PP amplification [mmHg]	20.8 \pm 4.8	34.0 \pm 7.3 t(28) = -5.9, p < 0.001 *	21.0 \pm 7.3 t(28) = -0.12, p = 0.90
dP/dt [mmHg/s]	349.9 \pm 101.2	754.0 \pm 186.3 t(12) = -6.4, p < 0.001 *	343.7 \pm 69.7 t(25) = 0.2, p = 0.85
Compliance [ml/mmHg]	1.63 \pm 0.49	1.03 \pm 0.22 t(28) = 4.6, p < 0.001 *	1.29 \pm 0.36 t(23) = 2.1, p = 0.04 *
Stroke volume [ml]	59.9 \pm 13.0	61.1 \pm 10.5 t(22) = -0.2, p = 0.78	56.02 \pm 13.7 t(17) = 0.7, p = 0.45
Peak flow [ml/s]	323.9 \pm 52.8	389.1 \pm 65.1 t(15) = -2.7, p = 0.015 *	297.9 \pm 67.3 t(15) = 1.1, p = 0.30
$\Delta q/\Delta t_{ES}$ [ml/s ²]	3193.6 \pm 793.0	4848.3 \pm 450.4 t(22) = -6.8, p < 0.001 *	2807.0 \pm 675.8 t(21) = 1.4, p = 0.18
$\Delta q/\Delta t_{LS}$ [ml/s ²]	1433.6 \pm 235.8	2020.0 \pm 404.8 t(12) = -4.2, p = 0.001 *	1235.4 \pm 288.4 t(16) = 1.9, p = 0.08
γ_{peak} [-]	2.01 \pm 0.39	2.56 \pm 0.66 t(47) = -3.7, p < 0.001 *	1.95 \pm 0.21 t(26) = 0.7, p = 0.48
RC_{peak} [-]	0.66 \pm 0.05	0.57 \pm 0.07 t(47) = 4.9, p < 0.001 *	0.69 \pm 0.03 t(31) = -2.3, p = 0.03 *

TABLE D.3: Variations in haemodynamic quantities with administration of GTN in the invasive cohort. Haemodynamic quantities of the *in vivo* invasive cohort measured at baseline (second column) and after administration of glyceryl trinitrate (GTN, 500 μg ; third column). Haemodynamic quantities are central pulse pressure (cPP), peripheral pulse pressure (pPP), pulse pressure (PP) amplification, contractility index (dP/dt), and time constant of the exponential relaxation decay (Mariscal-Harana et al., 2021) of the central blood pressure waveform. Values are reported as mean \pm SD. Two-sample t-tests were performed to compare the haemodynamic quantities at baseline and with GTN administration. Results are reported in the third column as $t(\text{df}) = t\text{-value}$, where df stands for degrees of freedom from the t-test statistics. Asterisks indicate a significant difference between the haemodynamic variable at baseline and after drug dose administration.

	Baseline	GTN
PP [mmHg]	62.2 \pm 20.2	45.2 \pm 17.8 $t(44) = 3.0, p = 0.004 *$
pPP [mmHg]	73.1 \pm 22.5	68.9 \pm 17.9 $t(44) = 0.7, p = 0.49$
PP amplification [mmHg]	33.4 \pm 16.3	30.3 \pm 12.2 $t(44) = 0.7, p = 0.48$
dP/dt [mmHg/s]	378.8 \pm 130.5	331.7 \pm 117.5 $t(44) = 1.3, p = 0.20$
Time constant [s]	0.47 \pm 0.19	0.82 \pm 0.68 $t(44) = -2.45, p = 0.02 *$

TABLE D.4: Fiducial points of the central and peripheral BP waves measured in the 45-year-old virtual subject at baseline (first row), with increased contractility (second row) and with decreased compliance (third row). Percentage changes from baseline are shown in the second and third rows. P1 is the first inflection point of the central BP wave; P2 is the second systolic peak in the central BP wave; pSBP is the first systolic shoulder in the peripheral BP wave; pSBP2 is the second peak or shoulder in the peripheral BP wave.

Simulation	P1 [mmHg]	P2 [mmHg]	pSBP [mmHg]	pSBP2 [mmHg]
Baseline	100	111	130	104
Increased contractility	110 (+9%)	112 (0%)	143 (+10%)	102 (-2%)
Decreased compliance	102 (+1%)	122 (+9%)	132 (+2%)	118 (+13%)

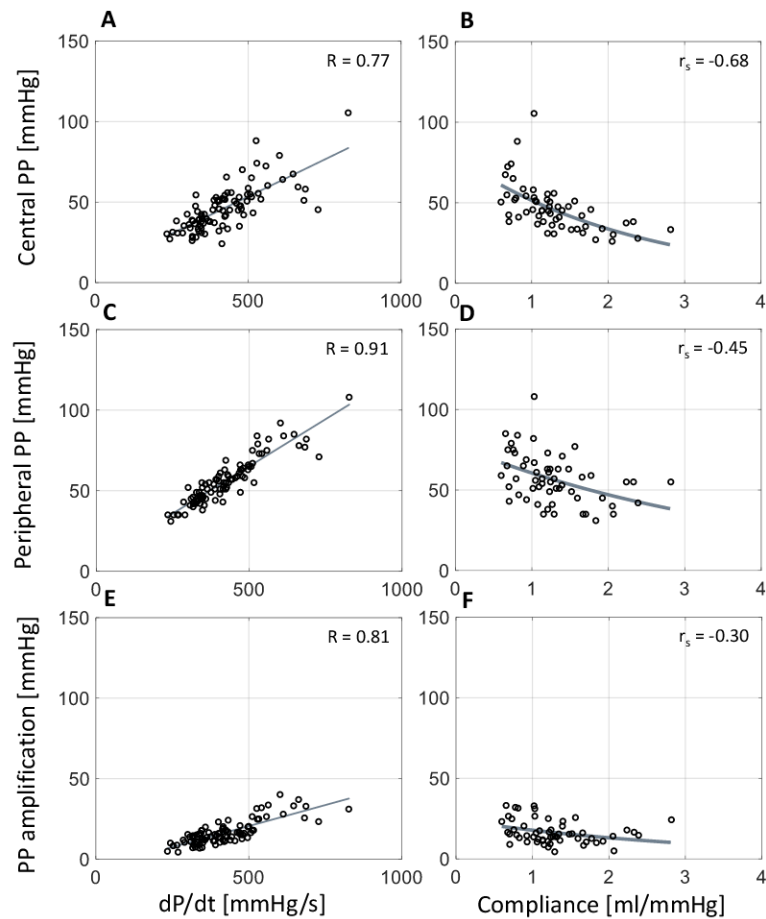


FIGURE D.1: The relationship between the systolic index of contractility (dP/dt , left) or arterial compliance (right) and central pulse pressure (top), peripheral pulse pressure (middle), and pulse pressure (PP) amplification (bottom) in the hypertensive cohort. Pearson correlation coefficients (R) are provided for dP/dt ((A) $R=0.77$, (C) $R=0.91$, (E) $R=0.81$) and Spearman correlation coefficients (r_s) are given for compliance ((B) $r_s=-0.68$, (D) $r_s=-0.45$, (F) $r_s=-0.30$).

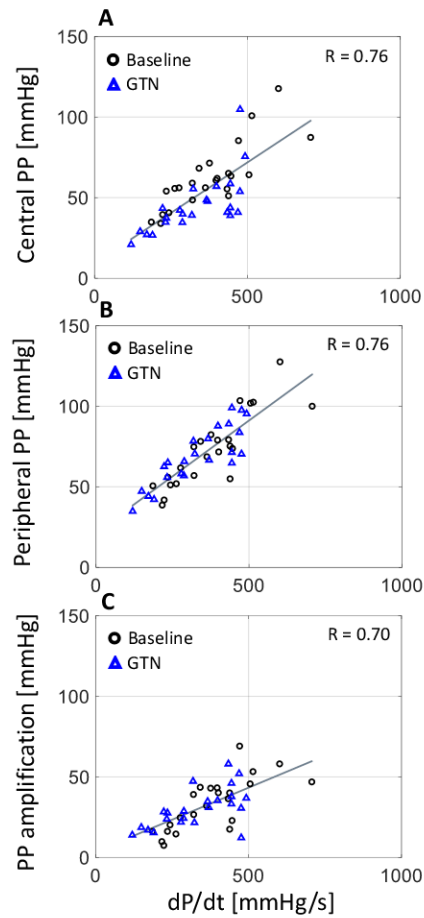


FIGURE D.2: The relationship between the systolic index of contractility (dP/dt) and central pulse pressure (top), peripheral pulse pressure (middle), and pulse pressure (PP) amplification (bottom) in the invasive normotensive cohort receiving a dose infusion of glyceryl trinitrate (GTN). Pearson correlation coefficients (R) are provided ((A) $R=0.76$, (B) $R=0.76$, (C) $R=0.70$).

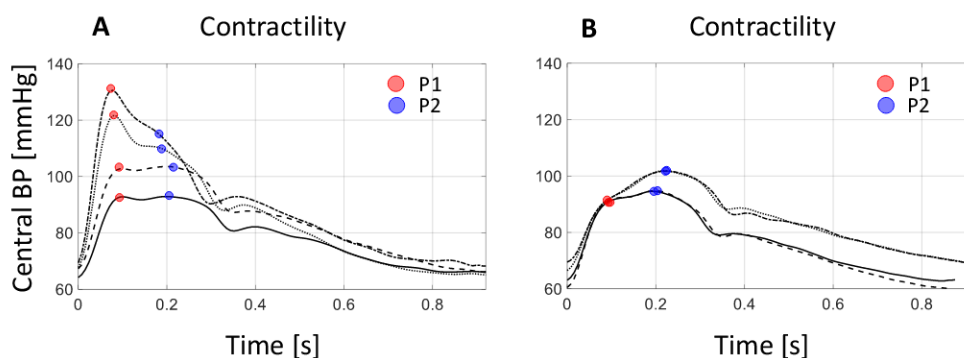


FIGURE D.3: *In vivo* central blood pressure waveform variations with administration of dobutamine (A) and noradrenaline (B) (baseline: solid line; dose 1: dashed line; dose 2: dotted line; dose 3: dash-dotted line). Increasing dose of dobutamine raised the first systolic shoulder (P1) and, to a lesser extent, the second systolic shoulder (P2) in central pressure. Increasing dose of noradrenaline predominantly raised peak or second shoulder in central pressure (P2) and, to a lesser extent, the first systolic shoulder (P1) in central pressure.

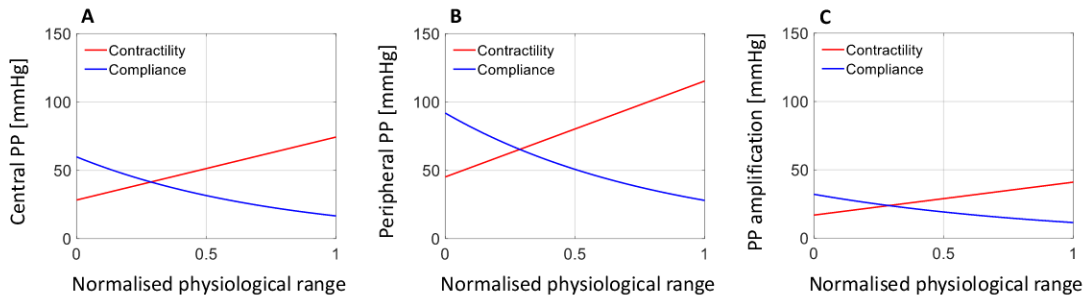


FIGURE D.4: Variations in central pulse pressure (A), peripheral pulse pressure (B), and pulse pressure (PP) amplification (C) with normalised contractility (red) and compliance (blue) in the normotensive cohort. Trends calculated using the corresponding fitted curves in Figure 5.5. The normalised intervals reported in the x-axis were calculated using the minimum and maximum values of contractility and compliance observed in the cohort: from 230 to 990 mmHg/s for contractility and from 0.7 to 3.0 ml/mmHg for compliance.

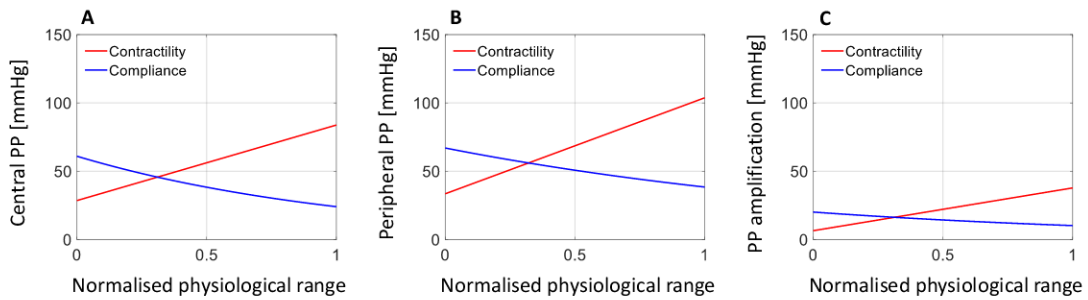


FIGURE D.5: Variations in central pulse pressure (A), peripheral pulse pressure (B), and pulse pressure (PP) amplification (C) with normalised contractility (red) and compliance (blue) in the hypertensive cohort. Trends calculated using the corresponding fitted curves in Figure D.1. The normalised intervals reported on the x-axis were calculated using the minimum and maximum values of contractility and compliance observed in the cohort: from 230 to 830 mmHg/s for contractility and from 0.6 to 2.8 ml/mmHg for compliance.

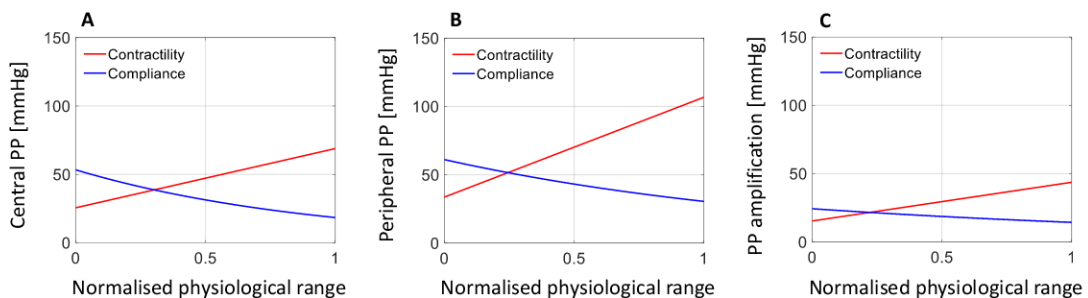


FIGURE D.6: Variations in central pulse pressure (A), peripheral pulse pressure (B), and pulse pressure (PP) amplification (C) with normalised contractility (red) and compliance (blue) in the *in silico* model. Trends calculated using the corresponding fitted curves in Figure 5.6. The normalised intervals reported on the x-axis were calculated using the maximum and minimum values of contractility and compliance observed in the *in silico* data: from 250 to 920 mmHg/s for contractility and from 1.1 to 2.9 ml/mmHg for compliance.

Bibliography

- Abdessalem, K. B., P. Flaud, and S. Zobaidi (2018). "New method for estimating arterial pulse wave velocity at single site". In: *Computer Methods in Biomechanics and Biomedical Engineering* 21 (1), pp. 55–64.
- Alastruey, J., K. H. Parker, and S. J. Sherwin (2012). "Arterial pulse wave haemodynamics". In: *BHR Group - 11th International Conferences on Pressure Surges* October 2012, pp. 401–442.
- Alastruey, J. et al. (2007). "Modelling the circle of Willis to assess the effects of anatomical variations and occlusions on cerebral flows". In: *Journal of Biomechanics* 40.8, pp. 1794–1805.
- Alastruey, J. et al. (2008). "Lumped parameter outflow models for 1-D blood flow simulations: Effect on pulse waves and parameter estimation". In: *Communications in Computational Physics* 4.2, pp. 317–336.
- Alastruey, J. et al. (2011). "Pulse wave propagation in a model human arterial network: Assessment of 1-D visco-elastic simulations against in vitro measurements". In: *Journal of Biomechanics* 44.12, pp. 2250–2258.
- Alastruey, J. et al. (2012). "Physical determining factors of the arterial pulse waveform: Theoretical analysis and calculation using the 1-D formulation". In: *Journal of Engineering Mathematics* 77.1, pp. 19–37.
- Ambrosi, D., A. Quarteroni, and G. Rozza (2012). *Modeling of Physiological Flows*. Springer.
- Armentano, R. et al. (1995a). "Effects of hypertension on viscoelasticity of carotid and femoral arteries in humans". In: *Hypertension* 26, pp. 48–54.
- Armentano, R. L. et al. (1995b). "Arterial Wall Mechanics in Conscious Dogs". In: *Circulation Research* 76.3, pp. 468–478.
- Armentano, R. L. et al. (2007). "Smart smooth muscle spring-dampers". In: *IEEE Engineering in Medicine and Biology Magazine* 26.1, pp. 62–70.
- Arts, T. et al. (2005). "Adaptation to mechanical load determines shape and properties of heart and circulation: The CircAdapt model". In: *American Journal of Physiology - Heart and Circulatory Physiology* 288.4 57-4, pp. 1943–1954.
- Ascher, U. M., S. J. Ruuth, and R. J. Spiteri (1997). "Implicit-explicit Runge-Kutta methods for time-dependent partial differential equations". In: *Applied Numerical Mathematics* 25.2-3, pp. 151–167.

- Avallone, E. A. and T. Baumeister III (1916). *Standard handbook for mechanical engineers*. McGraw-Hill Inc.
- Avolio, A. P. et al. (2009). "Role of pulse pressure amplification in arterial hypertension: Experts' opinion and review of the data". In: *Hypertension* 54.2, pp. 375–383.
- Battista, C. (2015). "Parameter Estimation of Viscoelastic Wall Models in a One-Dimensional Circulatory Network". PhD thesis. North Carolina State University.
- Baumgartner, H. et al. (2009). "Echocardiographic assessment of valve stenosis: EAE/ASE recommendations for clinical practice". In: *European Journal of Echocardiography* 10.1, pp. 1–25.
- Bermudez, A. and M. E. Vazquez (1994). "Upwind methods for hyperbolic conservation laws with source terms". In: *Computers & Fluids* 23.8, pp. 1049–1071.
- Berne, R. M., B. M. Koeppen, and B. A. Stanton (2010). *Berne & Levy Physiology*. 6th. Philadelphia, PA: Mosby/Elsevier.
- Bertaglia, G. (2019). "1D augmented fluid-structure interaction systems with viscoelasticity: from water pipelines to blood vessels". PhD Thesis. University of Ferrara.
- Bertaglia, G., V. Caleffi, and A. Valiani (2020). "Modeling blood flow in viscoelastic vessels: the 1D augmented fluid–structure interaction system". In: *Computer Methods in Applied Mechanics and Engineering* 360, p. 112772.
- Bertaglia, G. and L. Pareschi (2021). "Hyperbolic models for the spread of epidemics on networks: kinetic description and numerical methods". In: *ESAIM: Mathematical Modelling and Numerical Analysis* 55 (2), pp. 381–407.
- Bertaglia, G. et al. (2018). "Numerical methods for hydraulic transients in viscoelastic pipes". In: *Journal of Fluids and Structures* 81, pp. 230–254.
- Bertaglia, G. et al. (2020). "Computational hemodynamics in arteries with the one-dimensional augmented fluid-structure interaction system: viscoelastic parameters estimation and comparison with in-vivo data". In: *Journal of Biomechanics* 100, p. 109595.
- Bertaglia, G. et al. (2021). "Uncertainty quantification of viscoelastic parameters in arterial hemodynamics with the a-FSI blood flow model". In: *Journal of Computational Physics* 430, p. 110102.
- Bessemers, D. et al. (2008). "Experimental validation of a time-domain-based wave propagation model of blood flow in viscoelastic vessels". In: *Journal of Biomechanics* 41.2, pp. 284–291.
- Blanco, P. J. et al. (2014). "Blood flow distribution in an anatomically detailed arterial network model: criteria and algorithms". In: *Biomechanics and Modeling in Mechanobiology* 13.6, pp. 1303–1330.

- Blanco, P. J. et al. (2015). "An anatomically detailed arterial network model for one-dimensional computational hemodynamics". In: *IEEE Transactions on Biomedical Engineering* 62.2, pp. 736–753.
- Blanco, P. J. et al. (2020). "On the anatomical definition of arterial networks in blood flow simulations: comparison of detailed and simplified models". In: *Biomechanics and Modeling in Mechanobiology*.
- Boileau, E. et al. (2015). "A benchmark study of numerical schemes for one-dimensional arterial blood flow modelling". In: *International Journal for Numerical Methods in Biomedical Engineering* e02732.
- Bonow, R. O. (2013). "Chronic mitral regurgitation and aortic regurgitation: Have indications for surgery changed?" In: *Journal of the American College of Cardiology* 61.7, pp. 693–701.
- Caleffi, V., A. Valiani, and A. Bernini (2006). "Fourth-order balanced source term treatment in central WENO schemes for shallow water equations". In: *Journal of Computational Physics* 218.1, pp. 228–245.
- Campbell, K. B. et al. (1982). "Internal capacitance and resistance allow prediction of right ventricle outflow". eng. In: *The American journal of physiology* 243.1, H99–112.
- Carabello, B. A. (2001). "Progress in mitral and aortic regurgitation". In: *Progress in Cardiovascular Diseases* 43.6, pp. 457–475.
- Carpenter, P. W. and T. J. Pedley (2001). *Flow past highly compliant boundaries and in collapsible tubes, in Proceedings of the IUTAM Symposium*. 1st. Springer.
- Castro, M. J. et al. (2008). "Why many theories of shock waves are necessary: Convergence error in formally path-consistent schemes". In: *Journal of Computational Physics* 227.17, pp. 8107–8129.
- Cavallini, N., V. Caleffi, and V. Coscia (2008). "Finite volume and WENO scheme in one-dimensional vascular system modelling". In: *Computers and Mathematics with Applications* 56.9, pp. 2382–2397.
- Charlton, P. H. et al. (2018). "Assessing mental stress from the photoplethysmogram: A numerical study". In: *Physiological Measurement* 39.5.
- Charlton, P. H. et al. (2019). "Modeling arterial pulse waves in healthy aging: a database for in silico evaluation of hemodynamics and pulse wave indexes". In: *American Journal of Physiology - Heart and Circulatory Physiology* 317.5, H1062–H1085.
- Charlton, P. H. et al. (2022). "Wearable photoplethysmography for cardiovascular monitoring". In: [In Press].

- Chemla, D. et al. (1998). "Total arterial compliance estimated by stroke volume-to-aortic pulse pressure ratio in humans". In: *American Journal of Physiology - Heart and Circulatory Physiology* 274.2 43-2.
- Chen, C. H. et al. (1996). "Validation of Carotid Artery Tonometry as a Means of Estimating Augmentation Index of Ascending Aortic Pressure". In: *Hypertension* 27.2, pp. 168–175.
- Chengode, S. (2016). "Left ventricular global systolic function assessment by echocardiography". In: *Annals of Cardiac Anaesthesia* 19.5, S26–S34.
- Chirinos, J. A. et al. (2009). "Time-varying myocardial stress and systolic pressure-stress relationship: Role in myocardial-arterial coupling in hypertension". In: *Circulation* 119.21, pp. 2798–2807.
- Christensen, M. H. (1982). *Theory of Viscoelasticity*. 1st. Academic Press, Inc.
- Civilla, L. et al. (2021). "An integrated lumped-parameter model of the cardiovascular system for the simulation of acute ischemic stroke: description of instantaneous changes in hemodynamics". In: *Mathematical Biosciences and Engineering* 18.4, pp. 3993–4010.
- Colombo, . M. and M. Garavello (2008). "On the Cauchy Problem for the p -System at a Junction". In: *SIAM Journal on Mathematical Analysis* 39.5, pp. 1456–1471.
- Colombo, R. M., M. Herty, and V. Sachers (2008). "On 2×2 Conservation Laws at a Junction". In: *SIAM Journal on Mathematical Analysis* 40.2, pp. 605–622.
- Darne, B. et al. (1989). "Pulsatile versus steady component of blood pressure: A cross-sectional analysis and prospective analysis on cardiovascular mortality". In: *Hypertension* 13, pp. 392–400.
- Davies, J. E. et al. (2006). "Use of simultaneous pressure and velocity measurements to estimate arterial wave speed at a single site in humans". In: *American Journal of Physiology - Heart and Circulatory Physiology* 290.2, pp. 59–61.
- Davies, J. E. et al. (2012). "Attenuation of wave reflection by wave entrapment creates a "horizon effect" in the human aorta". In: *Hypertension* 60.3, pp. 778–785.
- De Hert, S. G. et al. (2006). "Evaluation of Left Ventricular Function in Anesthetized Patients Using Femoral Artery dP/dtmax". In: *Journal of Cardiothoracic and Vascular Anesthesia* 20.3, pp. 325–330.
- Drzewieck, G. M., J. Melbin, and A. Noordegraaf (1983). "Arterial tonometry: review and analysis". In: *Journal of Biomechanics* 16.141–152.
- Dumbser, M. and E. F. Toro (2011a). "A simple extension of the Osher Riemann solver to non-conservative hyperbolic systems". In: *Journal of Scientific Computing* 48.1-3, pp. 70–88.

- (2011b). “On universal Osher-type schemes for general nonlinear hyperbolic conservation laws”. In: *Communications in Computational Physics* 10.3, pp. 635–671.
- Elgendi, M. (2020). *PPG Signal Analysis: An Introduction Using MATLAB*. First edit. Boca Raton: CRC Press, p. 298.
- Elshobaki, M., A. Valiani, and V. Caleffi (2018). “Junction riemann problem for one-dimensional shallow water equations with bottom discontinuities and channels width variations”. In: *Journal of Hyperbolic Differential Equations* 15.2, pp. 191–217.
- (2019). “Numerical modelling of open channel junctions using the Riemann problem approach”. In: *Journal of Hydraulic Research* 57.5, pp. 662–674.
- Flores Gerónimo, J. et al. (2021). “Estimating Central Pulse Pressure From Blood Flow by Identifying the Main Physical Determinants of Pulse Pressure Amplification”. In: *Frontiers in Physiology* 12. February, pp. 1–15.
- Fok, H. et al. (2014a). “Augmentation pressure is influenced by ventricular contractility/relaxation dynamics. Novel mechanism of reduction of pulse pressure by nitrates”. In: *Hypertension* 63.5, pp. 1050–1055.
- (2014b). “Augmentation pressure is influenced by ventricular contractility/relaxation dynamics novel mechanism of reduction of pulse pressure by nitrates”. In: *Hypertension* 63.5, pp. 1050–1055.
- Fok, H. et al. (2014c). “Dominance of the forward compression wave in determining pulsatile components of blood pressure: Similarities between inotropic stimulation and essential hypertension”. In: *Hypertension* 64.5, pp. 1116–1123.
- Formaggia, L., D. Lamponi, and A. Quarteroni (2003). “One-dimensional models for blood flow in arteries”. In: *Journal of Engineering Mathematics* 47, pp. 251–276.
- Formaggia, L., A. Quarteroni, and A. Veneziani (2009). *Cardiovascular Mathematics. Modeling and simulation of the circulatory system*. Ed. by Springer. Springer.
- Formaggia, L. et al. (2006). “Numerical modeling of 1D arterial networks coupled with a lumped parameters description of the heart”. In: *Computer Methods in Biomechanics and Biomedical Engineering* 9.5, pp. 273–288.
- Frank, O. (1990). “The basic shape of the arterial pulse. First treatise: Mathematical analysis”. In: *Journal of Molecular and Cellular Cardiology* 22.3, pp. 255–277.
- Franklin, S. S. et al. (1997). “Hemodynamic patterns of pge-related changes in blood pressure. The Framingham Heart Study”. In: *Circulation* 96.1, pp. 308–315.
- Fullana, J. M. and S. Zaleski (2009). “A branched one-dimensional model of vessel networks”. In: *Journal of Fluid Mechanics* 621, pp. 183–204.
- Fung, Y. C. (1997). *Biomechanics: Circulation*. Ed. by Springer. Second Edi. Springer, p. 571.

- Gaddum, N. et al. (2013). "A technical assessment of pulse wave velocity algorithms applied to non-invasive arterial waveforms". In: *Annals of Biomedical Engineering* 41.12, pp. 2617–2629.
- Gaddum, N. et al. (2017). "Relative contributions from the ventricle and arterial tree to arterial pressure and its amplification: An experimental study". In: *American Journal of Physiology - Heart and Circulatory Physiology* 313.3, H558–H567.
- Garcia-Ortiz, L. et al. (2012). "Comparison of two measuring instruments, B-pro and SphygmoCor system as reference, to evaluate central systolic blood pressure and radial augmentation index". In: *Hypertension research: official journal of the Japanese Society of Hypertension* 35.6, 617—623.
- Ghigo, A. R. et al. (2017a). "Linear and Nonlinear Viscoelastic Arterial Wall Models: Application on Animals". In: *Journal of Biomechanical Engineering* 139.1, pp. 1–15.
- Ghigo, A. R. et al. (2017b). "Low-Shapiro hydrostatic reconstruction technique for blood flow simulation in large arteries with varying geometrical and mechanical properties". In: *Journal of Computational Physics* 331, pp. 108–136.
- Giannattasio, C. et al. (2008). "Simultaneous Measurement of Beat-to-Beat Carotid Diameter and Pressure Changes to Assess Arterial Mechanical Properties". In: *Hypertension* 52.5, pp. 896–902.
- Guilcher, A. et al. (2011). "Estimating central SBP from the peripheral pulse: Influence of waveform analysis and calibration error". In: *Journal of Hypertension* 29.7, pp. 1357–1366.
- Gurtin, M.E. and Eli Sternberg (1961). "On the quasi-static theory of viscoelasticity". In: *Archive for Rational Mechanics and Analysis* 7.1, pp. 402–411.
- Gutierrez-Lemini, D. (2014). *Engineering viscoelasticity*. Ed. by Springer. Springer, pp. 1–353.
- Hart, E. C. (2016). "Human hypertension, sympathetic activity and the selfish brain". In: *Experimental Physiology* 101.12, pp. 1451–1462.
- Hashimoto, J. and S. Ito (2010). "Pulse pressure amplification, arterial stiffness, and peripheral wave reflection determine pulsatile flow waveform of the femoral artery". In: *Hypertension* 56.5, pp. 926–933.
- Holenstein, R., P. Niederer, and M. Anliker (1980). "A viscoelastic model for use in predicting arterial pulse waves". In: *Journal of Biomechanical Engineering* 102.4, pp. 318–325.
- Hoskins, P. R., P. V. Lawford, and B. J. Doyle (2017). *Cardiovascular Biomechanics*. Springer, pp. 1–462.
- Huttunen, J. M. J. et al. (2020). "Deep learning for prediction of cardiac indices from photoplethysmographic waveform: A virtual database approach". In: *International Journal for Numerical Methods in Biomedical Engineering* 36.3, pp. 1–17.

- Ibrahim, E. S. et al. (2010). "Measuring aortic pulse wave velocity using high-field cardiovascular magnetic resonance: Comparison of techniques". In: *Journal of Cardiovascular Magnetic Resonance* 12.1, pp. 1–13.
- Jin, W. and J. Alastruey (2021). "Arterial pulse wave propagation across stenoses and aneurysms: Assessment of one-dimensional simulations against three-dimensional simulations and in vitro measurements". In: *Journal of the Royal Society Interface* 18.177.
- Kelly, R. P. (1989). "Non-invasive registration of the arterial pressure pulse waveform using high-fidelity applanation tonometry". In: *Journal of Vascular Medicine and Biology* 1.142–149.
- Kokalari, I., T. Karaja, and M. Guerrisi (2013). "Review on lumped parameter method for modeling the blood flow in systemic arteries". In: *Journal of Biomedical Science and Engineering* 06.01, pp. 92–99.
- Kondiboyina, A. et al. (2022). "Optimized design of an arterial network model reproduces characteristic central and peripheral haemodynamic waveform features of young adults". In: *Journal of Physiology* 600.16, pp. 3725–3747.
- Lakes, R. (2009). *Viscoelastic Materials*. Ed. by Cambridge University Press. Cambridge University Press.
- Latson, T. W. et al. (1986). "Time sequential prediction of ventricular-vascular interactions". eng. In: *The American journal of physiology* 251.6 Pt 2, H1341–53.
- Le Gall, A. et al. (2020). "Monitoring of cardiovascular physiology augmented by a patient-specific biomechanical model during general anesthesia. A proof of concept study". In: *PLoS ONE* 15.5, pp. 1–19.
- Leguy, C. (2019). *Cardiovascular Computing: Methodologies and Clinical Applications. Chapter 11: Mathematical and Computational Modelling of Blood Pressure and Flow*. Springer, pp. 231–246.
- Leibinger, J. et al. (2016). "A path-conservative Osher-type scheme for axially symmetric compressible flows in flexible visco-elastic tubes". In: *Applied Numerical Mathematics* 105, pp. 47–63.
- Levenson, J. A. et al. (1981). "Pulsed doppler: Determination of diameter, blood flow velocity, and volumic flow of brachial artery in man". In: *Cardiovascular Research* 15.3, pp. 164–170.
- Li, Y. et al. (2017). "Forward and Backward Pressure Waveform Morphology in Hypertension". In: *Hypertension* 69.2, pp. 375–381.
- Li, Y. et al. (2021). "Relationship between fiducial points on the peripheral and central blood pressure waveforms: rate of rise of the central waveform is a determinant of peripheral systolic blood pressure". In: *American Journal of Physiology - Heart and Circulatory Physiology* 320.4, H1601–H1608.

- Liang, F., D. Guan, and J. Alastruey (2018). "Determinant Factors for Arterial Hemodynamics in Hypertension: Theoretical Insights from a Computational Model-Based Study". In: *Journal of Biomechanical Engineering* 140.3, p. 031006.
- Liang, F. et al. (2011). "A computational model study of the influence of the anatomy of the circle of willis on cerebral hyperperfusion following carotid artery surgery". In: *BioMedical Engineering Online* 10.1, p. 84.
- Liang, F. Y. et al. (2009). "Biomechanical characterization of ventricular-arterial coupling during aging: A multi-scale model study". In: *Journal of Biomechanics* 42.6, pp. 692–704.
- Lim, S. S. et al. (2012). "A comparative risk assessment of burden of disease and injury attributable to 67 risk factors and risk factor clusters in 21 regions, 1990–2010: A systematic analysis for the Global Burden of Disease Study 2010". In: *The Lancet* 380.9859, pp. 2224–2260.
- Little, W. C. and G. L. Freeman (1987). "Description of LV pressure-volume relations by time-varying elastance and source resistance". In: *American Journal of Physiology - Heart and Circulatory Physiology* 253.1 (22/1).
- Luisada, A. A. et al. (1975). "Correlates of the Echocardiographic Waves of the Mitral Valve in Normal Subjects of Various Ages". In: *Journal of the American Geriatrics Society* 23.5, pp. 216–223.
- MacMahon, S. et al. (2008). "Blood–pressure–related disease is a global health priority". In: *The Lancet* 371, pp. 1480–1482.
- Maksuti, E. et al. (2016). "Contribution of the arterial system and the heart to blood pressure during normal aging - A simulation study". In: *PLoS ONE* 11.6, pp. 1–12.
- Mariscal-Harana, J. et al. (2021). "Estimating central blood pressure from aortic flow: development and assessment of algorithms". In: *American Journal of Physiology - Heart and Circulatory Physiology* 320.2, H494–H510.
- Matthys, K. S. et al. (2007). "Pulse wave propagation in a model human arterial network: Assessment of 1-D numerical simulations against in vitro measurements". In: *Journal of Biomechanics* 40.15, pp. 3476–3486.
- McEniery, C. M. et al. (2005). "Increased stroke volume and aortic stiffness contribute to isolated systolic hypertension in young adults". In: *Hypertension* 46.1, pp. 221–226.
- McEniery, C. M. et al. (2014). "Central blood pressure: Current evidence and clinical importance". In: *European Heart Journal* 35.26, pp. 1719–1725.
- Milišić, V. and A. Quarteroni (2004). "Analysis of lumped parameter models for blood flow simulations and their relation with 1D models". In: *Mathematical Modelling and Numerical Analysis* 38.4, pp. 613–632.

- Millasseau, S. C. et al. (2000a). "Noninvasive assessment of the digital volume pulse: Comparison with the peripheral pressure pulse". In: *Hypertension* 36.6, pp. 952–956.
- (2000b). "Noninvasive assessment of the digital volume pulse: Comparison with the peripheral pressure pulse". In: *Hypertension* 36.6, pp. 952–956.
- Mitchell, G. F. et al. (2010). "Hemodynamic correlates of blood pressure across the adult age spectrum: Noninvasive evaluation in the Framingham Heart Study". In: *Circulation* 122.14, pp. 1379–1386.
- Mitsotakis, D. et al. (2019). "On some model equations for pulsatile flow in viscoelastic vessels". In: *Wave Motion* 90, pp. 139–151.
- Montecinos, G. I., L. O. Müller, and E. F. Toro (2014). "Hyperbolic reformulation of a 1D viscoelastic blood flow model and ADER finite volume schemes". In: *Journal of Computational Physics* 266, pp. 101–123.
- Morimont, P. et al. (2012). "Arterial dP/dt maxaccurately reflects left ventricular contractility during shock when adequate vascular filling is achieved". In: *BMC Cardiovascular Disorders* 12.
- Mrsic, Z. et al. (2018). "Valvular Heart Disease". In: *Primary Care - Clinics in Office Practice* 45.1, pp. 81–94.
- Müller, L. O. and P. J. Blanco (2015). "A high order approximation of hyperbolic conservation laws in networks: Application to one-dimensional blood flow". In: *Journal of Computational Physics* 300, pp. 423–437.
- Müller, L. O., G. Leugering, and P. J. Blanco (2016). "Consistent treatment of viscoelastic effects at junctions in one-dimensional blood flow models". In: *Journal of Computational Physics* 314, pp. 167–193.
- Müller, L. O., G. I. Montecinos, and E. F. Toro (2013). "Some issues in modelling venous haemodynamics". In: *Numerical Methods for Hyperbolic Equations: Theory and Application. An international conference to honour Professor E.F. Toro*, pp. 347–354.
- Müller, L. O. and E. F. Toro (2013). "Well-balanced high-order solver for blood flow in networks of vessels with variable properties". In: *International Journal for Numerical Methods in Biomedical Engineering* 29.12, p. 2013.
- (2014a). "A global multiscale mathematical model for the human circulation with emphasis on the venous system". In: *International Journal for Numerical Methods in Biomedical Engineering* 30.7, pp. 681–725.
- (2014b). "Enhanced global mathematical model for studying cerebral venous blood flow". In: *Journal of Biomechanics* 47.13, pp. 3361–3372.

- Müller, L. O. et al. (2016). "A high-order local time stepping finite volume solver for one-dimensional blood flow simulations: application to the ADAN model". In: *International Journal for Numerical Methods in Biomedical Engineering* 32.10, e02761.
- Müller, L. O. et al. (2019). "The Selfish-Brain Hypothesis as possible cause of arterial hypertension: a modelling study". In: *6th International Conference on Computational & Mathematical Biomedical Engineering*. Sendai City, Japan, pp. 592–595.
- Munir, S. et al. (2008). "Peripheral augmentation index defines the relationship between central and peripheral pulse pressure". In: *Hypertension* 51.1, pp. 112–118.
- Murgo, J. P. et al. (1980). "Aortic input impedance in normal man: Relationship to pressure wave forms". In: *Circulation* 62.1, pp. 105–116.
- Murillo, J., A. Navas-Montilla, and P. García-Navarro (2019). "Formulation of exactly balanced solvers for blood flow in elastic vessels and their application to collapsed states". In: *Computers and Fluids* 186, pp. 74–98.
- Mynard, J. P. (2011). "Computer modeling and wave intensity analysis of perinatal cardiovascular function and dysfunction". PhD Thesis. University of Melbourne, pp. 76–125.
- Mynard, J. P. and P. Nithiarasu (2008). "A 1D arterial blood flow model incorporating ventricular pressure, aortic valve and regional coronary flow using the locally conservative Galerkin (LCG) method". In: *Communication in Numerical Methods in Engineering* 24.5, pp. 367–417.
- Mynard, J. P. and J. J. Smolich (2014). "The case against the reservoir-wave approach". In: *International Journal of Cardiology* 176.3, pp. 1009–1012.
- (2015). "One-Dimensional Haemodynamic Modeling and Wave Dynamics in the Entire Adult Circulation". In: *Annals of Biomedical Engineering* 43.6, pp. 1443–1460.
- (2017). "Wave potential: A unified model of arterial waves, reservoir phenomena and their interaction". In: *Artery Research* 18, pp. 55–63.
- Mynard, J. P. and D. A. Steinman (2012). "Effect of Velocity Profile Skewing on Blood Velocity and Volume Flow Waveforms Derived From Maximum Doppler Spectral Velocity". In: *Ultrasound in Medicine and Biology* 39.5, pp. 870–881.
- Mynard, J. P. et al. (2011). "A simple, versatile valve model for use in lumped parameter and one-dimensional cardiovascular models". In: *International Journal for Numerical Methods in Biomedical Engineering* 28.6-7, :626–41.
- Mynard, J. P. et al. (2012). "Non-linear separation of pressure, velocity and wave intensity into forward and backward components". In: *Medical and Biological Engineering and Computing* 50.6, pp. 641–648.
- Mynard, J. P. et al. (2020). "Measurement, Analysis and Interpretation of Pressure / Flow Waves in Blood Vessels". In: *Frontiers in Physiology*.

- Navas-Montilla, A. (2018). "Accurate simulation of shallow flows. Using arbitrary order ADER schemes and overcoming numerical shockwave anomalies". PhD Thesis. Universidad de Zaragoza.
- Nichols, W. W. et al. (2011). *McDonald's blood flow in arteries theoretical, experimental and clinical principles*. Ed. by CRC Press. 6th. CRC Press, pp. 1–742.
- Nürnbergger, J. et al. (2002). "Augmentation index is associated with cardiovascular risk". In: *Journal of Hypertension* 20.12, pp. 2407–2414.
- Oates, C. (2001). *Cardiovascular Haemodynamics and Doppler Waveforms Explained*. Greenwich Medical Media LTD.
- O'Rourke, M. F. and J. Hashimoto (2007). "Mechanical factors in arterial aging. A clinical perspective". In: *Journal of the American College of Cardiology* 50.1, pp. 1–13.
- O'Rourke, M. F. and G. Mancia (1999). "Arterial stiffness". In: *Journal of Hypertension* 17.1, pp. 1–4.
- O'Rourke, M. F. and W. W. Nichols (2005). "Aortic diameter, aortic stiffness, and wave reflection increase with age and isolated systolic hypertension". In: *Hypertension* 45.4 SUPPL. Pp. 652–658.
- Pagoulatou, S. et al. (2021). "The effect of left ventricular contractility on arterial hemodynamics: A model-based investigation". In: *PLoS ONE* 16.8 August, pp. 1–14.
- Pai, R. G. and P. Varadarajan (2010). "Prognostic implications of mitral regurgitation in patients with severe aortic regurgitation". In: *Circulation* 122.11 SUPPL. 1, pp. 43–47.
- Pareschi, L. and G. Russo (2001). "Implicit-explicit Runge-Kutta schemes for stiff systems of differential equations". In: *Recent trends in numerical analysis* 3.5, pp. 269–288.
- (2005). "Implicit-explicit Runge-Kutta schemes and applications to hyperbolic systems with relaxation". In: *Journal of Scientific Computing* 25.1, pp. 129–155.
- Parker, K. H. (2009). "An introduction to wave intensity analysis". In: *Medical and Biological Engineering and Computing* 47.2, pp. 175–188.
- Parker, K. H. and C. J. H. Jones (1990). "Forward and backward running waves in the arteries: Analysis using the method of characteristics". In: *Journal of Biomechanical Engineering* 112.3, pp. 322–326.
- Pauca, A. L. et al. (1992). "Does Radial Artery Pressure Accurately Reflect Aortic Pressure?" In: *Chest* 102.4, pp. 1193–1198.

- Peñáz, J. (1973). "Photoelectric measurement of blood pressure, volume and flow in the finger". In: *Proceedings of the Digest of the 10th International Conference on Medical and Biological Engineering*.
- Piccioli, F. et al. (2022a). "Modeling blood flow in networks of viscoelastic vessels with the 1-D augmented fluid-structure interaction system". In: *Journal of Computational Physics* 464, p. 111364.
- Piccioli, F. et al. (2022b). "The effect of cardiac properties on arterial pulse waves: An in-silico study". In: *International Journal for Numerical Methods in Biomedical Engineering* 38.12, e3658.
- Picone, D. S. et al. (2017). "Accuracy of Cuff-Measured Blood Pressure: Systematic Reviews and Meta-Analyses". In: *Journal of the American College of Cardiology* 70.5, pp. 572–586.
- Quarteroni, A. and L. Formaggia (2004a). *Mathematical modelling and numerical simulation of the cardiovascular system*. Ed. by N. Ayache and P. G. Ciarlet. Amsterdam: Elsevier, pp. 3–129.
- (2004b). "Mathematical Modelling and Numerical Simulation of the Cardiovascular System". In: *Computational Models for the Human Body*. Vol. 12. Handbook of Numerical Analysis. Elsevier, pp. 3–127.
- Quarteroni, A., A. Manzoni, and C. Vergara (2017). "The cardiovascular system: Mathematical modelling, numerical algorithms and clinical applications". In: *Acta Numerica* 26, pp. 365–590.
- Quarteroni, A., A. Veneziani, and C. Vergara (2016). "Geometric multiscale modeling of the cardiovascular system, between theory and practice". In: *Computer Methods in Applied Mechanics and Engineering* 302, pp. 193–252.
- Quinones, M. A., W. H. Gaasch, and J. K. Alexander (1976). "Influence of acute changes in preload, afterload, contractile state and heart rate on ejection and iso-volumic indices of myocardial contractility in man". In: *Circulation* 53.2, pp. 293–302.
- Raghu, R. et al. (2011). "Comparative study of viscoelastic arterial wall models in nonlinear one-dimensional finite element simulations of blood flow". In: *Journal of Biomechanical Engineering* 133.8.
- Randall, O. S. et al. (1976). "Arterial compliance in hypertension". In: *Australian and New Zealand Journal of Medicine* 6.s2, pp. 49–59.
- Reddy, Y. N. V. and R. A. Nishimura (2021). *Hemodynamics for the structural interventionalist*. Ed. by Charanjit S. Rihal and Claire E. Raphael. Philadelphia: Elsevier. Chap. Chapter 4, 43–56.e1.
- Reymond, P., N. Westerhof, and N. Stergiopulos (2012). "Systolic hypertension mechanisms: Effect of global and local proximal aorta stiffening on pulse pressure". In: *Annals of Biomedical Engineering* 40.3, pp. 742–749.

- Reymond, P. et al. (2009). "Validation of a one-dimensional model of the systemic arterial tree". In: *American Journal of Physiology - Heart and Circulatory Physiology* 297.1, pp. 208–222.
- Reymond, P. et al. (2011). "Validation of a patient-specific one-dimensional model of the systemic arterial tree". In: *American Journal of Physiology - Heart and Circulatory Physiology* 301.3, pp. 1173–1182.
- Sabry, F. et al. (2022). "Machine Learning for Healthcare Wearable Devices: The Big Picture". In: *Journal of Healthcare Engineering* 2022.
- Safar, Michel E., Bernard I. Levy, and Harry Struijker-Boudier (2003). "Current perspectives on arterial stiffness and pulse pressure in hypertension and cardiovascular diseases". In: *Circulation* 107.22, pp. 2864–2869.
- Salvi, P. (2012). *Pulse Waves: How Vascular Hemodynamics Affects Blood Pressure*. Ed. by Springer. Springer.
- Schultz, M. G. et al. (2013). "Exercise central (Aortic) blood pressure is predominantly driven by forward traveling waves, not wave reflection". In: *Hypertension* 62.1, pp. 175–182.
- Seed, W. A. and N. B. Wood (1971). "Velocity patterns in the aorta". In: *Cardiovascular Research* 5.3, pp. 319–30.
- Segers, P., N. Stergiopoulos, and N. Westerhof (2000). "Quantification of the contribution of cardiac and arterial remodeling to hypertension". In: *Hypertension* 36.5, pp. 760–765.
- Segers, P. et al. (2000). "Left ventricular wall stress normalization in chronic pressure-overloaded heart: A mathematical model study". In: *American Journal of Physiology - Heart and Circulatory Physiology* 279.3 48-3, pp. 1120–1127.
- Segers, P. et al. (2003). "Systemic and pulmonary hemodynamics assessed with a lumped-parameter heart-arterial interaction model". In: *Journal of Engineering Mathematics* 47.3-4, pp. 185–199.
- Seo, J. H. and R. Mittal (2013). "Effect of diastolic flow patterns on the function of the left ventricle". In: *Physics of Fluids* 25.11.
- Shapiro, Ascher H. (1977). "Steady Flow in Collapsible Tubes". In: *Journal of Biomechanical Engineering* 99, pp. 126–147.
- Sharma, G. V. R. K. et al. (2002). "Evaluation of a noninvasive system for determining left ventricular filling pressure". In: *Archives of Internal Medicine* 162.18, pp. 2084–2088.
- Sharman, J. E. et al. (2009). "Augmentation index, left ventricular contractility, and wave reflection". In: *Hypertension* 54.5, pp. 1099–1105.

- Sherwin, S. J. et al. (2003a). "Computational modelling of 1D blood flow with variable mechanical properties and its application to the simulation of wave propagation in the human arterial system". In: *International Journal for Numerical Methods in Fluids* 43.6-7, pp. 673–700.
- Sherwin, S. J. et al. (2003b). "One-dimensional modelling of a vascular network in space-time variables". In: *Journal of Engineering Mathematics* 47.3-4, pp. 217–250.
- Shroff, S. G., J. S. Janicki, and Weber (1983). "Left ventricular systolic dynamics in terms of its chamber mechanical properties". eng. In: *The American journal of physiology* 245.1, H110–24.
- (1985). "Evidence and quantitation of left ventricular systolic resistance". eng. In: *The American journal of physiology* 249.2 Pt 2, H358–70.
- Sigovan, M. et al. (2011). "Comparison of four-dimensional flow parameters for quantification of flow". In: *Journal of Magnetic Resonance Imaging* 31.1226–1230.
- Simakov, S. S. (2019). "Lumped parameter heart model with valve dynamics". In: *Russian Journal of Numerical Analysis and Mathematical Modelling* 34.5, pp. 289–300.
- Spiller, C. et al. (2017). "On the exact solution of the Riemann problem for blood flow in human veins, including collapse". In: *Applied Mathematics and Computation* 303, pp. 178–189.
- Steeds, R. P. and S. G. Myerson (2020). "Imaging assessment of mitral and aortic regurgitation: current state of the art". In: *Heart (British Cardiac Society)* 106.22, pp. 1769–1776.
- Steele, B. N. et al. (2003). "In vivo validation of a one-dimensional finite-element method for predicting blood flow in cardiovascular bypass grafts". In: *IEEE Transactions on Biomedical Engineering* 50.6, pp. 649–656.
- Stein, P. D. and H. N. Sabbah (1976). "Turbulent blood flow in the ascending aorta of humans with normal and diseased aortic valves". In: *Circulation Research* 39.1, pp. 58–65.
- Stergiopoulos, N., J. J. Meister, and N. Westerhof (1994). "Simple and accurate way for estimating total and segmental arterial compliance: The pulse pressure method". In: *Annals of Biomedical Engineering* 22.4, pp. 392–397.
- (1996). "Determinants of stroke volume and systolic and diastolic aortic pressure". In: *American Journal of Physiology - Heart and Circulatory Physiology* 270.6 39-6, H2050–H2059.
- Stettler, J. C., P. Niederer, and M. Anliker (1981). "Theoretical analysis of arterial hemodynamics including the influence of bifurcations - Part I: Mathematical model and prediction of normal pulse patterns". In: *Annals of Biomedical Engineering* 9.2, pp. 145–164.

- Suga, H., K. Sagawa, and A. A. Shoukas (1973). "Load independence of the instantaneous pressure-volume ratio of the canine left ventricle and effects of epinephrine and heart rate on the ratio." In: *Circulation research* 32.3, pp. 314–322.
- Sun, Y. et al. (1995). "Mathematical model that characterizes transmitral and pulmonary venous flow velocity patterns". In: *American Journal of Physiology - Heart and Circulatory Physiology* 268.1 37-1.
- Swillens, A. et al. (2008). "Effect of an abdominal aortic aneurysm on wave reflection in the aorta". In: *IEEE Transactions on Biomedical Engineering* 55.5, pp. 1602–1611.
- Torjesen, A. A. et al. (2014). "Forward and backward wave morphology and central pressure augmentation in men and women in the Framingham Heart Study". In: *Hypertension* 64.2, pp. 259–265.
- Toro, E. F. (2009). *Riemann Solvers and Numerical Methods for Fluid Dynamics. A Practical Introduction*. Ed. by Springer. Springer.
- (2016). "Brain venous haemodynamics, neurological diseases and mathematical modelling. A review". In: *Applied Mathematics and Computation* 272 - Part, pp. 542–579.
- Toro, E. F. and A. Siviglia (2012). "Simplified blood flow model with discontinuous vessel properties: analysis and exact solutions". In: *Modeling of Physiological Flows. MS&A — Modeling, Simulation and Applications, vol 5*. Ed. by D. Ambrosi, A. Quarteroni, and G. Rozza. Springer, pp. 19–39.
- (2013). "Flow in collapsible tubes with discontinuous mechanical properties: Mathematical model and exact Solutions". In: *Communications in Computational Physics* 13.2, pp. 361–385.
- Toro, E. F. et al. (2015). "Impact of Jugular Vein Valve Function on Cerebral Venous Haemodynamics." eng. In: *Current neurovascular research* 12.4, pp. 384–397.
- Tortora, G. J. and B. H. Defrickson (2013). *Principles of anatomy and physiology*. 12th. John Wiley & Sons, Inc.
- Valdez-Jasso, D. et al. (2009). "Analysis of viscoelastic wall properties in ovine arteries". In: *IEEE Transactions on Biomedical Engineering* 56.2, pp. 210–219.
- Valdez-Jasso, D. et al. (2011). "Linear and Nonlinear Viscoelastic Modeling of Aorta and Carotid Pressure–Area Dynamics under *in vivo* and *ex vivo* Conditions". In: *Annals of Biomedical Engineering* 39.5, pp. 1438–1456.
- Van Bortel, L M and J J Spek (1998). "Influence of aging on arterial compliance". In: *Journal of Human Hypertension* 12.9, pp. 583–586.
- Vennin, S. et al. (2017). "Identifying hemodynamic determinants of pulse pressure: A combined numerical and physiological approach". In: *Hypertension* 70.6, pp. 1176–1182.

- Vennin, S. et al. (2021). "Novel Pressure Wave Separation Analysis for Cardiovascular Function Assessment Highlights Major Role of Aortic Root". In: *IEEE Transactions on Biomedical Engineering* 69.5, pp. 1707–1716.
- Verbeke, F. et al. (2005). "Noninvasive assessment of local pulse pressure: importance of brachial-to-radial pressure amplification". In: *Hypertension* 46.1, pp. 244–8.
- Vermeersch, S. J. et al. (2009). "The reservoir pressure concept: The 3-element windkessel model revisited? Application to the Asklepios population study". In: *Journal of Engineering Mathematics* 64.4, pp. 417–428.
- Wang, T. et al. (2021). "Machine learning-based pulse wave analysis for early detection of abdominal aortic aneurysms using in silico pulse waves". In: *Symmetry* 13.5.
- Wang, X. F., J. M. Fullana, and P. Y. Lagrée (2015). "Verification and comparison of four numerical schemes for a 1D viscoelastic blood flow model". In: *Computer Methods in Biomechanics and Biomedical Engineering* 18.15, pp. 1704–1725.
- Wang, Z. and N. C. Chesler (2012). "Role of collagen content and cross-linking in large pulmonary arterial stiffening after chronic hypoxia". In: *Biomechanics and Modeling in Mechanobiology* 11.1-2, pp. 279–289.
- Wang, Z., M. J. Golob, and N. C. Chesler (2016). "Viscoelastic Properties of Cardiovascular Tissues". In: *Viscoelastic and Viscoplastic Materials*. Chap. 7, pp. 141–163.
- Weber, T. et al. (2004). "Arterial Stiffness, Wave Reflections, and the Risk of Coronary Artery Disease". In: *Circulation* 109.2, pp. 184–189.
- Weber, T. et al. (2010). "Pulse waveform characteristics predict cardiovascular events and mortality in patients undergoing coronary angiography". In: *Journal of Hypertension* 28.4, pp. 797–805.
- Wesseling, K. H. (1995). "Physiocal, calibrating finger vascular physiology for Finapres". In: *Homeostasis* 36.1, pp. 67–82.
- Westerhof, N., J. W. Lankhaar, and B. E. Westerhof (2009). "The arterial Windkessel model". In: *Medical and Biological Engineering and Computing* 47.2, pp. 131–141.
- Westerhof, N. and A. Noordergraaf (1970). "Arterial viscoelasticity: a generalized model Effect on input impedance and wave travel in the systematic tree". In: *Journal of Biomechanics* 3.3, pp. 357–379.
- Westerhof, N. and B. E. Westerhof (2017). "Waves and Windkessels reviewed". In: *Artery Research* 18, pp. 102–111.
- Westerhof, N. et al. (1972). "Forward and backward waves in the arterial system". In: *Cardiovascular Research* 6.6, pp. 648–656.
- Westerhof, N. et al. (2019). *Snapshots of Hemodynamics: An Aid for Clinical Research and Graduate Education*. 3rd. Springer.

- White, F. M. (1998). *Fluid Mechanics*. Fourth edit. New York: McGraw-Hill Higher Education, p. 1023.
- Willemet, M. and J. Alastruey (2014). "Arterial Pressure and Flow Wave Analysis Using Time-Domain 1-D Hemodynamics". In: *Annals of Biomedical Engineering* 43.1, pp. 190–206.
- (2015). "Arterial Pressure and Flow Wave Analysis Using Time-Domain 1-D Hemodynamics". In: *Annals of Biomedical Engineering* 43.1, pp. 190–206.
- Willemet, M., S. Vennin, and J. Alastruey (2016). "Computational assessment of hemodynamics-based diagnostic tools using a database of virtual subjects: Application to three case studies". In: *Journal of Biomechanics* 49.16, pp. 3908–3914.
- Williams, B. et al. (2018). "2018 ESC/ESH Guidelines for the management of arterial hypertension". In: *Journal of Hypertension* 36, pp. 1953–2041.
- Womersley, J. R. (1955). "XXIV. Oscillatory motion of a viscous liquid in a thin-walled elastic tube—I: The linear approximation for long waves". In: *The London, Edinburgh, and Dublin Philosophical Magazine and Journal of Science* 46.373, pp. 199–221.
- Wylie, E. B. and V. L. Streeter (1978). *Fluid Transients*. First edition. New York: McGraw-Hill Series International Book company, p. 384.
- Xiao, N., J. Alastruey, and C. A. Figueroa (2014). "A systematic comparison between 1-D and 3-D hemodynamics in compliant arterial models". In: *International Journal for Numerical Methods in Biomedical Engineering* 30.2, pp. 204–231.
- Xu, J. and G. P. Shi (2014). "Vascular wall extracellular matrix proteins and vascular diseases". In: *Biochimica Biophysica Acta* 1842.11, pp. 2106–2119.
- Zambanini, A. et al. (2005). "Wave-energy patterns in carotid, brachial, and radial arteries: A noninvasive approach using wave-intensity analysis". In: *American Journal of Physiology - Heart and Circulatory Physiology* 289.1 58-1, pp. 270–276.
- Zamir, M. (2000). *The Physics of Pulsatile Flow*. Ed. by AIP Press. Springer.
- Zhou, B. et al. (2017). "Worldwide trends in blood pressure from 1975 to 2015: a pooled analysis of 1479 population-based measurement studies with 19.1 million participants". In: *The Lancet* 389.10064, pp. 37–55.
- Zócalo, Y. et al. (2008). "Regional differences in veins wall viscosity, compliance, energetics and damping: Analysis of the pressure-diameter relationship during cyclical overloads". In: *Biological Research* 41.2, pp. 227–233.